

DISSERTATION

SPECTROSCOPIC ELLIPSOMETRY AS A PROCESS CONTROL TOOL FOR
MANUFACTURING CADMIUM TELLURIDE THIN FILM PHOTOVOLTAIC DEVICES

Submitted by

Westcott P. Smith

Department of Mechanical Engineering

In partial fulfillment of the requirements

For the Degree of Doctor of Philosophy

Colorado State University

Fort Collins, Colorado

Spring 2013

Doctoral Committee:

Advisor: Allan T. Kirkpatrick

Co-Advisor: Susan James

Christian Puttlitz

W.S. Sampath

Mingzhong Wu

Copyright by Westcott P. Smith 2013

All Rights Reserved

ABSTRACT

SPECTROSCOPIC ELLIPSOMETRY AS A PROCESS CONTROL TOOL FOR MANUFACTURING CADMIUM TELLURIDE THIN FILM PHOTOVOLTAIC DEVICES.

In recent decades, there has been concern regarding the sustainability of fossil fuels. One of the more promising alternatives is Cadmium Telluride (CdTe) thin-film photovoltaic (PV) devices. Improved quality measurement techniques may aid in improving this existing technology. Spectroscopic ellipsometry (SE) is a common, non-destructive technique for measuring thin films in the silicon wafer industry. SE results have also been tied to properties believed to play a role in CdTe PV device efficiency. A study assessing the potential of SE for use as a quality measurement tool had not been previously reported.

Samples of CdTe devices produced by both laboratory and industrial scale processes were measured by SE and Scanning Electron Microscopy (SEM). Mathematical models of the optical characteristics of the devices were developed and fit to SE data from multiple angles and locations on each sample. Basic statistical analysis was performed on results from the automated fits to provide an initial evaluation of SE as a quantitative quality measurement process. In all cases studied, automated SE models produced average stack thickness values within 10% of the values produced by SEM, and standard deviations for the top bulk layer thickness were less than 1% of the average values.

ACKNOWLEDGEMENTS

I am very grateful to my advisor, Dr. Allan Kirkpatrick, for his guidance throughout the writing of this dissertation. Without his help, this dissertation could not have reached the publication phase. I am also very grateful to my former advisor, Dr. Venkatesan Manivannan, for his encouragement throughout my research. I express my sincere thanks to my committee members, Drs. Susan James, Christian Puttlitz, W.S. Sampath, and Mingzhong Wu, for the time they have devoted to my doctoral studies.

I thank the National Renewable Energy Laboratory, Abound Solar, Inc., and J.A. Woollam, Inc., for providing tours of their facilities, information, and funding for related projects. I would also like to thank James Hilfiker at J.A. Woollam, Inc., for developing an initial material model and his advice and guidance. I thank the faculty and staff of the Central Instrument Facilities at CSU, particularly Sandeep Kholi and Pat McCurdy, and the Ellipsometry team at NREL, particularly Dean Levi and Xuanzhi Wu, for their time, the use of their equipment, and guidance in obtaining raw data used in this project.

I thank my fellow students within the materials and photovoltaics groups for their cooperation and assistance. I am particularly grateful to Toby Dhooge for his assistance with 3D CAD drawings presented in the appendix, and Paul Kobayakov, who provided assistance with XRD and SEM work.

Finally, I would like to thank my parents for their extraordinary patience and support during this time.

TABLE OF CONTENTS

Preliminaries

Abstract..	ii
Acknowledgments.	iii
Table of Contents..	iv
List of Tables.	viii
List of Figures.	xiii
List of Symbols..	xviii
List of Equations.	xxi

Text

1. Introduction.	1
1.1. Global Energy Supply and Demand.	1
1.2. Advantages of CdTe Photovoltaics as a Potential Solution.	3
1.3. Colorado State University's CdTe Manufacturing Process.	6
1.3.1. Deposition System Used prior to late 2010.	6
1.3.2. CSU Device Characterization Capabilities.	9
1.4. Spectroscopic Ellipsometry.	10
1.4.1. Optical Theory..	11
1.4.2. SE Operation, Data Collection, and Analysis.	20
1.4.3. Advantages of SE for Photovoltaic Study..	26
1.5. WVASE32 SE Software..	29
1.5.1. Ellipsometer Setup and Raw Data Collection Tasks.	30
1.5.2. Model Creation and Editing Tasks.	33

1.5.3. Modeling Optimization and Data Analysis Tasks..	34
1.6. Summary and Conclusions.	36
2. Objectives and Experimental Methodology.	38
2.1. Objectives.	38
2.2. Contributions of Work..	41
2.3. Methodology..	42
2.3.1. Woollam Study.	43
2.3.2. Baseline Study..	49
2.3.3. Multiple Angle Study.	52
2.3.4. Multiple Position Study.	53
2.3.5. Industrial Device Study.	55
2.3.6. Verification of Model Accuracy and Precision.	57
2.4. Summary and Conclusions.	58
3. Results.	60
3.1. Woollam Study Results.	61
3.1.1. SE Data and Model Values.	61
3.1.2. Results Derived from the Model Values..	76
3.1.3. XRD Results.	79
3.1.4. SEM Results.	80
3.2. Baseline Study.	81
3.2.1. TEC-15 Sample.	81
3.2.2. CdS Sample.	86
3.2.3. CdTe Sample..	91

3.2.4. Cl-Treated Sample..	96
3.2.5. Cu-Treated Sample.	100
3.2.6. Br-Treated Sample..	104
3.2.7. Overall Results..	109
3.3. Multiple Angle Study.	110
3.4. Multiple Position Study.	117
3.4.1. TEC-15 Sample.	118
3.4.2. CdS Sample.	121
3.4.3. CdTe Sample..	123
3.4.4. Cl-Treated Sample..	126
3.4.5. Cu-Treated Sample.	129
3.4.6. Br-Treated Sample..	131
3.4.7. Overall Results..	134
3.5. Industrial Device Study.	136
4. Discussion.	153
4.1. Statistical Significance..	157
4.2. Applicability of SE Data to Device Quality..	159
5. Summary and Conclusions.	163
5.1. Scientific Incentive.	163
5.2. Summary of Work.	164
5.3. Key Findings..	164
5.4. Specific Contributions to the Body of Knowledge.	166

Supplementaries

Bibliography.	168
Appendices.	177
Appendix 1. Additional Data.	177
Appendix 2. Additional Images.	188
A2.1. Photograph of the Deposition System.	188
A2.2. WVASE32 Screenshot Images.	188
Appendix 3. Practical Use Study	193
List of Abbreviations, Units, and Model Numbers.	197

LIST OF TABLES

2.1	Objectives.	41
3.1	Overview of Studies Presented in this Chapter.	60
3.2	Layer Thickness and Lorentz Oscillator Terms for Various Layers of TEC-15 Glass (values from reference [43]).	63
3.3	Fitted Thicknesses for Different Layers for Cl- and Cu-treated CdTe/CdS PV Device on TEC-15 Glass (values from reference [43]).	73
3.4	Summary of Values Measured for Completed Device (values from reference [43]).	73
3.5	Values for Individual Samples (values from reference [43]).	75
3.6	Fitted Thicknesses for Different Layers for the Woollam Study Cl- and Cu-treated Samples (values from reference [43]).	76
3.7	Various Energy Components for the CdTe Layer (values from reference [43]).	78
3.8	Summary of Selected Parameter Values for Woollam and Baseline Studies of TEC-15 Samples.	83
3.9	Summary of Selected Parameter Values for Woollam and Baseline Studies of CdS Samples.	88
3.10	Summary of Selected Parameter Values for Woollam and Baseline Studies of CdTe Samples.	93
3.11	Summary of Selected Parameter Values for Woollam and Baseline Studies of Cl-treated Samples.	99
3.12	Summary of Selected Parameter Values for Woollam and Baseline Studies of Cu-treated Samples.	103
3.13	Summary of Selected Parameter Values for the Baseline Study of the Br-treated Sample.	107
3.14	Stack Values for Woollam, Baseline SE, and Baseline SEM Studies.	110
3.15	Selected Multiple Angle Study Results for the TEC-15 Sample.. . . .	111
3.16	Selected Multiple Angle Study Results for the CdS Sample.. . . .	111

3.17	Selected Multiple Angle Study Results for the CdTe Sample.	112
3.18	Selected Multiple Angle Study Results for the Cl-treated Sample.. . . .	113
3.19	Selected Multiple Angle Study Results for the Cu-treated Sample.	114
3.20	Selected Multiple Angle Study Results for the Br-treated Sample.. . . .	114
3.21	Summary of Stack Thickness Values for the Multiple Angle Study and SEM.	115
3.22	Summary of Anderson-Darling Normality Testing for the Multiple Angle Study. Cells for non-normal distributions at 95% certainty are grayed.	115
3.23	Summary of SD% Values for the Multiple Angle Study. Cells Representing the Uppermost Bulk Layer are Highlighted.	115
3.24	Average Values at Various Locations for the TEC-15 Sample Multiple Position Study.	119
3.25	SD% Values for the TEC-15 Sample Multiple Position Study.	119
3.26	Anderson-Darling Normality Test P-Values for the TEC-15 Sample Multiple Position Study.	120
3.27	Average Values for the CdS Sample Locations.	121
3.28	Standard Deviation to Average Value Ratios for the CdS Sample Multiple Position Study.	121
3.29	Anderson-Darling Normality Test P-values for the CdS Sample Multiple Position Study.	122
3.30	Average Values for the CdTe Sample Locations.	124
3.31	Standard Deviation to Average Value Ratios for the CdTe Sample Multiple Position Study.	124
3.32	Anderson-Darling Normality Test P-values for the CdTe Sample Multiple Position Study.	124
3.33	Average Values for the Cl-treated Sample Locations.	127
3.34	Standard Deviation to Average Value Ratios for the Cl-treated Sample Multiple Position Study.	127

3.35	Anderson-Darling Normality Test P-values for the Cl-treated Sample Multiple Position Study.	127
3.36	Average Values for the Cu-treated Sample Locations.	130
3.37	Standard Deviation to Average Value Ratios for the Cu-treated Sample Multiple Position Study.	130
3.38	Anderson-Darling Normality Test P-values for the Cu-treated Sample Multiple Position Study.	130
3.39	Average Values for the Br-treated Sample Locations.	132
3.40	Standard Deviation to Average Value Ratios for the Br-treated Sample Multiple Position Study.	132
3.41	Anderson-Darling Normality Test P-values for the Br-treated Sample Multiple Position Study.	132
3.42	Summary of Stack Thickness Values for the Multiple Position Study.. . . .	135
3.43	% Difference Between SE and SEM Values (positive values indicate the SE model produced a thicker stack than SEM)..	135
3.44	Maximum Values for Standard Deviation to Average Ratio.. . . .	136
3.45	Optimization Results for Panel Location 9.. . . .	138
3.46	Optimization Results for Panel Location 12.	141
3.47	Optimization Results for Panel Location 21.	143
3.48	Optimization Results for Panel Location 25.	145
3.49	Optimization Results for Panel Location 30.	147
3.50	Optimization Results for Panel Location 41.	149
3.51	Summary of Stack Thickness Values for the Industrial Device Study.	150
3.52	Summary of Anderson-Darling Normality Testing Results for the Industrial Device Study.	150
3.53	Summary of SD% Values for the Industrial Device Study.	150

4.1	Portion of Distributions Testing Normal at Various Confidence Levels..	158
A1.1	Data for 3"x3" TEC-15 Sample Location C (center).	177
A1.2	Data for 3"x3" TEC-15 Sample Location O1.	178
A1.3	Data for 3"x3" TEC-15 Sample Location O2.	178
A1.4	Data for 3"x3" TEC-15 Sample Location O3.	178
A1.5	Data for 3"x3" TEC-15 Sample Location O4.	178
A1.6	Data for 3"x3" CdS Sample Location C (center).	179
A1.7	Data for 3"x3" CdS Sample Location O1.	179
A1.8	Data for 3"x3" CdS Sample Location O2.	179
A1.9	Data for 3"x3" CdS Sample Location O3.	180
A1.10	Data for 3"x3" CdS Sample Location O4.	180
A1.11	Data for 3"x3" CdTe Sample Location C (center).	180
A1.12	Data for 3"x3" CdTe Sample Location O1.	180
A1.13	Data for 3"x3" CdTe Sample Location O2.	181
A1.14	Data for 3"x3" CdTe Sample Location O3.	181
A1.15	Data for 3"x3" CdTe Sample Location O4.	181
A1.16	Data for 3"x3" Cl-treated Sample Location C (center).	182
A1.17	Data for 3"x3" Cl-treated Sample Location O1.	182
A1.18	Data for 3"x3" Cl-treated Sample Location O2.	182
A1.19	Data for 3"x3" Cl-treated Sample Location O3.	183
A1.20	Data for 3"x3" Cl-treated Sample Location O4.	183
A1.21	Data for 3"x3" Cu-treated Sample Location C (center).	183
A1.22	Data for 3"x3" Cu-treated Sample Location O1.	184

A1.23	Data for 3"x3" Cu-treated Sample Location O2.	184
A1.24	Data for 3"x3" Cu-treated Sample Location O3.	184
A1.25	Data for 3"x3" Cu-treated Sample Location O4.	184
A1.26	Data for 3"x3" Br-treated Sample Location C (center).	185
A1.27	Data for 3"x3" Br-treated Sample Location O1.	185
A1.28	Data for 3"x3" Br-treated Sample Location O2.	185
A1.29	Data for 3"x3" Br-treated Sample Location O3.	186
A1.30	Data for 3"x3" Br-treated Sample Location O4.	186
A1.31	Data for 16"x16" Panel Location 9.. . . .	186
A1.32	Data for 16"x16" Panel Location 12.	186
A1.33	Data for 16"x16" Panel Location 21.	187
A1.34	Data for 16"x16" Panel Location 25.	187
A1.35	Data for 16"x16" Panel Location 30.	187
A1.36	Data for 16"x16" Panel Location 41.	187

LIST OF FIGURES

1.1	TEC-15 Glass Structure.	8
1.2	Schematic of Typical Layered Structure of Samples Produced Using the CSU ERC Manufacturing System.	8
1.3	Optimized SE Model of a Si-SiO ₂ device.	11
1.4	Poincare Sphere.	13
1.5	Light Reflections Due to Material Surfaces.	14
1.6	Ellipsometer Concept.	21
1.7	SE Model Concept.	23
1.8	Typical SE Modeling Process.	24
2.1	General SE Process Diagram.	43
2.2	Woollam Study Concept.	43
2.3	Repeatability Study Concept.	53
2.4	Locations Used for the Multiple Position Study.	54
2.5	Industrial Device Study Concept.	55
2.6	Locations Selected for Industrial Device Study.	56
3.1	Ψ Plots for the Woollam TEC-15 Study.	62
3.2	Δ Plots for the Woollam TEC-15 Study.	62
3.3	n and k Plots for the Woollam TEC-15 Study.	63
3.4	Ψ Plots for the Woollam CdS Study.	65
3.5	Δ Plots for the Woollam CdS Study.	66
3.6	n and k Plots for the Woollam CdS Study.	66
3.7	Ψ Plots for the Woollam CdTe Study.	68
3.8	Δ Plots for the Woollam CdTe Study.	68

3.9	n and k Plots for the Woollam CdTe Study.	69
3.10	Ψ Plots for the Woollam Cl-treated Study.	70
3.11	Δ Plots for the Woollam Cl-treated Study.	70
3.12	Ψ Plots for the Woollam Cu-treated Study.	71
3.13	Δ Plots for the Woollam Cu-treated Study.	71
3.14	n and k Plots for the Woollam Cl-treated Study.	72
3.15	n and k Plots for the Woollam Cu-treated Study.. . . .	72
3.16	Modeled Real (ϵ_1) and Imaginary (ϵ_2) Dielectric Components for the CdTe Layer of Selected Samples (images from reference [43]).	77
3.17	Tauc Plots for CdTe Layer (image from reference [43]).	78
3.18	Second-order Derivative of the Real (ϵ_1) and Imaginary (ϵ_2) Components of the Dielectric Constant from various models (images from reference [43]).	79
3.19	Cross-section SEM Images of Woollam Study Samples. (images from reference [43]).	80
3.20	Ψ Plots for the TEC-15 Baseline Study.	82
3.21	Δ Plots for the TEC-15 Baseline Study.	82
3.22	n and k Plots for the Baseline TEC-15 Study.	83
3.23	SEM Image of TEC-15 Sample.	84
3.24	Ψ Plots for the Baseline CdS Study.	87
3.25	Δ Plots for the Baseline CdS Study.	87
3.26	n and k Plots for the Baseline CdS Study.	88
3.27	SEM Image of CdS Sample.	89
3.28	Ψ Plots for the Baseline CdTe Study.. . . .	92
3.29	Δ Plots for the Baseline CdTe Study.. . . .	92

3.30	n and k Plots for the Baseline CdTe Study..	93
3.31	SEM Image of CdTe Sample..	94
3.32	Ψ Plots for the Baseline Cl-treated Study.	97
3.33	Δ Plots for the Baseline Cl-treated Study.	98
3.34	n and k Plots for the Baseline Cl-treated Study.	98
3.35	SEM Image of Cl-treated Sample.	99
3.36	Ψ Plots for the Baseline Cu-treated Study.	101
3.37	Δ Plots for the Baseline Cu-treated Study.	102
3.38	n and k Plots for the Baseline Cu-treated Study.	102
3.39	SEM Image of Cu-treated Sample.	103
3.40	Ψ Plots for the Baseline Study for the Br-treated Sample.	105
3.41	Δ Plots for the Baseline Study for the Br-treated Sample.	106
3.42	n and k Plots for the Baseline Study for the Br-treated Sample.	106
3.43	SEM Image of the Br-treated Sample.	107
3.44	Locations Used for the Multiple Position Study.	118
3.45	SEM Image of TEC-15 Sample from Offset Location..	120
3.46	SEM Image of CdS Sample from Offset Location..	123
3.47	SEM Image of CdTe Sample from Offset Location.	126
3.48	SEM Image of Cl-treated Sample from Offset Location..	129
3.49	SEM Image of Cu-treated Sample from Offset Location.	131
3.50	SEM Image of Br-treated Sample from Offset Location..	134
3.51	Ψ Plots for Panel Location 9.	137
3.52	Δ Plots for Panel Location 9.	138

3.53	SEM Image for Panel Location 9..	139
3.54	Ψ Plots for Panel Location 12.	140
3.55	Δ Plots for Panel Location 12.	140
3.56	SEM Image for Panel Location 12.	141
3.57	Ψ Plots for Panel Location 21.	142
3.58	Δ Plots for Panel Location 21.	142
3.59	SEM Image for Panel Location 21.	143
3.60	Ψ Plots for Panel Location 25.	144
3.61	Δ Plots for Panel Location 25.	144
3.62	SEM Image for Panel Location 25.	145
3.63	Ψ Plots for Panel Location 30.	146
3.64	Δ Plots for Panel Location 30.	146
3.65	SEM Image for Panel Location 30.	147
3.66	Ψ Plots for Panel Location 41.	148
3.67	Δ Plots for Panel Location 41.	148
3.68	SEM Image for Panel Location 41.	149
4.1	Detail of Supplemental SEM Image of the Bromine-treated Sample.	154
A2.1	Engineering Research Center Solar Cell Manufacturing Facility Undergoing Renovation and Modifications in 2010.	188
A2.2	Screen Capture of WVASE32.	189
A2.3	“Experimental Data” Window.	190
A2.4	“Graph” Window.	190
A2.5	“Model” Window.	191
A2.6	User-Defined “Genosc” Layer Window.	191

A2.7	EMA Layer Window.	192
A2.8	MSE Test Results Window.. . . .	192
A3.1	Proposal for Installation of In-situ SE Capability into the ADS (model by Toby Dhooge)..	194
A3.2	Ellipsometry Bay Windows (model by Toby Dhooge).	195
A3.3	Ellipsometer Mounting Rack (model by Toby Dhooge)..	196

LIST OF SYMBOLS

<u>symbol</u>	<u>description</u>
<u>alphabetic</u>	
A	amplitude
A_f	amplitude of a forcing function
c	speed of light in the medium
C	broadening coefficient
E	Energy, also known as field strength or photon energy
e	base of the natural logarithm
E_0	peak transition energy of a photon prior to striking a surface, also known as electric field strength or initial energy.
E_g	optical band gap
h	Planck's constant
\hbar	Dirac constant ($h/2\pi$)
i	square root of -1
j	counting integer
k	extinction coefficient
m	mass
m_*	carrier effective mass
m_e	electron rest mass
N	carrier concentration
n	index of refraction
n_{dp}	number of data points sampled
n_v	number of model variables being optimized

P	Cauchy principal part
q_e	elementary charge (charge of an electron)
$R(\nu)$	complex response of a system with respect to ν
$R_e(\varepsilon)$	real part of ε
r_p	portion of light reflected by a surface in the polarization direction parallel to the plane formed by the incident and reflected beams
r_s	portion of light reflected by a surface in the polarization direction perpendicular to the plane formed by the incident and reflected beams
t	time
t_p	portion of light transmitted through a surface in the direction parallel to the plane formed by the incident and reflected beams
t_s	portion of light transmitted through a surface in the direction perpendicular to the plane formed by the incident and reflected beams
x	general variable
X and Y	2D rectilinear coordinate system
X , Y , and Z	3D rectilinear coordinate system
$x_{j,me}$	measured value of the j^{th} data point
$x_{j,mo}$	value predicted by a model for the j^{th} data point
z	displacement along the direction of propagation of a beam of light
<u>greek</u>	
α	absorption coefficient
γ	dampening coefficient
Δ	for elliptically – polarized light, the phase shift between the x and y components of polarization, equal to the eccentricity of the polarization ellipse.
$\Delta_{j,me}$	measured Δ value for the j^{th} wavelength
$\Delta_{j,mo}$	Δ value generated by a mathematical model for the j^{th} wavelength

∇	Laplace operator
ε	dielectric coefficient (complex number)
ε_0	Permittivity (dielectric coefficient) of a vacuum
ε_1	real part of ε , representing the storage capacity
ε_2	imaginary part of ε , represents energy dissipation
ε_∞	limit of $\varepsilon(E)$ as E becomes arbitrarily large, used by WVASE32 software as a fitting parameter.
θ_i	angle of incidence (the angle between a beam of light striking a surface and the surface normal at that point)
θ_t	angle of transmission (the angle between a beam of light transmitted through a surface and the surface normal at that point)
κ	spring constant
λ	wavelength
μ	carrier mobility
ν	frequency
ν_0	resonance frequency
ν_f	Forcing frequency
ξ	integration parameter representing a range of possible energy values
π	ratio of the circumference of a circle to its diameter
ρ	resistivity
σ	standard deviation
τ	scattering time
Ψ	for elliptically – polarized light, the angle of the major axis of polarization, equal to the angle of the major axis of the polarization ellipse.
$\Psi_{j,me}$	measured Ψ value for the j^{th} wavelength
$\Psi_{j,mo}$	Ψ value generated by a mathematical model for the j^{th} wavelength

LIST OF EQUATIONS

1.1	Wave Equation.	11
1.2	Photon Energy – Wavelength Relation.. . . .	12
1.3	Simplified Form of Fresnel’s Equations.	15
1.4	Dielectric Equation.	16
1.5	Definition of the Refractive Index.	16
1.6	Definition of the Extinction Coefficient.	16
1.7	Mechanical Oscillator System Under a Forcing Function.	17
1.8	Drude’s Original Electrical Oscillator Equation.	17
1.9	Modern Version of Drude’s Oscillator Equation.. . . .	18
1.10	Sum of Drude-Lorentz Oscillators.	18
1.11	Tauc-Lorentz Oscillator Model.. . . .	19
1.12	How Polarization State Data Is Related to Reflected Light Intensity.	21
1.13	Traditional Definition of MSE.	23
1.14	Definition of NSE Used By WVASE.	35
2.1	Drude Model Equation Used In This Study.	45
2.2	Tauc Law Formula.	46
2.3	Modified Tauc-Lorenz Model Used By WVASE32.. . . .	46
3.1	Definition of the Absorption Coefficient.. . . .	77

Introduction

1.1. Global Energy Supply and Demand.

While the current period of history has been one of great technological and scientific discovery, many believe the world's problems are growing more rapidly than they are being solved. Dr. Richard Smalley, a Nobel Laureate, argued that the current challenges facing humanity could be reduced to a “top 10 list” [1], and Smalley presents energy as the top concern. Most experts expect energy demand to grow substantially during the next century. In 2002, it was estimated that the world had used energy at an estimated average rate equivalent to 13.2 terawatts (1 terawatt (TW) = 10^{12} watts) during the previous year [2]; in 2011 energy use was projected to reach approximately 26 TW by 2035 and 40-50 TW by 2100 [3, 4].

In 2001, approximately 85% of energy used was produced by consumption of fossil fuels of some kind [2]. While fossil fuels have proven a highly effective power source, they suffer from two serious drawbacks: limited supply and pollution. While there are enough fossil fuels to supply the world's current needs for the next few decades and beyond [5], all economically viable current fossil fuel solutions produce considerable amounts of carbon dioxide [6, 7]. While carbon dioxide can be toxic to humans at high concentrations [8], much lower levels of carbon dioxide have been correlated to changes in Earth's climate in the fossil record [9]. Some models have predicted melting ice may raise the world's sea level [10], causing major problems for cities worldwide. To alleviate these concerns, many hope that “alternative energy”-the sources providing the remaining 15%, including such sources as wind and biofuels-will be able to one day replace fossil fuels as the dominant source of human energy. However, there are major

challenges that must be overcome if these energy sources are to provide a larger portion of future energy demand.

For some forms of alternative energy, such as hydroelectric, geothermal, tidal power, and algae production [11], the primary issue is geographic availability. While the theoretical energies available are huge, current technology limits the locations where power can be produced in an economically viable manner to only small areas of the Earth's surface. As a result, it is unlikely these sources will be able to provide more than several hundred gigawatts each without major breakthroughs. In the case of wind, while much of Earth's surface receives useful levels of wind, many windy areas are unsuitable due to local issues such as inconsistent wind patterns and public safety concerns. As a result, the practical limits of wind power are unclear. Some have suggested the practical global availability may be as low as 2 TW [12].

Other forms of alternate energy suffer from low energy density. For example, traditional biofuels such as corn ethanol, while an effective solution for niche markets, requires vast amounts of land to produce enough energy to compete with fossil fuels. In fact, it can be calculated from data [13] that to supply the 3.3 TW used by the United States in 2007, nearly two thirds of the nation's land area would be needed. Given the need for non-biofuel land to produce food, shelter wildlife, etc., clearly this is not sustainable. Similarly, early solar energy technologies provided less than 1% efficiency, translating to nearly 10% of the Earth's surface being required to convert the human energy economy to an all-solar future. In recent years, solar energy has seen huge advances in efficiency, with some devices achieving efficiencies of over 40% [14], but such devices are not economically viable at scales beyond laboratory use and niche markets where extreme costs are acceptable such as spacecraft.

Nuclear energy has enormous advantages due to having the highest energy density fuel of any current technology, but that fuel produces radioactive waste, which can create a severe health hazard, as seen at nuclear accident sites such as Three Mile Island, Chernobyl, and Fukushima. As a result, the costs for safeguarding nuclear reactors and nuclear material from accidental (or for that matter, deliberate) release are quite high; it is estimated that the cost of building a new nuclear plant today would be over twice the cost of building a fossil fuel plant generating equal amounts of power [15]. To provide many terawatts of power, many thousands of power plants would be required a task that may be too formidable for the current political environment, given that even providing safe storage for nuclear waste from existing plants has proven technically and politically difficult [16]. Historically, relative to the amount of energy produced per year, solar energy, while providing much less risk in case of a catastrophic accident, has been even more expensive. While more recent advances have made solar energy a much more competitive technology [17], typical costs are still around \$5.46 per watt, compared with \$2.10 for coal [18].

In summary, each of the alternative energy solutions faces its own combination of challenges that limit the ability to scale to levels where they could begin to replace fossil fuels as the primary energy source for human civilization. While there is plenty of energy for the next few decades, if we are to meet the expected 40 TW of global demand by 2100 and simultaneously limit the level of carbon dioxide to environmentally acceptable levels, it will likely require new innovations and breakthroughs that overcome these challenges.

1.2. Advantages of Cadmium Telluride Photovoltaics as a Potential Solution.

There are many reasons to pursue photovoltaics as a potential element in a future global energy solution. Every region of Earth receives useful amounts of solar energy during some part

of a typical year. Practical photovoltaic power supply systems have been built as small as a few square centimeters (to power an electronic calculator), and as large as multiple megawatt farms, offering the ability to place energy infrastructure wherever it is desired. The available energy density in space is over 1kW (1 kilowatt = 10^3 watts) per square meter, and even though Earth's surface receives less than a quarter of that on the average, Earth still receives far more energy from the sun than humans are expected to require in the foreseeable future. For example, at 20% efficiency, the roof space of all residential neighborhoods in the United States could supply much of the nation's energy use [19]. New forms of photovoltaics are beginning to approach the values necessary to make competitive solar energy a reality. As solar energy becomes more common, installation costs are likely to drop as manufacturers and installers develop better techniques.

For much of the history of photovoltaics, research focused on silicon wafer devices. While the materials required to produce early designs were abundant, the manufacturing techniques were technically delicate and labor intensive, resulting in a cost per watt that was only cost competitive for niche markets such as spacecraft. To improve on this, a number of strategies have been explored, one of which has been thin film devices. While thin film devices require a substrate, the amount of primary material required per device is very small, and the initial manufacturing process is generally entirely automated. A number of materials unsuitable for use in traditional photovoltaic manufacturing have shown promise for use in thin film photovoltaic devices, including Cadmium Telluride (CdTe).

The single biggest advantage of CdTe devices is the material cost. No other photovoltaic technology has been demonstrated on a commercial level to be producible at costs below \$1 per watt. Currently, First Solar Corporation is selling CdTe devices at prices approaching \$1/watt,

and current research suggests costs as low as 50 cents per watt may be achievable [20]. The energy required to produce a thin-film cell is also typically lower than that of traditional silicon cells, and CdTe devices are currently approaching a 1-year energy payback time [21], meaning that in its first year of use, a device will produce enough energy to manufacture its replacement.

Without efficiency, the cost of photovoltaic devices is not sufficient to drive a viable solution because of land use and support structure cost issues. Efficiency of commercially available devices is ~9%, though efficiencies as high as 13% are expected in the coming years [22], laboratory-scale manufacturing has produced devices over 16% [23], and higher efficiencies may be possible. Thermal issues and interaction between the device band gap and the solar spectrum provide a fundamental limitation of approximately 30% for a single band gap device [24]. CdTe is well positioned in the solar spectrum; so theoretically, efficiencies above 25% may be possible.

In order to be scalable to terawatt scales, sufficient material must be available. Tellurium is one of the rarest elements on earth, but recently, new reserves for earthly mining have been discovered [25] that should allow many terawatts worth of photovoltaic capacity to be manufactured at current efficiency levels. Another rare element, indium, is used in manufacture of the conductive surface of the film, but other solutions are available, such as fluorinated tin oxide (FTO). Cadmium is known to have toxicity effects at sufficiently high concentrations. However, because the amount used is only a few micrometers thick, the total release over the lifetime of a device is less than the cadmium released by burning the amount of coal that would provide the same amount of energy [26].

Preliminary life testing data also suggests CdTe may also be among the most durable of current photovoltaic technologies. The lifetime of a photovoltaic device is defined for laboratory

purposes as the time until the device is reduced in efficiency due to normal wear to 80% of the efficiency achieved by the cell when it came off the production line. Historically, for silicon-wafer-based solar panels, the target minimum lifetime has been about 20 years. Although historic data is not available for CdTe devices, preliminary data suggest a projected lifetime of 65 years [27].

As a result, while CdTe has not yet achieved the point where it is competitive with the cheaper forms of current energy, there is much reason to believe that with sufficient research and development, it could become a major component of a future energy supply mix. This research and development will require measurement techniques suited for the study of thin films. The objective of this research is to examine one of these techniques.

1.3. Colorado State University's CdTe Manufacturing Process.

To provide test samples of CdTe devices, Colorado State University (CSU) has developed a laboratory research and development facility in the Engineering Research Center (ERC). In 2010, this system underwent major modifications to enable production of a wider variety of layer designs. For this study, all samples used were manufactured prior to the modifications.

1.3.1. Deposition System Used prior to late 2010.

The original system could manufacture CdTe solar cells up to approximately 3.6" x 3.1" x 1/8" (91 mm x 79 mm x 3.2 mm) in size. Smaller cells were manufactured by inserting the substrate into a carrier plate. It was fully automated, with a typical cycle time of two minutes. The cells passed through several stations before emerging out the other side nearly complete. The system deposited material under a low-level vacuum (10^{-2} Pascals (Pa)) protected by seals which seal with the sides of the glass as the glass enters the vacuum area. The temperature,

deposition rate, and time-on-station for each stage could be varied by programming in necessary values. In addition, any combination of steps could be skipped. Devices began and ended the production process in a shirtsleeves laboratory environment close to standard temperature and pressure; however, only minimal environmental control was used, and the facility is at approximately 5,000 feet altitude. Photographs and schematics of the original system have been published [27]. A photograph of the system undergoing modification is shown in the appendix.

While the production facility produced samples with multiple sizes, thicknesses, and sources for substrates, the samples for this project all used "TEC-15 glass" substrates provided by Pilkington glass in the United Kingdom. The "TEC" series glass products are designed for technical applications. TEC-15 glass consists of four layers, as shown in Figure 1.1. The glass thickness is precisely controlled, and multiple thicknesses are available. Once a substrate entered the low pressure area of the deposition system it was subjected to the following processes: heating to the deposition system operating temperature, deposition of layers of Cadmium Sulfide (CdS) and CdTe , deposition of Cadmium Chloride (CdCl_2), heat treatment, annealing, stripping, ohmic contact formation via Copper Chloride (CuCl) deposition, and contact annealing. The CdCl_2 and CuCl deposition (often referred to as "Cl treatment" and "Cu treatment", respectively) did not produce distinct layers in the finished product. The general structure of a typical device produced by the deposition system is shown in Figure 1.2. Once devices exit the deposition chamber, they can be divided into cells by either sandblasting or laser etching, and contacts installed for performance testing. However, laboratory multimeters could be attached to unmodified cells if desired.

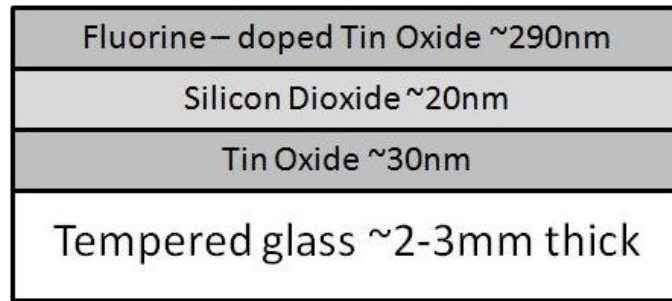


Figure 1.1: TEC-15 Glass Structure.



Figure 1.2: Schematic of Typical Layered Structure of Samples Produced Using the CSU ERC Manufacturing System.

Devices produced by this facility had consistent average efficiencies of over 10%. Individual batches had average efficiencies as high as 12.6%, and the National Renewable Energy Laboratory (NREL), located in Golden, Colorado, rated a champion device at 12.77%. Accelerated life testing over a 5,167 hour run showed a decrease in efficiency of less than 2% of the original output. After a 7,000 hour run outdoors, devices showed no statistically significant decrease. Based on this data, an expected lifetime of 65 years for CdTe cells was estimated [27].

The disposition system was able to operate within 10% of the desired deposition rate after 12 hours of continuous operation, demonstrating the potential of the manufacturing technology to operate on a larger scale with reasonable maintenance requirements. As a demonstration of the manufacturability of CSU's CdTe technology, a spinoff of the laboratory production line at CSU, a facility at Abound Solar, Inc., produced both 16 inch (16" or 400 mm) square and 2 foot by 4 foot (0.6m x 1.2m) panels between 2004 and 2012, at a rate that would allow a single facility to supply panels for a 1 Megawatt (MW, or 10^6 watts) installed capacity power plant.

1.3.2. CSU Device Characterization Capabilities.

CSU has used several techniques at multiple on-campus and outside facilities for analysis of solar cells. A preliminary characterization lab is available in the ERC, adjacent to the deposition system facility. A second performance measurement and diagnostic facility is located in the Engineering building on the main campus. Most of the remaining instruments commonly used to study the cells are located in the Central instrument Facility (CIF) in the Chemistry complex on the CSU main campus. CSU-manufactured photovoltaic devices have also been studied at outside facilities including laboratories at NREL and the J.A. Woollam Company in Nebraska.

Overall efficiency measurements are performed at the ERC using current-vs.-voltage-curve testing. The production facility also includes a reflectometer and accelerated life testing facility with a custom lamp setup. Devices are characterized before and after life testing to provide a projected life expectancy for the sample. Efficiency mapping is a standard technique applicable throughout the photovoltaic industry. The technique measures current and voltage produced by the device when a narrow beam of light is shone on the surface, allowing a map of the surface to be provided, showing fluctuations in output with position on the surface of the cell. While these systems provide a highly detailed image of performance, they do not provide data on material process quality.

Techniques available include profilometry, X-ray diffraction (XRD), X-Ray fluorescence (XRF), scanning electron microscopy (SEM), and spectroscopic ellipsometry (SE). The Veeco Dektak 150 profilometer uses a ball-tipped pin to detect the thickness of a film by physical contact. A scan of the surface away from the film area is used to determine a baseline, and distances as small as a few tens of nanometers can be measured. XRD is regarded as an industry

standard in thin film solar cell measurements as it is able to detect properties of material in the film to a high degree of precision. SEM is also a very important technique in this field, and provides a detailed view of film structure and can provide information on grain size, vacancies, and film thicknesses, as well as being potentially able to measure material composition through an attached electron or X-ray scattering sensor. SE is similar to X-Ray diffraction in that it measures the effect of radiation on a surface, but the ellipsometer uses a range of wavelengths that includes the visible spectrum and portions of infrared and ultraviolet.

1.4. Spectroscopic Ellipsometry.

SE is a technique for studying materials, polarization of light, refraction, and reflection. In recent decades, it has been commercialized as a specialized tool for quality measurement of thin films. While SE provides direct measurement of how a surface affects light, indirectly it has been shown to detect not only optical properties, but also physical properties such as film thickness and surface roughness. This is possible because of the nature of light and the large amount of data that can be collected from a single sample.

However, the need to take many measurements meant that while the optical theory behind SE had been largely set in place by Maxwell, Spottiswoode, and Drude [28, 29] prior to 1900, early ellipsometers were generally only of use in basic science as the rate of information that could be collected was quite limited. The dawn of the modern computer age allowed numerically controlled ellipsometers to automatically step through polarization states and collect data electronically. The latest high speed ellipsometers can perform a lower-resolution scan fast enough that data can be taken on silicon wafers on an assembly line without stopping the line [30].

While SE is not a well-known technique generally, it is a known technique in the silicon wafer industry. In fact, a silicon dioxide (SiO₂) thin film on a silicon (Si) substrate has become the industry standard for SE measurements, and is typically used for calibration samples. The optical properties of this material combination are sufficiently well-known that optimizations representing little more than device error are routinely achieved in only a minute of calculations, as shown in the screenshot in Figure 1.3, and changes in silicon dioxide thickness of less than 0.1% can be detected.

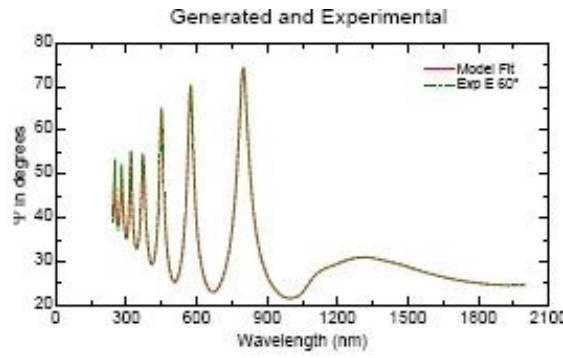


Figure 1.3: Optimized SE Model of a Si-SiO₂ device.

1.4.1. Optical Theory.

According to wave theory, light consists of a magnetic field and an electric field at right angles to each other. Both the magnetic and electric field components of a light wave can be represented as components in the X and Y directions, so that there are 4 linear wave components, but they are not independent. All four components will have the same wavelength and will also be in phase, with the amplitude of the Y component of the magnetic field varying linearly with the amplitude of the X component of the electric field, and vice versa. Mathematically, this is represented by the wave equation, one version of which is

$$\left(\nabla^2 - c^{-2} \left(\frac{d^2}{dt^2} \right) \right) E = 0 \quad (1.1)$$

where ∇ is the Laplace operator, c is the wave speed in the medium, t is time, and E is the field strength. Moreover, the maximum overall amplitude is defined by the photon energy, which is related to the wavelength by

$$E = h\nu = \frac{hc}{\lambda} \quad (1.2)$$

where E is the energy, h is Planck's constant, ν is the frequency, c is the speed of light in the medium, and λ is the wavelength. Thus the state of a single photon can be fully represented by a location, direction, energy, polarization angle, and phase shift.

However, in a given light beam, there will generally be many photons in any given wavelength band and volume. The field that represents the sum of any number of photons will have a potentially varying phase shift between the X and Y components of the electric field. Thus we can model light as having a polarization phase shift between the X and Y components at any given wavelength. If one imagines being able to see this sum of fields as one looks into the beam of light with the X and Y components of each field equal and offset by a phase shift of zero or 180° , each of the two fields would appear to trace out a sloping line. If the fields are equal and the phase shift is 90° or 270° , the fields trace out a circular path. Otherwise, an ellipse will result. This can be mathematically represented by two angles:

Ψ : the angle of the major axis of the ellipse, from $+90^\circ$ to -90° , and

Δ : the phase shift between the X and Y components, from $+180^\circ$ to -180° .

Poincare [31] mapped polarization states onto the surface of an imaginary three dimensional sphere with center at $(0, 0, 0)$ and radius 1, now known as a Poincare sphere, as sketched in Figure 1.4. Averaging a number of these polarization states on the imaginary Poincare sphere surface yields a position somewhere inside the sphere. Measuring the distance from the center point provides a means of measuring how polarized the resulting light beam

would be. For example, a location 90% of the way from the center of the sphere to its surface is said to be 90% polarized [31].

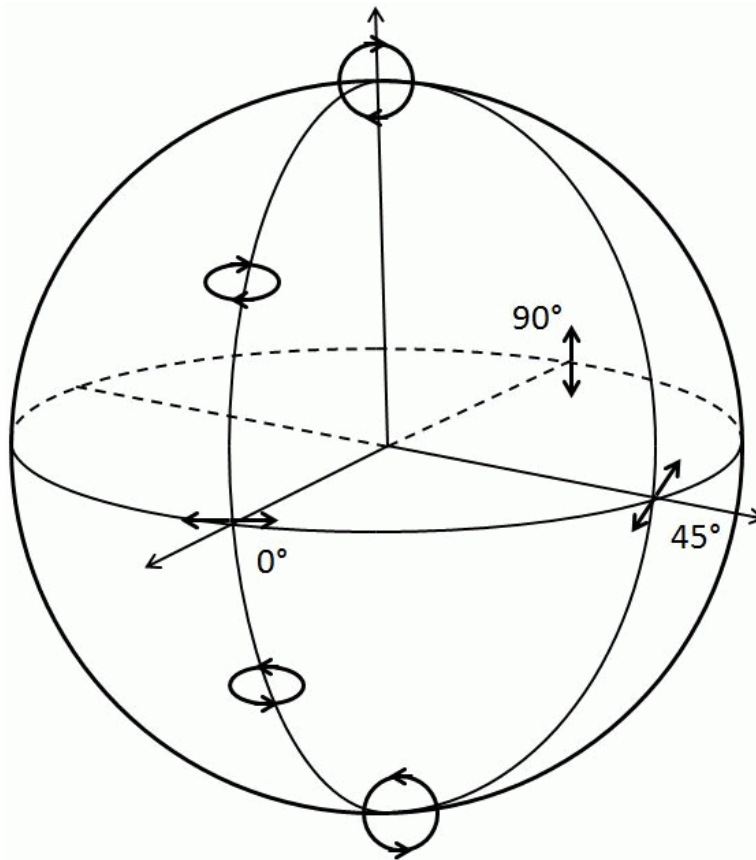


Figure 1.4: Poincare Sphere.

When light strikes a surface, it splits the beam in accordance with Maxwell's equations [32]. Except in cases where total internal reflection occurs [33], a portion is deflected into the material at a different angle than the incident beam depending on the index of refraction of the two materials [34], a portion is reflected, and a portion may be absorbed, as shown in Figure 1.5. Additional light may be absorbed as the transmitted and reflected beams travel. While some information about a surface, such as color, could be gleaned from looking at a single reflection, a pair of reflections can provide additional data. If two parallel surfaces are close enough to each other in comparison to the wavelength of light, the reflected beams from each surface will form

an interference effect [34]. The two beams are said to be linked at a quantum level. If the surfaces are farther away, the reflected beams are no longer linked, and rather than producing an interference effect, they simply add, reducing the usefulness of the data [35]. In the case of a thin film providing two linked beams, information about the two surfaces and the material between them will then be contained in the resulting light beam. While some of this information is provided by the energy level variations with wavelength, or spectrum, of the resulting beam, the majority of the information will be contained in the polarization states of the resulting photons [36].

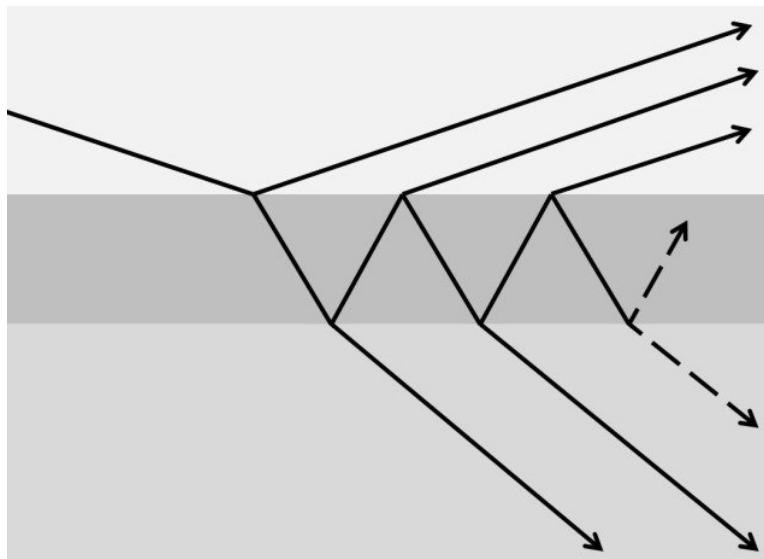


Figure 1.5: Light Reflections Due to Material Surfaces.

As light reflects or transmits at a surface, the polarization state of the resulting beam may be altered if the material is optically anisotropic [37]. In fact, precisely machined blocks of anisotropic materials are used in the manufacture of some ellipsometers for the purpose of changing linear polarization to circular [38]. However, even isotropic materials will generate a polarization state change. This can seem counter-intuitive, but is due in part because, at a surface, all materials have an anisotropic characteristic in that the surface has a normal direction. Polarization that is in the plane formed by the incoming ray and the surface normal is called p-

polarization, and polarization parallel to the surface is known as s-polarization [39]. Depending on material properties and the angle of incidence, reflected light polarized in the p-direction (referred to as p-polarized light) is affected differently from light polarized in the s-direction (referred to as s-polarized light). This effect is the result of Fresnel's equations, the generalized form of which is discussed in detail elsewhere [40]. The simplified form typically used in SE calculations is

$$r_s = \frac{n_1 \cos \theta_i - n_2 \cos \theta_t}{n_1 \cos \theta_i + n_2 \cos \theta_t} \quad (1.3)$$

$$t_s = \frac{2n_1 \cos \theta_i}{n_1 \cos \theta_i + n_2 \cos \theta_{tr}}$$

$$r_p = \frac{n_2 \cos \theta_i - n_1 \cos \theta_t}{n_1 \cos \theta_t + n_2 \cos \theta_i}$$

$$t_p = \frac{2n_1 \cos \theta_i}{n_1 \cos \theta_t + n_2 \cos \theta_i}$$

where r_s and t_s represent the portion of light reflected and transmitted, respectively, in the direction perpendicular to the plane formed by the incident and reflected beams; r_p and t_p represent the portion of light reflected and transmitted, respectively, in the direction parallel to the plane formed by the incident and reflected beams; n_1 and n_2 represent the index of refraction in the materials containing the incident and transmitted light, respectively; and θ_i and θ_t represent the angles of incidence and transmission, respectively. Under a given set of conditions, materials have a “Brewster angle” at which p-polarized light reaching a surface is not reflected, and all that remains is the s-polarized light [40]. Total internal reflection is another special case of Fresnel's equations for reflection, which predict that above the total internal reflection angle, reflected light is always phase shifted.

Mathematically, Fresnel's equations also predict that a phase shift between the s and p-polarized components of a beam will be induced when the index of refraction for a material is not a real number but a complex one [35]. The dielectric equation, which defines a relationship between the dielectric coefficient, index of refraction, and extinction coefficient [41], provides just such a complex value. This equation is

$$\varepsilon = \varepsilon_1 + i\varepsilon_2 = (n + ik)^2 \quad (1.4)$$

where n is index of refraction, k is the extinction coefficient, ε is the dielectric coefficient as a complex number, ε_1 is the real part of ε , ε_2 is the imaginary part of ε , and i is the square root of negative one. The real component ε_1 represents the storage capacity of the medium while the imaginary component ε_2 represents energy dissipation in the medium [35]. Materials that have a high extinction coefficient, such as CdTe, will introduce a significant phase shift, so that linearly polarized light will be reflected as elliptically polarized light.

The index of refraction of a material determines the angle at which light is refracted through a material according to the relationship

$$n_1 \sin(\theta_i) = n_2 \sin(\theta_t) \quad (1.5)$$

where n_1 and n_2 are the indices of refraction in two materials, and θ_i and θ_t are the angles of incidence and transmission, respectively. The extinction coefficient of a material determines the amount of light absorbed by a material, according to the equation

$$E(z, t) = e^{-2\pi k z} R_e(E_0 e^{i(kz - \nu t)}) \quad (1.6)$$

where E is the energy at time t , z is the distance the beam has propagated at time t , e is the base of the natural logarithm, π is the ratio of the circumference of a circle to its diameter, R_e indicates the real part, E_0 is the initial energy, i is the square root of -1, k is the extinction coefficient, and ν is the frequency. The values of n and k , and thus both parts of the dielectric,

can vary with wavelength. The polarization state of reflected and transmitted light is related to the material properties and angle of incidence as described by the Fresnel equations [34, 40].

When a photon interacts with a material, in addition to exciting electrons to a higher stable level, photons can also push on the atomic structure, causing a localized change in atomic vibration. For many materials, there will be many atoms, molecules, and lattice positions having similar potential vibration modes that can be triggered by this process, each with a characteristic "resonant frequency". This is known as an oscillator. The derivation of the equation for an oscillator is analogous to a mechanical oscillator system under a forcing function, derived by Newton as

$$m \frac{d^2x}{dt^2} + m\gamma \frac{dx}{dt} + \kappa x = A_f \cos(\nu_f t) \quad (1.7)$$

where t is time, x is the system response, m is the system mass, γ is a damping coefficient, κ is the spring constant, A_f is the forcing function amplitude, and ν_f is the forcing frequency [35].

Drude [35] solved this mechanical oscillator equation for an electrical system by substituting in the mass of an electron for the system mass, the charge of an electron multiplied by its electric field amplitude for the oscillator amplitude, and $e^{i\nu t}$ for $\cos(\nu t)$, resulting in

$$R(\nu) = \frac{q_e}{m_e} \frac{E_0}{\nu_0^2 - \nu_f^2 - i\gamma\nu_f} \quad (1.8)$$

where $R(\nu)$ is the complex response, q_e is the charge of an electron, m_e is the electron mass, E_0 is the electric field amplitude, ν_0 is the resonant frequency, and ν_f is the forcing frequency. For many materials, there is more than one resonance condition (e.g., the electron shell can vibrate relative to the nucleus, atomic nuclei can vibrate relative to each other, etc.), and these do not all have the same resonant frequency. Since the degrees of freedom for this resonance are

independent, they are additive. Multiplying through by Planck's constant, defining A_j as $q_e E_0 \hbar / m_e$ and E_j as $\hbar \nu_0$, and summing over multiple oscillators, one gets

$$R(\nu) = \sum_j \left(\frac{A_j}{E_j^2 - (\hbar \nu_f)^2 - i\gamma(\hbar \nu_f)} \right) \quad (1.9)$$

where ν_f is the forcing wavelength, \hbar is Planck's constant, γ is the dampening coefficient, i is the square root of -1, E_j is the resonance energy of the j^{th} oscillator, A_j is the electrical energy of the electron for the j^{th} oscillator, and $R(\nu)$ is the complex response. Note that the oscillator center value E_j is equal to the photon energy associated with the resonant frequency of one or more resonance degrees of freedom for the atomic structure of the material.

In the case Drude was interested in, $\gamma \ll E_j$, so that if it is *not* the case that $|(E_j - \hbar \nu_f)| \ll E_j$, the $i\gamma(\hbar \nu_f)$ term can be safely neglected, and as ν_f goes to zero, the right-hand side of equation 1.9 becomes $\sum_j (A_j / E_j^2)$; as ν_f goes to infinity, $R(\nu)$ goes to zero, suggesting that the oscillator dies down to a constant value. In fact, for most materials, the real part of the dielectric function at very high frequency radiation approaches a constant representing the electron gas behavior of the material as a plasma [35]. Thus the equation for a sum of Drude-Lorentz oscillators is

$$\epsilon_1(\hbar \nu) = \epsilon_\infty + \sum_j \left(\frac{A_j}{E_j^2 - (\hbar \nu_f)^2} \right) \quad (1.10)$$

The Drude oscillator, used primarily for metallic substances, represents a special case of equation 1.10, where $E_j = 0$, which is true for electrons already in the conductivity band. Drude's oscillator equation assumes that the oscillator has no dampening. While this was a good approximation for cases where E_j is well outside the frequencies studied, it does not model cases where E_j is close to the range of frequencies studied.

To increase their usefulness, many of the more recently-developed oscillator models also include a broadening coefficient. Physically, the broadening coefficient represents the effects of dampening in the oscillator as well as variations in the resonant frequency from atom to atom.

For example, the Tauc-Lorentz oscillator is modeled as

$$\varepsilon_1 = \varepsilon_\infty + \sum_{n=1}^3 \frac{2}{\pi} P \left(\int_0^\infty \left(\frac{\xi \cdot \varepsilon_2(\xi)}{\xi^2 - E^2} - E^2 \right) d\xi \right) \quad (1.11)$$

where

$$\varepsilon_2 = \frac{1}{E} \cdot \frac{A_j E_j C (E - E_g)^2}{(E^2 - E_j^2)^2 + C^2 E^2} \quad E > E_g$$

$$\varepsilon_2 = 0 \quad E < E_g$$

and where ε_1 and ε_2 are the real and imaginary parts, respectively, of the complex dielectric, P represents the Cauchy principal part, E is the energy at a given wavelength, ξ is an integration parameter representing the range of possible energies, A_j is the amplitude associated with the j^{th} oscillator, E_j represents energy associated with the j^{th} oscillator, C is a broadening term, E_g is the optical band gap, and ε_∞ is an additional fitting parameter [35]. The PSEMI oscillator has an additional set of parameters that allow the model to represent a non-symmetric oscillation effect. The resulting curve has a broader tail on one end. This can be due to interaction between the oscillations and the band gap, often due to noncrystallinity. The broadening coefficient, C , is said to be mathematically linked to E_j and A_j so that as E_j becomes large compared to $h\nu$, the effects of an oscillator with large C and small A_j on the n and k curves becomes similar to those for an oscillator with large A_j and small C . Also, as E_j approaches 0, the effect of the oscillator on the oscillator region studied will tend to approach the Drude model.

In addition to the dielectric properties and oscillators within a material, surface roughness also plays an important role in how a surface reflection affects polarization. Individual rays of

light may encounter different localized angles of incidence or layer thickness. As a result, the reflectance, phase shift, and interference effects that normally occur may vary with location within a given area. This will introduce depolarization, particularly in frequency ranges where absorption is highest, because the reflected light will be more due to surface reflection than reflections within the material, which will appear on a plot of Ψ and Δ polarization shift as noise. For semiconductors, high frequency light is preferentially absorbed, so noise will be seen at lower wavelengths [42].

1.4.2. SE Operation, Data Collection, and Analysis.

A highly simplified schematic diagram of a spectroscopic ellipsometer setup is shown in Figure 1.6. Most devices that detect light only detect the total amount of energy that falls on the detector within a very broad range of photon energy levels. To measure the portion of energy received within a given frequency range, a series of filters are used, including polarization filters which can be rotated to allow measurement in any given polarization direction. In order to measure how a material reflects light, the polarization and spectrum of incoming light must be known. While theoretically, a detector could simply sense the ambient light in the environment, a more efficient, precise, and useful method is to precisely control the incoming light beam. Therefore, ellipsometers are typically designed to operate in a darkened environment, and use a set of lamps which produce a clean, white light that is stable over a wide range of wavelengths. The light source can be filtered as well. While the detector can be used to scan this light source directly, most current ellipsometers use a calibration sample instead.

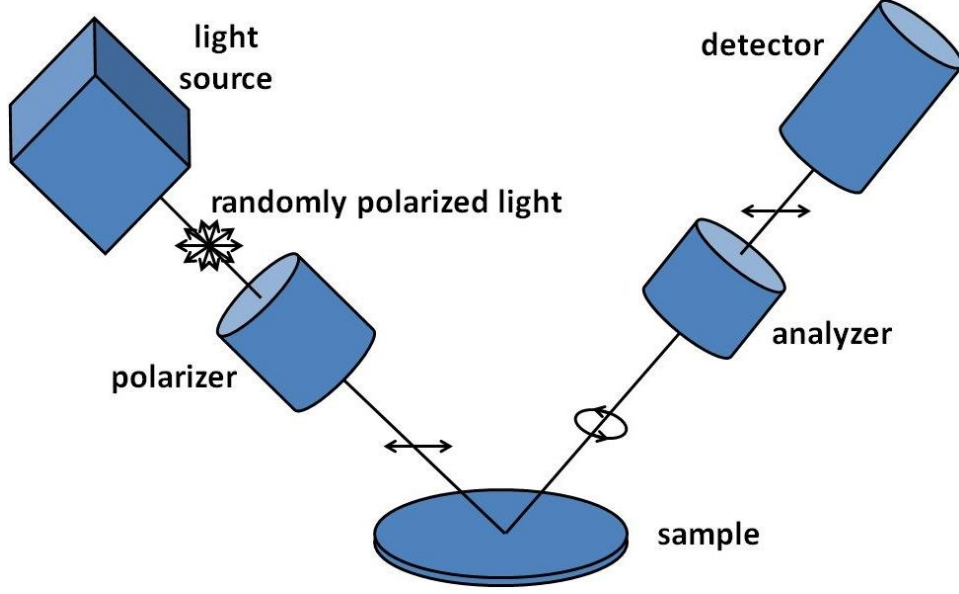


Figure 1.6: Ellipsometer Concept.

Ellipsometer raw data consists of a table of instrument optical geometry, polarization settings, and energy levels. Because energy levels can be measured for every combination of sample location, angle of incidence, wavelength, and polarization state, the amount of data obtainable from one sample can be considerable. This raw data is only meaningful in the context of the particular hardware setup. Converting that data into more useful information is a task involving a large amount of calculations.

Polarization state data is related to reflected light intensity by the equation

$$\frac{r_p}{r_s} = \tan(\Psi)e^{i\Delta} \quad (1.12)$$

where r_p and r_s represent the reflected light as a fraction of the incident light in the directions parallel and perpendicular to, respectively, the plane formed by the incident and reflected beams, Ψ is the angle of the polarization direction, and Δ is an angle indicating eccentricity of the polarization ellipse [35]. These conversion equations have been extensively studied and automated into software packages, so the calculations are typically done by the data collection

software in real time. The Ψ and Δ data is device-independent, and thus may be modeled separately from the data collection process.

To determine the material properties, a model is preloaded into a simulation and the model output compared to the data. The model contains a mathematical representation of a “best guess” of the thin film’s characteristics, with data on layers, thicknesses, and optical properties such as n , k , and oscillators. The data contains algorithms to allow the software to simulate a beam of light encountering the surface and create Ψ and Δ plots of the simulated reflected and transmitted light as shown in Figure 1.7. Because the model is optimized later, it is not critical that thickness values are highly accurate, but the materials present, optical properties of those materials and layer structure must closely represent the actual structure in order to provide simulated data that is close enough to the experimental data to be meaningful. Developing a model is itself an iterative process, as models can be improved due to outside measurements and trial and error as well as optimization. Initial models are developed from data based on measurements taken from other techniques such as microscopy or XRD, as well as SE measurements of standard samples, and supposition. Often, alternate model concepts are tested using optimization to the data, and the models that provide the best initial optimization result are then further modified until a single champion model is selected for final optimization.

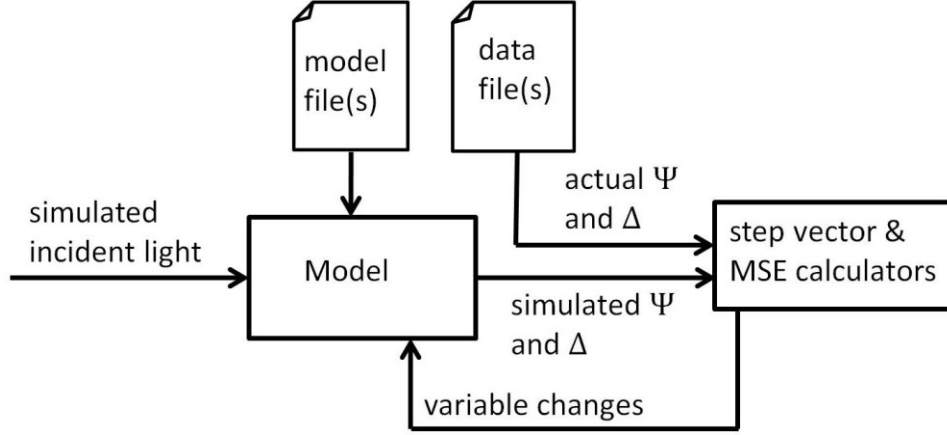


Figure 1.7: SE Model Concept

Optimization is typically performed against a single optimization variable that measures the difference between the data and model values for the Ψ and Δ values over the wavelengths and angles selected, such as the mean square error (MSE). Traditionally, MSE is defined as

$$\text{MSE} = \frac{1}{n_{\text{dp}}} \sum_{j=1}^{n_{\text{dp}}} (x_{j,\text{mo}} - x_{j,\text{me}})^2 \quad (1.13)$$

where n_{dp} is the number of data points sampled, j is a counting integer, and $x_{j,\text{mo}}$ and $x_{j,\text{me}}$ are the values predicted by the model and measured, respectively, for the j^{th} data point. However, because SE typically measures more than one variable (e.g., Ψ and Δ) for each data point, most optimization techniques use a different definition. Variables are selected for optimization, the optimization parameter is determined, and a fitting algorithm is used to determine a step vector. The step vector process is shown schematically in Figure 1.7. The optimization parameter is then recalculated, and so on, until a preset stopping condition is reached. The user then manually adjusts the software settings and tries again, until the model is judged sufficient. A flowchart of the overall modeling process is shown in Figure 1.8.

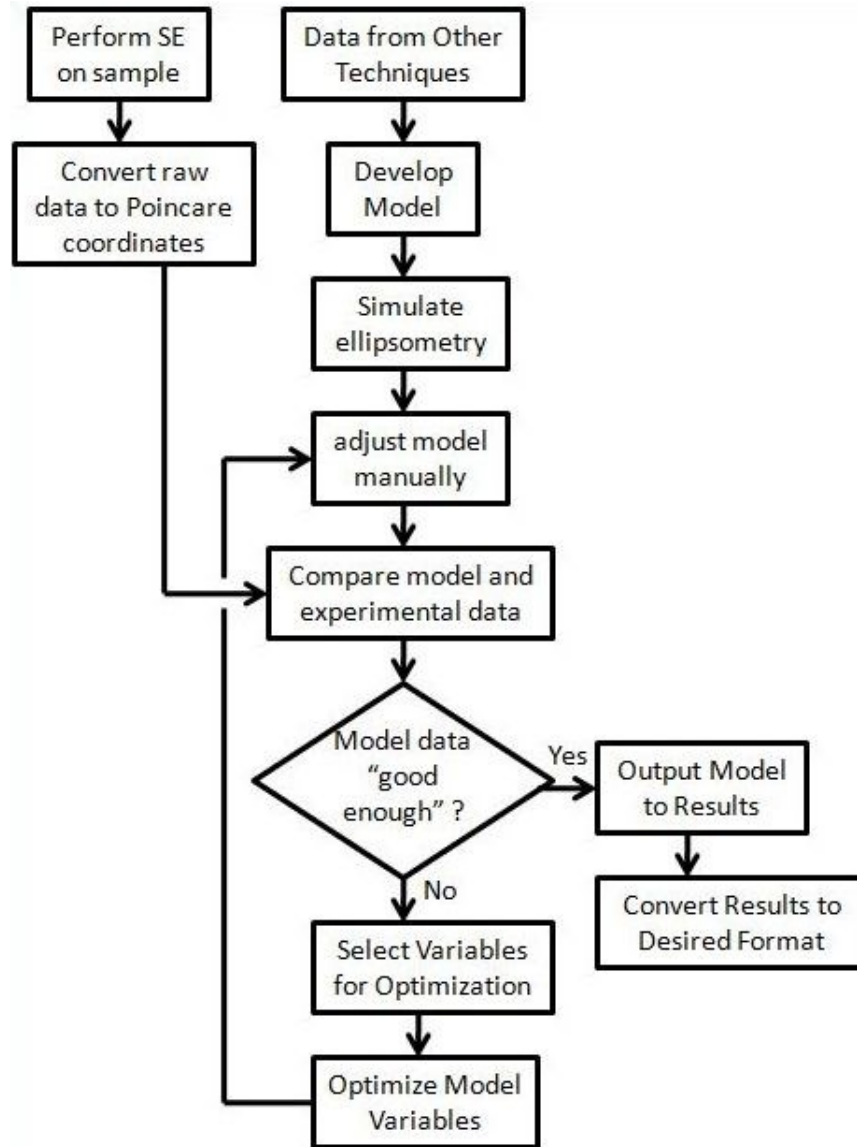


Figure 1.8: Typical SE Modeling Process.

Given that even simple models can have dozens of variables, the resulting mathematical situation can be imagined as a many-dimensional field with numerous local minimums. For any such situation, there will be a range of starting values, settings, etc. for which the model will optimize to the correct one. Typically, provided the model is based on known quantum interaction principles, the lowest MSE minimum will represent the "correct" solution, and the other local minimums are false positives. Selecting an initial model and settings that will

optimize to the correct solution can be a challenge even for an expert, and as it is usually not advisable to optimize against all variables at once, the selection of the sequence in which variables are optimized may also effect whether the model optimizes to an accurate representation of the material.

Analysis can take anywhere from seconds to days, depending on the quality of the data, model, and optimization strategy. In some cases, where the material is well characterized and variation modes are known, optimization can be fully automated. Otherwise, a human expert is needed to run a series of optimizations, changing model design and optimization parameters until a useful model is produced. Fortunately, efforts have been conducted on the behavior of actual materials in the laboratory to provide libraries of materials so that models are based on known facts rather than conjecture. Once an optimized model is judged sufficient, the final model parameter values are output as the results of the SE process.

Data from SE models can then be used for various purposes. For many applications, such as quality control for the thickness of SiO_2 films deposited on Si wafers, the model values are sufficient; however SE has also been used in conjunction with other techniques to produce a more complete picture of a thin film material. Though relatively few studies have done so, theoretically, with sufficient data, SE can be used for statistical analysis or as one of multiple techniques for correlation studies. Because SE provides such detailed information on the optical properties of a material, and optical properties are related to electrical and physical properties through oscillators and basic properties such as the index of refraction, it is believed that SE may be able to detect phenomena such as changes in grain structure [43].

1.4.3. Advantages of SE for Photovoltaic Study.

Optical properties of materials are important for photovoltaic materials as they represent the first step in the photovoltaic process: light capture. Extinction coefficient and thickness are what allows a material to absorb light; refractive index also aids in determining how effective a material is at capturing light at an angle. SE provides the capacity to measure the optical properties of a material in more detail than all but a few other techniques [44]. It can provide the n , k , and dielectric values over a wide spectrum range as well as the thickness of the material.

In the silicon wafer industry, the use of SE to measure layer thickness (and sometimes surface roughness as well) is a standard practice. However, SE can also be used to measure other physical properties. SE can model intermixes and oscillator values which may correspond to physically important material characteristics. Correlations between SE data and materials properties determined by other methods have been studied [43]. These studies found correlations between many properties, suggesting a link between SE-measurable data and difficult-to-measure properties such as crystallinity, grain structure, doping levels, and so on.

At the NREL in Golden Colorado, a vacuum chamber laboratory production facility for nanocrystalline silicon thin-film device manufacture was recently constructed with a custom-modified ellipsometer bolted to the chamber for fixed-angle in-situ measurements. According to a paper by Dean Levi et al [45], in addition to the normal properties measured by SE, it was discovered that the thickness of the film at the transition from amorphous to nanocrystalline growth correlated to conductivity. Because Photovoltaic (PV) devices convert optical energy into electrical energy, the ability of an optical technique to potentially measure electrical properties is of interest to PV research.

While there are numerous useful nondestructive methods of detecting properties of thin films, SE stands out along with reflectometry and efficiency mapping in that these techniques replicate actual use by exposing the cell to visible light, which the cell must be designed to withstand in order to function properly, while other methods use such particles as metal ions or x-rays which the cell would not normally be exposed to during its normal life, and which can affect the material with sustained exposure. As a nondestructive method, SE can be used in a variety of locations in the production process, scanning material in-situ, on the production line between steps, offline, or at a remote facility, and the data generated is of comparable quality and validity.

In addition to being among the least destructive methods for studying thin films, SE provides the potential to provide data on a combination of variables other single techniques do not offer. For example, while several techniques measure film thickness, SE has also been used to measure the average void content and surface roughness, providing a more detailed picture of the actual structure. SE has been shown to be capable of detecting voids and mixes of materials and both surface roughness and intermixes between layers [31]. Since other instruments have shown a correlation between these properties and properties of interest for solar cell behavior, such as grain size [43], it may be possible to use SE to detect these as well. Initial data from this project has shown that the band gap is detectable as well, although a proven technique for determining band gap from SE data to comparable levels of precision as film thickness has not been demonstrated. SE is also useful for measuring several properties known or suspected to have a significant impact on cell quality, such as refraction index and film thickness. In addition, SE provides a highly detailed picture of how the cell interacts with light, which is fundamental to

its function. SE can detect both light reflected by the cell as well as light transmitted through it at every step in the manufacturing process, while leaving the sample undamaged for other tests.

CdTe efficiency is believed to be dependent on many factors, including layer thicknesses, bandgap, and grain boundaries. SE has been shown to detect layer thickness to a high degree of accuracy in some applications, and has been anecdotally tied to band gap and grain structure. One goal of current efficiency research in terms of properties is to determine what properties correlate to higher efficiencies, and what process conditions correlate to those properties, allowing manufacturers to "dial in" appropriate properties. SE can provide large amounts of information and has the potential to detect many properties, maximizing the chance that a useful connection will be found.

Within larger devices, anecdotal evidence suggests that the efficiencies vary greatly with location on the device. SE can examine properties within a relatively small area (~ 1 mm in radius), and thus can compare properties within a small area to another area on the same device. By providing data about how devices are varying from location to location, SE may assist in the development of more efficient larger devices by correlating "bad spots" in efficiency to properties detectable by an ellipsometer.

While CdTe photovoltaics tend to be relatively stable, decaying only a small amount per year of constant use, this is also an area of possible improvement. Anecdotal evidence suggests that devices with properties that are more uniform and closer to those of monocrystalline CdTe, may not only be more efficient, but also more resistant to degradation, since a common failure mode is for "bad spots" on a device to grow over time. SE may be able to detect differences between devices or within a device that could indicate problems of this nature. SE data has been suggested to have the potential to detect changes in crystallinity [43]. This makes sense, since

changes in lattice structure could impact oscillator values. Some of these properties have been shown to be potentially measurable by multiple SE techniques; in other words, two sets of model variables suggest the same change [46, 47]. This wealth of plausible uses for SE combined with its nondestructive nature demonstrates the potential for SE to provide a unique capability not replicated by other techniques. However, further investigation will be needed to determine how well SE measures these specific properties in photovoltaic and related materials

In-situ use has the potential to improve the state of CdTe device materials research because it provides data about a device at varying stages in the manufacturing process, providing a better understanding of how each process step affects the overall device quality. For example, an in-situ measurement might allow a quality engineer to determine whether a quality issue is occurring before or after the process step being scanned, or determine whether a later process step is changing the thickness of a layer deposited in a previous step. As mentioned above, SE has been used in-situ for other thin film devices, so it has high potential for in-situ study of CdTe devices. Because SE is exceptionally nondestructive and data can be taken quickly, it is unlikely to substantially affect output. This means in-situ SE can potentially be performed in both research and production environments.

1.5. WVASE32 SE Software.

WVASE32 is the premier SE software produced by the J.A. Woollam Company for use with their ellipsometer product line. The name stands for “Variable Angle Spectroscopic Ellipsometry for 32-Bit Windows.” The software package manages SE data from initial data collection through optimization of SE models for a near-complete user solution. The software installation consists of a downloadable executable file and a software key in the form of a USB (Universal Serial Bus) thumb drive that must be connected to the machine running the software

at all times for the software to function properly. In addition, data collection tasks can only be performed while the machine running the WVASE32 software is connected to a running ellipsometer.

The user interface consists of main window and six sub-windows ("Experimental Data", "Fit", "Generated Data", "Graph", and "Hardware", and "Model"). Screenshots are shown in the appendix. Each of the seven windows has its own command bar and options; each of the major tasks handled by the software uses a different combination of these features; some tasks require multiple windows and menus. The main, or "global" menu consists of the "window" submenu, which controls the window arrangement, and the "generic" submenu, which allows users to save and upload files, and adjust settings that affect all windows, for options including memory allocation, default folders, and units of measure used in output displays. The global menu also has debugging tools for developers and hardware installation.

1.5.1. Ellipsometer Setup and Raw Data Collection Tasks

The data collection process includes several hardware tasks for which the software can manage the ellipsometer as a numeric control device; some are sufficiently automated that the user only selects the correct options, in other cases, the user interacts with the software while simultaneously making manual adjustments to the ellipsometer. Once the equipment is set up and properly activated, the first task to be performed is initialization; this is entirely an automated preparation of the hardware for the tasks to follow. Once initialized, and before a calibration can be run, the ellipsometer needs to be adjusted to provide optimum data. Calibration begins with manually mounting a calibration sample and alignment detector into the ellipsometer. This process varies with the ellipsometer but is generally a very straightforward process.

Once this is done, alignment may be performed in two steps: X and Y axis alignment, and Z alignment. X and Y axis alignment uses the "Hardware" and "Graph" windows and adjustment controls on the ellipsometer. First, the sample mount is automatically aligned to the detector. While some ellipsometers can perform X and Y axis alignment automatically, manual adjustment is still common. For manual adjustment, the user adjusts a set of knobs on the ellipsometer that control the orientation of the sample while reflectance data from the alignment detector is displayed on the "graph" window. The window plots the total reflectance along with a chart showing the amount of reflected light received by each of four equally spaced segments around the circumference of the alignment detector along with a set of crosshairs representing the calculated alignment error. The user adjusts the knobs to maximize the reflectance before adjusting a second time to match the crosshairs. This is done because at very low reflectance a false positive for crosshair alignment can occur. The response of the output can be highly nonlinear to the knob action, so some trial and error will occur even with experienced operators. Once the crosshairs are within a few pixels of each other, the system is considered sufficiently aligned. Then, the user clicks enter and the Z-axis alignment is performed. Z-axis alignment is similar to X and Y axis alignment, but in this case only a single knob is needed, and finding the maximum reflectance point is all that is required.

With a calibration sample aligned, calibration is performed to check for instabilities in the hardware system. The calibration process is similar to a data run, and while the user can select some options, the process is entirely automated with no user visibility of the process except for a plot showing output waveforms compared to expected output. Once initialization and calibration are performed, scan capabilities are unlocked. The calibration sample is removed and the new sample loaded at this time. For standard wafers, this is identical to mounting and aligning the

calibration sample. For unusual samples, an alternate mounting solution must be found. For some ellipsometers, such as the Woollam VASE (Variable Angle Spectroscopic Ellipsometer) model, the WVASE32 software can also allow the user to command the hardware to adjust the monochromator, polarizer, and incidence angles. The M-2000 ellipsometer can also be automated to adjust the sample position along the surface plane.

The WVASE32 software allows for several types of scans, including standard spectroscopic reflection and transmission, depolarization, transmission spectrum, dynamic, and translation scans. For each scan type, the user can select several options depending on the hardware. For the M-2000 ellipsometer, the ellipsometer hardware determines the wavelengths to be scanned; for the VASE ellipsometer, maximum, minimum, and step values are selected. The M-2000 also allows the user to select the number of microiterations to be performed on the raw data. For example, if 100 microiterations are selected, the ellipsometer will collect light from each point for a millisecond or so, 100 times, and then average the data, rather than take a single measurement, for each wavelength/angle combination. Both ellipsometers allow the user to select a minimum, maximum, and step in angle for multiple angle measurement. The user can also input a user-selected identification (ID) code for each data collection run. Once all inputs have been selected, the data collection process is entirely automated. The raw data is converted into, and stored in terms of, psi and delta data in real-time so the user has no visibility of the full raw data. Data is stored as .dat files, which store data in a table with numbers stored as ASCII characters. This allows the files to be read in other software such as Notepad and Excel, although editing the data in other software can corrupt the files for WVASE32 use. Data is displayed in text form in the experimental data window and graphically in the graph window.

1.5.2. Model Creation and Editing Tasks.

WVASE32 models consist of a series of layers. Each layer can consist of a pure material or a mix of materials. Pure material layers can have fixed properties or user defined ones. Woollam provides a basic set of the most common materials, including Si, SiO₂, and void. Alternately, the user can create a user-defined material. Each user-defined, single material layer (known as a “general oscillator” or “genosc” layer) has a set of layer-specific properties including the material band gap and ϵ_{∞} . In the standard layers, these values are fixed, but for user-defined materials they can be set to a user-determined value or allowed to vary as an optimization parameter. In addition to the general property values, approximately 30 different oscillator types are available, including the standard types such as Tauc-Lorenz, Drude, and PSEMI, as well as a number of variant oscillator types unique to the software. For each oscillator, all parameters are user adjustable and available as an optimization parameter. The n and k values can also be modified or fit directly, but direct fit has a much greater chance of producing a false positive.

Multi-material layers include surface roughness, intermix, effective medium approximation (EMA), and gradient layers. Surface roughness is modeled as a 50-50 mix of the composition of the layer immediately below and void. An intermix layer is modeled as a 50-50 mix of the materials in the layers above and below. Mathematically, its thickness is taken from the surrounding layers rather than added. For example, a stack consisting of two 100 nm (1 nanometer (nm) = 10^{-9} meters) thick layers and a 20 nm intermix is 200 nm thick, and equivalent to two 90 nm thick layers and a 20 nm thick intermix layer. EMA layers are additive, and thus are preferred for cases where the precise location of the intermix in the stack is important. EMA layers also allow the proportion of the materials to be varied. For maximum versatility, the

gradient layer option allows the mix of material to vary nonlinearly throughout the layers. A custom gradient is available for simulating layers where individual material properties, rather than material intermix, are varying throughout the layer.

Models may be created with almost as many or as few optimization parameters as the user wishes. For this study, an experiment was run to determine the maximum number of layers that could be loaded. 25 different custom layers were successfully added to a substrate before the WVASE32 software crashed running on a Windows Vista laptop. Data for custom materials may be stored separately (for use in other models) as a .mat file, which is similar to a .dat file, and a model may be stored separately as a .mod file. Alternately, models, materials, and raw data may be stored together as an .env (environment) file.

1.5.3. Modeling Optimization and Data Analysis Tasks.

Model optimization is done with a combination of windows. The "graph" window plots one of the properties scanned, such as psi, delta, or polarization, with either wavelength or photon energy. Nominally, the fit is done to psi and delta simultaneously, but only psi vs. wavelength is displayed; other combinations may be selected by the user. The data window is used to load the experimental data and define for what angles and wavelength range optimization will be performed. It is possible to load multiple data sets and perform optimization on several data files as if they were a single file. In the "model" window, the variables to be optimized are selected; these can be deselected or edited manually in the fit window under the "edit params" option; the generated data window allows the user to show or remove the generated data in the "graph" window. Optimization parameters, such as the maximum number of iterations allowed without user input, are selected in the "fit" window.

Once all the options are selected, a fit is run from the "fit" window, and the progress can be seen in changes in the MSE values and optimization parameters in the "fit" window, and the modeled waveforms in the "graph" window. If the user suspects the fit has gone badly, the user can hit escape to stop the fit and select "reset" from the fit window's menu to restore the optimization parameters to what they were. The "fit" window also outputs the end value and estimates for the uncertainty of each optimization variable. Once an optimization run is complete or cancelled, the user can go back and continue to edit the model. WVASE32 defines MSE as

$$\text{MSE} = \sqrt{\frac{1}{2n_{\text{dp}} - n_v} \sum_{j=1}^{n_{\text{dp}}} \left[\left(\frac{\Psi_{j,\text{mo}} - \Psi_{j,\text{me}}}{\sigma(\Psi_{\text{me}})} \right)^2 + \left(\frac{\Delta_{j,\text{mo}} - \Delta_{j,\text{me}}}{\sigma(\Delta_{\text{me}})} \right)^2 \right]} \quad (1.14)$$

where n_{dp} is the number of data points, n_v is the number of model variables (n , k , oscillator variables, etc.) being optimized, j is a counting integer, $\Psi_{j,\text{me}}$ and $\Psi_{j,\text{mo}}$ are the Ψ values generated by the model and measured, respectively, for the j^{th} wavelength, $\Delta_{j,\text{me}}$ and $\Delta_{j,\text{mo}}$ are the Δ values generated by the model and measured, respectively, for the j^{th} wavelength, and $\sigma(\Psi_{\text{me}})$ and $\sigma(\Delta_{\text{me}})$ are the standard deviations of the measured Ψ and Δ data, respectively [35]. Dividing by $\sigma(\Psi_{\text{me}})$ and $\sigma(\Delta_{\text{me}})$ normalizes the data to a nondimensional quantity. However, as a consequence of this definition, it is not necessarily meaningful to compare MSEs from optimizations having different numbers of data points or fit variables, different levels of noise in the raw data, or from different material samples. For example, for two otherwise identical models fit to identical data, the one with more model variables not fixed to a constant will have a larger MSE. In fact, for two similar models developed from different data sets, it is possible the better fit will produce a larger MSE. However, for the same set of data, model constants, and optimization variables, smaller MSE values do indicate a closer fit.

Data analysis is also run from the fit window. The MSE study allows you to compute the MSE for a given model without running the optimization. It also computes the MSE obtained by varying a single, user-selected parameter, which provides a sense of whether the variable is important to the model. The study does not provide any statistical significance. The “uniqueness study” optimizes the model after setting one user-selected parameter to each of several values. This is a very time-consuming process, but provides a good sense of how much the model fit and other parameters depend on the selected parameter, and whether there are other values of the parameter that produce low MSEs. In general, if different values of parameters result in multiple MSE minimums of similar value, or the minimum is a broad rather than a narrow valley, the data available may be insufficient to determine which minimum is the "correct" result and which is a false positive. In this case, it may be necessary to take a second set of data or fix the value of the selected parameter before continuing.

1.6. Summary and Conclusions.

One of the major challenges facing human civilization in the twenty-first century is energy. While there are currently more than enough energy supplies to meet present needs, demand is expected to increase, current use of fossil fuels present a possibly unacceptable threat to the Earth’s climate, and current alternate solutions will be difficult to scale to levels comparable to current fossil fuel use. As a result, new technologies will likely be needed to provide energy in the future. Solar energy promises the greatest potential source of energy available to current technology that does not rely on fuels that produce carbon dioxide or nuclear waste. Historically, however, it has been too expensive to provide energy beyond niche markets. CdTe thin-film photovoltaic devices are currently the least expensive solar technology that has

progressed beyond laboratory use. As such, this technology is a potential candidate for playing an important role in a future energy mix.

To optimize CdTe devices to the point that they can become fully competitive with other forms of energy, measurement techniques will be required. SE is a nondestructive optical measurement technique that is uniquely suited to use with thin films. In addition to measuring optical properties of thin films, SE has been shown to detect physical properties such as film thickness and electrical properties such as device band gap. SE is potentially well suited to the requirements for CdTe device property measurement. The moderately small sample area scanned allows multiple locations to be scanned on all but the smallest devices. As a high-speed, non-destructive process, SE can theoretically be integrated at any point in the manufacturing process as well as offline, with minimal impact on production. SE provides a unique set of properties with minimal impact capabilities that is not available with any other single technique. Therefore, SE appears promising as a material characterization and quality measurement tool for CdTe thin film photovoltaic devices. However, while SE has been used to study CdTe experimentally, it has not become an established tool in the CdTe industry as a whole.

CSU is well-suited for a study of this nature. In addition to the advanced deposition system, which has provided custom samples for student and research use, the PV program has access to multiple labs and techniques for sample characterization, including SE. Software available onsite can perform data collection and model optimization needed to analyze SE data.

Objectives and Experimental Methodology

2.1. Objectives.

As has been shown in the previous chapter, CdTe thin-film photovoltaic devices may become an important industry, as they appear to have strong potential for providing alternative energy on terawatt scales without encountering insurmountable issues such as impractically high cost or land use. Similarly, SE, a technique used as a nondestructive quality control tool in the silicon wafer industry, appears to have strong potential for use in the CdTe industry as it is capable of measuring both optical and physical properties on an offline, in-line, or in-situ basis. However, SE is not currently an established technique throughout the CdTe industry, and a statistical study of SE measurements of CdTe photovoltaic devices has not been reported previously.

The primary objective of this work was to assess the ability of SE to characterize CdTe thin-film photovoltaic devices. To be demonstrated as a potential manufacturing quality tool, SE must be shown to be capable of providing a physically practical solution, detecting properties known to impact performance, and providing timely, statistically meaningful, and accurate information. Physically practical means that the SE process must integrate into production and function without creating unacceptable problems. The process must also be sufficiently rapid that quality problems detected will be noticed in time to correct them in a reasonably timely manner. In industry, statistical meaningfulness is generally demonstrated by repeatability and reproducibility studies. Accuracy is demonstrated by comparison to other measurement techniques with which there is already a high degree of confidence.

Ideally, random error should produce normally distributed data [48]. Normally distributed data provides a roughly 95% confidence level for a range of 2 standard deviations above and below the mean [48]. However, a quality measurement tool must not merely provide confidence that its results are meaningful, but also useful. Typically, in order to be useful, a quality tool must detect that a process has drifted from a range safely within quality control limits before it goes outside acceptable limits. In this case, no quality limits have been developed, but statistics can still provide some measure of the meaningfulness of the data. For example, if it can be demonstrated that the data is normally distributed, and the value for a variable would nominally be reported as zero if it could not be measured, then a certain level of statistical confidence in the technique's ability to detect that quantity can be gained by comparing the difference between the average and zero with the standard deviation.

Prior to performing an assessment of SE's ability to measure CdTe devices, a baseline model must be developed that will allow the modeling process to optimize to an accurate result. While SE models of CdTe devices had been produced previously, it was desired to obtain models produced both externally and in-house to provide confidence in the modeling process as well as to produce a set of models specifically designed for use as an assessment tool in preparation for assessment studies. This included models from each of five production process stages in order to provide visibility of the full process.

In addition to assessing repeatability in the traditional quality engineering sense, a concern that had been raised was, "On what set of angles should SE be performed?" For this reason, it was desired to compare model outputs optimized on different angles to see whether that made a significant difference in the output. In the SE measurement industry there are several established presumptions with regard to angle. As explained in previous chapters, for a

given material and wavelength of light, there will typically be both a critical angle for total reflection, above which transmissivity issues will degrade the data, and a Brewster angle, which is generally considered the optimum for single-angle SE. However, because these angles can vary with properties and wavelength over a single sample, in general the angles used for SE are not the Brewster angles of the materials in the samples but angles thought to be reasonably close based on known Brewster angles of similar materials [31]. Measurements from multiple angles are usually considered necessary for ensuring that a model has both reasonable optical properties and thickness values. It was therefore desired to explore the validity of single angle measurements.

Finally, to demonstrate the versatility of the process, it was desired to assess the capability of SE to measure different samples or sample locations and samples produced by different processes. In addition to the 3"x3" samples used for the primary studies, a sample produced by the 16"x16" panel production line at Abound Solar was also scanned to demonstrate the versatility of the models and optimization developed for use with the 3"x3" samples.

Five objectives, summarized in Table 2.1, were identified as the end product of this research. These included baseline studies, studies of data from the same sample at different angles and locations, studies of devices from different facilities, and validation.

Table 2.1: Objectives.

objective	description	methods	expected outcome
1	development of a baseline model	collect data and develop practical models	properties of device: band gap, refractive index, etc.; confidence in measurement technique.
2	angular repeatability assessment	optimize model to data from various angles	preliminary data on accuracy, repeatability, and sensitivity of optimization process to angle.
3	spatial variability assessment	repeat (2) for multiple locations on the same sample	variations in properties across the surface of the cell; demonstration that data is statistically significant.
4	assessment of industrial applicability	repeat (3) using a production sample	properties of industrial-scale production device.
5	practical use assessment	design a solution for industrial use	design for industrial application

2.2. Contributions of Work.

As an assessment of the statistical accuracy and precision of SE measurements of CdTe devices has not been previously reported, it is the intent of this study to provide a contribution to the body of knowledge in that area. The study seeks to break ground in several areas. While numerous SE studies of CdTe and similar or related materials have been reported, including a study of the sensitivity of SE to model variables in terms of MSE values [49], a study of the repeatability of model values has not been reported. Angle of incidence is a topic of importance in SE technique, and the goal of this study is to provide information on the quantitative significance or importance of angle on the final results. A study of angle dependence for CdTe has also not been reported. Previously, most studies of CdTe thin films have been of either small devices (less than 1/2" (13 mm)) or center point data. However, it has been shown that typically PV devices do not operate at the same local efficiency at the center point as offset points, and the exact cause for this phenomenon is not fully understood. This study seeks to examine samples at multiple locations on a single sample to provide a more complete picture of a device from a

spatial variability perspective. A study of SE measurement of a commercial CdTe device at multiple locations has not been reported.

A key goal of SE research in the CdTe field is to determine what specific CdTe device material properties SE appears to have the potential to detect, and to assess to what degree they can be measured. This information will aid further research by suggesting what might or might not be determined at a given process step. This study provides a preliminary repeatability assessment in conjunction with verification by SEM measurements so that accuracy and precision are examined side by side. Study of devices produced by both laboratory and commercial process has the potential to reveal both similarities and differences between the two. In addition, this study also provides new knowledge in regard to modeling techniques and CdTe optical behavior.

2.3. Methodology.

The work described in this dissertation includes five separate SE studies, verification with SEM and statistical work, and modeling using a 3D drafting package. An overview of general SE methodology is shown in Figure 2.1. The boxes shaded in color indicate physical processes while those shaded in medium grey indicate computer analysis; the light grey pages represent results. As shown by the figure, data is produced by SE in three distinct stages. SE directly produces plots of the polarization state variables (Ψ , Δ , depolarization, and transparency) with wavelength. This data is used for model optimization, which produces a second set of result variables, such as layer thicknesses and porosity, oscillator parameters, and optical properties of each layer material, i.e., n , k , ϵ_{∞} , etc. The model data can then potentially be used for calculations or comparison with data from other techniques for verification to provide a third set of results.

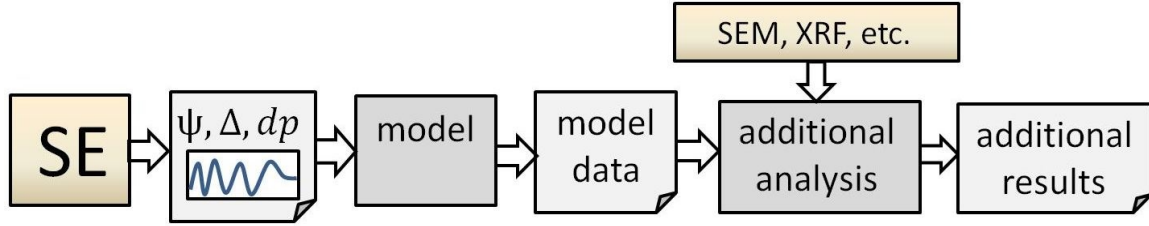


Figure 2.1: General SE Process Diagram.

2.3.1. Woollam Study.

In 2006, CSU sent CdTe device samples to the J.A. Woollam company for analysis. A sample from each of five production process points (TEC-15 glass prior to deposition, after CdS deposition, after CdTe deposition, after Cl treatment, and after Cu treatment) was provided as shown in Figure 2.2. SE was conducted on a single point from each sample. Results, including layer thicknesses and n and k values for the uppermost bulk layer from each sample were provided in a customer document. Additional information on this study has been published elsewhere [43, 50, 51].

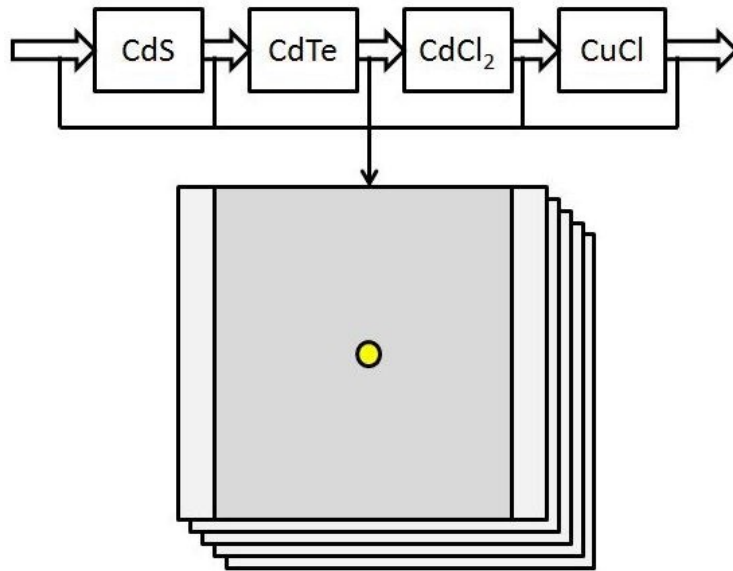


Figure 2.2: Woollam Study Concept.

Prior to this study, SE models of CdTe devices have provided interesting and promising results, but these models had much larger MSEs than those found in the silicon wafer industry,

and do not match the waveforms as closely as they should to provide the level of confidence and accuracy for model-optimized properties which the industry will require. One of the major challenges faced in this study was modeling the optical properties TEC-15 glass substrate. The Pilkington TEC-15 Glass is believed to be a structure consisting of three layers: Tin Oxide (SnO_2), SiO_2 , and SnO_xF , or fluorinated tin oxide (FTO), coated on a tempered glass substrate [52]. While silicon oxide-based materials generally have fairly well-understood optical behavior, this is less true for tin oxide. Rottkay and Rubin [52] fit SE data for TEC-15 glass. The TEC-15 model that they developed was comprised of three layers. The top layer was assumed to be 292 nm conducting FTO layer while the intermediate layer was a 20 nm non-conducting SiO_2 . A 30 nm non-conducting SnO_2 layer was assumed to be the bottom layer. The fitted results were also comprised of a surface roughness layer that was simulated by a Bruggemann effective medium approximation layer [53, 54], where a portion of 50% void was included to the FTO top layer. The model did not include variation in optical properties over the depth of the FTO layer. The TEC-15 glass in this study was initially modeled using the same approach. However, to obtain the best-fit results, a different approach was used for the FTO and surface roughness layer.

Because pure SiO_2 glass is a well understood model, optical property standard curves were available. The glass substrate was thus initially modeled as having fixed properties from Palik's Handbook of Optical Constants [55]. The SiO_2 insulation layer was initially assumed to have identical composition and structure as the substrate. Since a reasonable fit was obtained with these assumptions, the initial properties values were maintained throughout the modeling process. WVASE32 models the primary substrate as a "semi-inf" (semi-infinite) layer, meaning that it was sufficiently thick that beams reflected from the front and back surface are presumed to

no longer be coupled on a quantum level, and thus do not provide a useful interference effect for the purposes of the SE model. The substrate thickness was set at 1mm, while the thickness SiO₂ insulating film was allowed to vary as a model parameter. The bottom non-conducting SnO₂ layer was modeled with a single un-broadened oscillator, known as a “pole”, in the UV to account for electronic transitions. The mathematical description used was identical to that of a sum of Drude-Lorentz oscillators, as shown in Equation 1.10 in Section 1.4.1.

The conducting FTO layer was modeled with a combination of Drude and Tauc-Lorentz (TL) oscillators. The Drude model is particularly useful for modeling the infrared (IR) absorption edge due to free carriers in transparent conducting oxide (TCO) films. The classic Drude model describes free carrier effects on the dielectric response. Its form is a Lorentz oscillator with zero center energy (no restoring force). The version of the Drude model used in this study is comprised of resistivity and mean scattering time as free parameters, and can be represented as

$$\epsilon_{\text{Drude}}(E = \hbar\nu) = \frac{-\hbar^2}{\epsilon_0 \rho (\tau E^2 + i\hbar E)} \quad (2.1)$$

where

$$\rho = \frac{m_*}{N q_e^2} = \frac{1}{q_e \mu N}$$

and

$$\hbar = \frac{h}{2\pi},$$

and where ϵ_{Drude} is the oscillator complex dielectric, E is the photon energy, ν is the frequency, ϵ_0 is the vacuum dielectric constant, ρ is resistivity, τ is scattering time, i is the square root of -1, m_* is the carrier effective mass, N is the carrier concentration, q_e is the single electron charge, μ is the carrier mobility, and h is Planck's constant. The fit parameters are ρ and τ . The TL oscillator models the dielectric function of many amorphous materials particularly well. Close to the band edge, the absorption of the TL model follows a Tauc law formula,

$$\varepsilon(E) \propto \left[\frac{E - E_g}{E} \right]^2 \quad (2.2)$$

where ε is the complex dielectric coefficient, E is the photon energy, and E_g is the optical band gap, so that for frequencies near a band gap, the dielectric approaches zero. WVASE32 uses a modified version of the standard TL model (Equation 1.11). This model is defined as

$$\varepsilon_{TLn} = \varepsilon_{1n} + \varepsilon_{2n} \quad (2.3)$$

where

$$\varepsilon_{1j} = \frac{2}{\pi} P \left(\int_{E_{gn}}^{\infty} \left(\frac{\xi \cdot \varepsilon_{2j}(\xi)}{\xi^2 - E^2} - E^2 \right) d\xi \right)$$

and

$$\varepsilon_{2j} = \frac{1}{E} \frac{A_j E_{0j} C_j (E - E_{gj})^2}{(E^2 - E_{gj}^2)^2 + C_j^2 E^2} \quad E > E_{gj}$$

$$\varepsilon_{2j} = 0 \quad E < E_{gj}$$

and where, for the j^{th} oscillator, A_j is the amplitude, E_{0j} is the peak transition energy, C_j is the broadening coefficient, E_{gj} is the optical band gap, P is the Cauchy principal part, TL denotes Tauc-Lorentz, and ξ is an integration variable representing all possible energy values. The values of A_j , C_j , E_{0j} , E_{gj} , ε_{∞} , as well as film thickness, are all taken as fit parameters [43].

Subsequently the modeled FTO layer was refined to fit the experiment data and included index grading across the film thickness. The grading is primarily found in changes to the conductivity through the film. It was hypothesized that carrier concentration varied with depth throughout the FTO layer, presumably due to variations in the concentration of the fluorine dopant. The conductivity gradient is described through varying the Drude oscillator amplitude and broadening in the film, using a linear variation. The data behavior near the onset of near-infrared radiation (NIR) absorption is unlike many conductive TCOs, which suggests a more

complex grading profile. The most important factor in matching the data profile became the surface region of the FTO layer.

It was ineffective to model the surface roughness layer using a simple effective medium approximation (EMA) [56, 57] layer comprised of the underlying FTO material and void [52]. In all successful models, it was important for the surface roughness region to have higher conductivity than the bulk FTO film. However, it does appear that the surface region roughness reduces the overall dielectric function. For this purpose, an EMA for the surface mixed void with a surface region oscillator model comprised of a combination of Drude [58] and TL [57] oscillators. This allows the surface region to have its own conductivity, but still be mixed with void to account for roughness effects. In this manner, an effective model was realized that fitted the data well.

Once an effective model of the TEC-15 was developed and optimized, modeling was performed for the CdS and CdTe layers. The optical constants and thicknesses of TEC-15 glass layers obtained in the previous section were used as a starting point. The SE data on CdS film on TEC-15 glass was acquired and modeled. A series of Gaussian oscillators and a single PSEMI (“positive-type semiconductor”) oscillator [35] (for the direct gap) were matched to the different critical points of the CdS. The model layer thus obtained was used to describe the optical constants of the CdS. The MSE of the modeled data was determined to be 212. An improved fit (MSE ~112) was obtained by adding a low refractive index interface layer between FTO and CdS comprised of FTO, CdS and voids. A best-fit result with an MSE of 26 was obtained by adding surface roughness layer (50% void and 50% CdS) to the model. In order to improve model uniqueness, the TEC-15 sample was fit simultaneously with the CdS coated TEC-15 using a “Multi-sample” analysis approach [35] before final refinement.

Various attempts to model the SE data for the as-deposited CdTe layer were not successful. This was possibly due to large surface roughness (typically >10% of film thickness) of as-deposited samples. The treated CdTe layer was modeled using a series of oscillators. The oscillator model for the CdTe layer was developed fitting data collected by Aspnes et al. [54] using a series of PSEMI oscillators that were introduced to match the critical points in the optical constants of CdTe. Various oscillator parameters were then allowed to vary within $\pm 10\%$ of its starting values to fit the CdTe specimen layer. In modeling the SE data for the complete PV device (i.e., after copper treatment), it was noted that the modeling results were insensitive to the buried non-conducting SnO₂ and SiO₂ layers of TEC-15 glass. Hence, these layer thickness and optical constants were held constant at the values derived from fitting the as-received TEC-15 glass. Surface and interface layers were then added to improve the fit. An interface layer comprised of CdTe and CdS was introduced. This interface was likely formed as results of inter-diffusion between CdTe and CdS, and plays a vital role in the performance of the PV device [59]. Finally, a surface layer was introduced to get the best-fit result. To achieve the best-fit results, the surface layer was modeled by assuming multiple EMA layers with different void fractions. Variables in the modeled layers were refined to achieve the best-fit results.

Once SE data collection and modeling was completed, the samples were returned to CSU where further testing was conducted. Because it was believed that grain structure plays an important role in device efficiency, XRD was performed in hopes of providing more information about how chemical treatments affect the crystallinity of the devices. XRD data can be correlated to known crystal structure phases as well as providing information indicating orientation and lattice parameter size. After XRD, SEM was performed to provide verification of stack thickness as explained in Section 2.3.6.

2.3.2. Baseline Study.

To provide confidence in in-house capabilities, it was desired to replicate the Woollam Study as closely as possible with data collection and modeling performed by the author. The samples used in the Woollam Study were not available for repeating the study in-house because cutting 5 mm square pieces from the 3"x3" samples in preparation for performing SEM had destroyed the samples for further testing with SE. However, additional samples from each of the process steps were available, so it was decided to reproduce the study with new samples. For this study, existing 3"x3" samples produced at the ERC, one for each of the five process points used in the Woollam Study, as well as a second sample removed immediately after CdTe deposition, were selected for their apparent reasonably good condition. The second CdTe sample was etched by submerging it in a 200:1 methanol: bromine (Br:CH₃OH) solution for 3 seconds, and rinsed by immediate submersion in pure methanol, and allowed to dry. Then all samples were carefully washed with isopropyl alcohol and allowed to dry. Each sample was carefully placed in a Kimwipe folder inside a sample holder. Various methanol: bromine solutions have been reported as an etching technique for SE of CdTe [60]. The various samples were referred to as "The Baseline Study X Sample", where X referred to the final process step used for that sample, i.e., "TEC-15", "CdS", "CdTe", "Cl-treated", "Cu-treated", and "Br-treated".

A preliminary Baseline Study was performed using a VASE ellipsometer, taking 3 sets of reflection and transmission runs, with 4 angles, and data at 20 nm increments from 300 to 1700 nm for a total of 1704 data points per sample. The general technique used is described in Section 1.5.1. The VASE ellipsometer is fully programmable, allowing angles and wavelength ranges and sampling rates to be specified for each run. The ellipsometer is designed for use with silicon

wafer samples which are mounted vertically by suction pump. Unfortunately, the 3"x3" samples were too heavy to be mounted onto the VASE ellipsometer by the standard suction technique. As a result, a technique for mounting the samples had to be developed. This was done by adhesive tape, which degraded the samples, and made for a less stable situation. Testing showed that in general, the best technique was to use the existing vacuum pump supplemented by carefully but firmly applying a single strip of adhesive tape to the top center of the sample for additional support. Once setup and calibration were completed, the automated process required approximately 15-20 minutes for each of the 36 runs.

With the basic process demonstrated, a second Baseline Study was performed using an M-2000 ellipsometer, which more closely replicates the resolution used in the Woollam Study, and because the samples are nominally mounted horizontally, no additional support for the sample weight was required. Both VASE [50, 51, 61, 62] and M-2000 [63, 64] ellipsometers have been used by other research groups to study materials similar to those studied in this report. The results of this second study are reported in this document. A micrometer was used at a location near the edge to measure the thickness of the glass substrate. This provided a starting value for the substrate thickness in the software model. The length and width of each sample were measured by hand to determine the center point location. A total of 7 runs per sample were performed using the M-2000, providing data for the following set of angles of incidence: 45°, 50°, 55°, 60°, 65°, 70°, and 75°. The M-2000 ellipsometer examines a fixed set of over 700 different frequencies for each angle. For the Baseline Study, a total of 500 "microiterations" were collected for each point and averaged prior to the data being sent to the file, totaling 2.45 million data points, mathematically reduced to 4,900 data points for each sample in the data file. Despite the enormous amount of data, the M-2000 completed the task in less than 15 minutes per

sample. The scan was performed on a circular region approximately 3 mm in diameter located within a circle 5 mm in radius from the exact center of the sample.

After replicating the data collection procedure, a baseline set of models were developed. The general techniques used are described in Section 1.5.2. and 1.5.3. Modeling was performed at the ERC on an HP Pavilion dv6700 laptop running WVASE32 version 3.734. For each sample, a preliminary model file was created using the .env file created for the corresponding Woollam Study model with the raw data replaced with the measured Baseline Study data for all seven angles. To minimize the "averaging to absorption" effect seen in a number of cases, a single angle (45°) was selected for analysis for the initial portion of the fit. This also allowed greater visibility of the waveform shapes and peak and valley locations for manual fitting. The thickness of the substrate was set to the value determined by the micrometer, and the thickness of the uppermost bulk layer (FTO, CdS, or CdTe) was adjusted until the waveforms appeared to line up with the raw data. The next process was to determine which variables would be fixed and which variables would be allowed to vary as values measured by the completed model. For each layer, a subset of variables was allowed to vary for a total of four iterations, and the total value of each variable was compared to the WVASE32-calculated uncertainty value. If the absolute value of the uncertainty was greater than the absolute value of the variable in question after four iterations, the variable was locked at the Woollam Study model value. The remaining variables were reset, and the process repeated until all variables were tested.

Once it was determined which variables would be allowed to vary, the model was allowed to optimize on the data from one angle until the model appeared to be close enough that data from seven angles could be plotted on one graph without it being impossible to determine which model waveform went with each set of data. The model was then optimized for all seven

angles simultaneously. Periodically, the variables were checked to see if they appeared to be reasonable, the data reset with questionable variables locked, and the process repeated until a reasonable fit was obtained. Multiple approaches, using different sets of variables were tested, and the one that produced the closest fit with the least questionable n & k plot values was selected for the final fit. The fit process took approximately 8-16 hours per model.

Final results were performed by taking each model and selecting only the variables listed in the results to vary, selecting data for the frequency range in which there was minimal noise, and then selecting only the data from the desired angle or angles for the model to optimize on. The software was set to optimize until the MSE value no longer decreased with continuing iterations, or 10,000 iterations had been completed, without further human input. This process typically took about 1 hour per run.

2.3.3. Multiple Angle Study.

Once the Baseline Study was complete, a Multiple Angle Study was performed to examine the ability of SE to produce similar results when performed using the same sample, sample location, equipment, and personnel. To achieve this, multiple sets of data were to be taken from the same location on each sample, as shown in Figure 2.3, in order to study the consistency of the results for further determination of SE capabilities. To assess the effect of data from different angles, it was desired that the final optimization be performed on data from each of several angles; as the Baseline Study already included this data, the Multiple Angle Study was performed directly on the data and models output from the Baseline Study.

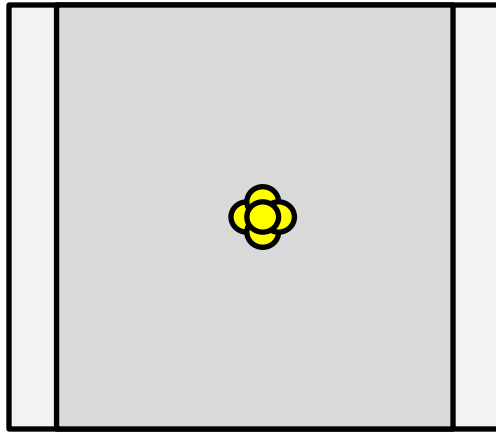


Figure 2.3: Multiple Angle Study Concept.

Final optimization was performed by taking each model and selecting only the thickness, porosity, and stack variation variables to vary, selecting data for the frequency range in which there was minimal noise, and then selecting only the data from one of the seven angles tested in the Baseline Study for the model to optimize on. The software was set to optimize until either the MSE value no longer decreased with continuing iterations, or 10,000 iterations had been completed, without further human input.

2.3.4. Multiple Position Study.

The Multiple Position Study was designed to use the same methods as the Multiple Angle Study, but different locations including the outer portion of the sample were used. Sample preparation was conducted as per the Baseline Study since this study used the same samples as the Baseline Study. SE was performed using the same techniques as the Baseline Study, except for the following:

1. Measurement parameters were set for a reduced amount of data collection. No transmission data was collected, only four angles were measured, and only 100 microiterations per data point were used.

2. Runs were taken at each of four angles at each of four positions. These positions were offset from the center point studied in the Multiple Angle Study by 2 cm (centimeter or 10^{-2} meters) in both the horizontal and vertical as shown in Figure 2.4. The M-2000 is equipped to adjust the sample position electronically to accomplish this.

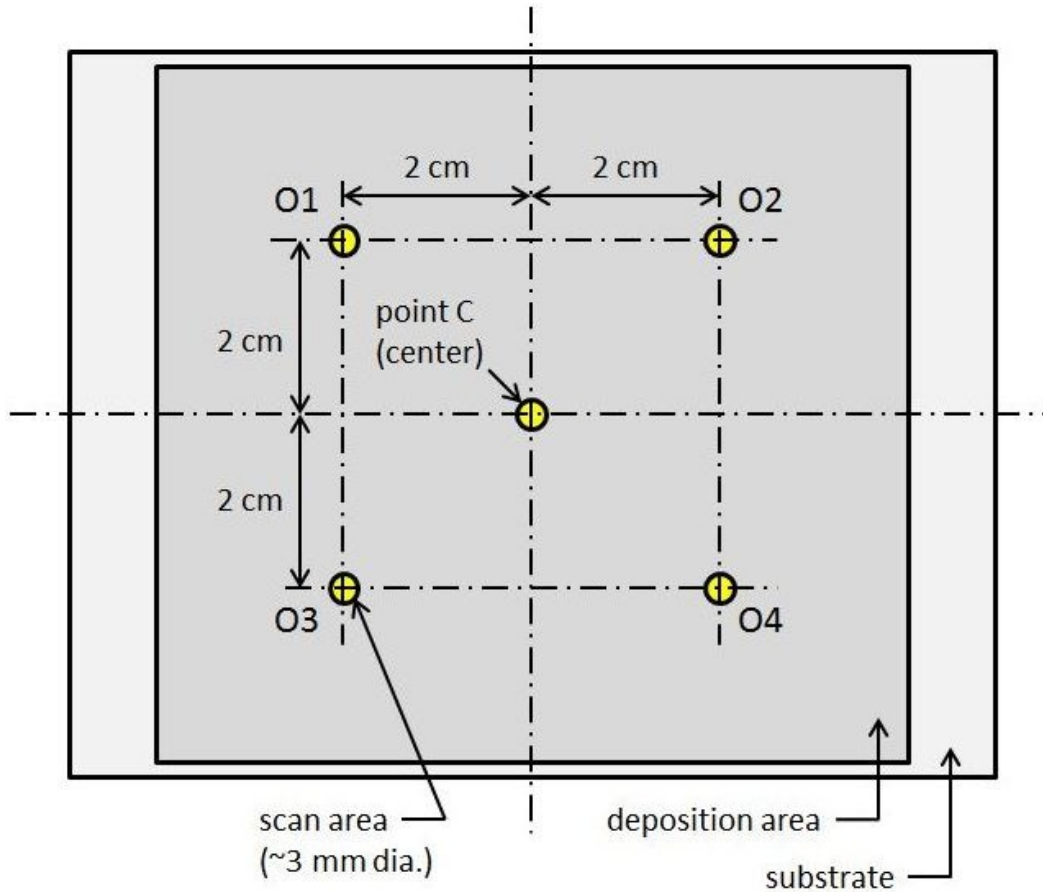


Figure 2.4: Locations Used for the Multiple Position Study.

Model optimization started with the Baseline Study model for the sample in question, repeating the process used for the Baseline and Multiple Angle Studies. However, testing of initial models to determine which variables would be fixed was kept to a minimum.

2.3.5. Industrial Device Study.

For this study, a 16"x16" panel produced by Abound Solar was used. This panel had been removed from the line immediately after the scribing process for testing. Since the scribing process is conducted immediately after the Cu-treatment and final heat treatment processes, the properties of the panel were believed to be very similar to the 3"x3" Cu-treated sample from the Baseline Study. A repeat of the Multiple Angle Study was to be performed, comparing data from different points on the surface as shown in Figure 2.5.

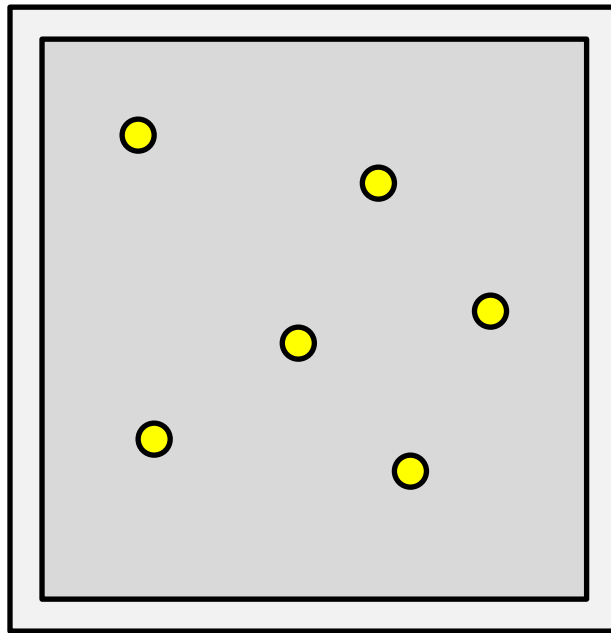


Figure 2.5: Industrial Device Study Concept.

Once the panel was obtained, it was carefully blown off and shaken to remove dust, and then scribed on the reverse side from the film into 64 two-inch squares. Two of the four edges proved unusable due to deposition issues and glass breakage. The remaining 49 usable samples were numbered as shown in Figure 2.6, and six (highlighted) selected for the study. The locations were selected to provide a sense of the overall distribution of the layers over the whole device. Once selected, the samples were shaken and very gently brushed to remove glass dust, and were placed in the sample holder without washing prior to performing SE.

1	2	3	4	5	6	7	x
8	9	10	11	12	13	14	x
15	16	17	18	19	20	21	x
22	23	24	25	26	27	28	x
29	30	31	32	33	34	35	x
36	37	38	39	40	41	42	x
43	44	45	46	47	48	49	x
x	x	x	x	x	x	x	x

Figure 2.6: Locations Selected for Industrial Device Study.

Measurement was conducted in a similar way to the Multiple Position Study; however, instead of the M-2000 ellipsometer, the VASE ellipsometer at the CIS was used. As with the preliminary Baseline Study, 71 wavelengths (300 to 1700 nm at 20 nm increments) per angle were used rather than 700 wavelengths. The 2"x 2" samples were approximately 60% lighter than the 3"x3" samples used for the Baseline Study and mounted easily in the vertical position. Since only data from the center point was taken, no adjustment to the position needed to be made once mounted, which also made for a more stable measurement. The ellipsometer settings were also reset to optimize performance specifically for this study. This increased the runtime to 30 minutes per sample, further increasing the quality of the data.

The starting model selected was the Cu-treated model from the Baseline Study. This model underwent further refinement based on what had been learned from the 3"x3" Industrial Device Study prior to adaptation to the new data to provide the best possible model. The data collection process for this study was conducted in an identical way to the Multiple Angle Study for the Cu-treated sample, including fixing the TEC-15 layers and allowing the remaining layer thicknesses to vary.

2.3.6. Verification of Model Accuracy and Precision.

To demonstrate accuracy of the results, it was decided that measurements should also be taken by an additional technique (not SE) and compared to the SE results. SEM was selected for this purpose, as it provides a direct visual representation and measurement of thickness, and thus is a fairly concrete source for comparison. SEM data has also been reported for this purpose [46]. SEM cannot verify most of the optical properties measured by SE, but verifying the thicknesses will suggest that other values are reasonable, since erroneous values for the optical properties would tend to throw off the thickness values in the SE model.

A small piece of each sample, approximately 5 mm on a side, was scribed and broken from the glass within 1 cm of the location scanned with SE. A total of 18 samples were measured by SEM: one from the center and one near one of the outlying positions on each of the six 3"x3" samples, and one from the center of each of the 2"x2" samples. The sample was secured into a standard electron microscopy mounting cartridge, and 5 nm of gold was plated onto the exposed cross section of the sample. SEM was performed using a JSM-6500F field emission scanning electron microscope with In-Lens Thermal Field Emission Electron Gun and Thermo Electron Energy Dispersive X-ray Spectroscopy (EDS) at the CIF. The SEM image was analyzed for the presence of thin film layers and the total stack thickness of those layers prior to data collection. CSU's SEM capabilities include electronic imaging and measurement by pixel count in comparison with a known scale. For validation, the focus was placed on the stack thickness of the film. This was compared with SE data to determine accuracy of SE thickness measurements.

Once some sense of accuracy was obtained, it was desired to study the statistical precision, or repeatability, of the data. After SEM had been performed, data from the model files

was exported into Excel 2007 for the first stage of statistical analysis. Averages, standard deviations, and other initial calculations were performed in Excel before exporting the data into Minitab 15 for normality testing. For each data location, the Anderson-Darling normality test was performed in Minitab to determine normality; results were exported back to Excel 2007. Results from the normality tests and ratios between the SE model data averages, standard deviations, and thickness values provided by SEM were used to provide a preliminary estimate of the repeatability of SE data.

The Anderson-Darling normality test is a commonly-used test for normality that provides an function that takes a list of a set of real number values as input, and returns a single real number (referred to here as “P”) between zero and one. A detailed discussion of the mathematics behind the Anderson-Darling normality test is found elsewhere [65]. This value represents an estimate that the probability that the data presented is from a normal distribution, and if you have a large number of normal distributions, it can be expected that approximately 5% of them will produce P values less than 0.05. Thus, values near one represent sets of data that closely resemble a normal distribution, and values near zero represent the least normally-distributed data. Generally, the methodology used in industry is to test for non-normality at a 95% confidence level, meaning that if $P < 0.05$, the data is judged to not be normally distributed.

2.4. Summary and Conclusions.

For the purpose of providing a preliminary proof-of-concept study demonstrating the potential of SE as a technique for measuring CdTe devices, and moving toward the goal of establishing SE as a standard technique for this application, a series of studies were performed. A Baseline Study produced an initial set of models which were then used for a series of studies examining multiple reflection angles and sample positions, which were then validated by SEM

and basic statistics to demonstrate both accuracy and precision of the SE model data. In addition, the study examined SE data and literature to study the potential of SE to detect material properties believed to be related to device performance. This study provides a unique combination of data as it examined SE data at offset points and compared models for different angles at the same location. Such a study for CdTe applications has not been previously reported.

Results

Due to the large amount of data produced by this study, selected results are presented in Chapter 3 in the order of the objectives presented in Table 2.1. Additional results are found in the appendix. For the first objective (development of a Baseline Study model), results from the Woollam Study are presented first, followed by more detailed results from the Baseline Study. Table 3.1 summarizes the studies for which results are reported.

Table 3.1: Overview of Studies Presented in this Chapter.

Study	Samples and Physical Methods	Results Reported
Woollam Study	Sample set #1 (5 3"x3" samples): 1. TEC-15 substrate 2. TEC-15 with CdS layer 3. TEC-15 with CdS & CdTe layers 4. per (3), but with Cl treatment 5. per (4), but with Cu treatment SE (M-2000 ellipsometer) at Woollam XRD & SEM at CIF	<ul style="list-style-type: none">• SE (Ψ and Δ)• Modeled variables• Derived variables• XRD results• SEM results
Baseline Study	Sample set #2 (6 3"x3" samples): 1. TEC-15 substrate 2. TEC-15 with CdS layer 3. TEC-15 with CdS & CdTe layers 4. per (3), but with Cl treatment 5. per (4), but with Cu treatment 6. per (5), but with Br: CH ₃ OH treatment SE (M-2000 ellipsometer) at NREL SEM at CIF	<ul style="list-style-type: none">• SE (Ψ and Δ)• Modeled variables• SEM images (except for multiple angle study)• Statistics (except for Baseline Study)
Multiple Angle Study		
Multiple Position Study		
Industrial Device Study	16"x16" Panel after Cu treatment. 6 samples from various locations (see Figure 2.6) SE (VASE ellipsometer) at CIF SEM at CIF	

For the Woollam, Baseline, and Multiple Angle and Position Studies, the results are presented in the sample order listed in Table 3.1. For each sample, Ψ and Δ values are presented first, followed by the modeling results. For the Woollam Study, additional results are presented at the end of the section; for the remaining studies, this information is provided at the end of the results for each sample.

3.1. Woollam Study Results.

Five samples were modeled by James Hilfiker at J.A. Woollam as described in Section 2.3.1. While the top priority was to establish a preliminary model sufficient to allow for SE measurement of the deposited layers, it was also desired to show evidence that SE detects properties indicative of changes in crystal structure, chemical composition, and other material properties of interest to the device manufacturer.

3.1.1. SE Data and Model Values.

Results from the measured and modeled Woollam Study results for the TEC-15 glass sample are shown in Figures 3.1 through 3.3 and Table 3.2. Figure 3.1 shows a comparison of the Ψ values produced by actual SE measurements (dashed lines) with Ψ values produced by the model (solid lines) at all angles measured. Figure 3.2 shows the corresponding Δ values. In these and all following Ψ and Δ data figures, dashed lines represent SE data, and model data is shown by solid lines. The modeled optical constants n and k for the bulk FTO layer are shown in Figure 3.3. The two sets of values represent the top and bottom of the bulk FTO layer. The various parameters for the poles and oscillators, along with layer thicknesses, are shown in Table 3.2. In this table, photon energy is given in electron volts (eV). Note the presence of two oscillators for the FTO layer.

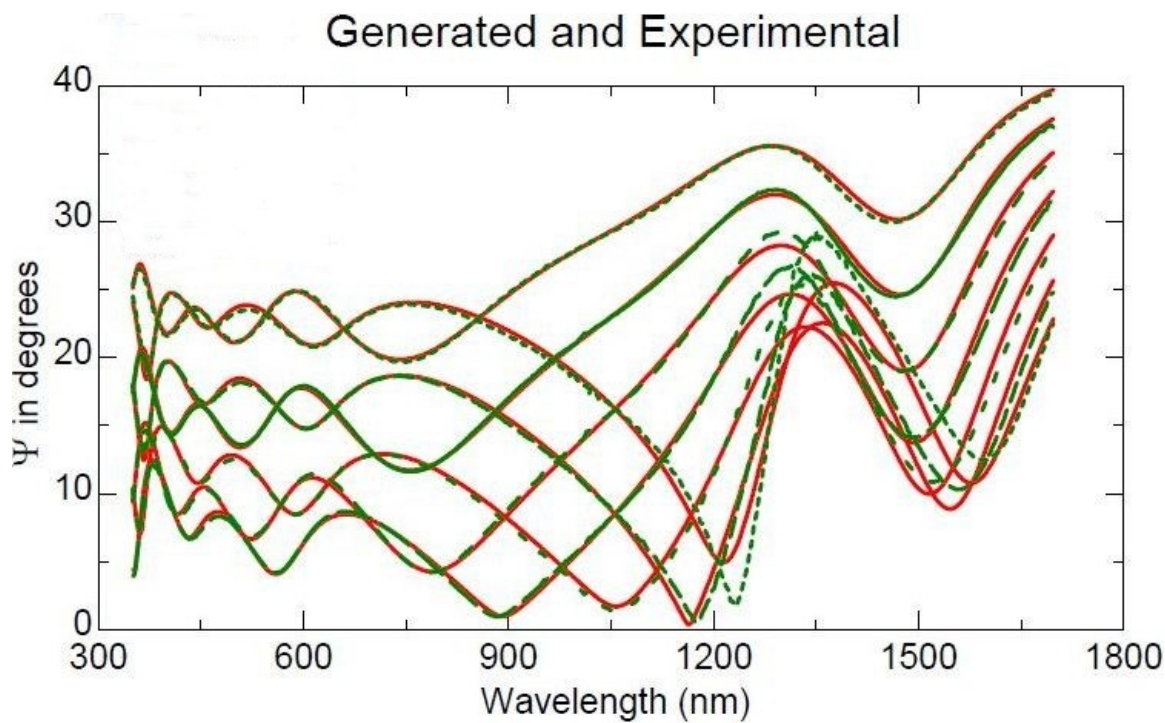


Figure 3.1: Ψ Plots for the Woollam TEC-15 Study.

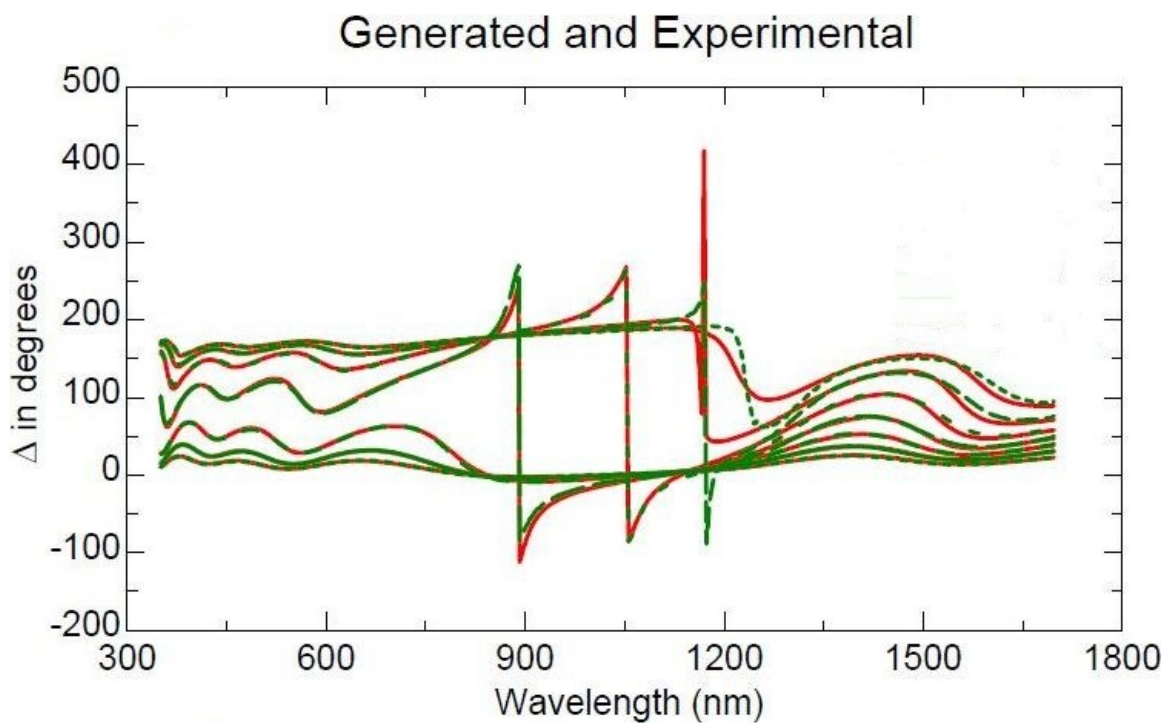


Figure 3.2: Δ Plots for the Woollam TEC-15 Study.

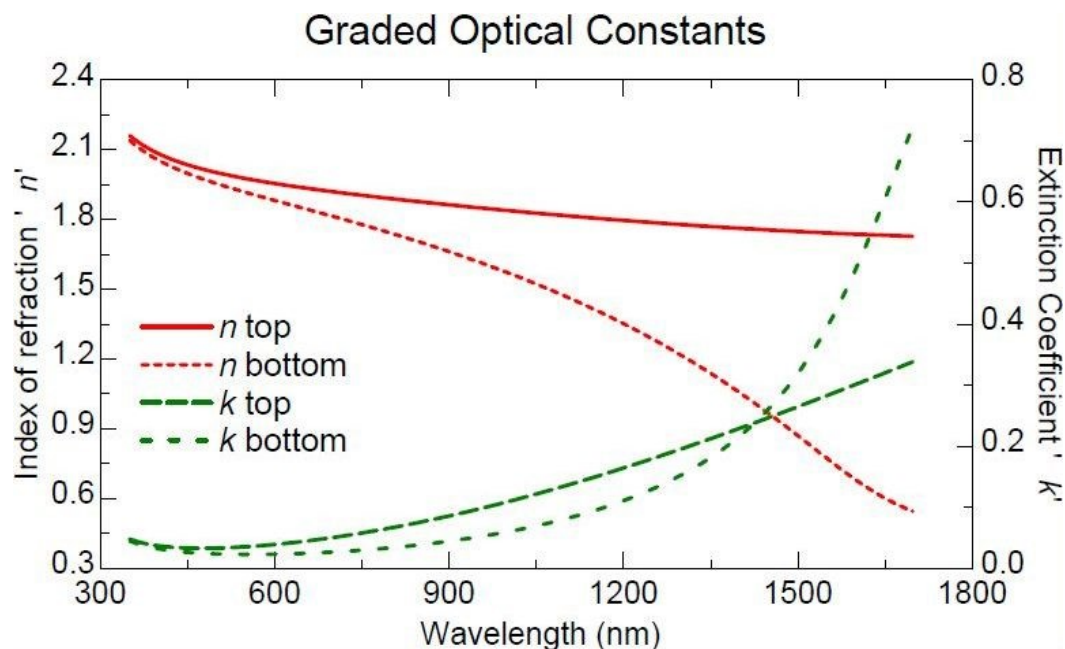


Figure 3.3: n and k Plots for the Woollam TEC-15 Study.

Table 3.2: Layer Thickness and Lorentz Oscillator Terms for Various Layers of TEC-15 Glass (values from reference [43]).

Layer	Thickness	Oscillator	Terms					
Surface Roughness	30 nm	Surface layer roughness was modeled using an EMA layer comprised of 38.4% surface layer material and 61.6% void.						
Surface Layer		Tauc-Lorentz	ϵ_{∞} 2.3139	Amp ((eV) ²) 225	E _n 5.6358	C 4.3075	E _g 3.138	
		Rho-Tau Drude	ϵ_{∞} 2.3139	ρ 1.1178	τ 6.1306	m 1	N 5.179e+21	ν 10.782
SnOx:F	293 nm	Tauc-Lorentz	ϵ_{∞} 1.1665	Amp ((eV) ²) 160.65	E _n 6.7794	C 6.1656	E _g 3.8751	
		Rho-Tau Drude	ϵ_{∞} 2.3139	ρ 4.3241e-4	τ 6.1275	m 1	N 1.3394e+21	ν 10.776
SiO ₂	24 nm							
SnO ₂	30 nm	Lorentz	ϵ_{∞} 1.0	Amp ((eV) ²) 1	E _n 3	Br 0.2		
Glass	1mm							

Modeling the TEC-15 glass posed a significant challenge. Because the component materials are well known, and the raw data plots for Ψ and Δ showed good curves without excessive noise, it was possible to develop a preliminary model that was believed to represent a reasonable approximation. Subsequent refinement showed a reduction in MSE, first from 212 to 112, and later to 9.336. As shown in Table 3.5 and Figures 3.4 and 3.5, the Woollam Study CdS

model, which was based directly on the TEC-15 model, gave an MSE of 13.2, which further suggests that the TEC-15 glass model is sufficient to allow for useful measurement of the overlying layers. Preliminary SEM appeared to confirm the three-layer structure and approximate thicknesses.

Of particular note is the significance of the complex structure of the FTO layer. Comparing the results of the final Woollam Study model to models lacking either the gradient in the bulk layer or the surface roughness, the complex model invariably produced a better MSE. It is believed the change in properties was due primarily to variations in impurities in the tin oxide, such as the amount of fluorine doping and void fraction. Impurities of this type are believed to substantially impact the local conductivity of the layer. Although a conductive oxide, from the standpoint of the ellipsometer, the FTO showed properties similar to a metal near the low-energy portion of the Ψ and Δ . Because the outermost shell electrons in metals are already in the conduction band or at nearby energy levels, low energy photons are sufficient to move charge carriers, causing the large features in the Ψ and Δ plots near 1500 nm.

Results from the measured and modeled Woollam Study for the CdS sample are shown in Figures 3.4 through 3.6. Figures 3.4 and 3.5 show a comparison of the Ψ and Δ values, respectively, produced by actual SE measurements (dashed lines) and the model (solid lines). The modeled optical constants n and k for the bulk CdS layer are shown in Figure 3.6. Interestingly, addition of an intermix layer between the FTO and CdS comprised of FTO, CdS and void to the initial model provided for a reduction in MSE of nearly a factor of two, but adding the intermix layer back into to the final Woollam Study model did not improve the MSE. A uniqueness fit using the first model suggested that the FTO thickness, intermix oscillator values, and intermix thickness were interrelated. This suggests that the refined model may not

represent the actual structure of the FTO layer, but rather, it simulates the conductivity of the TEC-15 glass well enough that measurement of the CdS proceeds smoothly. A similar approach for inclusion of an interface between CdS and CdTe also resulted in a better fit and hence was adopted for subsequent samples.

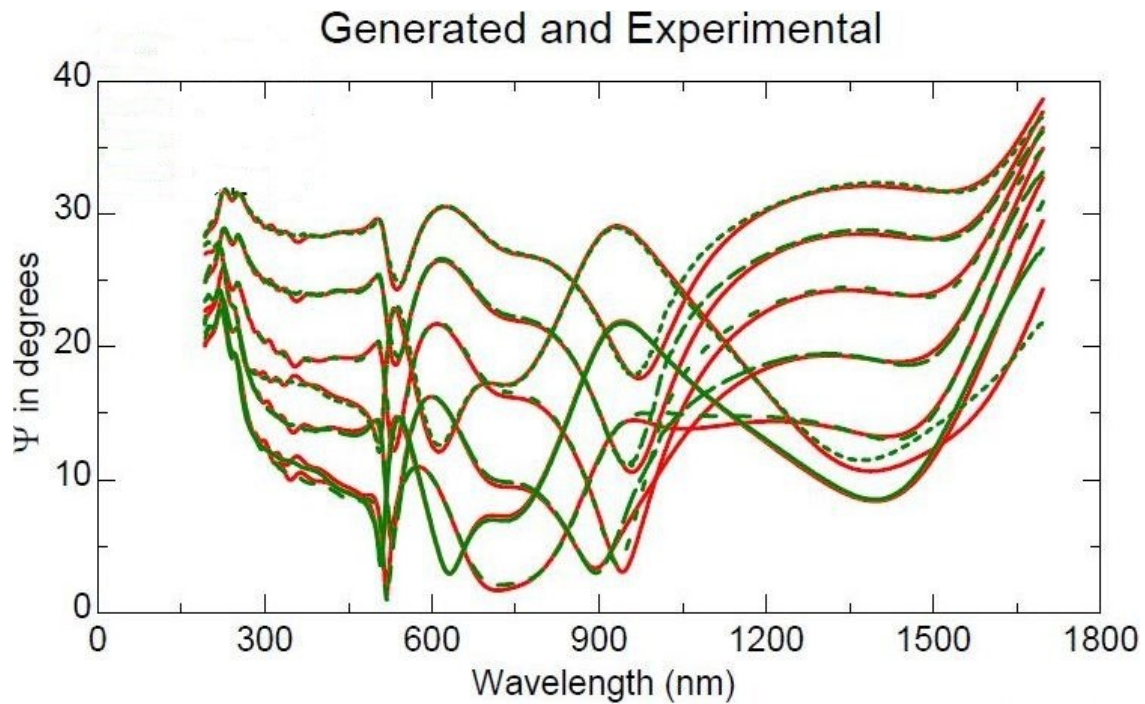


Figure 3.4: Ψ Plots for the Woollam CdS Study.

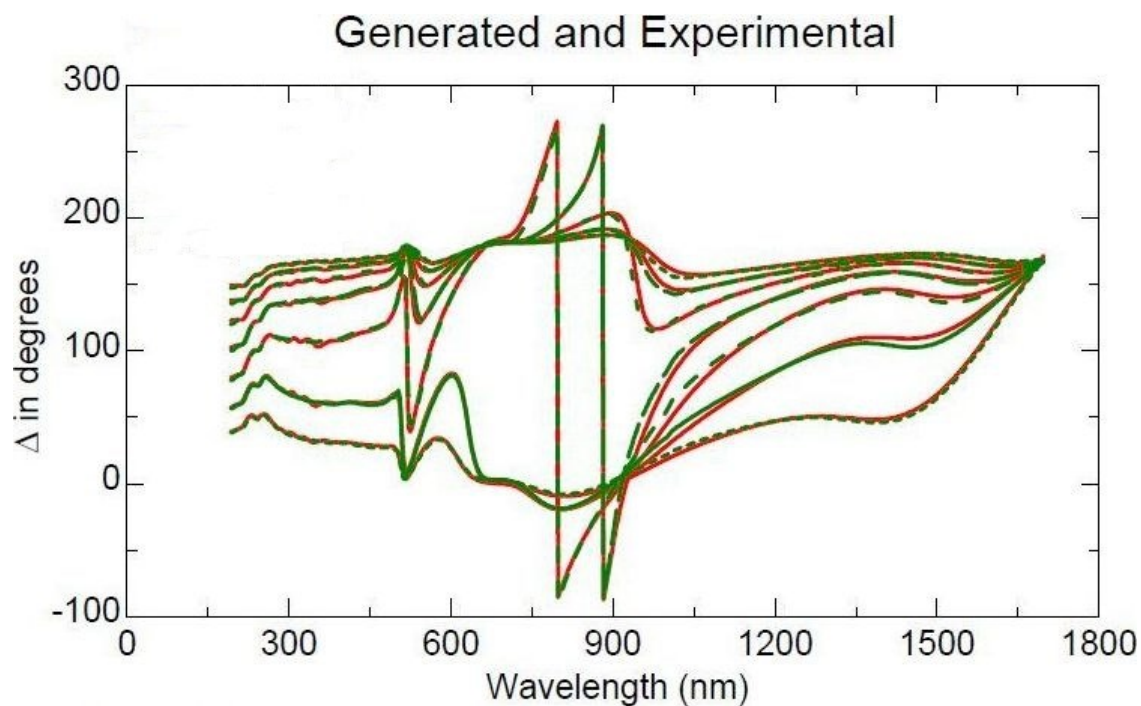


Figure 3.5: Δ Plots for the Woollam CdS Study.

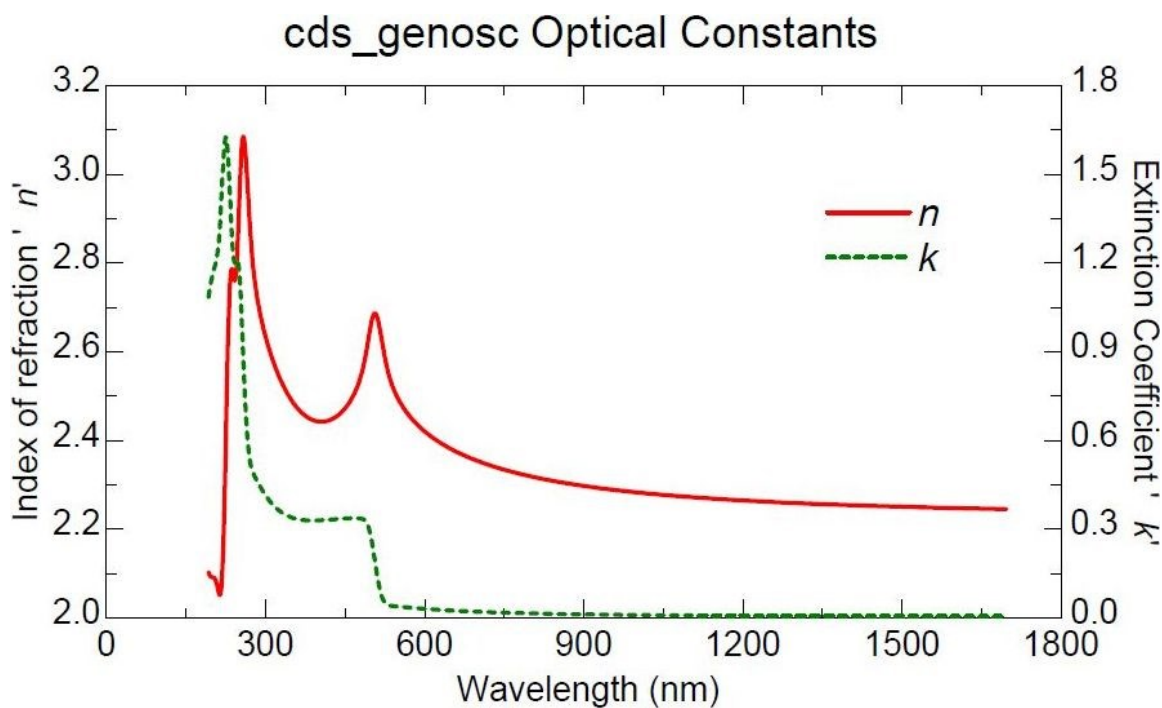


Figure 3.6: n and k Plots for the Woollam CdS Study.

Various attempts to model the untreated CdTe data were unsuccessful; the closest fit achieved is shown in Figures 3.7 through 3.9. Figures 3.7 and 3.8 show a comparison of the Ψ

and Δ values, respectively, produced by actual SE measurements (dashed lines) and the model (solid lines). The modeled optical constants n and k for the bulk CdTe layer are shown in Figure 3.9. The CdTe sample sent to J.A. Woollam produced data that was noticeably noisier than the TEC-15 or CdS. As a result, it was necessary to disregard the high-energy portion of the spectrum to allow a model that provided a close approximation of the waveforms in the low energy wavelengths as shown in Figures 3.7 and 3.8. The raw data appeared to show the absorption and transmission spectrum regions characteristic of a direct-band gap semiconductor; however, due to the noise and omission of some wavelengths, the final fit appeared to represent a less accurate fit. As a result the J.A. Woollam report concluded that the results may not be quantitatively valid [66]. However, SEM showed that the stack thickness was close enough (less than 5%) to suggest that at least some values may have been meaningful even if most were not. This Model showed an unusually thick surface roughness, over 100 nm. It was suggested that the surface roughness contributed to the difficulties in modeling. It is believed that surface roughness presents a constantly changing angle of incidence which diffuses the reflected light, a phenomena known to increase noise [66]. Based on these results, Br treatment was used in the Baseline Study in an attempt to reduce the surface roughness.

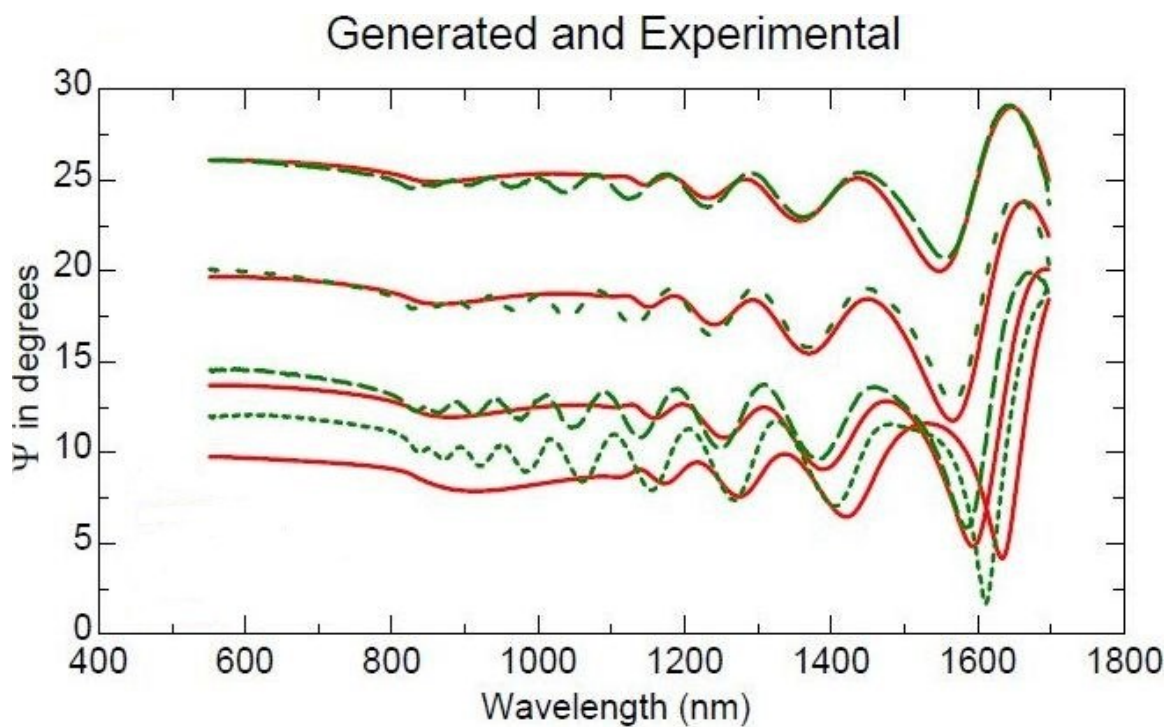


Figure 3.7: Ψ Plots for the Woollam CdTe Study.

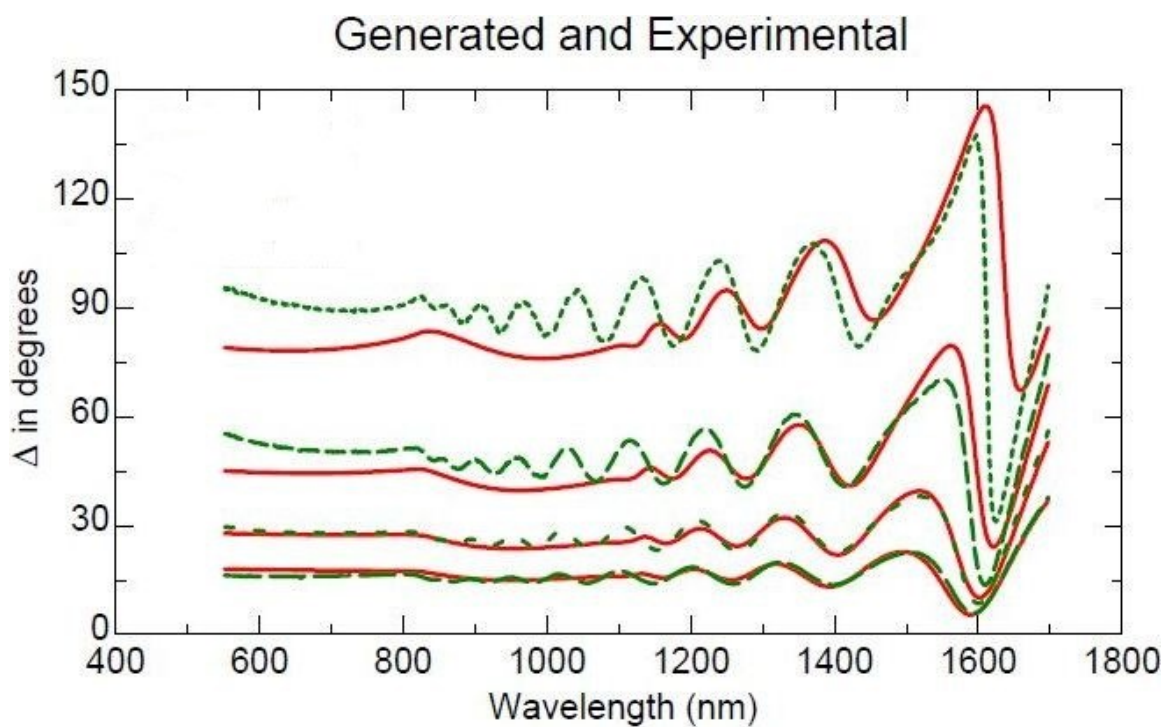


Figure 3.8: Δ Plots for the Woollam CdTe Study.

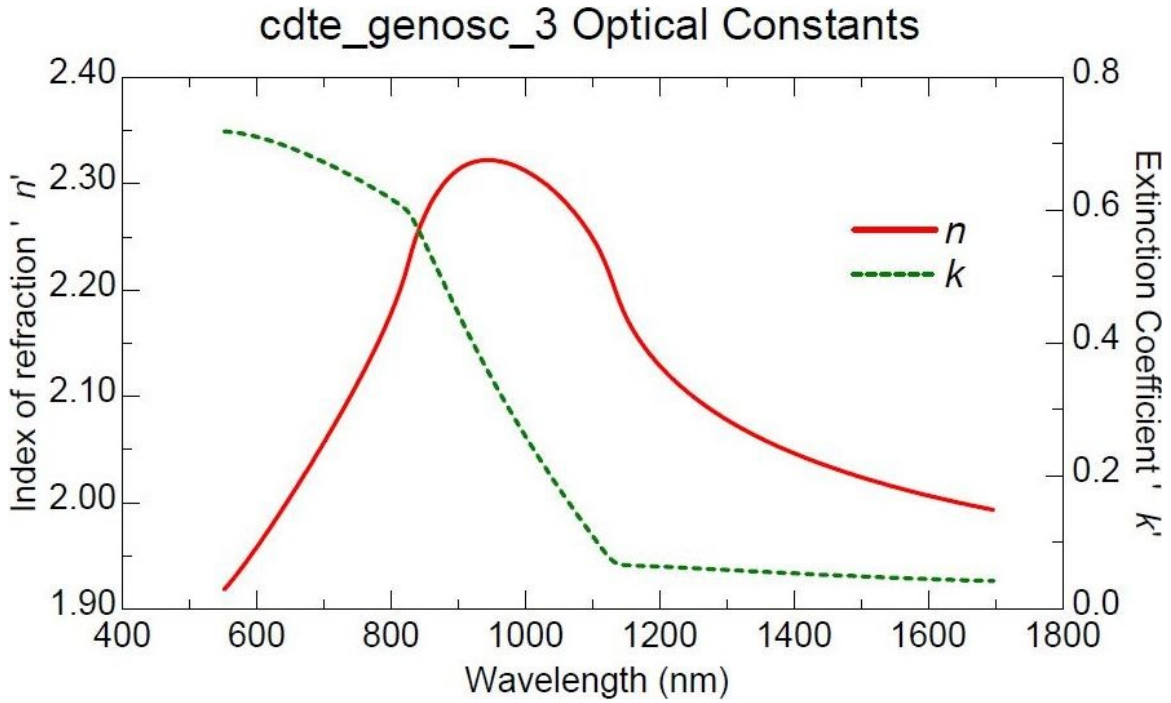


Figure 3.9: n and k Plots for the Woollam CdTe Study.

Results for the Cl and Cu-treated samples are shown in Figures 3.10 through 3.15 and Tables 3.3 and 3.4. Figures 3.10 and 3.11 show a comparison of the Ψ and Δ values, respectively, produced by actual SE measurements (dashed lines) and the model (solid lines) for the Cl-treated sample. Figures 3.12 and 3.13 show the corresponding data for the Cu-treated sample. The modeled optical constants n and k for the bulk CdTe layer for the Cl and Cu-treated samples are shown in Figures 3.14 and 3.15. Table 3.3 lists the model layer thicknesses for the Cl (left 2 columns) and Cu (right two columns)-treated samples for comparison. The identical values for the bottom 5 values out of 11 are due to these values being fixed at values determined by previous fits. It was believed that the relatively large differences in the upper layer thicknesses were primarily due to physical differences between the individual devices; this was later confirmed by SEM. Table 3.4 shows the n and k values at 900 nm as well as thickness and porosity values estimated for the completed (copper-treated) device.

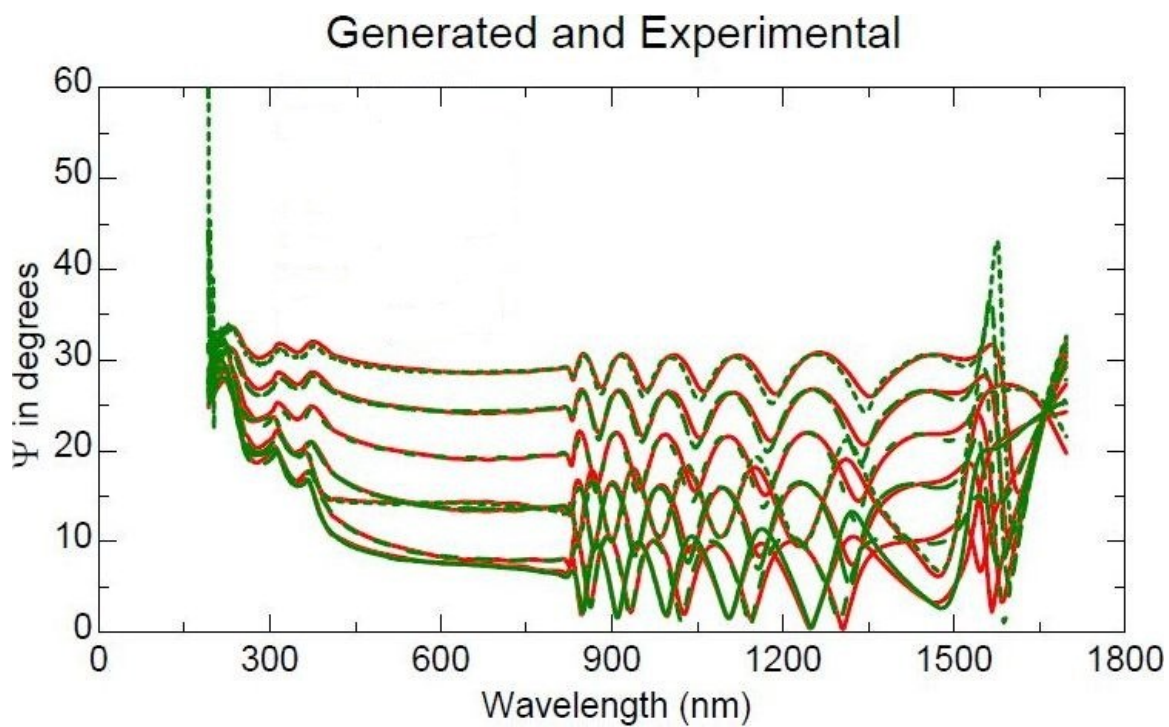


Figure 3.10: Ψ Plots for the Woollam Cl-treated Study.

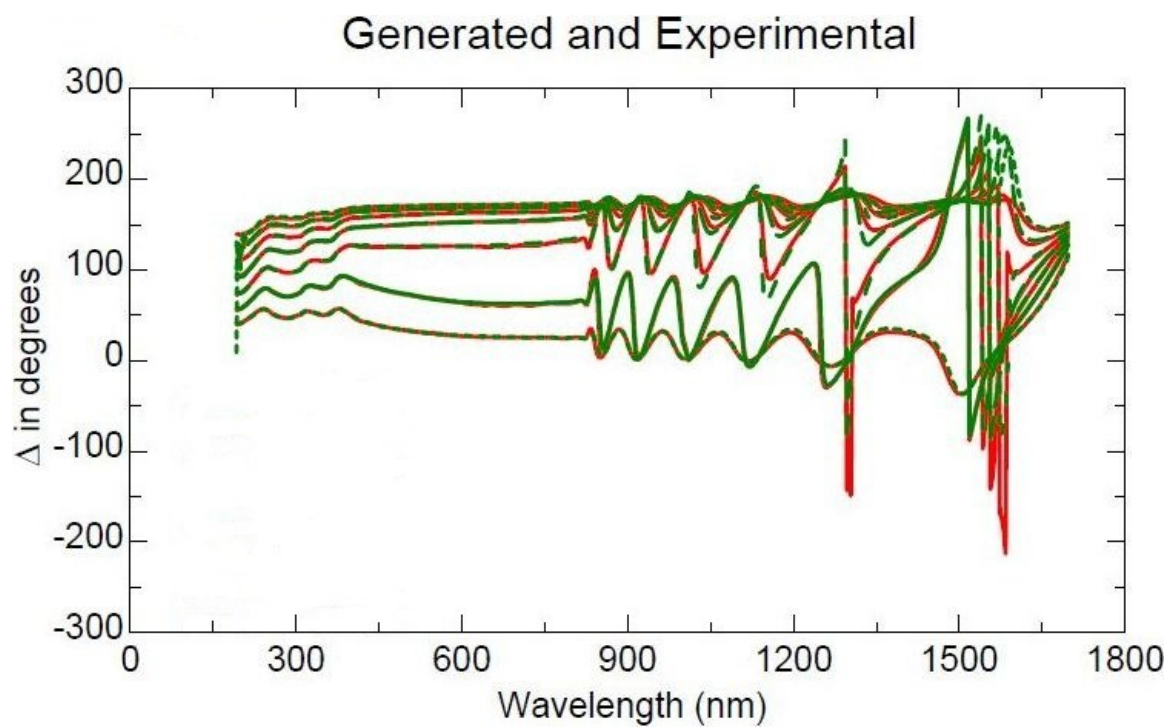


Figure 3.11: Δ Plots for the Woollam Cl-treated Study.

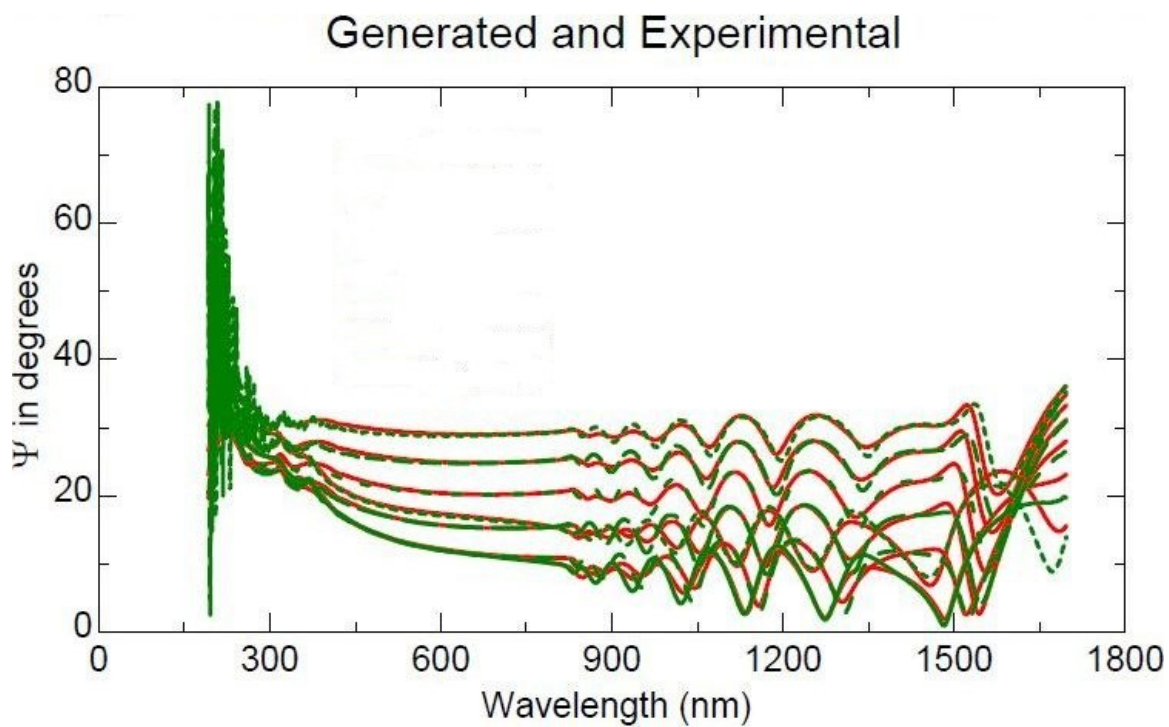


Figure 3.12: Ψ Plots for the Woollam Cu-treated Study.

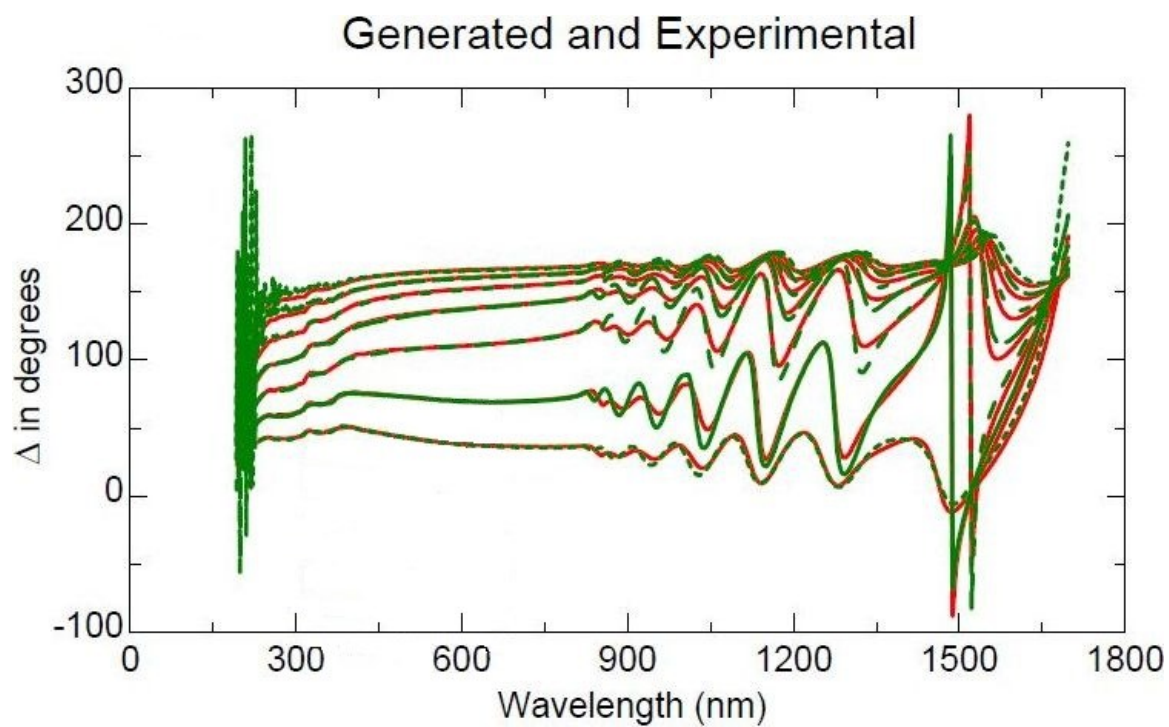


Figure 3.13: Δ Plots for the Woollam Cu-treated Study.

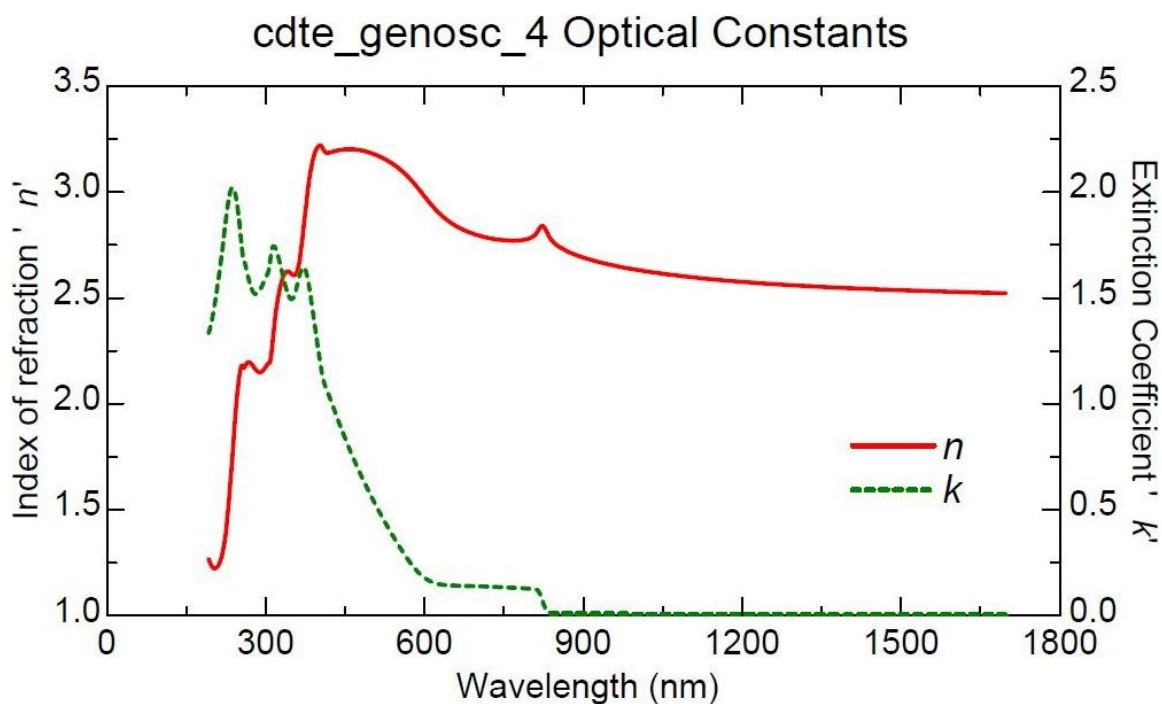


Figure 3.14: n and k Plots for the Woollam Cl-treated Study.

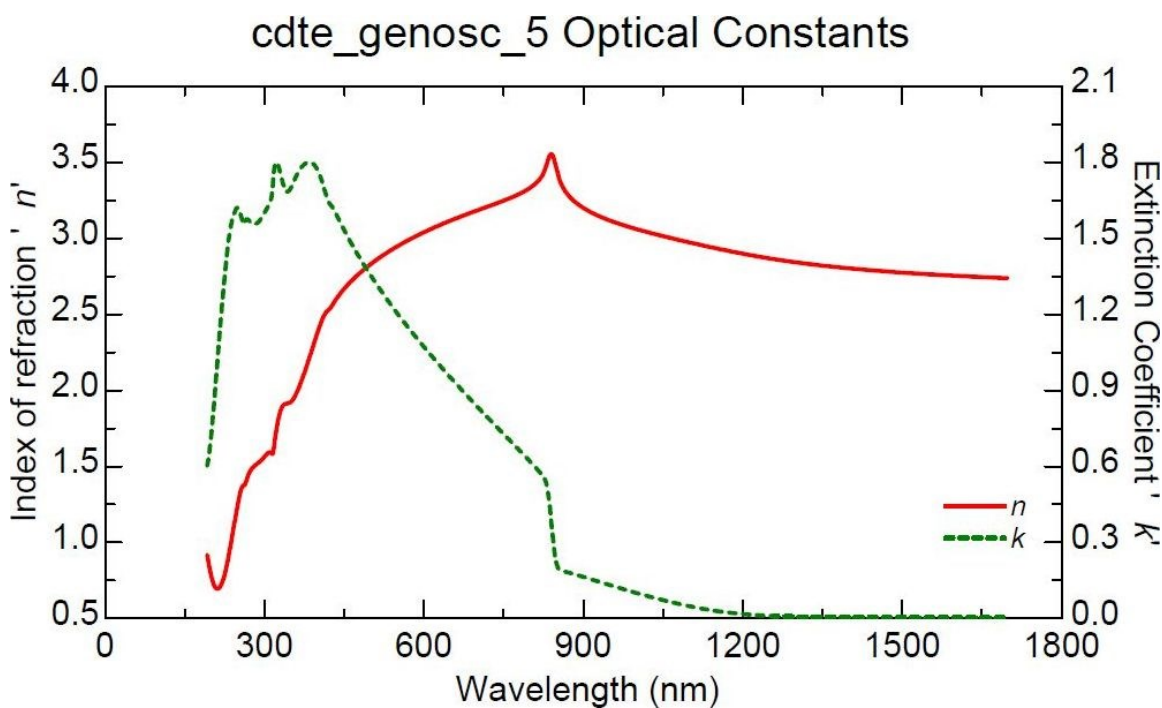


Figure 3.15: n and k Plots for the Woollam Cu-treated Study.

Table 3.3: Fitted Thicknesses for Different Layers for Cl- and Cu-treated CdTe/CdS PV Device on TEC-15 Glass (values from reference [43]).

(a) Cl-treated		(b) Cu-treated	
Layer	Thickness (nm)	Layer	Thickness (nm)
Surface Roughness 1 EMA (50% CdTe + 50% Void)	6	Surface Roughness 1 EMA (50% CdTe + 50% Void)	15
Surface Roughness 2 EMA (78% CdTe + 22% Void)	11	Surface Roughness 2 EMA (88% CdTe + 12% Void)	44
Surface Roughness 3 EMA (92% CdTe + 8% Void)	48	Surface Roughness 3 EMA (92% CdTe + 14% Void)	10
CdTe layer	843	CdTe layer	1453
Interface Layer EMA (50% CdS + 50% CdTe)	116	Interface Layer EMA (50% CdS + 50% CdTe)	150
CdS	211	CdS	201
Surface FTO	13	Surface FTO	13
Graded FTO	300	Graded FTO	300
SiO ₂	18	SiO ₂	18
SnO ₂	30	SnO ₂	30
Glass	1 mm	Glass	1 mm

Table 3.4: Summary of Values Measured for Completed Device (values from reference [43]).

layer	n	k	thickness	void %
tempered glass	2.1	0	1 mm	0%
interface	2.05	0.02	0.0 nm	0%
SnO ₂	2	0.05	30 nm	0%
interface	2.05	0.02	0.0 nm	0%
SiO ₂	2.1	0	24 nm	0%
interface	1.4	0.05	23 nm	0%
FTO	0.6	0.1	290 nm	0%
interface	0.5	0.05	13 nm	27%
CdS	0.4	0	210 nm	0%
interface	1.4	0.2	112 nm	0%
CdTe	2.3	0.4	1458 nm	0%
surface roughness	2.3	0.4	52 nm	22%

The Woollam Study results for the Cl- and Cu-treated samples showed reduced noise and surface roughness compared to the raw CdTe. As a result, these samples provided lower MSE

values of 21.55 and 34.62, respectively. It was noted that the modeling results were insensitive to the buried non-conducting SnO_2 and SiO_2 layers of TEC15 glass. Hence, these layer thickness and optical constants were held constant at the values derived from fitting the as-received TEC15 glass. The shape of the n and k curves (see Figures 3.14 and 3.15) differed markedly from those of the untreated CdTe in Figure 3.9. The relatively narrow peaks in the treated data is typical of more crystalline materials, while the very broad peak shown in Figure 3.9 is more typical of amorphous materials. Although these plots are for the bulk layer, it is believed that it is possible a large surface roughness can affect the values measured for the bulk layer [42]. It is generally believed that an increase in the index of refraction of a material at visible (or longer) wavelengths can be caused by changes in crystal microstructure, density (e.g., porosity), or composition. It has been seen that crystalline materials will generally have higher but narrow absorption peaks, while their disordered counterpart will have broad but lower overall absorption peaks (e.g. amorphous vs. crystalline Si) [67]. In crystalline materials, photon absorption is concentrated at electronic transitions defined by the atomic arrangement, resulting in sharp peaks; in amorphous ones, organized atomic structure breaks down to an amorphous distribution of atoms, randomizing photon interaction.

Results from modeling attempts by other authors indicated that subtle shift observed in the chemically treated CdTe layers were more an artifact of surface roughness than an actual shift in the values of CPs [68]. XRD showed a loss of preferred orientation in the CdTe layer with successive chemical surface treatment. This is likely the result of grain growth occurring due to annealing, whereas the newly-deposited CdTe would have had a preferential orientation due to the deposition process. This is generally associated with more amorphous properties in regard to a broadening of the overall peak structure for n and k , which is seen clearly in the

Woollam Study data, and to a lesser extent in the Baseline Study data. This, along with surface roughness parameters, and other factors, may provide a means for SE data to have some visibility of the grain structure, which has been shown to be an important factor in photovoltaic performance. The peak associated with the band gap appears redshifted in the Woollam Study Cu-treated model as opposed to the Cl-treated model. There can be several reasons for such a shift, such as variation in alloy composition, but in this case it was possible [43, 66] to eliminate everything but changes in lattice parameter (from 6.487 to 6.484 Å) and the corresponding energy state structural changes.

Results from all models are shown in Tables 3.5 and 3.6. Table 3.5 shows the band gap and MSE values generated from SE models of the various samples. Table 3.6 lists the fitted thicknesses for these samples.

Table 3.5: Values for Individual Samples (values from reference [43]).

Sample	Device E_g	Best MSE
TEC-15	-	4.3
CdS	-	13.2
CdTe	1.5028	44.4
Cl-treated	1.4069	48.4

Table 3.6: Fitted Thicknesses for Different Layers for the Woollam Study Cl- and Cu-treated Samples (values from reference [43]).

Sample	TEC-15	CdS	Cl-treated	Cu-treated
Layer	Thickness			
Surface Roughness EMA (top layer + void)	-	11 nm (void 50%)	51 nm (void 17.7%)	52 nm (void 22.3%)
CdTe	-	-	1499 nm	1458 nm
Interface EMA layer (50% CdTe + 50% CdS)	-	-	198 nm	112 nm
CdS	-	209 nm	227 nm	210 nm
EMA (Surface roughness or interface layer)	30 nm	13 nm (void 26.5%)	13 nm (void 26.5%)	13 nm (void 26.5%)
FTO	293 nm	288 nm	300 nm	300 nm
SiO ₂	24 nm	24 nm	24 nm	24 nm
SnO ₂ (Fixed)	30 nm	30 nm	30 nm	30 nm
Glass	1 mm	1 mm	1 mm	1 mm

3.1.2. Results Derived from the Model Values.

Figure 3.16 shows the modeled real and imaginary components of dielectric constant for the CdTe layer before (\square) and after (O) exposure to the CuCl vapor flux. Optical constants for the bulk CdTe layer from a model fitted to Aspnes' [54] data are also shown (Δ) for comparison. As can be seen in Figure 3.16, below 3.5 eV, the Cu-treated sample exhibited higher values of the ϵ_1 (and hence a higher refractive index) than the Cl-treated sample. However, above 3.5 eV, the ϵ_1 and n values for the Cu-treated sample were lower. The modification of absorption shape affects the real part of the dielectric function through Kramers-Kronig consistency, which leads to a larger index at longer wavelengths for amorphous materials than their crystalline counterparts. It is likely that this increase in the ϵ_1 (and hence the refractive index) at energies below 3 eV for the Cu-treated CdTe layer, was a result of increased disorder in this layer.

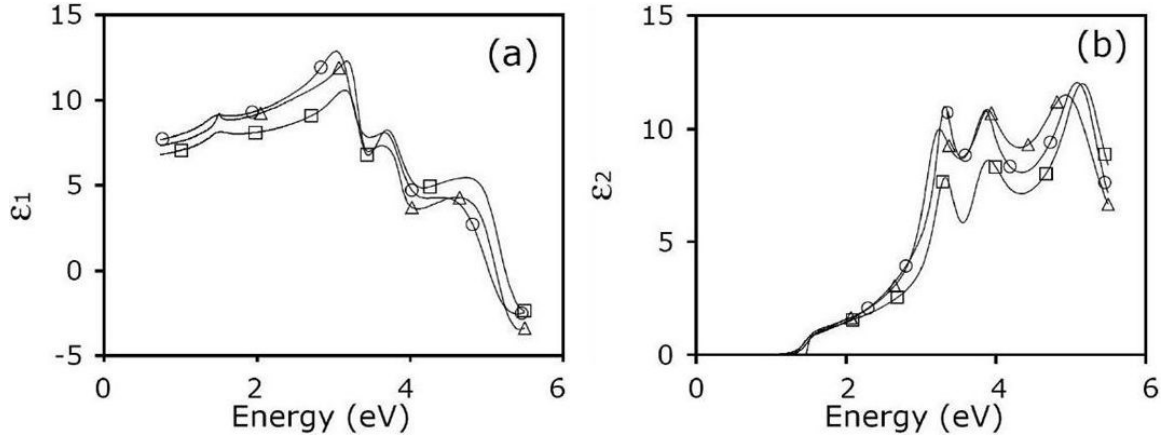


Figure 3.16: Modeled Real (ϵ_1) and Imaginary (ϵ_2) Dielectric Components for the CdTe Layer of Selected Samples (images from reference [43]).

The optical constants of the CdTe layers were used to derive the values for optical band gap and critical points (CP) of CdTe [66]. The spectral dependence of the absorption coefficient of a material can be used to estimate the direct and indirect band gaps of CdTe layers using a Tauc plot [69]. The absorption coefficient of a material is defined by the relation

$$\alpha = \frac{4\pi k}{\lambda} \quad (3.1)$$

where λ is the wavelength of the incident photon, k is the extinction coefficient, and α is the absorption coefficient. Figure 3.17 shows Tauc plots for the direct (○) and indirect (□) band gaps (a) before and (b) after exposure to Cu treatment. Results are shown in Table 3.7 along with energy components for from the model fitted to Aspnes' data [54]. It is believed [42] that the subtle shift observed in the chemically treated CdTe layers may be more an artifact of surface roughness than an actual shift in the values of CPs.

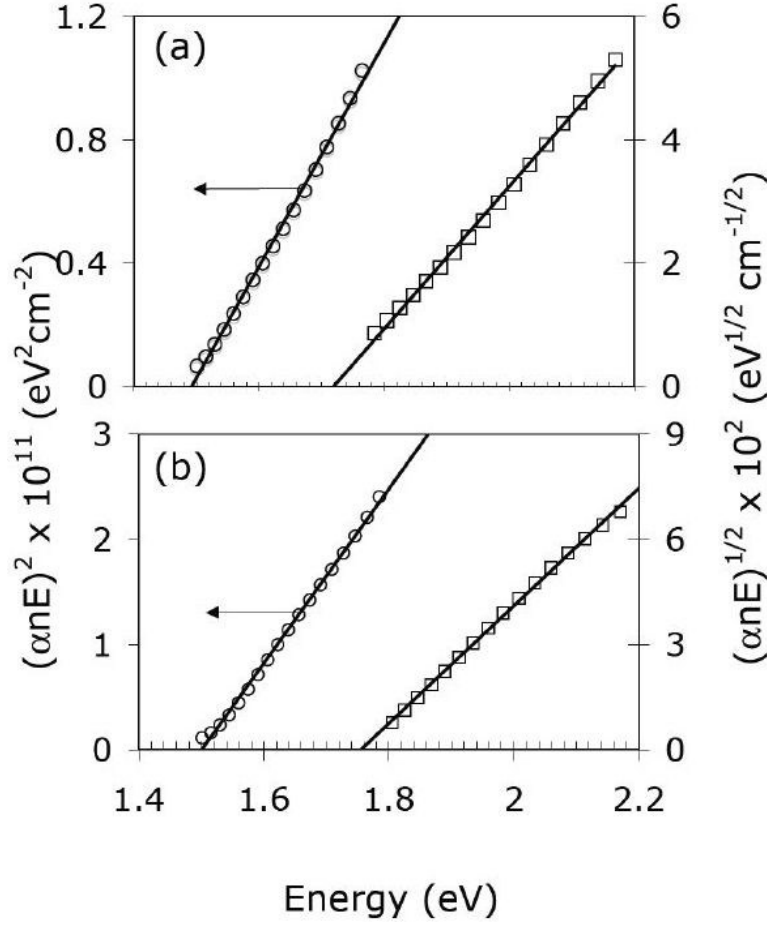


Figure 3.17: Tauc Plots for CdTe Layer (image from reference [43]).

Table 3.7: Various Energy Components for the CdTe Layer (values from reference [43]).

	$E_{g1}(\text{eV})$	$E_{g2}(\text{eV})$	$E'_0(\text{eV})$	$E_1 + \Delta_1(\text{eV})$	$E_1(\text{eV})$
Aspnes data	1.46 ± 0.04	1.70 ± 0.04	5.1 ± 0.1	3.88 ± 0.05	3.30 ± 0.05
Cl-treated	1.49 ± 0.04	1.72 ± 0.04	5.2 ± 0.1	3.94 ± 0.05	3.27 ± 0.05
Cu-treated	1.50 ± 0.04	1.75 ± 0.04	5.1 ± 0.1	3.85 ± 0.05	3.19 ± 0.05

Figure 3.18 shows the second-order derivative of the real (ϵ_1) and imaginary (ϵ_2) components of dielectric constants as a function of wavelength. The graphs show optical constants from models fitted to the Cl (\square) and Cu (O)-treated samples, as well as the Aspnes [54] data (Δ). The critical points for CdTe were obtained by fitting critical-point parabolic band (CPPB) model [68] to the second derivative of ϵ_1 and ϵ_2 .

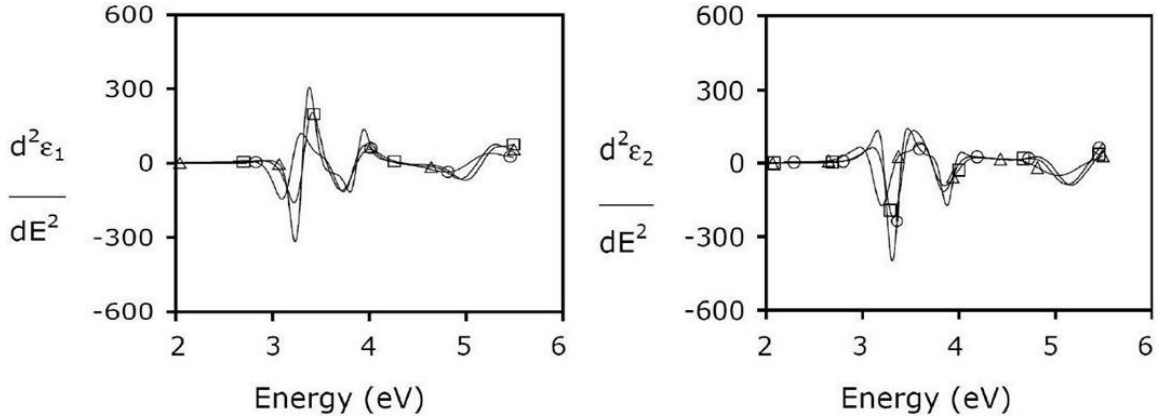


Figure 3.18: Second-order Derivative of the Real (ϵ_1) and Imaginary (ϵ_2) Components of the Dielectric Constant from various models (images from reference [43]).

3.1.3. XRD Results.

XRD scans of the samples used for the Woollam Study indicated the presence of several crystalline phases within the PV device. The crystalline peaks in the XRD spectra could be identified with cubic CdTe [70], tetragonal SnO₂ [71], and hexagonal CdS [72] phases. The stoichiometry of the CdS was confirmed with EDS. A comparison of the relative intensities of CdTe XRD peaks with those of the standard JCPDS (Joint Committee on Powder Diffraction Standards) data revealed that the as-deposited CdTe layer had planes preferentially oriented along the (111) axis. With the Cl treatment, a loss of this orientation was observed which was further reduced with the Cu treatment. XRD spectra were used to estimate the CdTe crystallite size and strain using the Williamson-Hall method. In comparison to the as-deposited CdTe layer, no significant change in the lattice parameter for the Cl-treated CdTe layer was seen ($a = 6.4869 \pm 0.0006 \text{ \AA}$), where a is the lattice parameter and 1 angstrom (\AA) is 10^{-10} meters.

However, further Cu treatment led to reduction of the CdTe lattice parameter ($a = 6.4840 \pm 0.0003 \text{ \AA}$). It was observed that while the Cu-treated sample had CdTe crystallite size of 179 nm and an RMS (root mean square) strain value of 7.6×10^{-4} , the untreated CdTe and Cl-treated samples had CdTe crystallite size of 250 nm and an RMS strain value of 9.6×10^{-4} . This change in lattice

structure is likely due to the replacement of higher ionic radii Cadmium (Cd, 0.97 Å) by low ionic radii copper (Cu, 0.73 Å) at crystallographic lattice sites. Since SE shows changes in the optical properties between the Cl- and Cu-treated samples, SE may provide a potential means to measure the extent to which Cu atoms are substituted into the CdTe structure (as opposed to being present interstitially or along grain boundaries), causing the lattice parameter to shrink. These results are consistent with lattice changes in the CdTe layer with the Cu treatment. More details for these results have been published elsewhere [43].

3.1.4. SEM Results.

The thickness of the PV device was confirmed using cross-section SEM. Figure 3.19 shows the cross-section SEM images the Cl (left) and Cu (right)-treated samples. Device thickness measurements from the SE models and SEM images agreed with each other to within 5% [43].

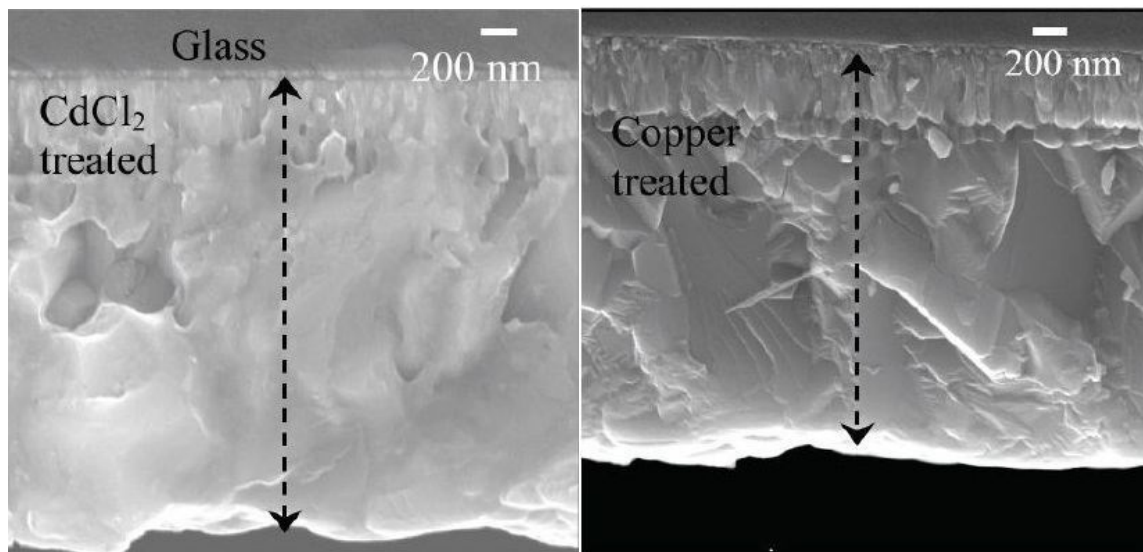


Figure 3.19: Cross-section SEM Images of Woollam Study Samples. (images from reference [43]).

3.2. Baseline Study.

3.2.1. TEC-15 Sample.

Baseline Study Results for the TEC-15 sample are shown in Figures 3.20 through 3.23 and Table 3.8. Figures 3.20 and 3.21 show the measured and modeled Ψ and Δ plots, respectively. The corresponding Woollam Study data is shown in Figures 3.1 and 3.2. The waveform shapes followed the same general pattern, with the Baseline Study data having fewer peaks and a taller peak in Δ near 1200 nm; the Woollam Study data showed substantial noise below 350 nm which was not present in the Baseline Study data, allowing the waveform to be modeled down to 192 nm. Micrometer measurement at a location near the edge showed the glass substrate to be approximately 3.18 mm (3.18 millimeters, or 0.125 inch) thick for all samples; this value was therefore used for all the models in the Baseline Study. The n and k values were modeled for all three thin film layers, the substrate, and the surface roughness. As with the original Woollam Study model, the SiO_2 and substrate glass optical constants were fixed at known values and not measured by the experiment. The optical constants n and k for top and bottom of the bulk FTO layer are shown in Figure 3.22. The corresponding values for the Woollam Study are found in Figure 3.3. The thickness and porosity values obtained are summarized in Table 3.8, along with the SEM thickness value and the MSE values for the models. The overall stack value for the Baseline Study model was higher than the Woollam Study and SEM data. The SEM image produced for this sample is shown in Figure 3.23. The underlying SnO_2 and SiO_2 layers are faintly visible in the image.

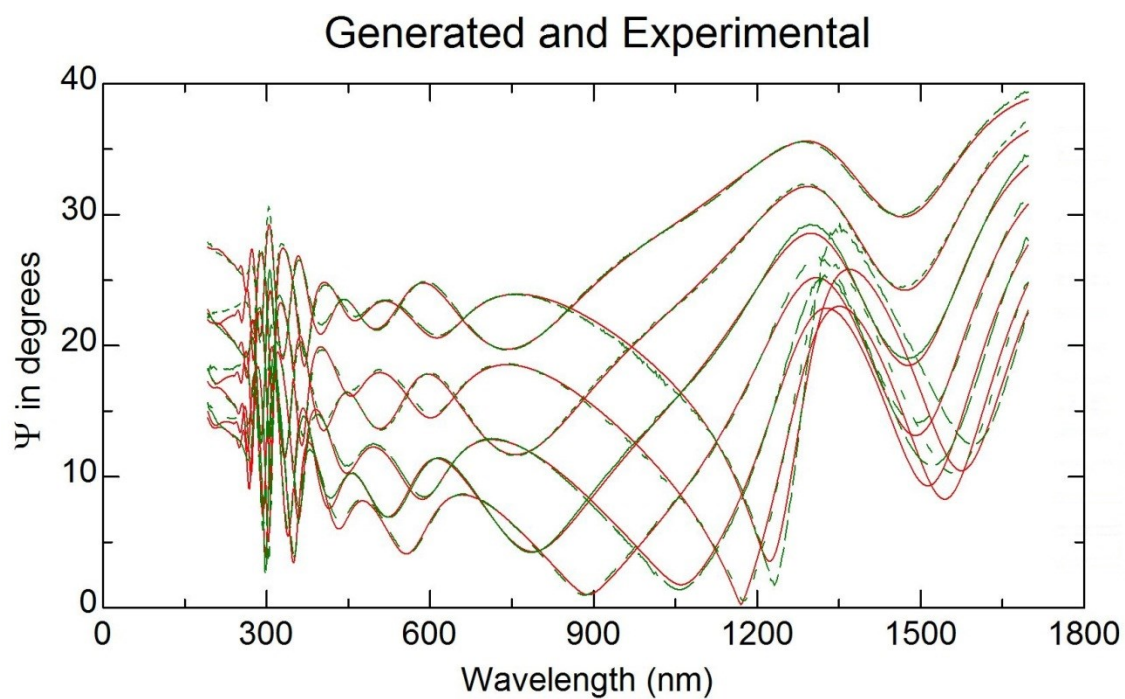


Figure 3.20: Ψ Plots for the TEC-15 Baseline Study.

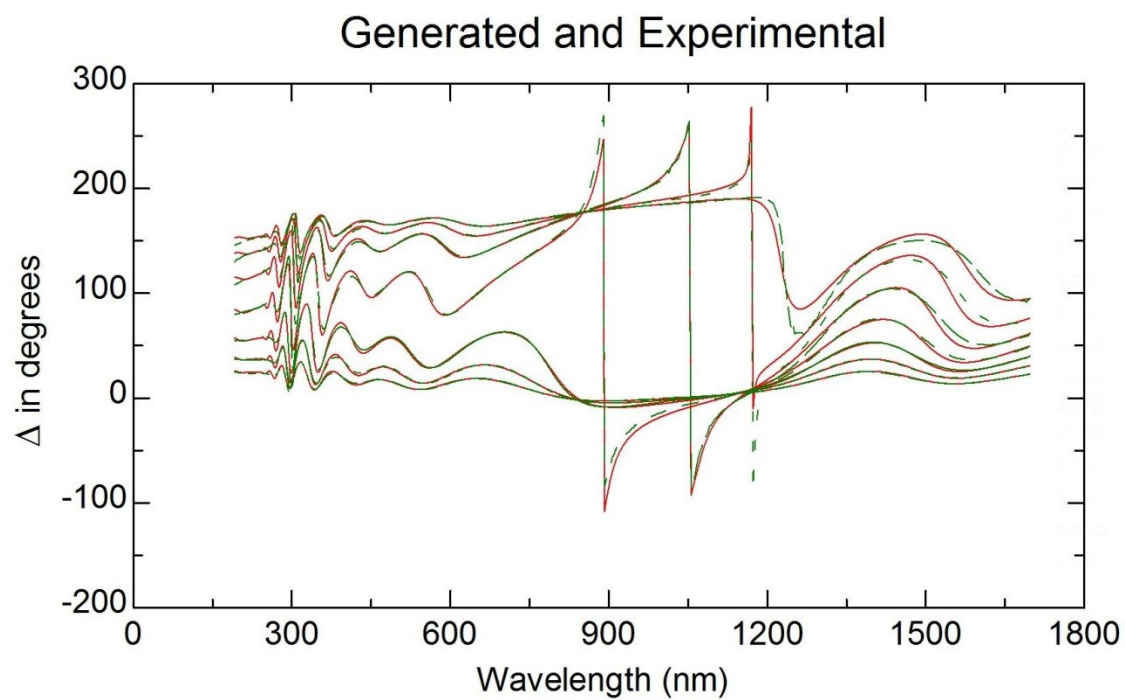


Figure 3.21: Δ Plots for the TEC-15 Baseline Study.

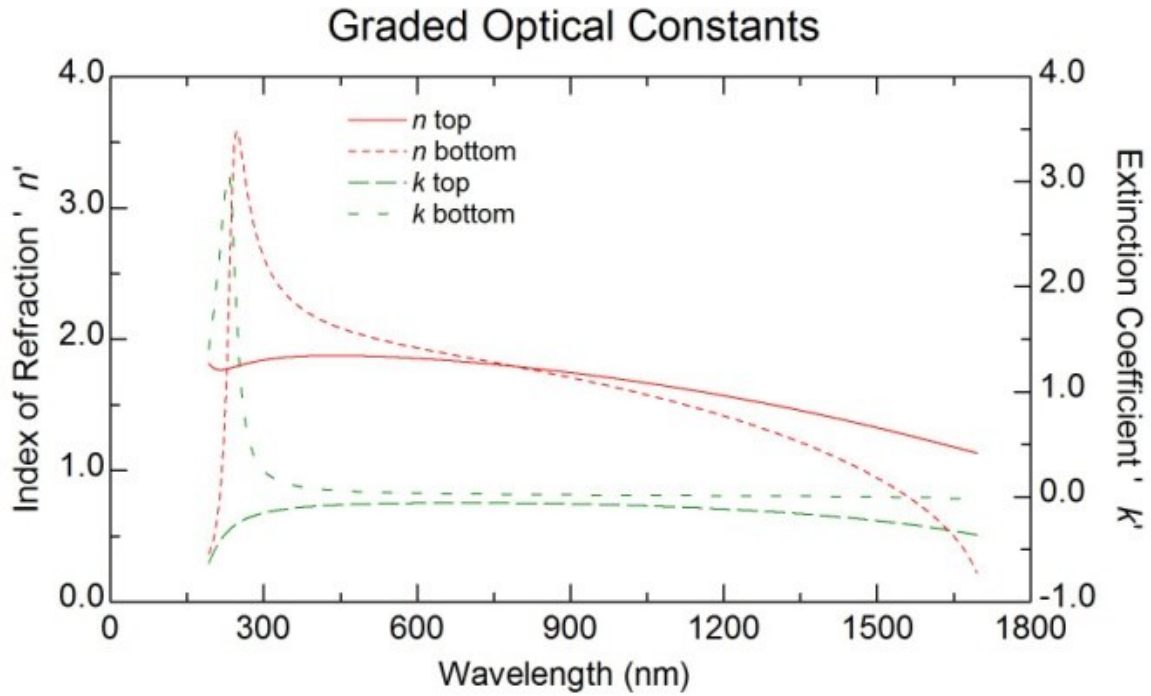


Figure 3.22: n and k Plots for the Baseline TEC-15 Study.

Table 3.8: Summary of Selected Parameter Values for Woollam and Baseline Studies of TEC-15 Samples.

data	Woollam Study	Baseline Study	SEM
surface roughness void	$34.38 \pm 0.13\%$	$57.60 \pm 0.03\%$	-
surface roughness thickness	$311 \pm 1 \text{ \AA}$	$394 \pm 0.5 \text{ \AA}$	
FTO thickness	$2955 \pm 4 \text{ \AA}$	$2980 \pm 0.7 \text{ \AA}$	
SiO ₂ thickness	$271 \pm 7 \text{ \AA}$	$268 \pm 0.6 \text{ \AA}$	
SnO ₂ thickness	$261 \pm 13 \text{ \AA}$	$233 \pm 0.4 \text{ \AA}$	
glass thickness	1 mm (semi-inf)	3.18 mm (semi-inf)	
stack thickness nonuniformity	0%	0%	
MSE	9.336	15.63	3732 Å
stack thickness	$3798 \pm 25 \text{ \AA}$	$3875 \pm 2 \text{ \AA}$	

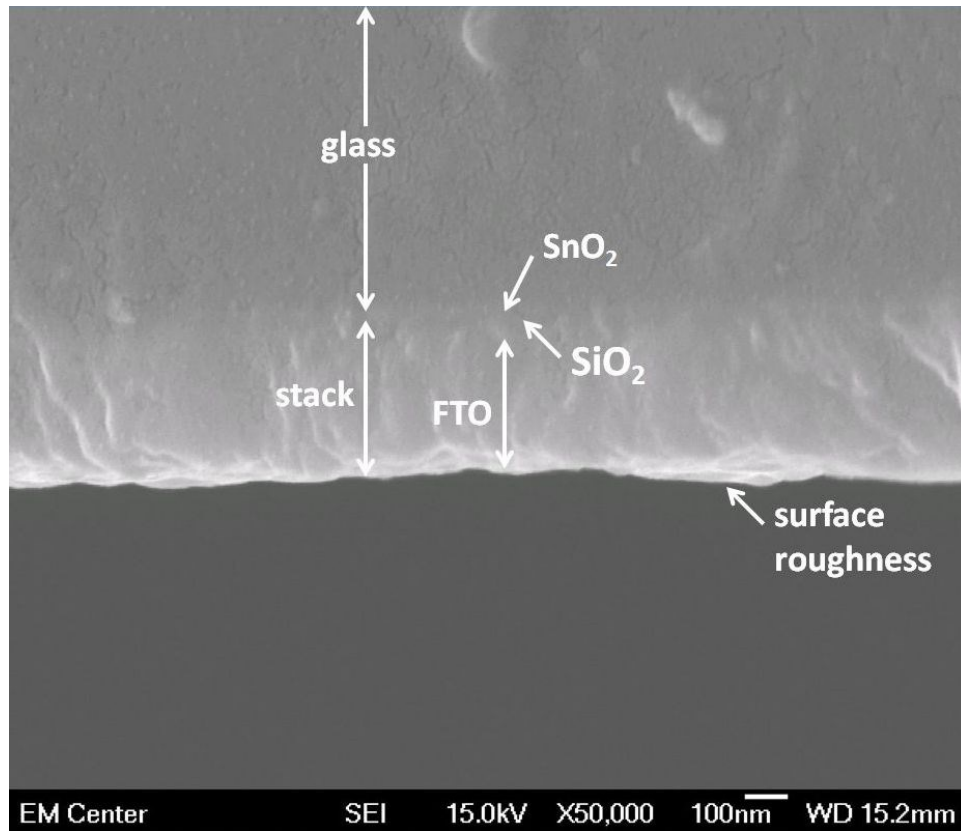


Figure 3.23: SEM Image of TEC-15 Sample.

For the TEC-15 sample, the match of the model to the raw data (Figures 3.20 and 3.21) shows a very close fit between the model and raw data at low to middle wavelengths; the corresponding Woollam Study data is shown in Figures 3.1 and 3.2. Nominally, the shortest wavelengths carry data about the surface properties, while those from middle frequencies carry data from the transparent bulk layers, and those from still longer wavelengths carry data from the underlying layers and the conduction band [42]. In the case of TEC-15, the region near 1500 nm appears to be dominated by the conduction band of the FTO layer, which acts as a metal for energies in that range [42, 73, 74]. This suggests that the Baseline Study TEC-15 model modeled the overall optical characteristics of the surface roughness and bulk FTO layer accurately, but the conductivity of the FTO layer was not as well modeled.

The n and k values for this model (Figure 3.22) appeared redshifted relative to the corresponding Woollam Study values (Figure 3.3). There are a number of possible reasons for this. First, the samples used were different. Although Pilkington glass was selected for its consistency, batches can vary; it is unknown whether the samples came from the same batch. In addition, the sample used for this study, while in good overall condition, had been in storage for some time and experienced wear and chemical exposure prior to testing. All of these may have contributed to differences in optical properties.

A comparison of thicknesses derived using the model developed in this study, the Woollam Study model, and SEM (Table 3.8) shows a number of differences. While some of the differences may be due to batch and differences in location of the sample, discrepancies in the measurement and modeling techniques, i.e., systematic and random error, are also possible. In the case of the SEM readings, the thickness was measured by selection of the surface and substrate / film interface with a cursor by hand, and it is unknown what, if any, distortions may have been present in the image, for example, due to errors in the sample mounting angle. In the case of the SE model, because any error in surface roughness porosity will tend to result in a corresponding error in thickness, and the properties of the SiO_2 layer are very similar to the substrate, the thicknesses of those layers are more difficult to model. Despite these sources of possible error, both the Woollam and Baseline Study models showed a stack thickness within 5% of the corresponding SEM values, suggesting that the models are close enough to the actual values for meaningful measurement of thickness.

3.2.2. CdS Sample.

Baseline Study results for the CdS sample are shown in Figures 3.24 through 3.27 and Table 3.9. Figures 3.24 and 3.25 show the Ψ and Δ plots for all seven angles. The corresponding Woollam Study data is shown in Figures 3.4 and 3.5. The n and k values were modeled for all film layers, the substrate, and the surface roughness. The optical constants n and k for the bulk CdS layer are shown in Figure 3.26. The corresponding Woollam Study data is found in Figure 3.6. While both plots show similar peak locations, the height of the peak near 300 nm was different between the plots. In the graph title at the top of each figure, “cds_genosc” is the filename for the data file containing material properties for the CdS layer; the “genosc” model layer type is described in Section 1.5.2. The thickness and porosity values obtained are summarized in Table 3.9, along with the SEM thickness value and the MSE values for the models. The Baseline Study model produced a thickness within 15 nm of the SEM value, as well as a lower MSE than had been achieved with the Woollam Study model. The SEM image produced for this sample is shown in Figure 3.27. Again, all four main layers were clearly, albeit barely, visible.

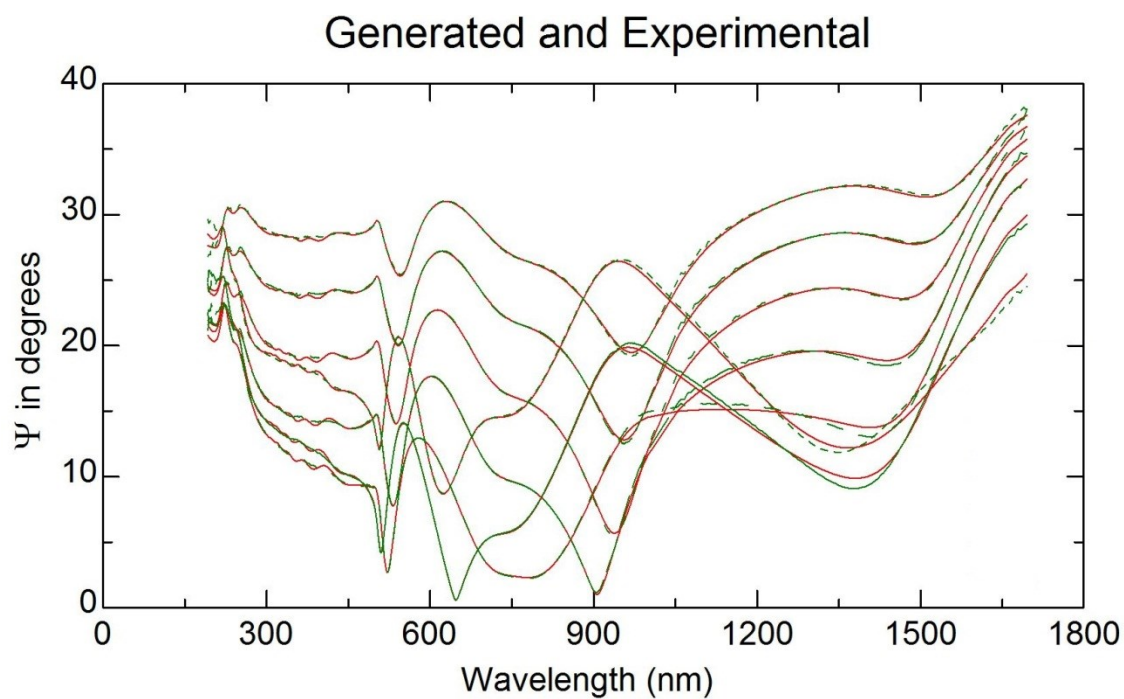


Figure 3.24: Ψ Plots for the Baseline CdS Study.

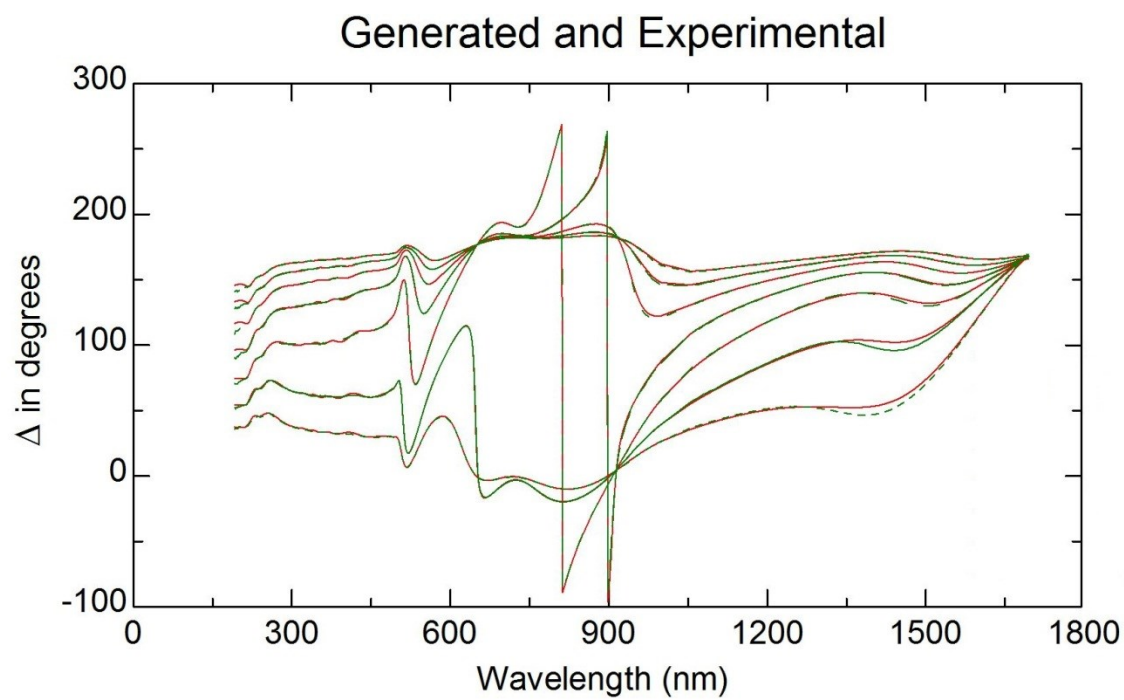


Figure 3.25: Δ Plots for the Baseline CdS Study.

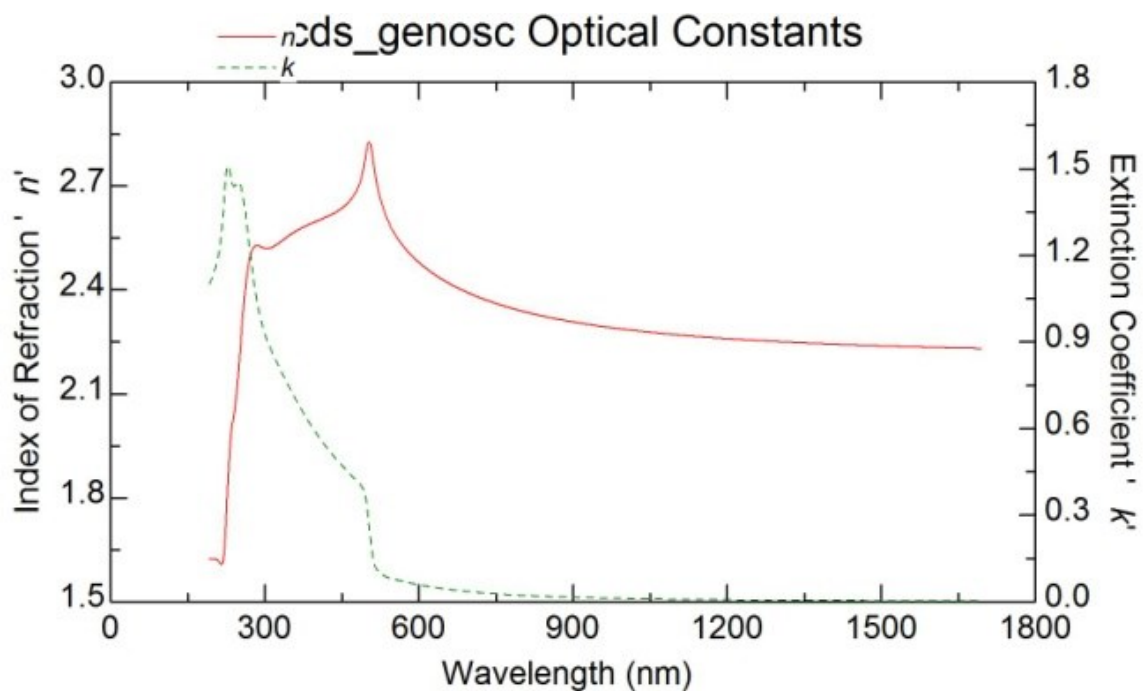


Figure 3.26: n and k Plots for the Baseline CdS Study.

Table 3.9: Summary of Selected Parameter Values for Woollam and Baseline Studies of CdS Samples.

data set	Woollam Study	Baseline Study	SEM
surface roughness void	50%	33.5±0.08%	-
surface roughness thickness	108±0.5Å	171±0.3Å	
CdS thickness	2141±2Å	2000±0.4Å	
FTO thickness	2912±5Å	3228±1.5Å	
SiO ₂ thickness	271 Å	231±1.2Å	
SnO ₂ thickness	261 Å	238±0.9Å	
glass thickness	1 mm (semi-inf)	3.18 mm (semi-inf)	
stack thickness nonuniformity	0%	0%	
MSE	26	9.473	5883 Å
stack thickness	5693±8Å	5868±4Å	

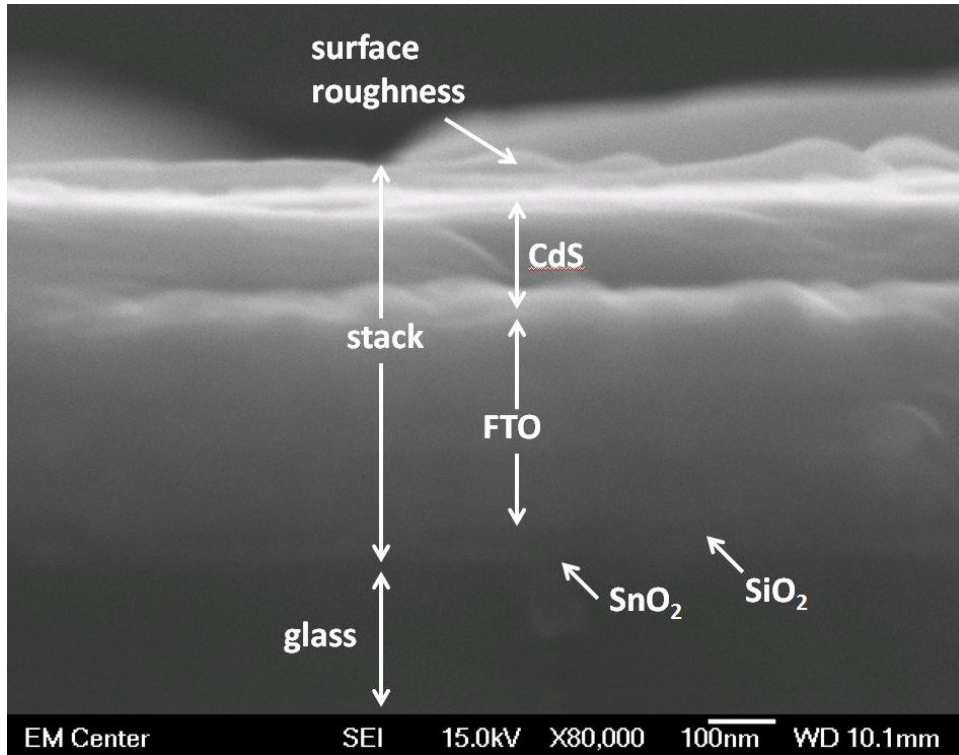


Figure 3.27: SEM Image of CdS Sample.

The model and measured waveform shapes for CdS for the Baseline (Figures 3.24 and 3.25) and Woollam (Figures 3.4 and 3.5) Studies were very similar; one noticeable difference is in the sharp features near 900 nm, which were slightly more vertical for the Baseline Study data. The effect of the conductivity of the FTO layer appears to be visible as a sharp peak in Ψ starting at ~ 1500 nm. This fit was able to slightly improve on the Woollam Study fit both visually and in terms of MSE, particularly in the region near 1000 nm. It appears that this model more correctly matches the effect of the conductivity of the FTO layer than the model of the TEC-15 without CdS, but because the peak extends outside the scanned wavelength range, it is not certain.

The n and k values for the Baseline (Figure 3.26) and Woollam (Figure 3.6) Study models also show the same basic shape. There is a sharp spike in n at ~ 500 nm; at the same location, there is a shift in k , and sharp features in both the Ψ and Δ waveforms. This pattern is characteristic of a shift from an absorption region to a transparency region or a band gap. The

band gap of monocrystalline CdS is 512 nm, so it is likely an indication of the sample's crystallinity. A second peak in n occurs at ~ 300 nm, accompanied by a deep valley. This peak appears to be associated with a bifurcated peak in the Ψ data. The height of this peak varied between the two sets of data. It is possible that wear and chemical exposure, as well as manufacturing differences, played a role. Oxide formation has also been reported as a possible issue for CdTe, CdS, and related materials [51, 75].

The two small layers in the TEC glass are barely visible in Figure 3.27. Since the image renders more dense materials as brighter, the SiO₂ layer appears dark, similar to the glass. The boundary of the FTO and CdS layers is also clearly visible, but it is difficult to discern whether the boundary is sharp or an interface mixture, and no grain boundaries in the CdS are clearly visible. Table 3.9 shows all thickness values determined for the CdS Baseline Study. The Woollam Study model fixed the values for the thicknesses of the innermost layer to the values obtained from the TEC-15 glass. This is believed to be a reasonable strategy as there appears to be little reason to expect them to change with the addition of CdS; however it does not account for the possibility that the layers vary between samples. For the Baseline Study model, these layers were allowed to vary. The Baseline Study CdS model did not include an interface layer between the FTO and CdS layer despite the presence of a significant surface roughness in the TEC-15 model. Data suggested that the model had limited sensitivity to this interface; it is believed that for many materials, SE has difficulty discerning between bulk layer and interface thickness [42]. The resulting model had a thicker bulk FTO layer than for the TEC-15 Baseline model, at the expense of the surrounding layers. Possible explanations include differences between samples, physical changes during the deposition and heat treatment process, and changes in other characteristics, such as conductivity, that can be interpreted by the model

optimization as a shift in thickness. SEM and SE stack thicknesses are within about 15 nm, or approximately 0.3%, which suggests the CdS model is in fact physically more accurate than the TEC-15 model.

3.2.3. CdTe Sample.

Baseline Study results for the CdTe sample are shown in Figures 3.28 through 3.31 and Table 3.10. Figures 3.28 and 3.29 show the Ψ and Δ plots for all seven angles. The corresponding data for the Woollam Study is shown in Figures 3.7 and 3.8. While the general pattern of the experimental data is similar, the shapes and frequency of the waveforms varied noticeably between the two sets of raw data. The Baseline Study model appeared to show a closer fit, in terms of the average distance between the experimental and model data at a given wavelength, in the range between 800 and 1200 nm. The n and k values were modeled for all film layers, the substrate, and the surface roughness. The optical constants for the bulk CdTe layer are shown in Figure 3.30. The corresponding values for the Woollam Study are shown in Figure 3.9. While the general trend of the optical constants is the same, the Baseline Study data showed an additional small peak near 300 nm. The thickness and porosity values are summarized in Table 3.10, along with SEM thickness value and the MSE values for the models. Layer thicknesses for the inner layers were fixed. The SiO_2 , SnO_2 , and surface roughness were excluded from the calculated stack thickness because they were not clearly visible in the SEM image used to calculate the SEM stack thickness. The Baseline Study model produced a stack thickness significantly higher than the Woollam Study model and SEM, even ignoring the surface roughness and the innermost two layers, which were not visible in the SEM image. The SEM image produced for this sample is shown in Figure 3.31. Four distinct layers (glass, FTO, CdS, and CdTe) are visible.

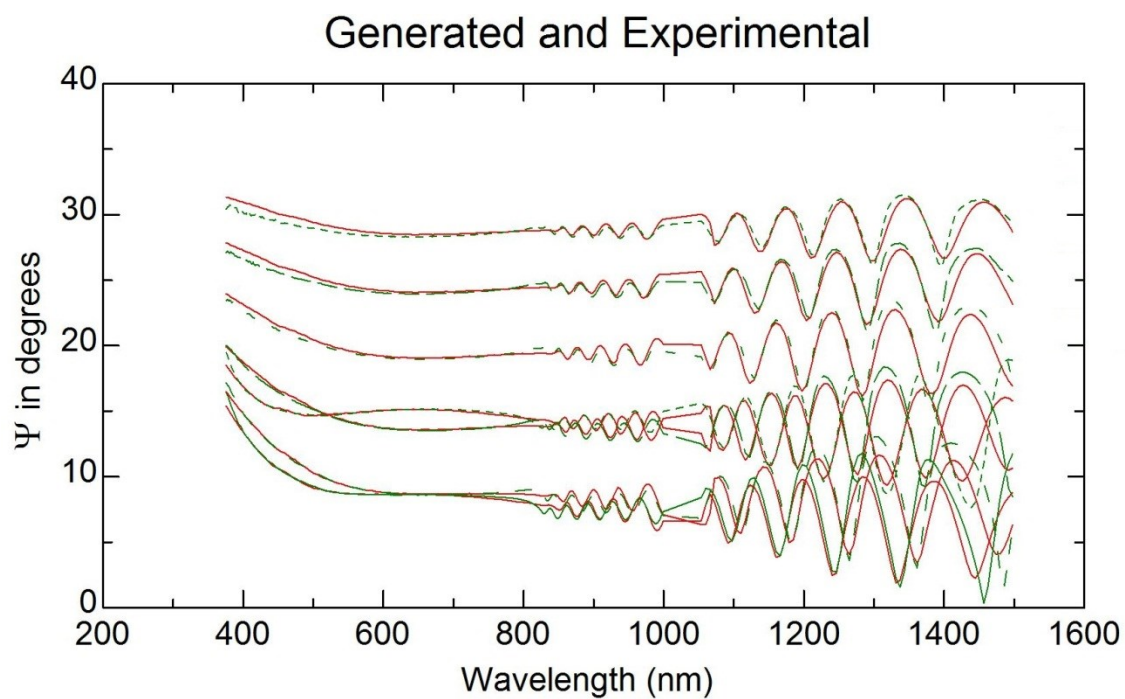


Figure 3.28: Ψ Plots for the Baseline CdTe Study.

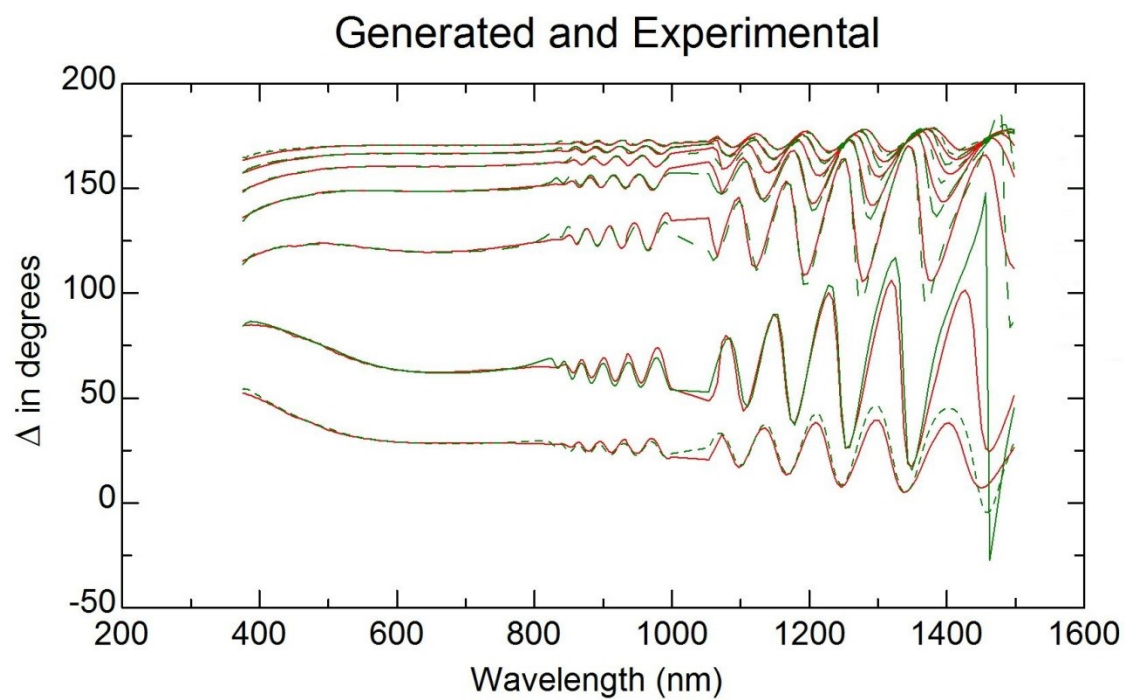


Figure 3.29: Δ Plots for the Baseline CdTe Study.

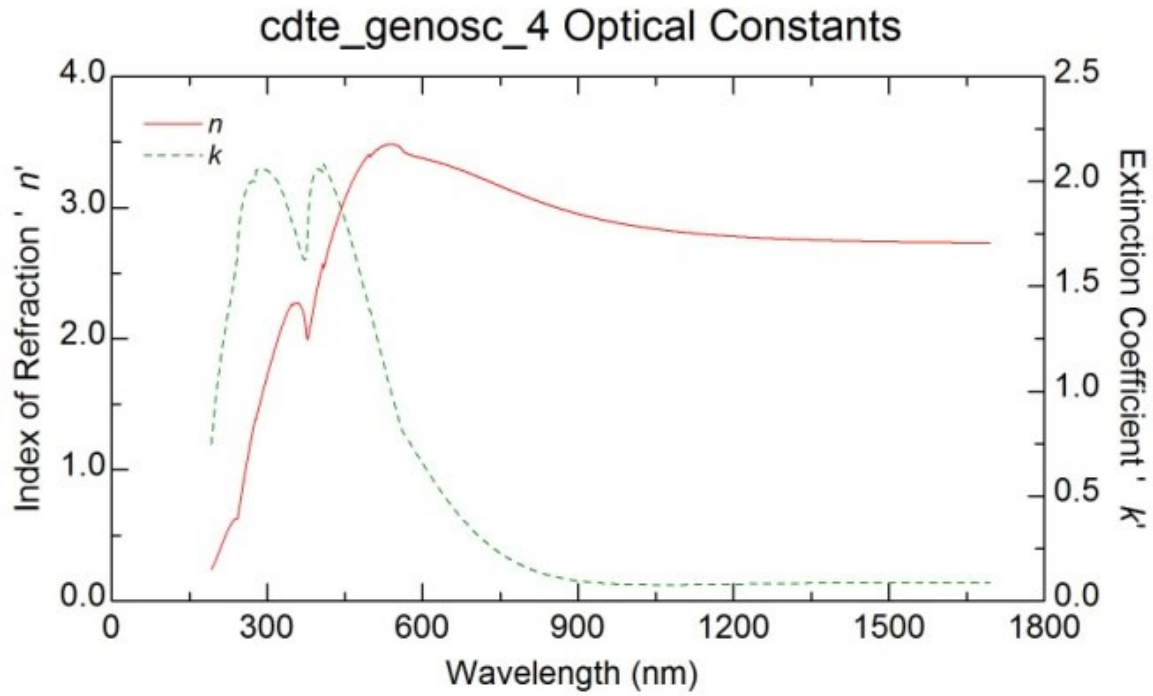


Figure 3.30: n and k Plots for the Baseline CdTe Study.

Table 3.10: Summary of Selected Parameter Values for Woollam and Baseline Studies of CdTe Samples.

data set	Woollam Study	Baseline Study	SEM
surface roughness void	$32.5 \pm 0.13\%$	$24.9 \pm 0.03\%$	-
surface roughness thickness	$1187 \pm 6 \text{ \AA}$	$492 \pm 0.7 \text{ \AA}$	
CdTe thickness	$25361 \pm 109 \text{ \AA}$	$29963 \pm 10 \text{ \AA}$	
CdS thickness	1467 \AA	1467 \AA	
FTO thickness	2800 \AA	2800 \AA	
SiO ₂ thickness	271 \AA	271 \AA	
SnO ₂ thickness	261 \AA	261 \AA	
glass thickness	1 mm (semi-inf)	3.18 mm (semi-inf)	
stack thickness nonuniformity	$10.6 \pm 0.2\%$	$0.7 \pm 0.2\%$	
MSE	22.78	25.21	
stack thickness	$29628 \pm 115 \text{ \AA}$	$34230 \pm 11 \text{ \AA}$	32810 \AA

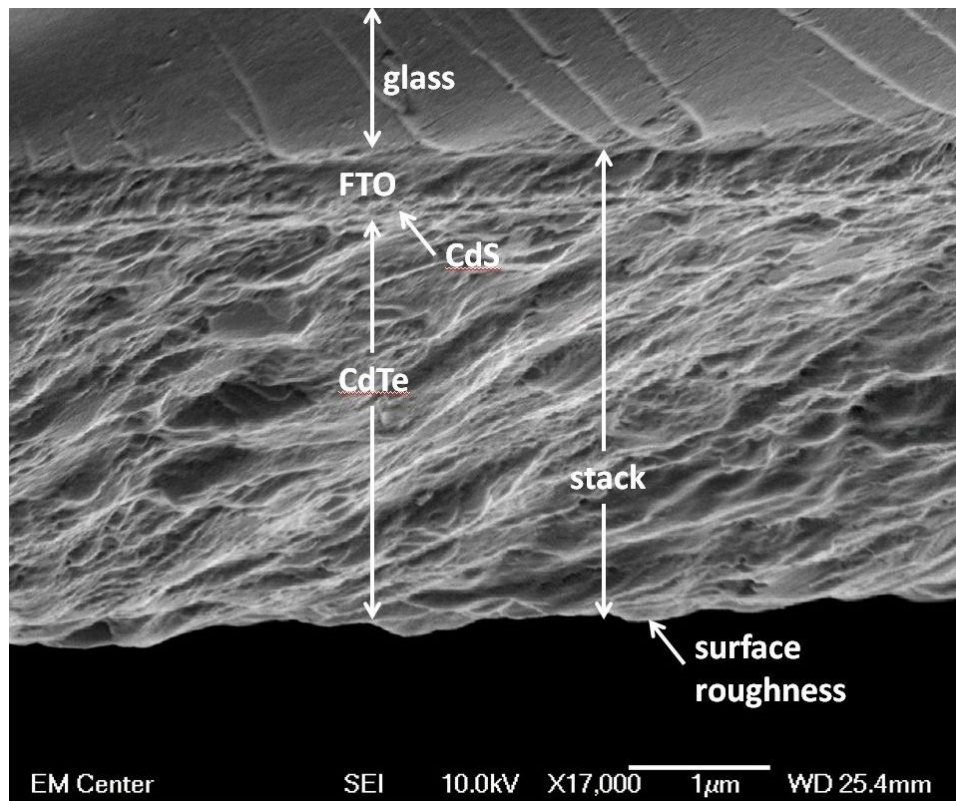


Figure 3.31: SEM Image of CdTe Sample.

The measured Ψ and Δ data waveforms (Figures 3.28 and 3.29) can be divided into a number of distinct regions. At low wavelengths, the data was very noisy and discarded for modeling. This is followed by a relatively flat absorption band, and short waveforms that become progressively larger starting between 800 and 900 nm. The shift from a flat region to one with peaks is typical of materials with a direct band gap in the optical region, and the band gap for monocrystalline CdTe is ~ 862 nm. For wavelengths in the absorption region, just above the band gap in energy, few photons survive to reach the bottom of the first bulk layer (CdTe), so the waveforms representing the interference pattern between transmitted and reflected light are not present. The Baseline Study data had shorter and more closely spaced waveforms in the transparency region than the corresponding Woollam Study data (Figures 3.7 and 3.8). Both these features are indicative of a thicker layer that acts in a more absorptive manner. Near 1500

nm, there is a large peak that appears to correspond to the conduction band effect of the FTO, suggesting that there is some absorption and reflection of light occurring as deep in the stack as the FTO layer. The model fit for the Woollam Study data gave a good match at these energies, but the waveforms in the middle wavelengths (800-1200 nm) were not modeled as well. For the Baseline Study model, it was believed that large waveforms tend to “drown out” details in modeling other details, so the 1500 nm region was deliberately excluded during initial modeling, which allowed the middle frequency waveforms to be more effectively matched.

The n and k data shown in Figure 3.30 show the same general shape as the Woollam Study data in Figure 3.9, with the Baseline Study model having a small peak near 300 nm. This frequency was excluded from the Woollam Study data as being too noisy, so the spike may actually be present in both data sets. The Baseline Study model also showed the n and k values varying over a wider vertical range, which is also partially due to the wider frequency range studied. In both models, the overall appearance suggests a much more amorphous material than the CdS. However, this may be due to surface effects [68], rather than accurately representing the true state of the material.

SEM (Figure 3.31) shows two distinct layers separated by what appears to be a third, very thin, layer. The middle layer may be the CdS, but it appears surprisingly thin. This "shrinkage" of the CdS layer has been reported previously [73], and may be due to the formation of a thick intermix between CdS and CdTe, which are more chemically compatible than CdS is with FTO, and heating during the deposition process may have sped diffusion. Table 3.10 shows the thickness values generated for this part of the Baseline Study. Both the Woollam and Baseline Study models held the thicknesses of the lower layers constant. The Baseline Study model was determined experimentally to be too insensitive to these values to provide an accurate

measurement, so the values used in the Woollam Study model were substituted as an approximation. The Woollam Study model itself used a similar strategy [73]. However, the SE model was still able to determine the CdTe layer thickness within 10% of the SEM value.

The CdTe data demonstrates some of both the limitations and capabilities of SE. The Woollam Study model showed a very thick surface roughness, so thick that it may have interfered with the ability of the model to measure the optical properties and thicknesses of the underlying layers [50]. In the case of the Baseline Study data, the thicker CdTe layer limits the amount of light that reaches the underlying layers, which makes determination of the thicknesses of those layers more difficult. However, SE still provided useful and accurate information about the surface quality and CdTe layer thickness. Accurate SE measurement of CdTe layers up to 8-12 μm (80,000-120,000 \AA) in thickness on single-layer substrates has been reported [46, 76].

3.2.4. Cl-Treated Sample.

Baseline Study results for the Cl-treated sample are shown in Figures 3.32 through 3.35 and Table 3.11. Figures 3.32 and 3.33 show the Ψ and Δ plots for all seven angles. The corresponding results for the Woollam Study are shown in Figures 3.10 and 3.11. While the overall shape is similar, the waveform count was different between the sets of raw data, as was the shape of some waveforms. The n and k values were modeled for all film layers, the substrate, and the surface roughness. The optical constants for the bulk CdTe layer are shown in Figure 3.34. The corresponding Woollam Study values are plotted in Figure 3.14. Similarly to the CdS data, the overall shape and location of the peaks were similar between the two studies, but the height of the peaks at lower wavelengths was reduced in the Baseline Study model. The thickness and porosity values are summarized in Table 3.11, along with SEM thickness value and the MSE values for the models. The SEM image produced for this sample is shown in

Figure 3.35. Only two layers were clearly visible. It appeared this sample may have received more gold than expected, obscuring some features. Because these layers were not clearly visible in the SEM image, the SiO_2 , SnO_2 , FTO, and surface roughness were excluded from the calculation of the stack thickness for the model. Assuming that the TEC-15 layers are not visible and ignoring surface roughness, the fit of the Baseline Study model to SEM is within 2%.

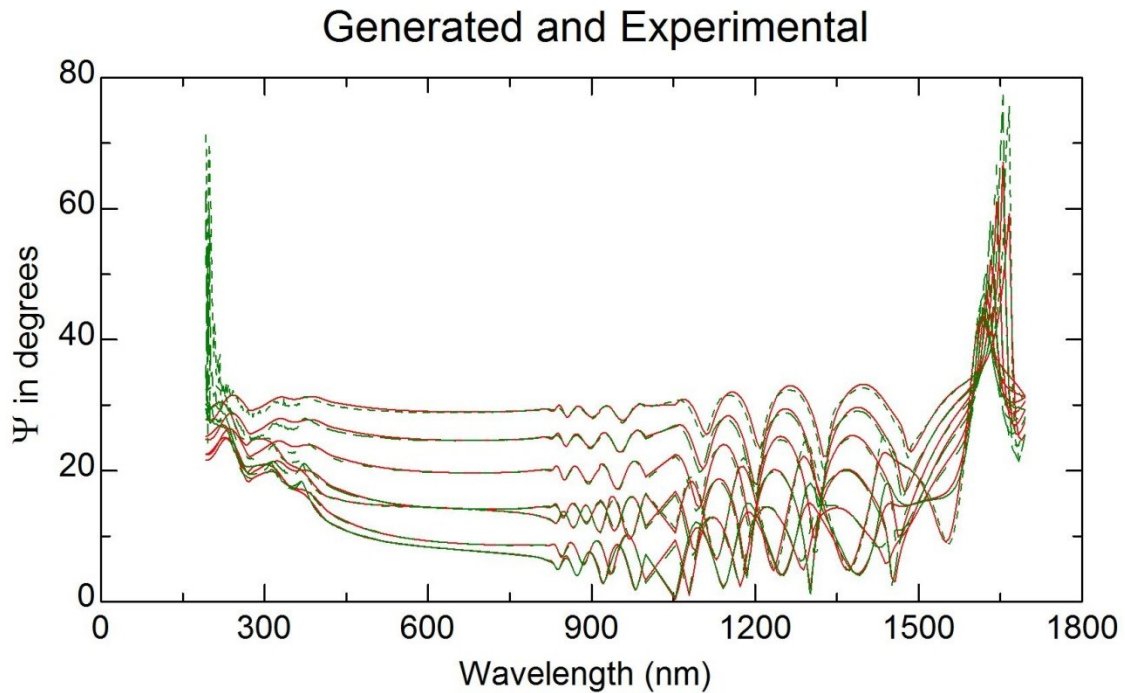


Figure 3.32: Ψ Plots for the Baseline Cl-treated Study.

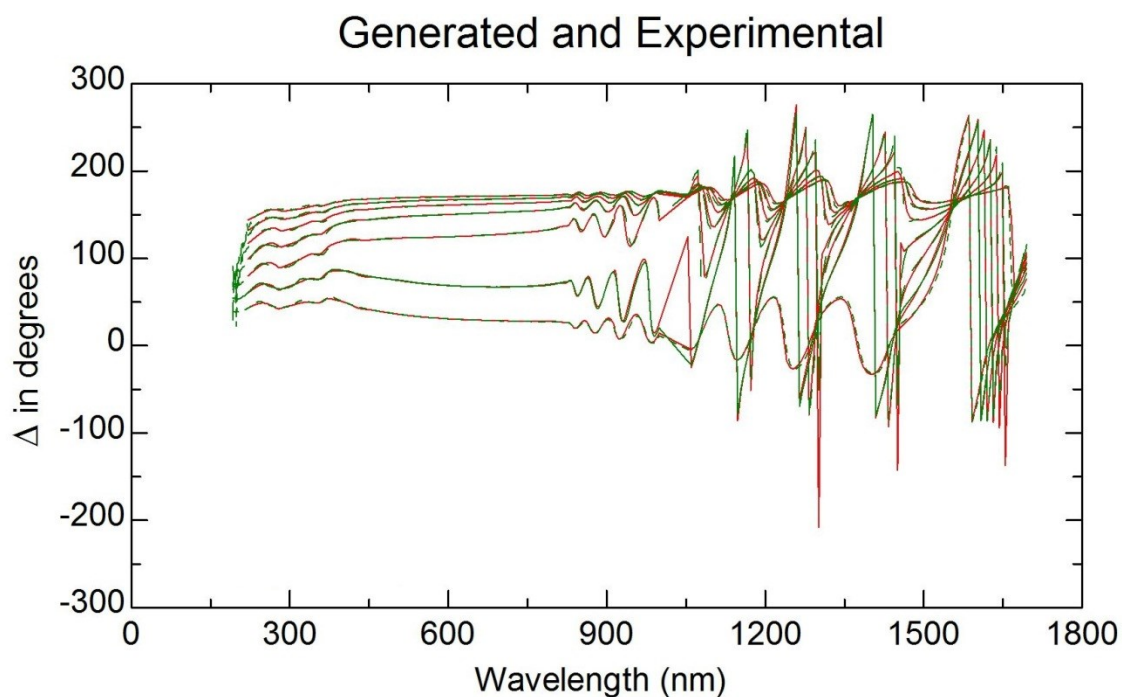


Figure 3.33: Δ Plots for the Baseline Cl-treated Study

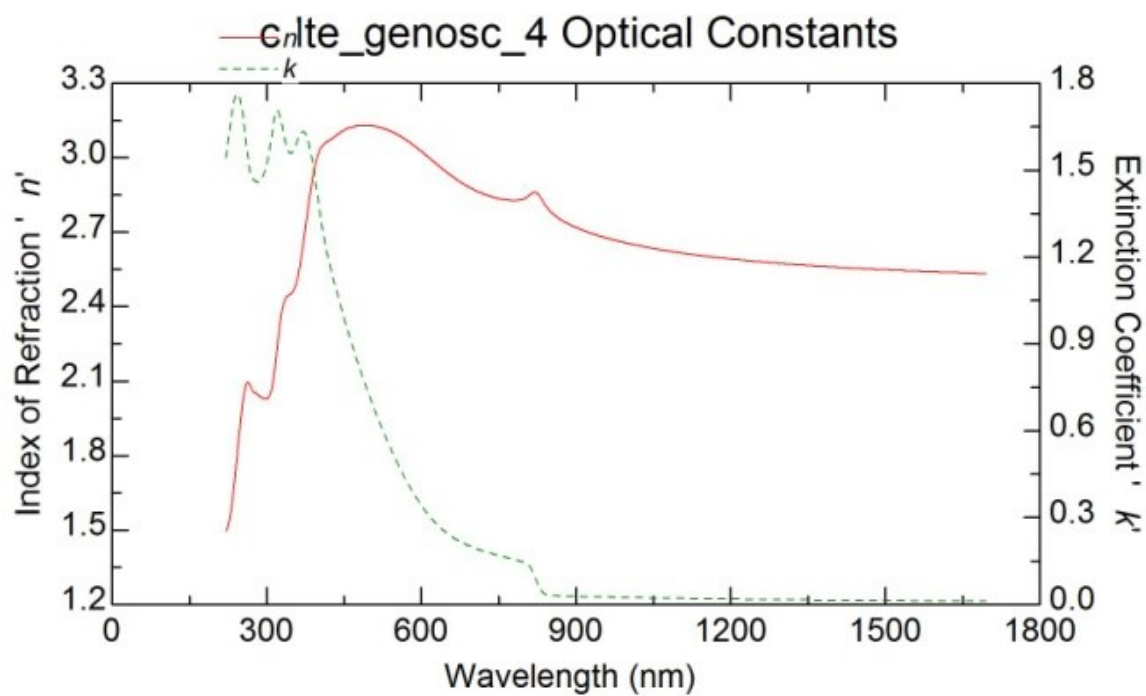


Figure 3.34: n and k Plots for the Baseline Cl-treated Study.

Table 3.11: Summary of Selected Parameter Values for Woollam and Baseline Studies of Cl-treated Samples.

data set	Woollam Study	Baseline Study	SEM
surface roughness void	22.8±0.1%	21.8±0.04%	-
surface roughness thickness	356±1.8 Å	396±1 Å	
CdTe thickness	15122±12 Å	21463±2 Å	
CdS thickness	1484±4 Å	2022±9 Å	
FTO thickness	3251±18 Å	3344±49 Å	
SiO ₂ thickness	271 Å	174±58 Å	
SnO ₂ thickness	261 Å	274±6 Å	
glass thickness	1 mm (semi-inf)	3.18 mm (semi-inf)	
stack thickness nonuniformity	5.78±0.07%	2.7±0.05%	
MSE	21.55	30.32	23160 Å
stack thickness	16606±36 Å	23485±125 Å	

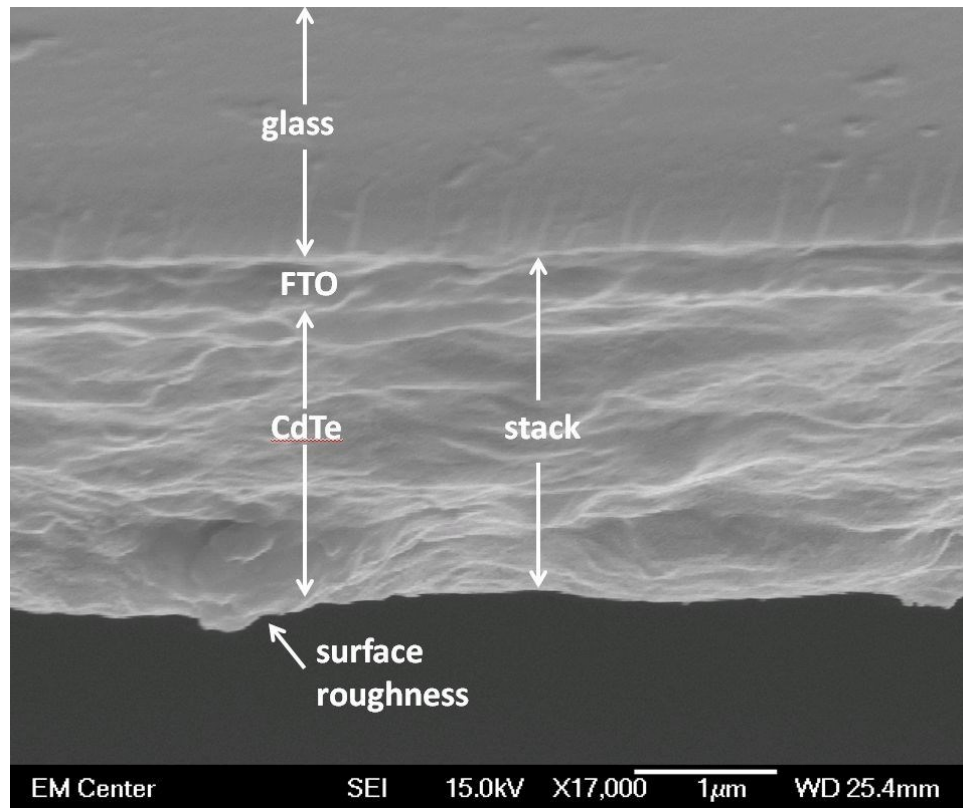


Figure 3.35: SEM Image of Cl-treated Sample.

The overall pattern of the measured and modeled response shown in Figures 3.32 and 3.33 is very similar to the corresponding Woollam Study data in Figures 3.10 and 3.11, but the

Baseline Study data shows the smaller, more tightly packed waveforms typical of a thicker substrate. The noise is reduced, allowing visibility of the critical points at ~ 300 nm. The points are more pronounced for the Woollam Study data, suggesting more crystalline surface features. Finally, the Baseline Study model has a more pronounced, and redshifted FTO conductivity peak, suggesting possible differences in the underlying layers between the two samples. Similarly, the Baseline Study Cl-treated model n and k plots (Figure 3.34) are similar to the Woollam Study model (Figure 3.14), but the peak heights vary, particularly the small peak near 400 nm. The band gap spike at ~ 850 nm is clearly visible in both the n and k waveforms for both models. The higher peak in the Woollam Study model suggests a more crystalline layer. SEM data (Figure 3.35) shows what appear to be two layers. Grain structure may be represented by the nodules visible near the surface, but is not distinct. Table 3.11 shows the thickness values summary. The uncertainties in some of the underlying layers, particularly SiO_2 , were relatively high, suggesting the thickness values for the underlying layers may be questionable; however, the SEM stack thickness value was within 2% of the model thickness stack for the CdTe and CdS layers.

3.2.5. Cu-Treated Sample.

Baseline Study results for the Cu-treated sample are shown in Figures 3.36 through 3.39 and Table 3.12. Figures 3.36 and 3.37 show the Ψ and Δ plots for all seven angles. Corresponding Woollam Study results are found in Figures 3.12 and 3.13. While the general shape is nearly identical, the Baseline Study model showed a reduction in both noise and waveform count. The n and k values were modeled for all film layers, the substrate, and the surface roughness. The optical constants for the bulk CdTe layer are shown in Figure 3.38; the corresponding Woollam Study data is shown in Figure 3.15. Similarly to the Cl-treated models,

the data showed similar overall shape and peak locations, but the heights and contrast were reduced for the Baseline Study data, and the sharp peak in the Woollam Study data near 900 nm is not clearly visible in the Baseline Study data. The thickness and porosity values are summarized in Table 3.12, along with SEM thickness value and the MSE values for the models. The Baseline Study model is a close fit to the SEM data assuming the apparent stack height encompasses all layers other than the glass substrate. The SEM image produced for this sample is shown in Figure 3.39. Similarly to the Cl-treated sample, the individual layers are difficult to discern.

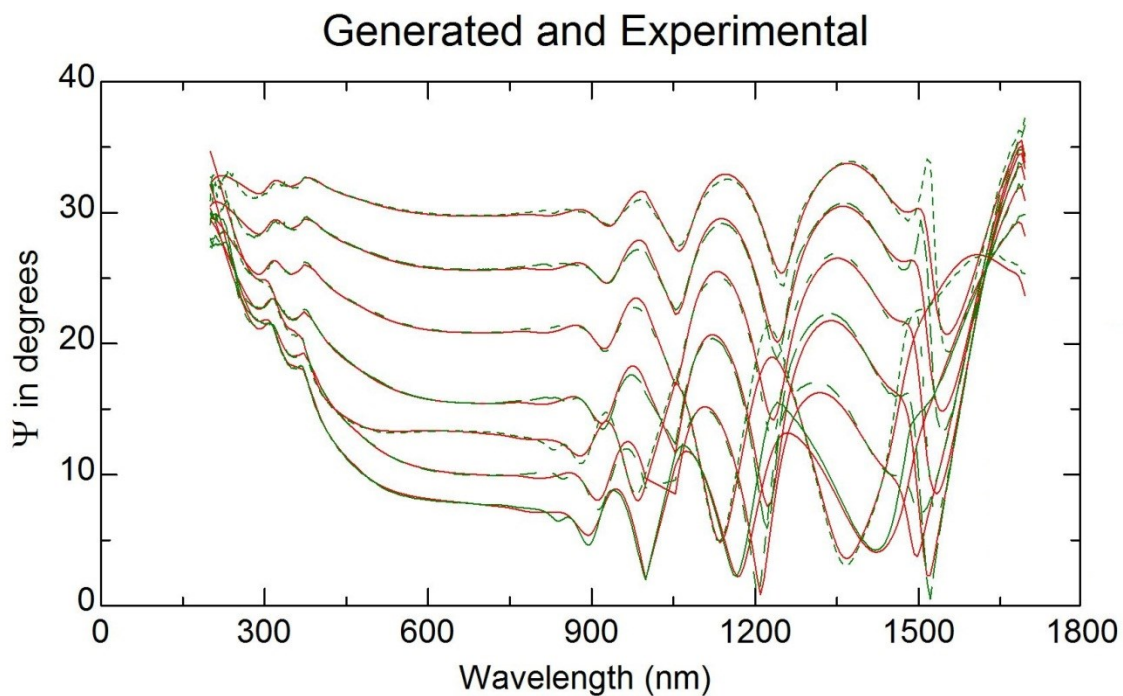


Figure 3.36: Ψ Plots for the Baseline Cu-treated Study.

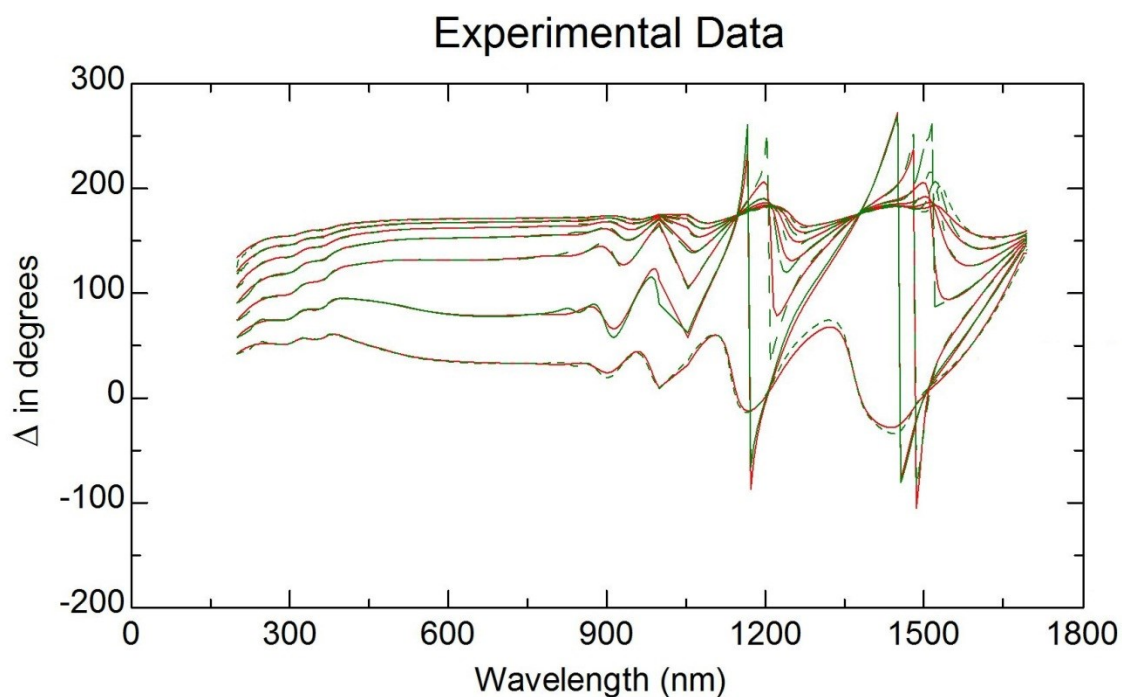


Figure 3.37: Δ Plots for the Baseline Cu-treated Study.

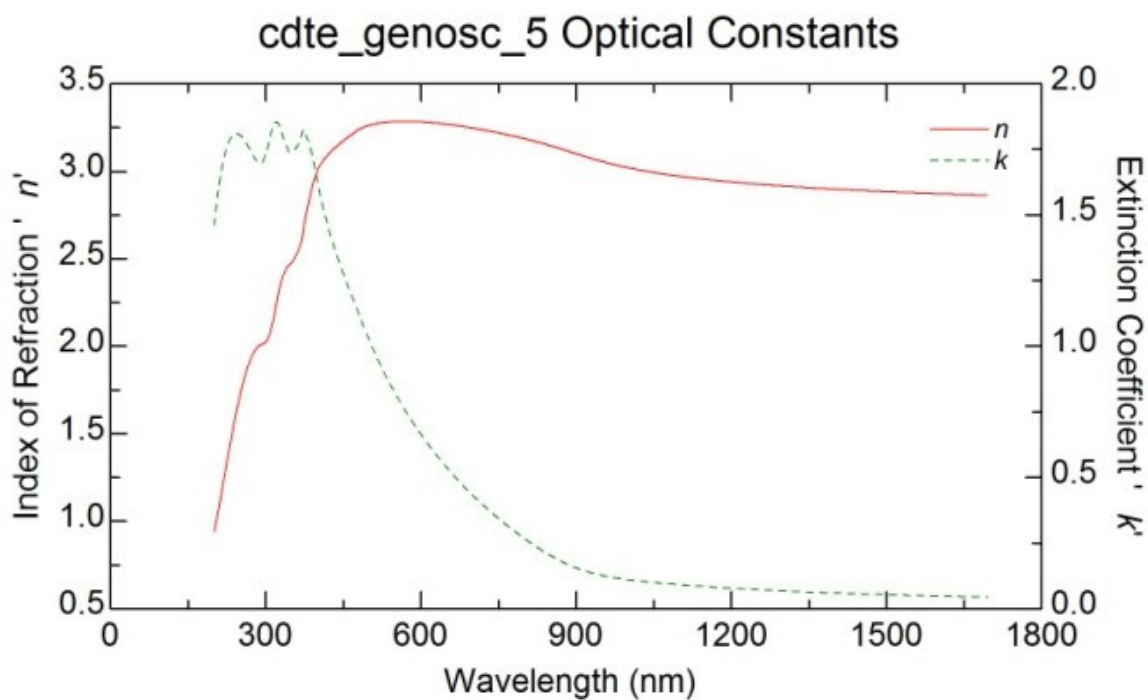


Figure 3.38: n and k Plots for the Baseline Cu-treated Study.

Table 3.12: Summary of Selected Parameter Values for Woollam and Baseline Studies of Cu-treated Samples.

data set	Woollam Study	Baseline Study	SEM
surface roughness void	27.8±0.1%	21.7±0.02%	-
surface roughness thickness	547±2 Å	446±0.7 Å	
CdTe thickness	12722±21 Å	8779±1 Å	
CdS thickness	1920±6 Å	2142±11 Å	
FTO thickness	2800 Å	3339±35 Å	
SiO ₂ thickness	271 Å	136±39 Å	
SnO ₂ thickness	261 Å	333±17 Å	
glass thickness	1 mm (semi-inf)	3.18 mm (semi-inf)	
stack thickness nonuniformity	5.0±0.1%	5.1±0.2%	
MSE	34.62	26.03	15220 Å
stack thickness	18521±29 Å	15175±104 Å	

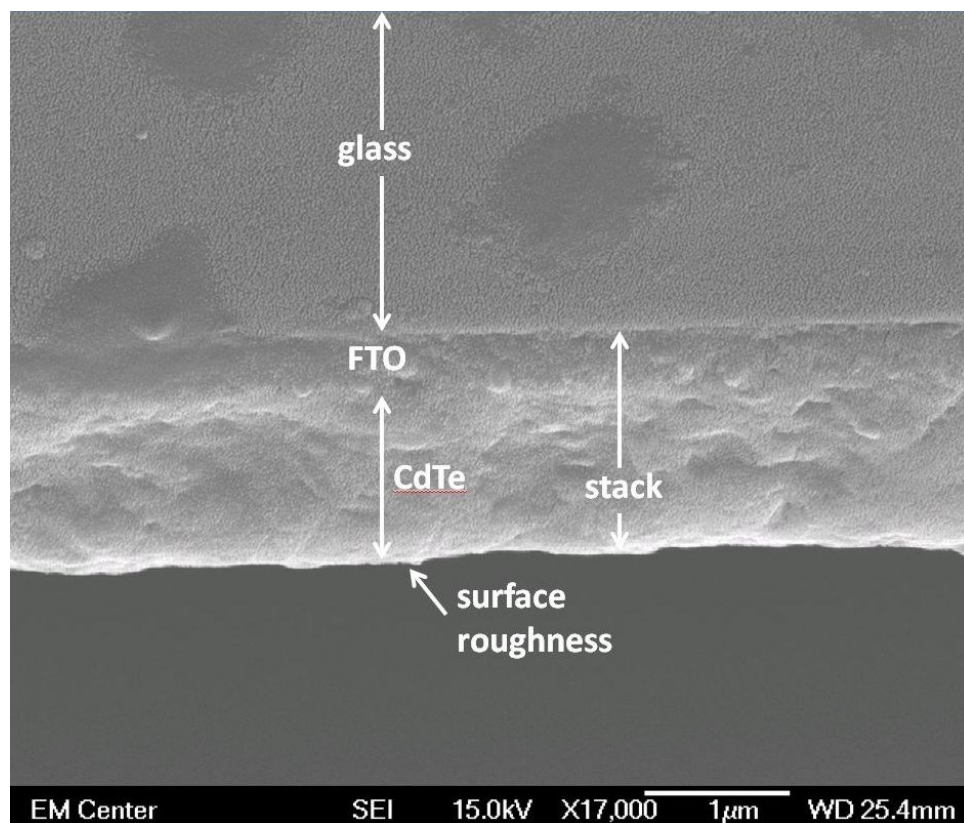


Figure 3.39: SEM Image of Cu-treated Sample.

While the Woollam Study Cu-treated Ψ and Δ data (Figures 3.12 and 3.13) is fairly similar to the Woollam Study Cl-treated data (Figures 3.10 and 3.11), the corresponding Baseline

Study data (Figures 3.36 and 3.37) shows widely spaced waveforms indicative of a smaller stack thickness. The FTO conductivity peak in the raw data is also much more pronounced for the Baseline Study data, which is consistent with more photons penetrating to this depth. The Woollam Study model Cu-treated had optical constant plots (Figure 3.15) that resembled the Cl-treated data; the Baseline Study n and k values (Figure 3.38) had the same general shape but appeared to lack the sharp peak at the band gap, despite the band gap being clearly visible as the end of the absorption region in the Ψ and Δ data. While this result may be in error, the reasonable Ψ and Δ fit suggest it may be due to other causes, such as surface roughness effects.

SEM (Figure 3.39) data is fairly indistinct. It is possible to discern what might be a two-layer structure and grains. However, the stack thickness, the value of interest to this study as an outside check for SE results, is clearly visible. Thickness values obtained (Table 3.12) for the Woollam and Baseline Study data differ, but this is not surprising considering the differences in the Ψ and Δ plots. The Baseline Study model data was very close ($\sim 0.3\%$) to the SEM data; of note is the very small value of the SiO_2 for this sample; at first this was assumed to be in error; however, it was later discovered in the course of this work that the SiO_2 layer may be smaller than previously thought.

3.2.6. Br-Treated Sample.

Baseline Study results for the Br-treated sample are shown in Figures 3.40 through 3.43 and Table 3.13. Figures 3.40 and 3.41 show the Ψ and Δ plots, respectively. Unlike the other samples in the study, the Woollam Study data did not include a Br-treated sample. The raw data waveform shape bore a strong resemblance to that of the Baseline Study Cu-treated sample. Several models were tested as starting points; the Cu-treated Baseline Study model proved the best fit. The n and k values were modeled for all film layers, the substrate, and the surface

roughness. Initially, the starting model for the fit was based on the Cu-treated Baseline Study model; the optimized optical constants appeared to show little change from the Cu-treated model. However, when using the n and k values from the model of the Cl-treated sample from the Woollam Study instead, the optical constants for the bulk CdTe layer optimized to a state more clearly showing the peak at $\sim 850\text{nm}$, as shown in Figure 3.42. The thickness and porosity values are summarized in Table 3.13, along with SEM thickness value and the MSE values for the models. Because the surface roughness was not measured as part of the stack thickness in the SEM image, it was excluded from the calculation of the stack thickness for the model. Ignoring the surface roughness, the fit of the Baseline Study model to the SEM data was within $\sim 2\%$. The SEM image produced for this sample is shown in Figure 3.43. At least two layers are clearly, though barely, visible. SEM showed that the thickness for this sample was almost identical to the Cu-treated one.

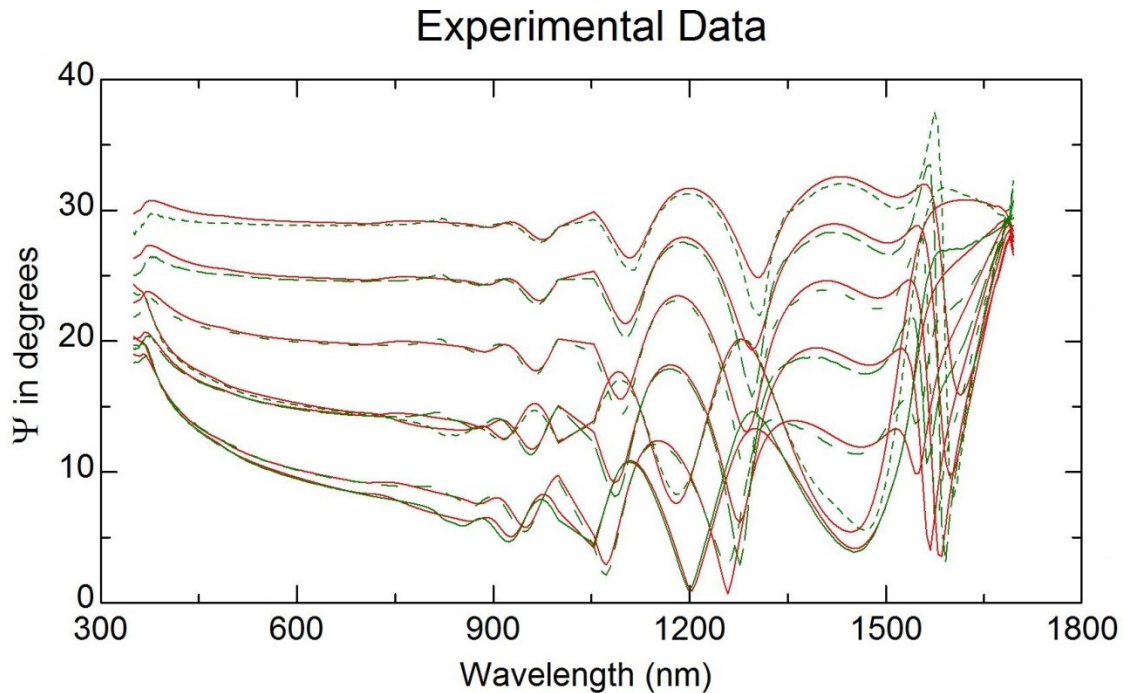


Figure 3.40: Ψ Plots for the Baseline Study for the Br-treated Sample.

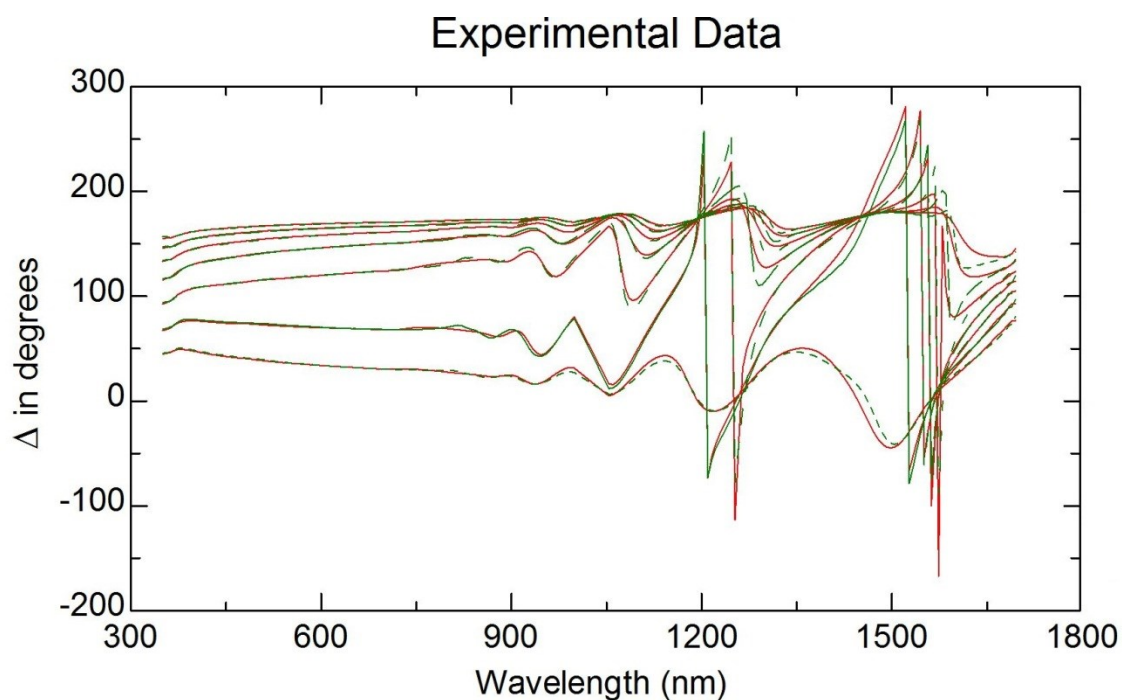


Figure 3.41: Δ Plots for the Baseline Study for the Br-treated Sample.

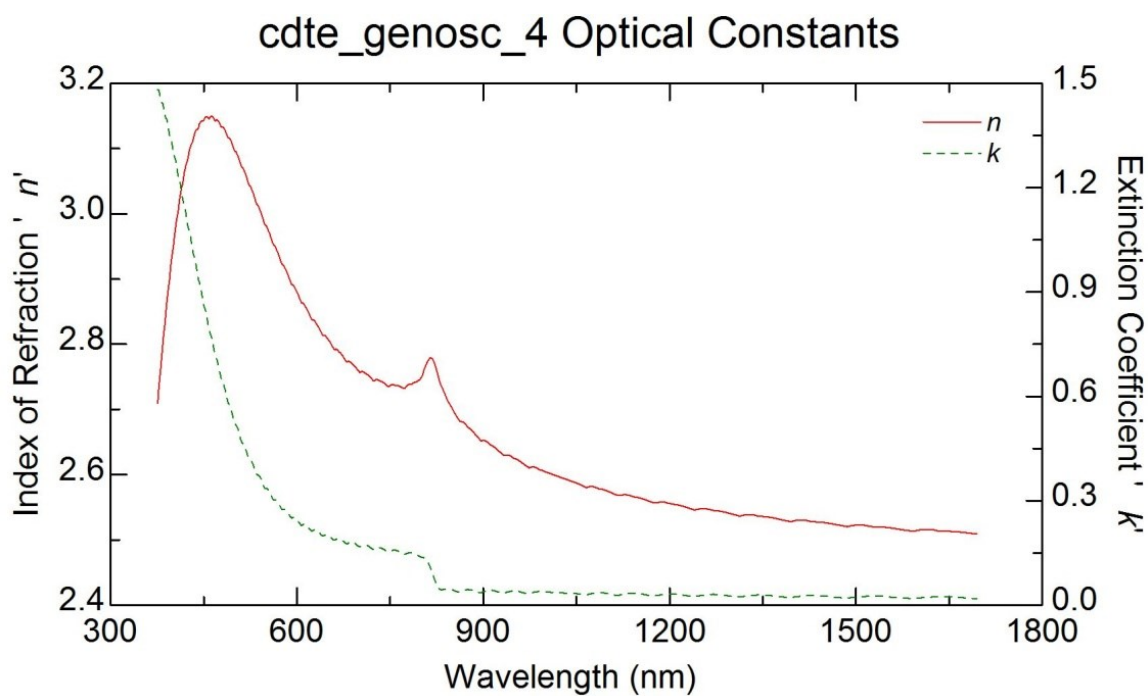


Figure 3.42: n and k Plots for the Baseline Study for the Br-treated Sample.

Table 3.13: Summary of Selected Parameter Values for the Baseline Study of the Br-treated Sample.

data set	Woollam Study	Baseline Study	SEM
surface roughness void	No Br-treated sample used	$18.2 \pm 0.03\%$	-
surface roughness thickness		$552 \pm 1 \text{ \AA}$	
CdTe thickness (nm)		$9648 \pm 37 \text{ \AA}$	
CdS thickness (nm)		$2568 \pm 39 \text{ \AA}$	
FTO thickness		2800 \AA	
SiO ₂ thickness		271 \AA	
SnO ₂ thickness		261 \AA	
glass thickness		$3.18 \text{ mm (semi-inf)}$	
stack thickness nonuniformity		$6.4 \pm 0.14\%$	
MSE		31.41	
stack thickness		$15548 \pm 77 \text{ \AA}$	15220 \AA

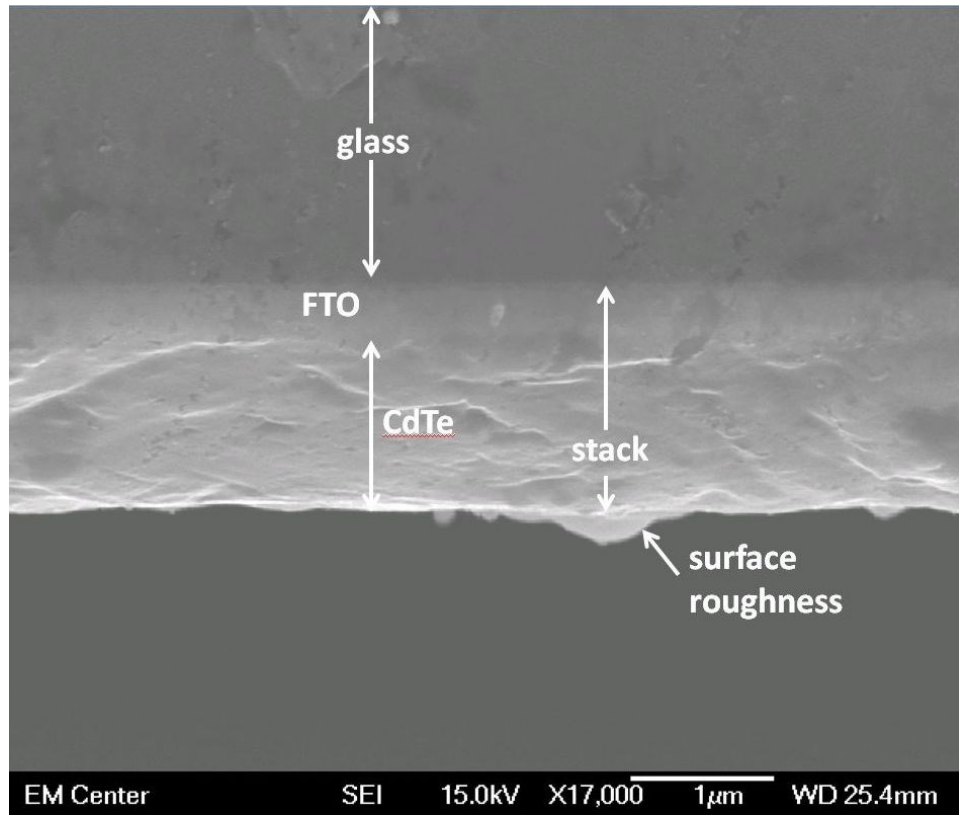


Figure 3.43: SEM Image of the Br-treated Sample.

Not only are the Ψ and Δ waveforms for the Baseline Study Br-treated (Figures 3.40 and 3.41) and Cu-treated sample (Figures 3.36 and 3.37) similar in general appearance, the number of peaks is also similar, indicating a similar thickness; however, the shape of the individual waveforms was noticeably different. Error between the simulated and actual results suggests room for improvement in the model. Figure 3.42 shows the n and k plot for the final Baseline model of the Br-treated sample. Initially, it had appeared the n and k waveforms had changed little from the Cu-treated model (Figure 3.38). This suggests that the effect on the optical properties of CdTe due to Br treatment is minimal, and that the difference between the Cu-treated and Br-treated Ψ and Δ waveform shapes may be due to thickness differences and underlying layers. However, a later run showed a more crystalline-looking profile shown in the figure, suggesting the more amorphous-looking profile may have been a false positive. If this is correct and the amorphous appearance of the CdTe n and k plots is due in part to the surface roughness, then the Br treatment may in fact have the desired effect of reducing optical effects of the surface roughness and better revealing the bulk CdTe layer's true nature. Thickness values obtained are summarized in Table 3.13. SEM data (Figure 3.43) showed that the thickness of the Br-treated sample was indeed similar to that of the Baseline Study Cu-treated one (Figure 3.39). While the stack thickness is clear, the grain structure and individual layers are not clearly visible, so only the stack thickness value was used. The stack thickness measured by SEM was within about 2% of the model value without the surface roughness, suggesting the model thicknesses are reasonably accurate.

3.2.7. Overall Results.

All six Baseline Study models appear to model the Ψ and Δ response and stack thickness effectively, though there is still room for improvement. Using seven angles provides some assurance that both optical properties and thicknesses used in the models were optimized to values close to the actual parameters. Unfortunately, underlying layers often proved difficult to model, especially when either the surface roughness or an upper layer was of greater than typical thickness, or two or more layers had similar optical properties or a significant interface. Thickness values for the upper layer appeared to be accurate to within about 5% in many cases, and for the thinner films the total stack was even closer to the value derived by SEM. In addition to measuring thickness, SE appears to have the capability to measure several other properties, including the n and k values, bandgap, and crystal structure changes. The Woollam and Baseline Studies, while they could not provide statistically analyzed results, did provide significant confidence in the ability of CSU to perform SE as an in-house process. The results suggest that the techniques and equipment used in this study are sufficient to generate not only useful results, but data that is comparable to other, more destructive techniques for measuring CdTe materials. Table 3.14 shows a summary of the stack values and variations of the Baseline Study relative to the Woollam Study and the SEM values. All Baseline Study SE stack thickness values were within 5% of the SEM values.

Table 3.14: Stack Values for Woollam, Baseline SE, and Baseline SEM Studies.

data set	Woollam Study	Baseline Study	SEM	Baseline Study data vs SEM
TEC-15 (nm)	3798±25Å	3875±2Å	3732 Å	+3.83%
CdS (nm)	5693±8Å	5868±4Å	5883 Å	-0.25%
CdTe (nm)	29628±115 Å	34230±11 Å	32810 Å	+4.33%
Cl-treated (nm)	16606±36 Å	23485±125 Å	23160 Å	+1.40%
Cu-treated (nm)	18521±29 Å	15175±104Å	15220 Å	-0.30%
Br-treated (nm)	-	15548±77 Å	15220 Å	+2.16%

3.3. Multiple Angle Study.

Selected values from the Multiple Angle Study are shown in Tables 3.15 through 3.23. Additional data may be found in the appendix. Data for the Multiple Angle Study TEC-15 sample results are shown in Table 3.15. In this table and subsequent tables, “average” is the average value from the seven models for the seven angles studied (45°, 50°, 55°, 60°, 65°, 70°, and 75°), “SD%” is the absolute value of the sample standard deviation divided by the average for the values tested, and “P” is the result of the Anderson-Darling normality test for the values. All tested variables other than MSE showed deviations of less than 3% of the average. The Anderson-Darling normality test for each parameter across the seven models showed that none tested as non-normal with a 95% level of confidence. As shown in Table 3.15, agreement between runs for the TEC-15 models was good, as all tested variables other than MSE showed deviations of less than 3% of the average, and there were no obvious outliers. For the FTO, SnO₂, and surface roughness layers, the thickness variation was minimal, demonstrating that in general SE supplies consistent data. However, correlations for most of the variables were above 0.9, suggesting that there is significant systematic error, albeit small compared to the overall result. Despite this, all the distributions test as normal to the 95% confidence level.

Table 3.15: Selected Multiple Angle Study Results for TEC-15 Sample.

	average	SD%	P
MSE	15.10	19.07 %	0.553
SnO ₂ thickness	232 Å	0.75 %	0.885
SiO ₂ thickness	270 Å	2.09 %	0.885
FTO thickness	2981 Å	0.06 %	0.616
surface roughness thickness	391 Å	1.86 %	0.161
Surface roughness void	57.6 %	1.76 %	0.574

Selected data for the Multiple Angle Study CdS sample results is shown in Table 3.16.

All tested variables other than MSE and surface roughness thickness showed deviations of less than 4% of the average. None tested as non-normal with a 95% level of confidence. CdS

Multiple Angle Study data, shown in Table 3.16, was similar to that of the TEC-15 data in that variables other than MSE showed deviations of less than 4% of the average; however, only the two thickest layers (FTO and CdS) were within 1%. The CdS proportionate variation was just 0.16%. The surface roughness and CdS layers also had correlations over 0.9. As with the TEC-15 data, none of the variables studied for normality for the CdS model were non-normal to 95% confidence.

Table 3.16: Selected Multiple Angle Study Results for the CdS Sample.

	average	SD%	P
MSE	14.91	28.58 %	0.602
SnO ₂ thickness	234 Å	1.48 %	0.596
SiO ₂ thickness	241 Å	3.20 %	0.824
FTO thickness	3237 Å	0.21 %	0.139
CdS thickness	1998 Å	0.16 %	0.562
surface roughness thickness	173 Å	7.29 %	0.352
Surface roughness void	33.0 %	0.87 %	0.574

Selected data for the Multiple Angle Study CdTe sample results is shown in Table 3.17.

Testing different modeling parameters suggested that the model was insensitive to the underlying layer properties except the FTO conductivity-related values, as well as stack variability, so these values were fixed to the values from the Woollam Study model. None tested as non-normal with

a 95% level of confidence. Table 3.17 shows the CdTe data for this part of the study. The underlying thicknesses were fixed based on experimental evidence suggesting the model was not able to measure them accurately. The CdTe bulk and surface roughness thicknesses only varied by about 0.1%, demonstrating that the CdTe layer could be measured with a high level of consistency. Again, no variables tested as non-normal, though only four were tested due to the difficulty in measuring properties from underlying layers.

Table 3.17: Selected Multiple Angle Study Results for the CdTe Sample.

	average	SD%	P
MSE	30.68	19.05 %	0.055
CdTe thickness	29949 Å	0.06 %	0.874
surface roughness thickness	492 Å	0.07 %	0.185
Surface roughness void	24.85 %	0.17 %	0.473

Selected data for the Multiple Angle Study Cl-treated sample results is shown in Table 3.18. The model appeared to be insensitive to the two bottom-most layers, so they were fixed to the values from the Woollam Study model, but the remainder of the variables tested had less than 15% variation. The MSE and non-uniformity (greyed cells) tested as non-normal with a 95% level of confidence. Data for the Cl-treated sample is shown in Table 3.18. The SiO₂ layer in particular was effectively indeterminate; the stack uncertainty varied by nearly 15%, and the SnO₂ layer variation was close to 8%. The CdS variation, however, was only 2%, the surface roughness less than 1%, and the CdTe thickness value varied by a mere 0.05%, suggesting that the model was sufficiently sensitive to these values that the values appeared to be meaningful. Two of the six variables tested as non-normal. These two variables (MSE and nonuniformity) also showed the highest variability, suggesting the value of measuring these two particular quantities with a single angle is questionable at best.

Table 3.18: Selected Multiple Angle Study Results for the Cl-treated Sample.

	average	SD%	P
MSE	33.19	11.34 %	0.022
CdS thickness	2051 Å	2.02 %	0.178
CdTe thickness	21460 Å	0.05 %	0.526
nonuniformity	2.5 %	14.79 %	0.046
surface roughness thickness	397 Å	0.52 %	0.183
Surface roughness void	21.78 %	0.64 %	0.647

Selected data for the Multiple Angle Study Cu-treated results is shown in Table 3.19.

The model appeared to be insensitive to the two bottom-most layers, so they were fixed to the values from the Woollam Study model, but the remainder of the variables tested had less than 20% variation. The CdS thickness (greyed cell) tested as non-normal with a 95% level of confidence. As shown in Table 3.19, the values for the Cu-treatment show a similar pattern to those of Cl-treated sample, but were slightly worse, which is surprising considering the CdTe layer of this sample was thinner, which should have increased sensitivity to the underlying layers. However, much of this seems to be due to the TEC-15 layers; the indeterminate inner layers appeared to “trade thickness” with the FTO layer, driving variation in all three as well as the nonuniformity value, while the modeled CdS layer thickness remained close to that of the Cl-treated sample. The CdS thickness was the only one which tested as non-normal. The striking difference between the P value for CdS thickness and other tested variables suggests that systematic error due to angle may have had a more dominant effect on variation in this value, suggesting measurement of underlying data by a single angle may be less advisable than doing so for the uppermost layer.

Table 3.19: Selected Multiple Angle Study Results for the Cu-treated Sample.

	average	SD%	P
MSE	30.98	16.53 %	0.364
CdS thickness	2157 Å	1.85 %	0.014
CdTe thickness	8782 Å	0.25 %	0.954
nonuniformity	4.5 %	18.38 %	0.359
surface roughness thickness	446 Å	1.71 %	0.911
Surface roughness void	21.76 %	0.22 %	0.459

Selected data for the Multiple Angle Study Br-treated sample results is shown in Table 3.20. The model appeared to be insensitive to the TEC-15, so they were fixed to the values from the Woollam Study Cu-treated model, but the remainder of the variables tested had less than 15% variation, and the CdTe and surface roughness thicknesses variations were less than 0.5%. None tested as non-normal with a 95% level of confidence. The CdTe thickness, however, tested as non-normal to a 90% confidence level.

Table 3.20: Selected Multiple Angle Study Results for the Br-treated Sample.

	average	SD%	P
MSE	36.63	14.97 %	0.208
CdS thickness	2584 Å	1.16 %	0.409
CdTe thickness	9633 Å	0.26 %	0.078
nonuniformity	6.58 %	1.62 %	0.172
surface roughness thickness	549 Å	0.45 %	0.520
Surface roughness void	18.49 %	2.38 %	0.532

Table 3.21 shows a summary of the average stack values and variations from the Multiple Angle SE Study relative to the SEM values. All Multiple Angle Study stack thickness values were within 9% of the SEM values. Table 3.22 shows a summary of the results of the Anderson-Darling normality test for the Multiple Angle Study. All but three of the 35 distributions test as normal at the 95% confidence level. Table 3.23 shows a summary of the results of comparing the standard deviation to average values. The uppermost bulk layer (colored cells) for each film stack has a standard deviation within 0.26% of the average.

Table 3.21: Summary of Stack Thickness Values for the Multiple Angle Study and SEM.

sample	SE	SEM	difference from SEM
TEC-15	3837 Å	3732 Å	+2.81%
CdS	5883 Å	5883 Å	+0.0%
CdTe	30441 Å	32810 Å	-7.22%
Cl-treated	23510 Å	23160 Å	+1.51%
Cu-treated	15117 Å	15220 Å	-0.68%
Br-treated	16587 Å	15220 Å	+8.98%

Table 3.22: Summary of Anderson-Darling Normality Testing for the Multiple Angle Study. Cells for non-normal distributions at 95% certainty are grayed.

sample	TEC-15	CdS	CdTe	Cl-treated	Cu-treated	Br-treated
MSE	0.553	0.602	0.055	0.022	0.364	0.208
SnO ₂ thickness	0.885	0.596	-	-	-	-
SiO ₂ thickness	0.885	0.824	-	-	-	-
FTO thickness	0.616	0.139	-	-	-	-
CdS thickness	-	0.562	-	0.178	0.014	0.409
CdTe thickness	-	-	0.874	0.526	0.954	0.078
nonuniformity	-	-	-	0.046	0.359	0.172
surface roughness thickness	0.161	0.352	0.185	0.183	0.911	0.520
Surface roughness void	0.574	0.574	0.473	0.647	0.459	0.532

Table 3.23: Summary of SD% Values for the Multiple Angle Study. Cells Representing the Uppermost Bulk Layer are Highlighted.

Sample	TEC-15	CdS	CdTe	Cl-treated	Cu-treated	Br-treated
MSE	19.07	28.58	19.05	11.34	16.53	14.97
SnO ₂ thickness	0.75	1.48	-	-	-	-
SiO ₂ thickness	2.09	3.20	-	-	-	-
FTO thickness	0.06	0.21	-	-	-	-
CdS thickness	-	0.16	-	2.02	1.85	1.16
CdTe thickness	-	-	0.06	0.05	0.25	0.26
Nonuniformity	-	-	-	14.79	18.38	1.62
surface roughness thickness	1.86	7.29	0.07	0.52	1.71	0.45
Surface roughness void	1.76	0.87	0.17	0.64	0.22	2.38

Examining data from all six samples for this study, MSE standard deviation to average ratios all fell between 11 and 29%; of the six MSE distributions, one (the Cl-treated sample) tested as non-normal. Although MSE values from different data sets are not directly comparable, ideally, a good fit should be nearly equally good for all angles, representing correct optical responses under all conditions. In at least some cases, it appears this was not the case. The stack nonuniformity value had variations of 14-19% for the Cl and Cu-treated samples, but a variation of just 2% for the Br-treated sample. The nonuniformity value distribution for the Cl-treated sample tested as non-normal. Surface roughness values were more consistent, in all cases having relative variation of less than 3% for the porosity and 2% for the thickness, and none tested as non-normal, suggesting that the ability of SE to measure surface properties is not greatly affected by angle. The upper bulk layer thickness value was the most consistent of all tested variables in nearly every case; all 6 samples had a standard deviation to average ratio of less than 0.27%, and none tested as non-normal to 95% confidence. Underlying layer results varied more substantially. In a number of cases, they were not clearly measurable and were fixed; however, in most cases where they appeared to be measurable, the inner layers also showed consistent values, though less so than the uppermost layer.

One question this research sought to determine was the dependence of the model on angle. While correlations between the values and angles suggest that choice of angle may play an important role in systematic error for SE model accuracy, the ratio of mean to standard deviation values was generally small, and few of the values tested as non-normal, suggesting that the “penalty” for using angles other than the Brewster angle is relatively low. Moreover, the combination of the apparent consistency of the data both between angles and between SE and SEM suggests that if the materials present are well known and have already been modeled, a

single angle may be able to provide sufficient data to provide a meaningful measurement of thickness values, at the expense of other quantities such as nonuniformity. However, establishment of a Baseline Study model would have been difficult without multiple angles because the modeling technique used involved comparing differences between the error between the simulated and actual Ψ and Δ values across multiple angles, so reliance on a single angle for more detailed analysis than thickness process control is not recommended.

In one sense, this experiment represents something of a worst case scenario, as traditional repeatability testing would have used the same set of angles rather than comparing results from different angles, and in all cases, three or more thin films were stacked on one another, adding to the modeling challenge represented by the raw data. Nonetheless, consistent results were achieved, demonstrating this technique as a potentially reliable methodology.

3.4. Multiple Position Study.

A Multiple Position Study was conducted using data from the same samples, but from different sample locations and a reduced data set. The goals of this study included both supplying more data to support the results of the Multiple Angle Study and providing information on variations in device properties with location. Variation in efficiency data showed that the highest efficiencies tended to occur toward the center of each sample, and lower efficiencies toward the edges. It was desired to see if SE could detect possible causes for the efficiency variations. The multiple position study examined data from five points as shown in Figure 2.4, repeated for convenience as Figure 3.44. Data was taken from each of four angles (45°, 55°, 65°, and 75°) at each of the four offset points 01, 02, 03, and 04 and combined with the data from the Multiple Angle Study. For each of the offset points, a repeat of the Multiple

Angle Study with this more limited set of angles was run to compare offset data to the Multiple Angle Study results.

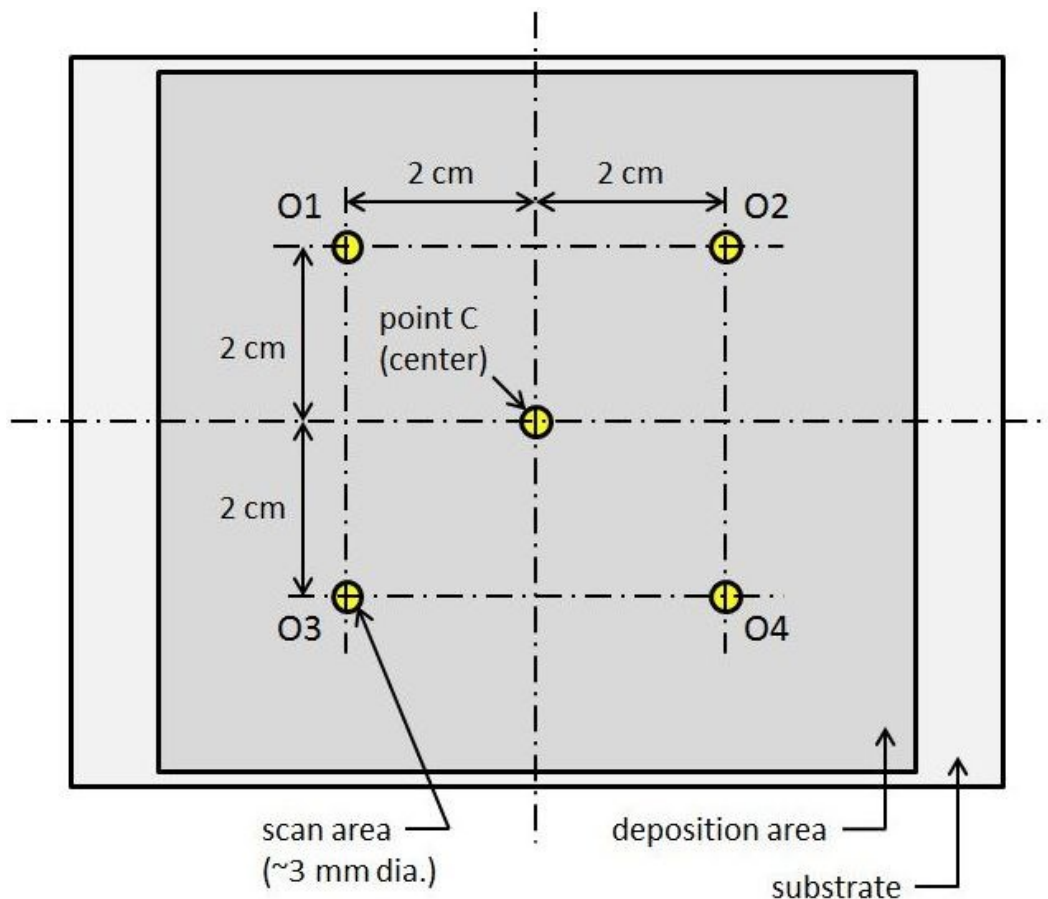


Figure 3.44: Locations Used for the Multiple Position Study.

3.4.1. TEC-15 Sample.

Average values at each of the five locations are shown in Table 3.24. During measurement, it was noticed that there was a significant amount of non-diffuse reflection (i.e., glare) at high angles at the offset locations for this sample. This manifested itself as a vertical shift in the Ψ plot for the 75° data relative to the model. Since the backside reflection value was indeterminate, this glare could not be modeled directly from the data. For this reason, the 75° data was excluded from calculation of the average value. Curiously, this phenomenon did not occur with the center point. It is believed that this may be due to a combination of factors. First,

the center point may have been exposed to different wear from the offset areas, due to handling and mounting. In addition, some glare may have been introduced by the instrument itself, as the appearance of the backplate on the sample mount from the point of view of the detector changed due to adjusting the sample location. Standard deviations to average value ratios for all TEC-15 single-angle model runs are shown in Table 3.25. Additional data for this experiment is shown in the appendix. Excluding MSE values, all ratios were below 4%, with values for the FTO thickness all being within 0.6%. Table 3.26 shows the P-values from the Anderson-Darling normality test. The Anderson-Darling normality test for each parameter across the seven models showed that none tested as non-normal with a 95% level of confidence ($P < 0.05$). The SEM image from the offset point of the TEC-15 sample is shown in Figure 3.45. The three-layer structure was barely, yet clearly, visible. Total thickness for the two inner layers was estimated at 45 nm, with the SiO_2 layer appearing to be the smaller of the two. The center point image for this sample is shown previously in this document in Figure 3.23.

Table 3.24: Average Values at Various Locations for the TEC-15 Sample Multiple Position Study.

location	C	O1	O2	O3	O4
MSE	15.10	22.42	24.05	18.66	22.15
SnO_2 thickness	232Å	239Å	229Å	322Å	295Å
SiO_2 thickness	270Å	270Å	221Å	263Å	251Å
FTO thickness	2981Å	2985Å	3101Å	3145Å	3199Å
surface roughness thickness	391Å	405Å	405Å	607Å	645Å
surface roughness void %	57.6%	64.5%	51.2%	43.3%	45.5%

Table 3.25: SD% Values for the TEC-15 Sample Multiple Position Study.

location	C	O1	O2	O3	O4
MSE	19.07%	22.52%	23.69%	33.94%	28.49%
SnO_2 thickness	0.75%	2.24%	2.63%	1.28%	1.67%
SiO_2 thickness	2.09%	0.94%	0.27%	2.96%	3.23%
FTO thickness	0.06%	0.50%	0.51%	0.55%	0.60%
surface roughness thickness	1.86%	2.60%	3.69%	2.50%	2.48%
surface roughness void %	0.15%	1.76%	1.29%	2.63%	2.42%

Table 3.26: Anderson-Darling Normality Test P-Values for the TEC-15 Sample Multiple Position Study.

location	C	O1	O2	O3	O4
MSE	0.553	0.427	0.147	0.076	0.885
SnO ₂ thickness	0.885	0.631	0.584	0.374	0.565
SiO ₂ thickness	0.885	0.169	0.404	0.096	0.092
FTO thickness	0.616	0.201	0.198	0.279	0.389
Surface roughness thickness	0.161	0.612	0.439	0.098	0.128
Surface roughness void %	0.574	0.527	0.450	0.381	0.128

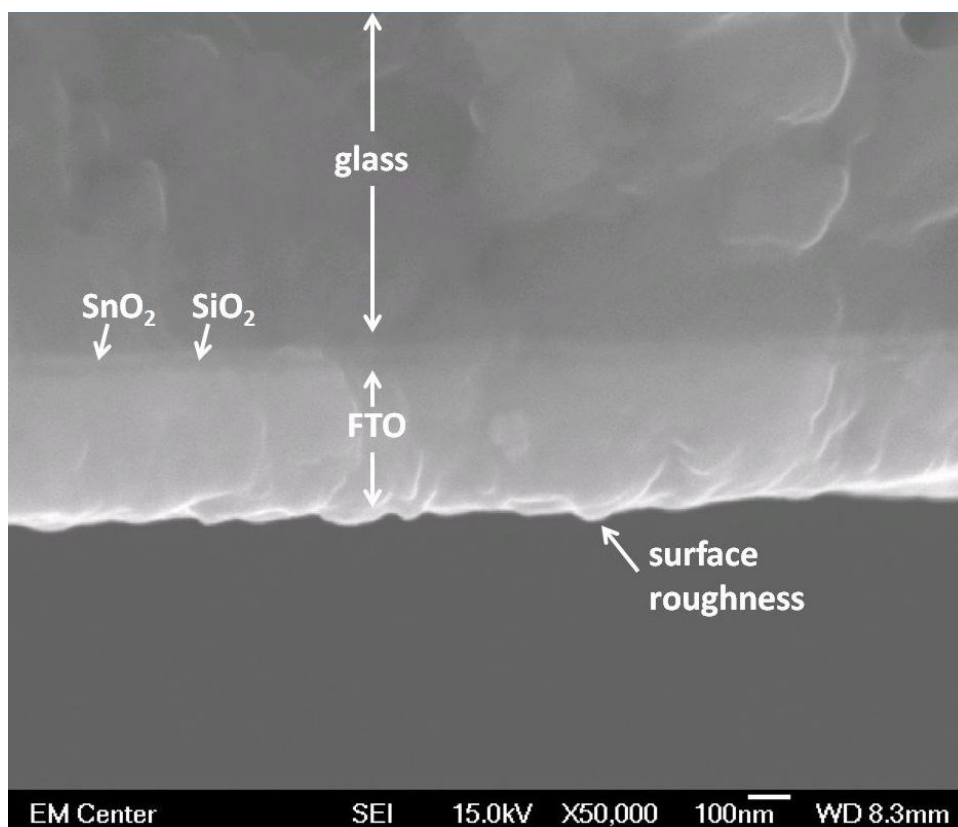


Figure 3.45: SEM Image of TEC-15 Sample from Offset Location.

As shown in Tables 3.24 through 3.26, SE performed fairly well for the TEC-15 Multiple Position Study, with variations for all variables other than MSE being all less than 4%. The FTO layer variability was within 1%, but that was worse than the Multiple Angle Study data, for which the SD% value was only 0.06%. Moreover, none of the distributions tested as non-normal. The calculated stack thicknesses were also all well within 10% of both each other and

the values determined by SEM (Figure 3.45), suggesting that the TEC-15 glass model is sufficiently reliable, accurate, and precise to conclude that TEC-15 is measurable by SE.

3.4.2. CdS Sample.

Average values at each of the five locations are shown in Table 3.27. Standard deviations to average value ratios for all CdS single-angle model runs are shown in Table 3.28. In all cases, excluding MSE values, this ratio was within 15%, and less than 1.5% for CdS thickness. Table 3.29 shows the P-values from the Anderson-Darling normality test. The Anderson-Darling normality test for each parameter across the seven models showed that none tested as non-normal with a 95% level of confidence.

Table 3.27: Average Values for CdS Sample Locations.

Location	C	O1	O2	O3	O4
MSE	14.91	25.45	35.38	36.63	41.02
SnO ₂ thickness	234Å	259Å	221Å	258Å	160Å
SiO ₂ thickness	241Å	268Å	282Å	269Å	340Å
FTO thickness	3237Å	2932Å	3048Å	2951Å	3045Å
CdS thickness	1998Å	1963Å	1853Å	1972Å	1722Å
Surface roughness thickness	173Å	266Å	191Å	195Å	165Å
Surface roughness void %	33.0%	16.08%	32.17%	20.78%	27.08%

Table 3.28: Standard Deviation to Average Value Ratios for the CdS Sample Multiple Position Study.

Location	C	O1	O2	O3	O4
MSE	28.58%	42.77%	39.71%	26.27%	38.69%
SnO ₂ thickness	1.48%	2.03%	3.28%	3.28%	2.68%
SiO ₂ thickness	3.20%	1.11%	0.88%	7.60%	1.64%
FTO thickness	0.21%	0.28%	0.49%	0.30%	0.44%
CdS thickness	0.16%	0.71%	0.94%	0.83%	1.23%
Surface roughness thickness	1.58%	7.29%	9.91%	10.46%	13.79%
Surface roughness void %	2.06%	0.87%	7.25%	4.29%	0.84%

Table 3.29: Anderson-Darling Normality Test P-values for the CdS Sample Multiple Position Study.

Location	C	O1	O2	O3	O4
MSE	0.602	0.100	0.105	0.296	0.099
SnO ₂ thickness	0.824	0.374	0.185	0.179	0.288
SiO ₂ thickness	0.596	0.630	0.289	0.359	0.672
FTO thickness	0.139	0.230	0.059	0.485	0.375
CdS thickness	0.562	0.298	0.433	0.304	0.332
Surface roughness thickness	0.352	0.293	0.390	0.358	0.390
Surface roughness void %	0.154	0.630	0.439	0.313	0.439

For the CdS sample, as with the TEC-15 sample, glare interfered with the 75° data, so data for that angle was again excluded. Overall, SE was able to measure the FTO and CdS layers with a standard deviation of just 1.25% of average as shown in Tables 3.27 through 3.29.

Unfortunately, the values for the surface roughness had much greater variation. A likely issue is difficulties modeling the porosity of this sample, as roughness thickness and porosity data are linked in the model, so that fixing the porosity at an incorrect value would prevent the thickness value from optimizing accurately, but allowing an indeterminate porosity value to vary can cause the thickness value to become indeterminate. The surface roughness layer for this model was relatively thin (~200 nm), and the Woollam Study model had fixed the porosity at 50%.

The SEM image from the offset point of the CdS sample is shown in Figure 3.46. The layer structure was unclear; while there appeared to be two layers, the image looked rather odd. This may have been due to using too much gold in the sample preparation process, or the way the break in the glass occurred. The center point image for this sample is shown previously in this document in Figure 3.27. Despite difficulties modeling the surface roughness, the correlation of SE stack thickness values to SEM (Figure 3.46) was impressive, with the center point value being within 0.1% and offset location #2 being within 0.3%. The values showed a reduction in stack thickness on the order of 10% from the center to the offset points; this

appeared to be almost entirely due to the CdS layer, which agreed with the hypothesis that deposition favored the center region of the sample. As with the TEC-15 data, one of the variables tested for normality showed as non-normal to a 95% confidence level. This appears to strongly support the evidence from the Baseline and Multiple Angle Studies demonstrating SE's ability to measure CdS deposited onto a TEC-15 substrate.

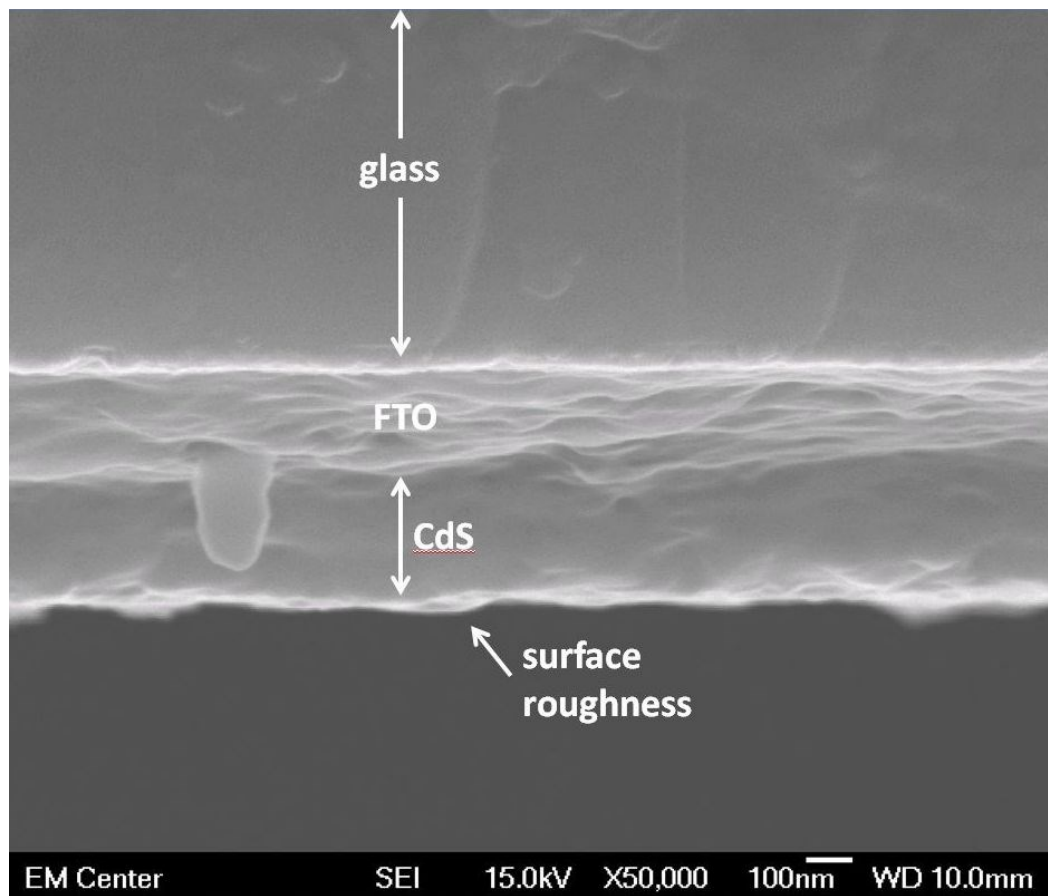


Figure 3.46: SEM Image of CdS Sample from Offset Location.

3.4.3. CdTe Sample.

Average values at each of the five locations are shown in Table 3.30. Standard deviations to average value ratios for all CdTe single-angle model runs are shown in Table 3.31. Since the underlying layers were indeterminate for the Multiple Angle Study, they were not allowed to vary for the Multiple Angle Study. The remaining properties, excluding MSE, were

within 1.5%. Table 3.32 shows the P-values from the Anderson-Darling normality test. The Anderson-Darling normality test for each parameter across the seven models showed that two tested as non-normal with a 95% level of confidence.

Table 3.30: Average Values for CdTe Sample Locations.

Location	C	O1	O2	O3	O4
MSE	30.68	45.61	85.60	82.60	107.77
CdTe thickness	29949Å	20304Å	22607Å	26270 Å	26636 Å
Surface roughness thickness	492Å	518Å	524Å	489 Å	485 Å
Surface roughness void %	24.85%	25.19%	27.98 %	25.09 %	25.90 %

Table 3.31: Standard Deviation to Average Value Ratios for the CdTe Sample Multiple Position Study.

Location	C	O1	O2	O3	O4
MSE	19.05%	21.86%	12.20%	19.06%	19.86%
CdTe thickness	0.06%	0.15%	0.43%	0.65%	0.51%
Surface roughness thickness	0.07%	1.17%	0.23%	0.51%	0.78%
Surface roughness void %	0.17%	0.56%	1.31%	0.26%	0.24%

Table 3.32: Anderson-Darling Normality Test P-values for the CdTe Sample Multiple Position Study.

Location	C	O1	O2	O3	O4
MSE	0.055	0.697	0.070	0.397	0.035
CdTe thickness	0.874	0.225	0.746	0.746	0.514
Surface roughness thickness	0.185	0.737	0.683	0.795	0.257
Surface roughness void %	0.607	0.414	0.033	0.474	0.473

As the CdTe sample was less reflective, the glare effect was not noticeable. However, during the Multiple Angles Study, the underlying layer thicknesses were found to be indeterminate, so they were fixed for this experiment. CdTe thickness and the surface roughness properties had a variability of less than 1.5% in all cases; as with the Multiple Angle Study experiment, the stack thickness nonuniformity value was indeterminate for the data from location 4, and gave relatively poor performance for the remaining locations. For all four locations, the

bulk CdTe layer and surface roughness thicknesses, while still highly repeatable, performed worse than for the Multiple Angle Study data. This is likely due to in part to a lower quality model: not only was the quality of the data deliberately reduced, the fit for the offset points was assumed to have properties similar to the center point, and so less effort was put into each individual model. As a result, the models produced were slightly less robust. Two of the value distributions tested for normality tested as non-normal at a 95% confidence level.

The SEM image from the offset point of the CdTe sample is shown in Figure 3.47. The image seemed to show a three layer structure; the upper layer may represent a change in crystallinity or surface damage; it is uncertain whether the innermost layer visible is the CdS, FTO, or a combination of both. The center point image for this sample is shown previously in this document in Figure 3.31. Not surprisingly, since the thicker layer obscured information from deep within the stack, the stack thickness comparison to SEM (Figure 3.47) was less accurate than for the CdS study; however, in all cases the values were still within about 10% of the SEM values, with the stack for location 2 being exceptionally close to the SEM value. It is believed that the offset sample observed by SEM was from location 2, so it is possible that much of the variation seen between locations was due to asymmetries in the CdTe chamber. Also, none of the bulk CdTe layer distributions tested as non-normal. Thus, despite difficulties with modeling the CdTe samples, the ability of SE to detect the thickness of the uppermost bulk layer was again supported by the data.

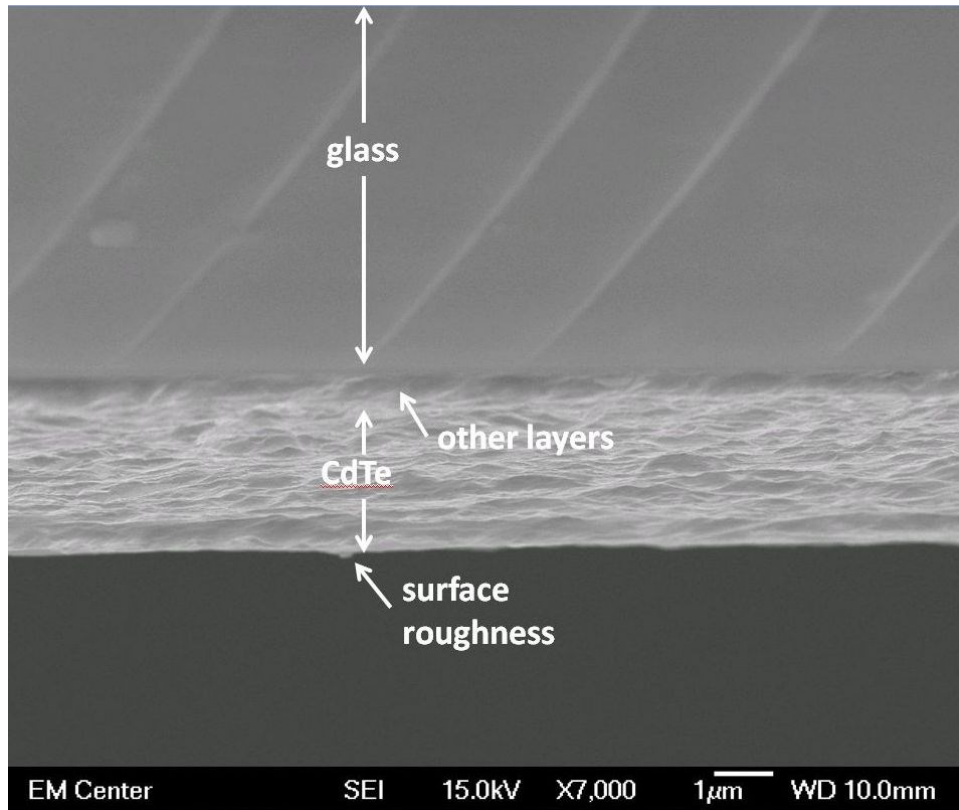


Figure 3.47: SEM Image of CdTe Sample from Offset Location.

3.4.4. Cl-Treated Sample.

Average values at each of the five locations are shown in Table 3.33. Standard deviations to average value ratios for all Cl-treated single-angle model runs are shown in Table 3.34. For the offset points, the TEC-15 layer thicknesses were fixed. Excluding MSE and non-uniformity, all remaining properties were within 8%, and for the CdTe layer, all tested properties were within 2%. Table 3.35 shows the P-values from the Anderson-Darling normality test. The Anderson-Darling normality test for each parameter across the seven models showed that two tested as non-normal with a 95% level of confidence. The SEM image from the offset point of the Cl-treated sample is shown in Figure 3.48. Although the layer structure is difficult to discern, a thin stripe near the middle of the image appears to be the other layers; the CdS layer is

not clearly visible as a separate layer. The center point image for this sample is shown previously in this document in Figure 3.35.

Table 3.33: Average Values for Cl-treated Sample Locations.

location	C	O1	O2	O3	O4
MSE	33.19	43.51	41.44	38.51	45.68
CdS thickness	2051Å	1772Å	2109Å	2006Å	2059Å
CdTe thickness	21460Å	17585Å	17801Å	19853Å	21054Å
Surface roughness thickness	397Å	364Å	420Å	378Å	384Å
Surface roughness void %	21.78%	23.06%	21.65%	22.46%	26.16%
non-uniformity	2.5%	5.5%	3.4%	6.2%	3.5%

Table 3.34: Standard Deviation to Average Value Ratios for the Cl-treated Sample Multiple Position Study.

location	C	O1	O2	O3	O4
MSE	11.34%	29.96%	32.64%	32.46%	33.59%
CdS thickness	2.02%	7.77%	0.92%	3.50%	1.21%
CdTe thickness	0.05%	0.54%	0.17%	0.14%	0.19%
Surface roughness thickness	0.52%	1.20%	0.13%	0.36%	0.36%
Surface roughness void %	0.64%	0.68%	1.26%	1.69%	1.14%
non-uniformity	14.79%	18.04%	7.13%	26.55%	10.74%

Table 3.35: Anderson-Darling Normality Test P-values for the Cl-treated Sample Multiple Position Study.

Location	C	O1	O2	O3	O4
MSE	0.022	0.243	0.240	0.619	0.247
CdS thickness	0.178	0.110	0.462	0.092	0.309
CdTe thickness	0.526	0.230	0.474	0.177	0.871
Surface roughness thickness	0.183	0.693	0.693	0.359	0.301
Surface roughness void %	0.647	0.606	0.242	0.524	0.799
non-uniformity	0.046	0.215	0.806	0.056	0.391

For the three treated samples, the TEC-15 glass layers were fixed, and the remaining layers allowed to vary. Overall, the Cl-treated models performed well, as shown in Tables 3.33 through 3.35, with the exception of MSE, nonuniformity, and the CdS thickness of location #1, where variability was nearly 8%. Stack thickness nonuniformity was particularly variable,

especially for location #3. For the CdTe thickness, standard deviation to average ratios were less than 0.6% in all cases, and the surface roughness properties were within 2%. None of the distributions tested from the Cl-treated sample offset points tested as non-normal to a confidence level of 95%. Similarly to the CdTe data, with a few exceptions, the models in the Multiple Position Study were less consistent than those in the Multiple Angle Study; however, overall performance suggested that even with the lower quality data, SE was still able to produce reasonably consistent results. The Cl-treated thickness stack values were remarkably consistent; interestingly, unlike for the CdTe and CdS samples, this sample had a nearly flat profile across all five points. It seems likely this sample came from a different batch which had different manufacturing conditions; this data also suggests factors other than thickness discrepancies may have been largely the cause of the drop-off in efficiency from the center that is seen in almost every sample produced from the old deposition system.

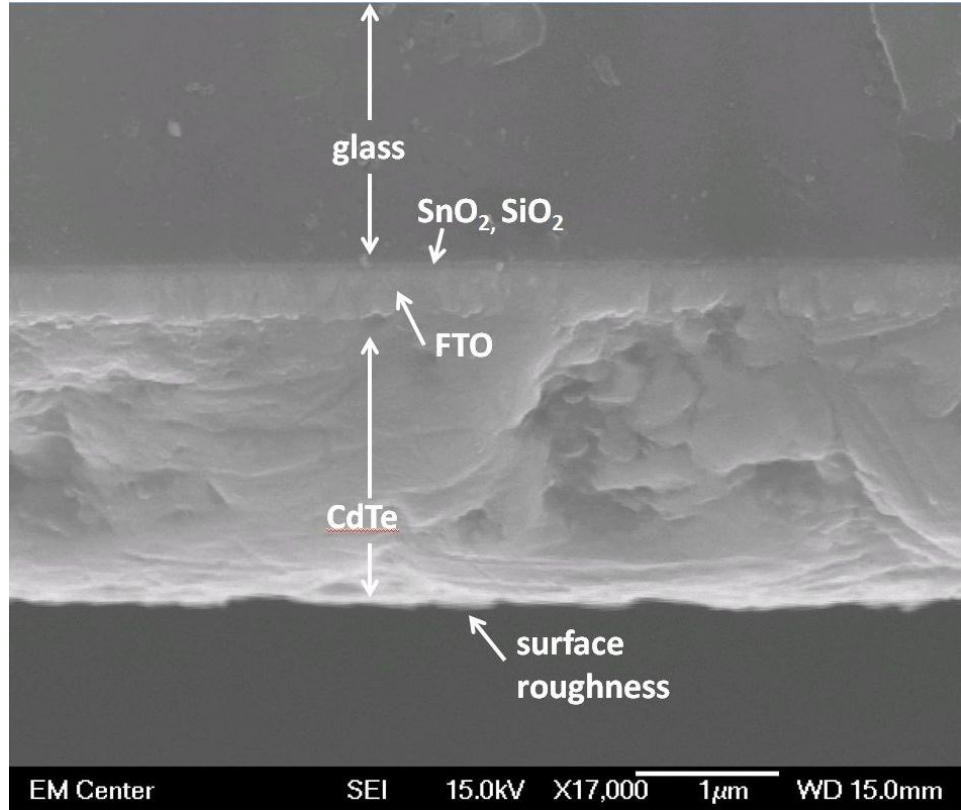


Figure 3.48: SEM Image of Cl-treated Sample from Offset Location.

3.4.5. Cu-Treated Sample.

Average values at each of the five locations are shown in Table 3.36. Standard deviations to average value ratios for all Cu-treated single-angle model runs are shown in Table 3.37. For the offset points, the TEC-15 layer thicknesses were fixed. Excluding MSE and non-uniformity, all the remaining values were within 10%, and for the CdTe layer, properties were within 2.1%. Table 3.38 shows the P-values from the Anderson-Darling normality test. The Anderson-Darling normality test for each parameter across the seven models showed that three tested as non-normal with a 95% level of confidence. These values are shaded in gray in the table. The SEM image from the offset point of the Cu-treated sample is shown in Figure 3.49. Although there seems to be a two-layer structure in this image, it is not clear whether that is an

actual layer or simply a fracture feature. It is likely this sample was exposed to too much gold and thus the overall structure is obscured. The center point image for this sample is shown previously in this document in Figure 3.39.

Table 3.36: Average Values for Cu-treated Sample Locations.

Location	C	O1	O2	O3	O4
MSE	30.98	60.25	38.30	52.14	54.14
CdS thickness	2157Å	2074Å	2126Å	2377Å	1901Å
CdTe thickness	8782Å	8432Å	7731Å	7058Å	7075Å
Surface roughness thickness	446Å	449Å	429Å	442Å	440Å
Surface roughness void %	21.76%	21.24%	22.58%	20.25%	16.90%
non-uniformity	4.5%	7.1%	6.8%	6.4%	2.8%

Table 3.37: Standard Deviation to Average Value Ratios for the Cu-treated Sample Multiple Position Study.

location	C	O1	O2	O3	O4
MSE	16.53%	19.92%	31.74%	30.53%	29.01%
CdS thickness	1.85%	9.63%	2.05%	1.51%	2.50%
CdTe thickness	0.25%	2.04%	0.54%	0.44%	0.62%
Surface roughness thickness	1.71%	1.45%	1.85%	0.97%	2.40%
Surface roughness void %	0.22%	0.71%	0.34%	1.51%	1.09%
non-uniformity	18.38%	21.10%	6.35%	23.59%	8.35%

Table 3.38: Anderson-Darling Normality Test P-values for the Cu-treated Sample Multiple Position Study.

location	C	O1	O2	O3	O4
MSE	0.364	0.407	0.011	0.201	0.026
CdS thickness	0.014	0.418	0.119	0.556	0.587
CdTe thickness	0.954	0.609	0.531	0.059	0.058
Surface roughness thickness	0.911	0.559	0.870	0.590	0.786
Surface roughness void %	0.459	0.081	0.150	0.330	0.799
non-uniformity	0.359	0.174	0.297	0.274	0.671

Data for the Cu-treated sample, as shown in Tables 3.36 through 3.38, was remarkably similar to that from the Cl-treated data. Notably, the location O1 data, which was modeled first, gave a less consistent result except for the surface thickness; the trends in the remaining data closely paralleled the trends in the Cl-data, with the Multiple Position Study data in most cases

being only very slightly worse than the Multiple Angle Study results. Of 24 distributions tested, 2 tested as non-normal to 95% confidence, both of which were for MSE values. Thickness values for the Cu-treated sample matched SEM data (Figure 3.49) to within about 10%, with location 1 being the outlier in both thickness and variability. The remaining data show the hypothesized lenticular film distribution, with about a 20% decrease in stack thickness from the center to offset point ~28 mm away.

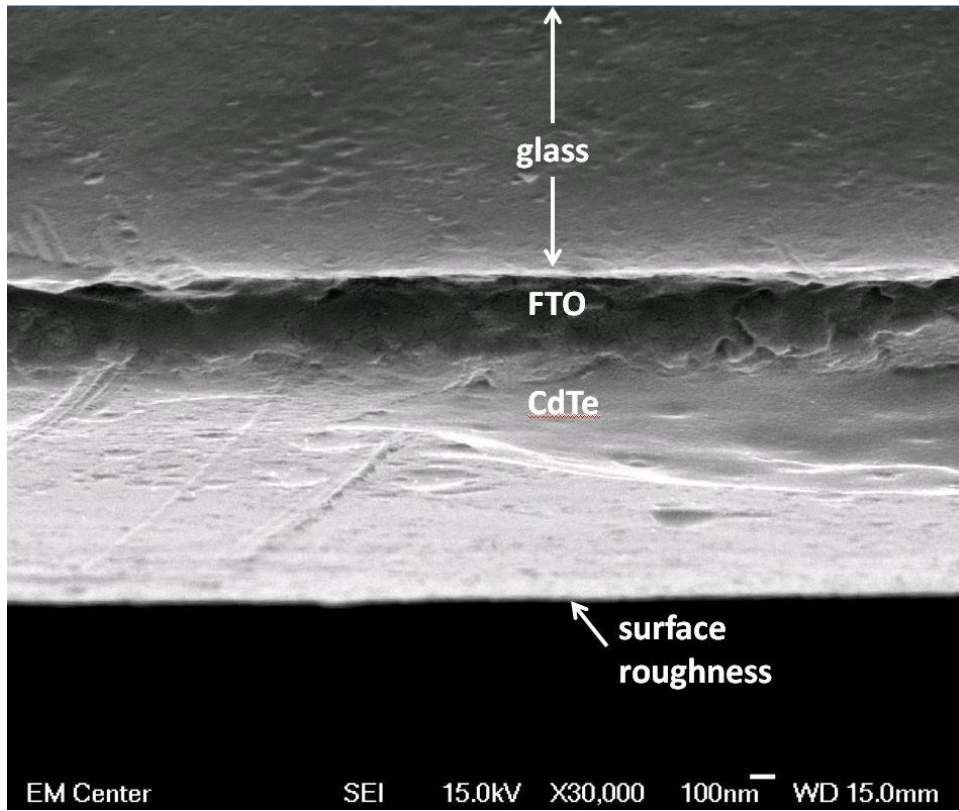


Figure 3.49: SEM Image of Cu-treated Sample from Offset Location.

3.4.6. Br-Treated Sample.

Average values at each of the five locations are shown in Table 3.39. Standard deviations to average value ratios for all Br-treated single-angle model runs are shown in Table 3.40. For both the center the offset points, the TEC-15 layer thicknesses were fixed. For the CdTe thickness, all values were within 2.8%. Table 3.41 shows the P-values from the Anderson-

Darling normality test. The Anderson-Darling normality test for each parameter across the seven models showed that one tested as non-normal with a 95% level of confidence. The SEM image from the offset point of the Br-treated sample is shown in Figure 3.50. Again, the exact layer structure is unclear. The center point image for this sample is shown previously in this document in Figure 3.43.

Table 3.39: Average Values for Br-treated Sample Locations.

Location	C	O1	O2	O3	O4
MSE	36.63	37.26	42.53	45.91	59.31
CdS thickness	2584Å	2603Å	800Å	542Å	1036Å
CdTe thickness	9633Å	9618Å	13141Å	15060Å	16094Å
Surface roughness thickness	549Å	547Å	363Å	181Å	341Å
Surface roughness void %	18.49%	18.80%	23.62%	32.60%	25.36%
non-uniformity	6.58%	6.58%	6.13%	2.82%	4.19%

Table 3.40: Standard Deviation to Average Value Ratios for the Br-treated Sample Multiple Position Study.

Location	C	O1	O2	O3	O4
MSE	14.97%	26.44%	14.26%	28.36%	20.15%
CdS thickness	1.16%	0.99%	42.84%	32.85%	2.35%
CdTe thickness	0.26%	0.26%	2.75%	1.17%	0.12%
Surface roughness thickness	0.45%	0.36%	3.44%	9.27%	1.51%
Surface roughness void %	2.38%	1.55%	1.79%	6.04%	4.51%
non-uniformity	1.62%	1.15%	12.69%	10.01%	14.10%

Table 3.41: Anderson-Darling Normality Test P-values for the Br-treated Sample Multiple Position Study.

location	C	O1	O2	O3	O4
MSE	0.208	0.180	0.505	0.046	0.432
CdS thickness	0.409	0.784	0.427	0.458	0.720
CdTe thickness	0.078	0.620	0.416	0.609	0.750
Surface roughness thickness	0.520	0.508	0.834	0.597	0.303
Surface roughness void %	0.532	0.829	0.571	0.581	0.774
non-uniformity	0.172	0.748	0.527	0.506	0.651

For the Br-treated sample, as shown in Tables 3.39 through 3.41, it was location O3 that produced less consistent results, while location O1 outperformed the Multiple Angle Study data.

O3 also produced the sole value that tested as non-normal, the MSE for that location. Much of the inconsistency for this set of models was for the CdS layer, which in turn impacted the modeling of the remaining values. The Br-treated sample seemed to show a reversal in the thickness distribution that was seen in the other samples, with the center values being thinner than the offset values. This may have been an artifact of the treatment process, since testing showed that the bromine solution, when a sample was exposed to it indefinitely, appeared to eventually remove the CdTe and CdS layers entirely. The variability of the thickness values between the offset points was considerable (~25- 30%). It is not clear how much of this was due to inaccuracies in the model, and how much was due to uneven distribution of the effects of the bromine treatment, but it is certainly possible the actual variation could have been in this range.

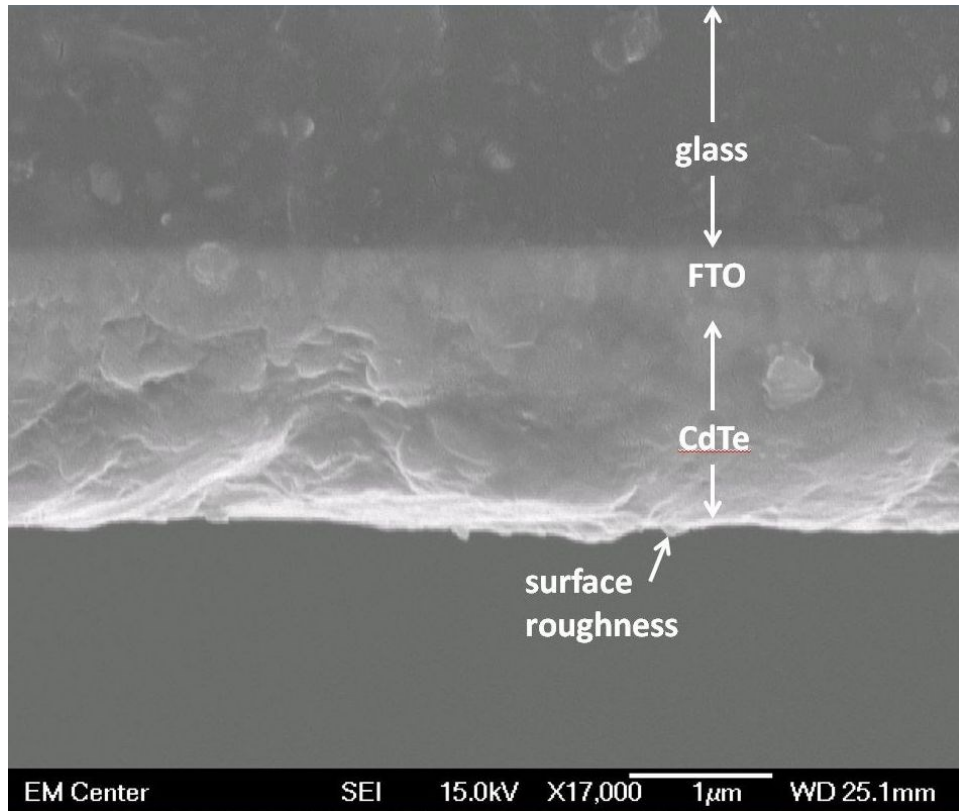


Figure 3.50: SEM Image of Br-treated Sample from Offset Location.

3.4.7. Overall Results.

Table 3.42 shows a summary of the average stack values and SEM stack values. Table 3.43 shows the percent deviation values between the SE and SEM stack thickness values. Table 3.44 shows the maximum standard deviation to average ratio for each variable, for the five locations. In this table and subsequent tables, surface roughness is abbreviated “SR.” The values for the top bulk layer (colored cells) were all within 3% of the average. As shown in Tables 3.26, 3.29, 3.32, 3.35, 3.38, and 3.41, the Anderson-Darling normality test indicated that 8 out of 175 distributions tested, or 4.6%, tested as non-normal at a 95% confidence level. Of those, 5 were MSE values. On the whole, results for the Multiple Position Assessment showed that SE was able to provide reasonably consistent and accurate results for the offset points even

with a reduced amount of data and modeling time; however, the quality of the results was significantly reduced, suggesting the importance of obtaining high quality data and models for complex films. Unfortunately, it was not clear from the initial analysis what might be causing the reduction in efficiency away from the center point.

Table 3.42: Summary of Stack Thickness Values for the Multiple Position Study.

sample	location					SEM	
	C	O1	O2	O3	O4	C	O1
TEC-15	3873Å	3898Å	3758Å	3730Å	3745Å	3732Å	3732Å
CdS	5883Å	5423Å	5267Å	5450Å	5432Å	5883Å	5250Å
CdTe	30441Å	26082Å	29680Å	28732Å	28261Å	32810Å	29460Å
Cl-treated	23510Å	23504Å	23462Å	24810Å	23497Å	23160Å	23490Å
Cu-treated	15117Å	13756Å	12914Å	12386Å	12758Å	15220Å	12750Å
Br-treated	16587Å	15680Å	17492Å	19080Å	20675Å	15220Å	18250Å

Table 3.43: % Difference Between SE and SEM Values (positive values indicate the SE model produced a thicker stack than SEM).

SEM location	sample	location				
		C	O1	O2	O3	O4
Center	TEC-15	+3.78%	+4.45%	+0.70%	-0.05%	+0.35%
	CdS	+0.00%	-7.82%	-10.47%	-7.36%	-7.67%
	CdTe	-7.22%	-20.51%	-9.54%	-12.43%	-13.86%
	Cl-treated	+1.51%	+1.49%	+1.30%	+7.12%	+1.46%
	Cu-treated	-0.68%	-9.62%	-15.15%	-18.62%	-16.18%
	Br-treated	+8.98%	+3.02%	+14.93%	+25.36%	+35.84%
offset	TEC-15	+3.78%	+4.45%	+0.70%	-0.05%	+0.35%
	CdS	+12.06%	+3.30%	+0.32%	+3.81%	+3.47%
	CdTe	+3.33%	-11.47%	+0.75%	-2.47%	-4.07%
	Cl-treated	+0.09%	+0.06%	+0.12%	+5.62%	+0.03%
	Cu-treated	+18.56%	+7.89%	+1.29%	-2.85%	+0.06%
	Br-treated	-9.11%	-14.08%	-4.15%	+4.55%	+13.29%

Table 3.44: Maximum Values for Standard Deviation to Average Ratio.

Sample	TEC-15	CdS	CdTe	Cl-treated	Cu-treated	Br-treated
MSE	33.94%	42.77%	21.86%	33.59%	31.74%	28.36%
SnO ₂ thickness	2.63%	3.28%	-	-	-	-
SiO ₂ thickness	3.23%	7.60%	-	-	-	-
FTO thickness	0.60%	0.49%	-	-	-	-
CdS thickness	-	1.23%	-	7.77%	9.63%	42.84%
CdTe thickness	-	-	0.65%	0.54%	2.04%	2.75%
SR thickness	3.69%	13.79%	1.17%	1.20%	2.40%	9.27%
SR void %	2.63%	7.25%	1.31%	1.69%	1.51%	6.04%
non-uniformity	-	-	-	26.55%	23.59%	14.10%

3.5. Industrial Device Study.

In addition to the Woollam, Baseline, Multiple Angle Study, and Multiple Position Studies conducted on 3"x3" laboratory production devices, a study was also conducted on a partially completed panel to demonstrate the potential applicability of SE to industrial as well as laboratory-scale CdTe photovoltaic devices. For this study, a 16"x16" panel produced by Abound Solar was used. This panel had been removed from the line immediately after the scribing process for XRD testing. Since the scribing process is conducted immediately after the Cu-treatment and final heat treatment processes, the properties of the panel were believed to be very similar to the 3"x3" Cu-treated sample from the Baseline Study. After a set of runs with different samples showing high amounts of noise rendering the data useless, there was significant concern about using the VASE ellipsometer. However, after implementing slight improvements to the sample handling technique, raw data waveforms appeared to contain far less noise than the earlier runs. This was likely a combination of using the new settings and reflection data only to maximize the amount of light available to the detector, and the lighter samples, which proved much easier to mount on the sample arm. Unfortunately, the exact shapes of the smaller waveforms, which contain much of the optical property data for the CdTe layer, were obscured,

so the focus of the modeling process was on matching the locations of the peaks rather than the overall waveform shape.

Ψ and Δ results for location 9 is shown in Figures 3.51 and 3.52. Table 3.45 shows the optimization results for location 9. Other than the MSE and non-uniformity values, all variables had standard deviations within 8% of their average value. Additional data for this experiment may be found in the appendix. The Anderson-Darling normality test for each parameter across the seven models showed that none tested as non-normal with a 95% level of confidence. The SEM image generated for panel location 9 is shown in Figure 3.53. The CdTe, CdS, and FTO layers are clearly visible. The SnO₂ and SiO₂ layers may be represented by the crease-like feature at the base of the FTO layer. The measurements show that the CdTe layer thickness was 2.270 micrometers (μm), the CdTe and CdS layers combined were 2.417 μm thick, and the FTO, SnO₂, and SiO₂ layers combined were 0.375 μm thick.

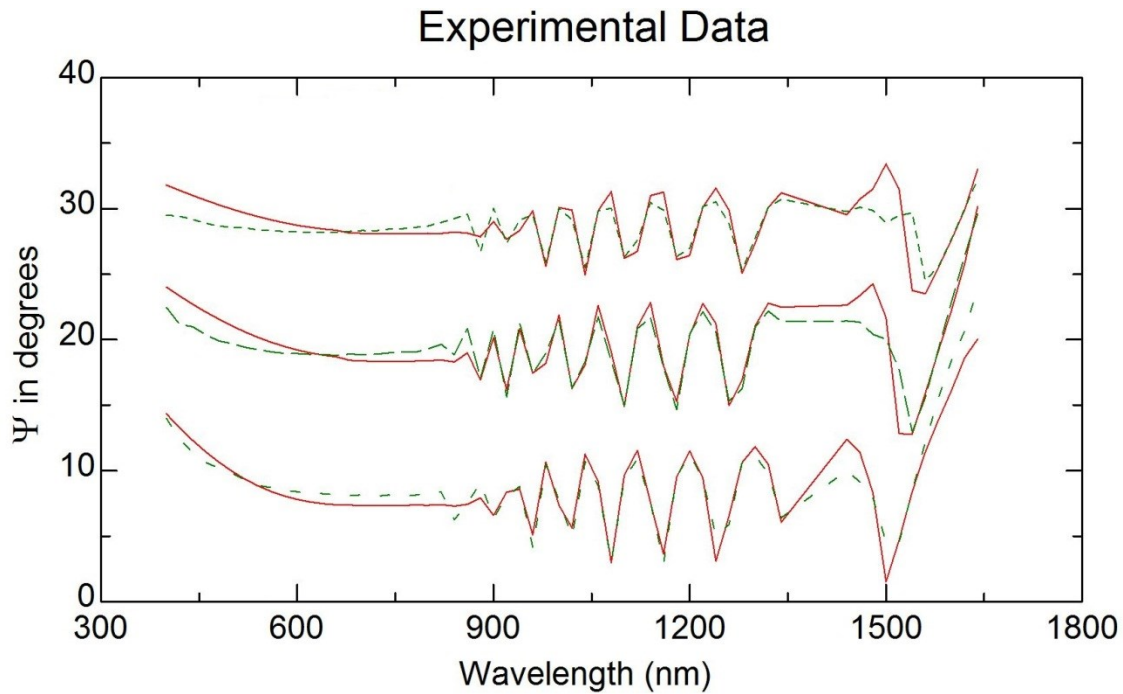


Figure 3.51: Ψ Plots for Panel Location 9.

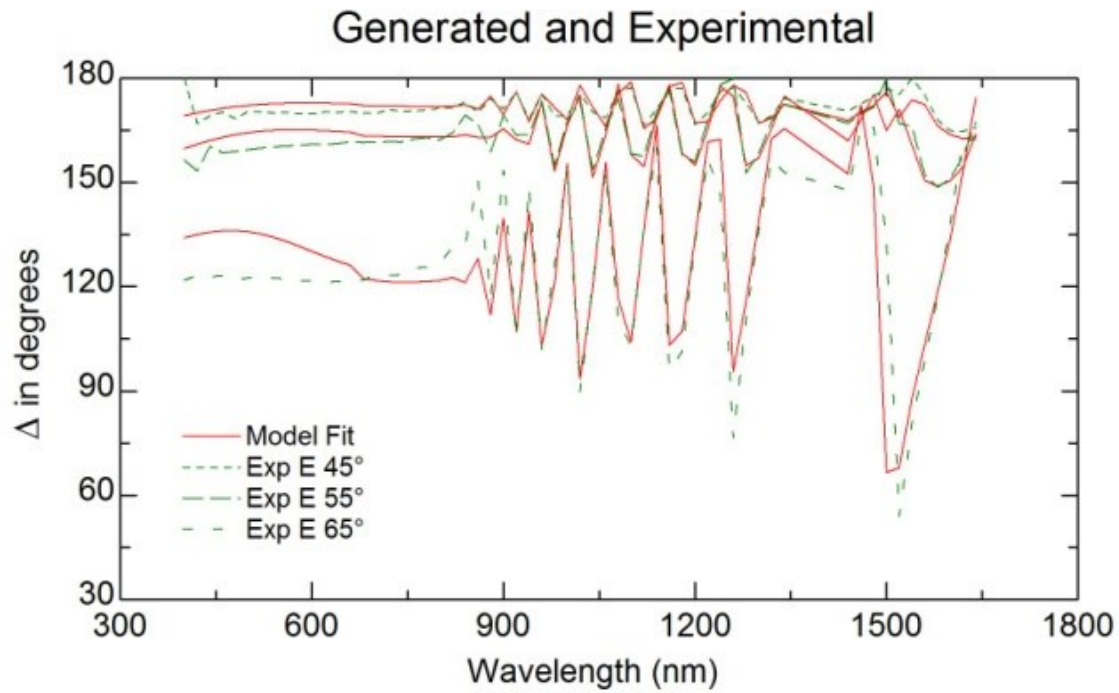


Figure 3.52: Δ Plots for Panel Location 9.

Table 3.45: Optimization Results for Panel Location 9.

Data	angles				statistics		
	45°	55°	65°	75°	average	SD%	P
MSE	13.93	19.28	23.93	31.89	22.26	34.20%	0.824
CdS thickness	1823Å	1779Å	1628Å	1535Å	1691Å	7.89%	0.516
CdTe thickness	23031Å	23133Å	23273Å	23392Å	23207Å	0.68%	0.806
surface roughness	553Å	545Å	544Å	514Å	539Å	3.14%	0.105
SR void %	23.9%	23.1%	21.4%	23.5%	23.0%	4.79%	0.247
non-uniformity	4.36%	2.78%	1.12%	2.86%	2.78%	47.69%	0.476

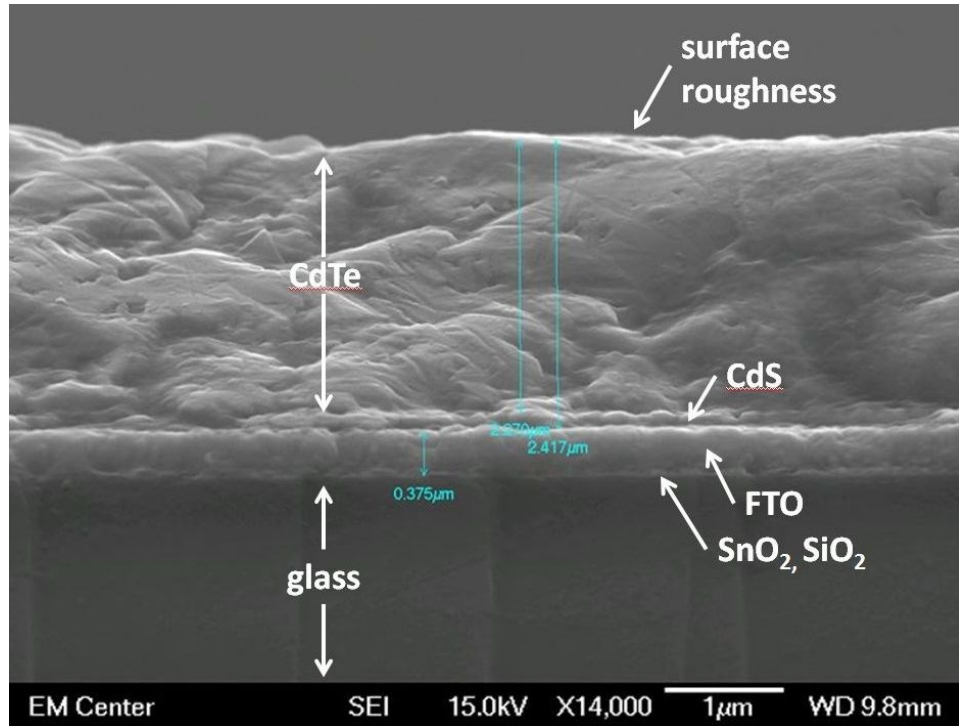


Figure 3.53: SEM Image for Panel Location 9.

Ψ and Δ results for location 12 is shown in Figures 3.54 and 3.55. Table 3.46 shows optimization results for location 12. Other than the MSE and non-uniformity values, all variables had standard deviations within 6% of their average value. The Anderson-Darling normality test for each parameter across the seven models showed that none tested as non-normal with a 95% level of confidence. The SEM image generated for panel location 12 is shown in Figure 3.56. Not surprisingly, the image appeared similar to that for location 9. The measurements show that the CdTe layer thickness was 2.469 μm , the CdTe and CdS layers combined were 2.633 μm thick, and the FTO, SnO₂, and SiO₂ layers combined were 0.395 μm thick.

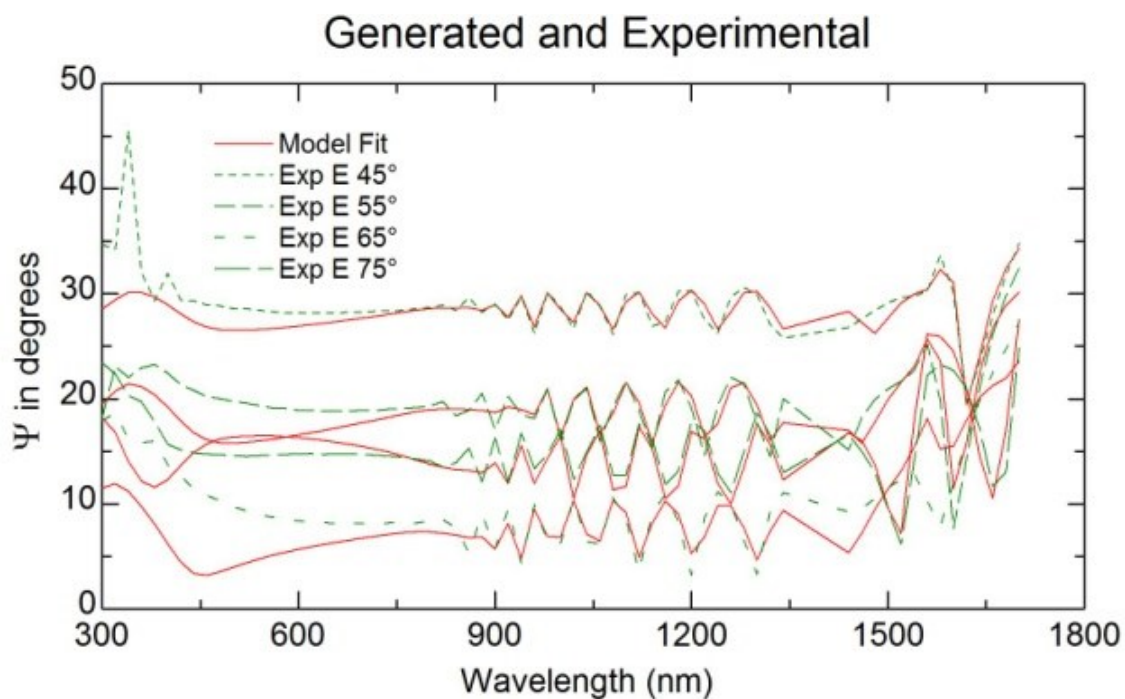


Figure 3.54: Ψ Plots for Panel Location 12.

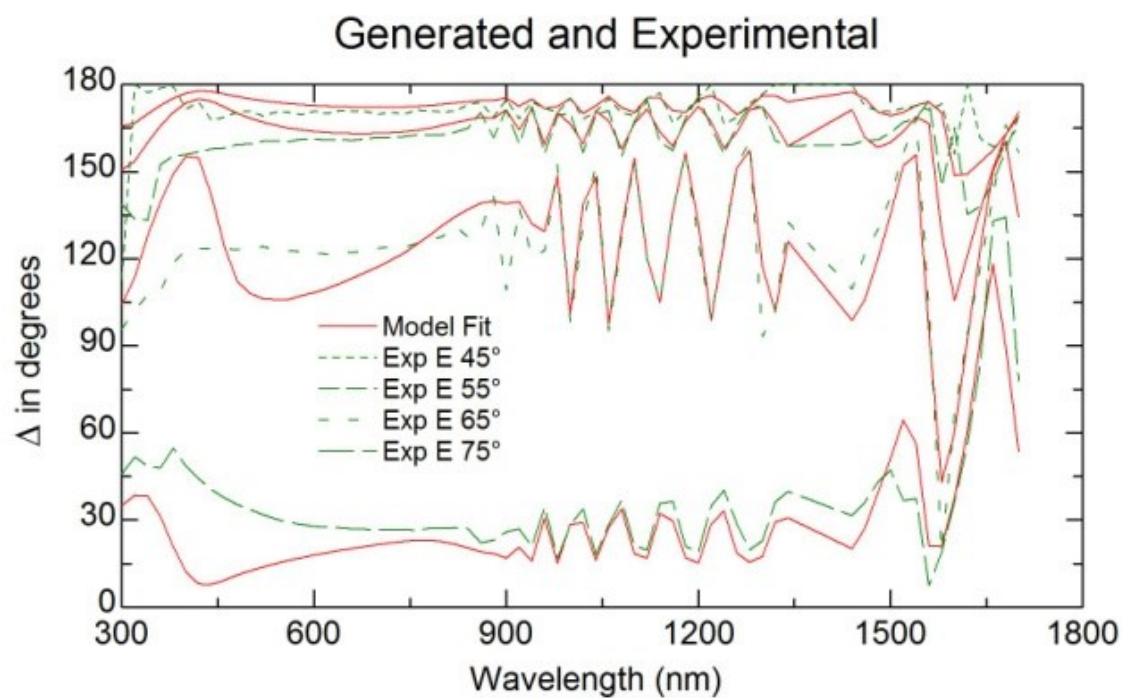


Figure 3.55: Δ Plots for Panel Location 12.

Table 3.46: Optimization Results for Panel Location 12.

Data	angles				statistics		
	45°	55°	65°	75°	average	SD%	P
MSE	5.87	7.24	11.59	18.83	10.88	53.60%	0.406
CdS thickness	1675Å	1660Å	1585Å	1683Å	1651Å	2.71%	0.104
CdTe thickness	24152Å	24113Å	24191Å	24072Å	24132Å	0.21%	0.860
surface roughness	499Å	512Å	532Å	566Å	527Å	5.51%	0.611
SR void %	21.9%	20.4%	20.7%	20.1%	20.8%	3.80%	0.276
non-uniformity	2.38%	1.91%	2.46%	3.72%	2.62%	29.64%	0.212

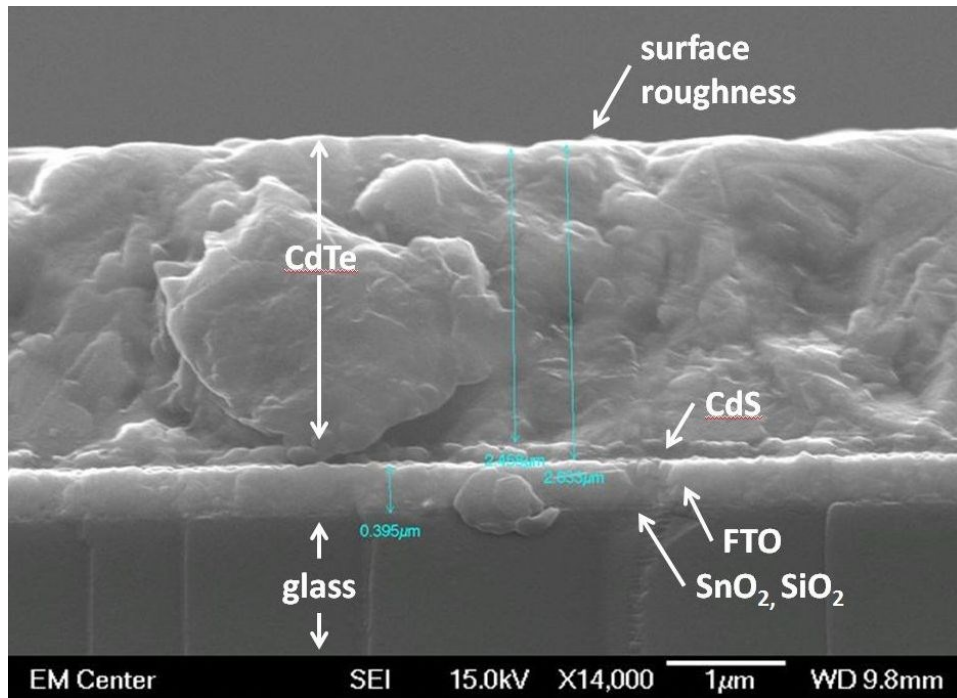


Figure 3.56: SEM Image for Panel Location 12.

Ψ and Δ results for location 21 is shown in Figures 3.57 and 3.58. Table 3.47 shows the optimization results for location 21. Other than the MSE and non-uniformity values, all variables had standard deviations within 6% of their average value. The Anderson-Darling normality test for each parameter across the seven models showed that one (grayed cell) tested as non-normal with a 95% level of confidence. The SEM image generated for panel location 21 is shown in Figure 3.59. The measurements show that the CdTe layer thickness was 2.229 μm, the

CdTe and CdS layers combined were 2.377 μm thick, and the FTO, SnO_2 , and SiO_2 layers combined were 0.368 μm thick.

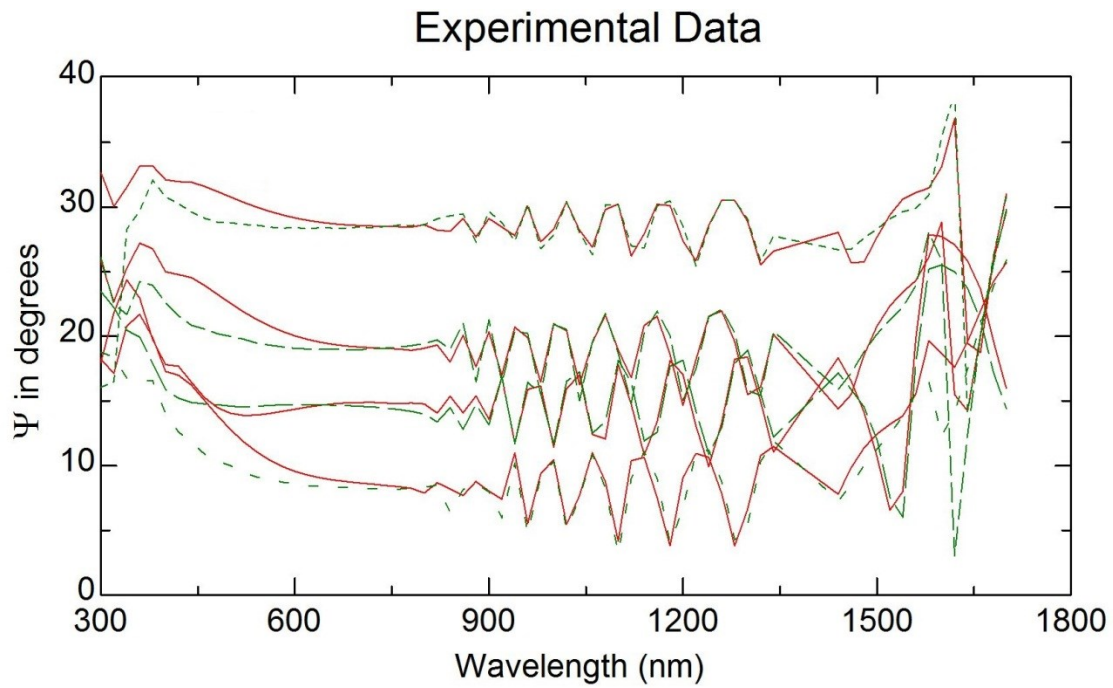


Figure 3.57: Ψ Plots for Panel Location 21.

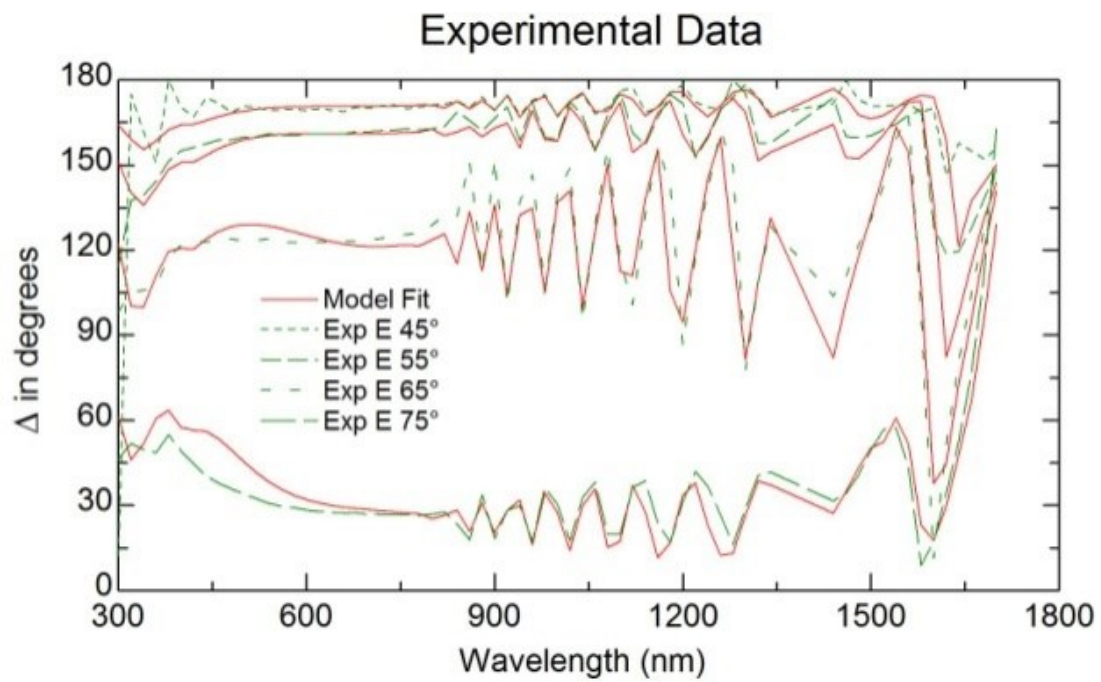


Figure 3.58: Δ Plots for Panel Location 21

Table 3.47: Optimization Results for Panel Location 21

Data	angles				statistics		
	45°	55°	65°	75°	average	SD%	P
MSE	8.27	9.27	16.57	18.92	13.26	39.88%	0.266
CdS thickness	1751Å	1713Å	1670Å	1737Å	1718Å	2.06%	0.543
CdTe thickness	21515Å	21518Å	21529Å	21417Å	21494Å	0.24%	0.033
surface roughness	496Å	515Å	549Å	565Å	531Å	5.87%	0.620
SR void %	20.2%	18.6%	17.8%	19.1%	19.0%	5.26%	0.812
non-uniformity	2.14%	2.70%	3.39%	4.39%	3.15%	30.66%	0.777

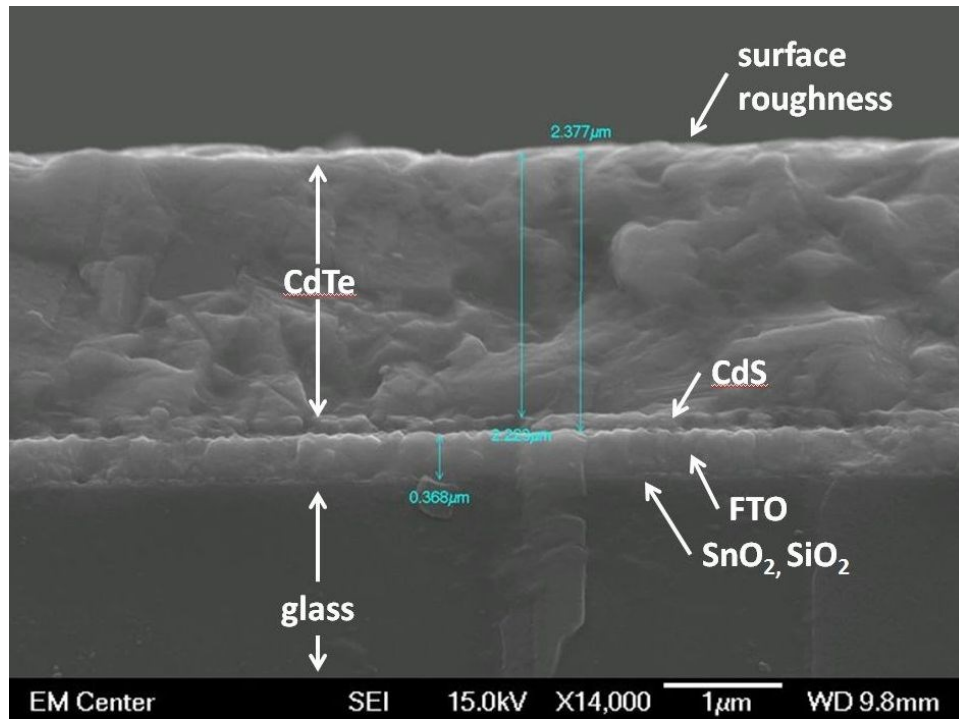


Figure 3.59: SEM Image for Panel Location 21.

Ψ and Δ results for location 25 is shown in Figures 3.60 and 3.61. Table 3.48 shows the optimization results for location 25. Other than the MSE and non-uniformity values, all variables had standard deviations within 4% of their average value. The Anderson-Darling normality test for each parameter across the seven models showed that none tested as non-normal with a 95% level of confidence. The SEM image generated for panel location 25 is shown in Figure 3.62. The measurements show that the CdTe layer thickness was 2.508 μm, the CdTe and

CdS layers combined were 2.712 μm thick, and the FTO, SnO_2 , and SiO_2 layers combined were 0.382 μm thick.

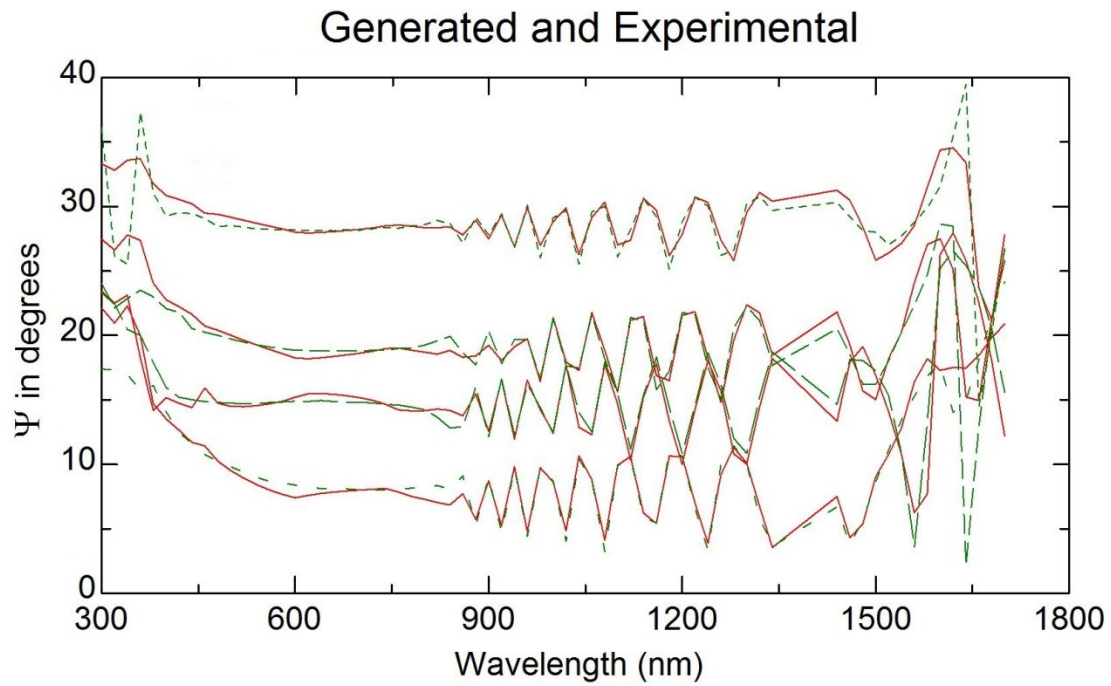


Figure 3.60: Ψ Plots for Panel Location 25.

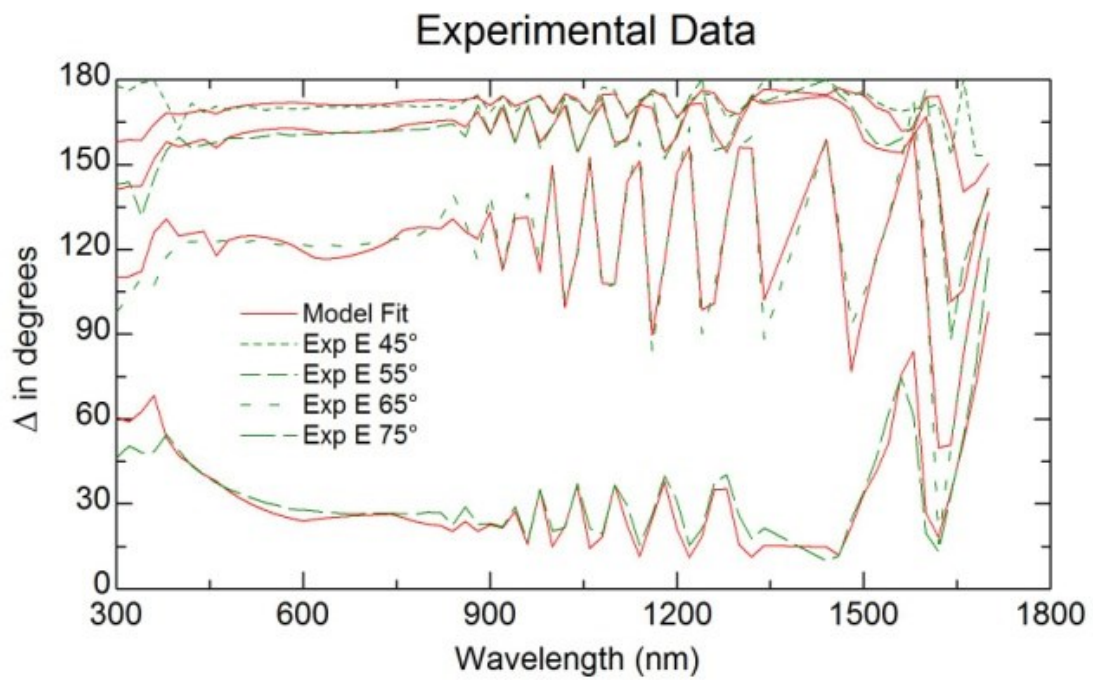


Figure 3.61: Δ Plots for Panel Location 25.

Table 3.48: Optimization Results for Panel Location 25.

data	angles				statistics		
	45°	55°	65°	75°	average	SD%	P
MSE	8.85	7.31	10.57	14.26	10.25	29.15%	0.608
CdS thickness	1772Å	1757Å	1715Å	1724Å	1742Å	1.54%	0.450
CdTe thickness	24833Å	24871Å	24895Å	24903Å	24876Å	0.13%	0.441
surface roughness	536Å	515Å	547Å	564Å	541Å	3.76%	0.846
SR void %	21.4%	21.2%	19.9%	20.2%	20.7%	3.53%	0.304
non-uniformity	2.44%	2.27%	2.58%	3.75%	2.76%	24.35%	0.085

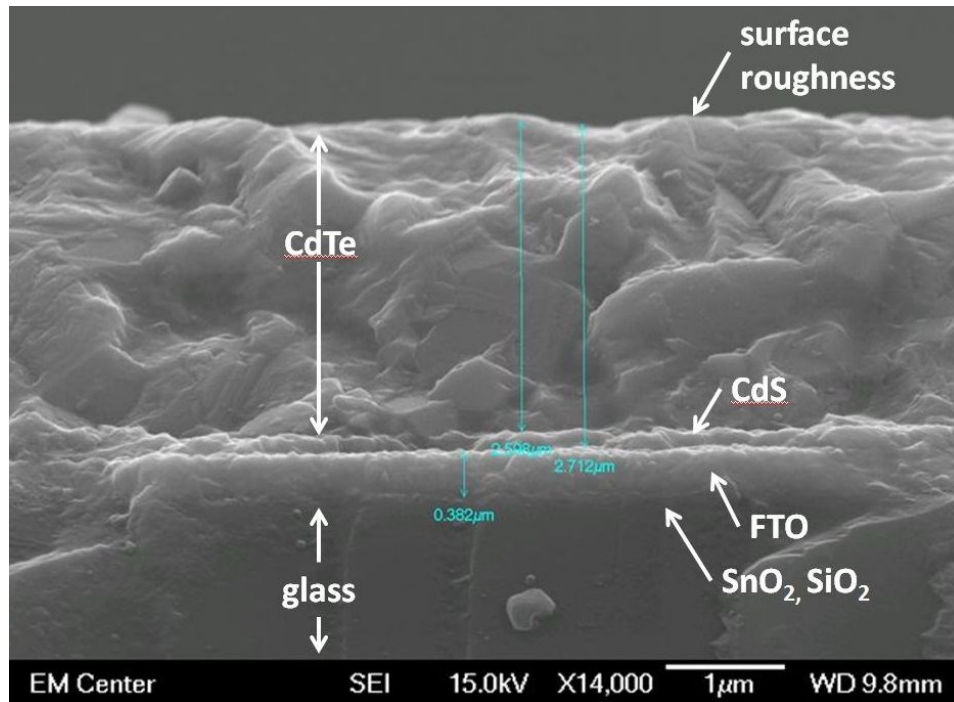


Figure 3.62: SEM Image for Panel Location 25.

Ψ and Δ results for location 30 is shown in Figures 3.63 and 3.64. Table 3.49 shows the optimization results for location 30. Although the averages were significantly different from location 25, the variability values (SD%) were very similar. The Anderson-Darling normality test for each parameter across the seven models showed that none tested as non-normal with a 95% level of confidence. The SEM image generated for panel location 30 is shown in Figure 3.65. The measurements show that the CdTe layer thickness was 2.310 μm , the CdTe and CdS

layers combined were $2.357\text{ }\mu\text{m}$ thick, and the FTO, SnO_2 , and SiO_2 layers combined were $0.348\text{ }\mu\text{m}$ thick.

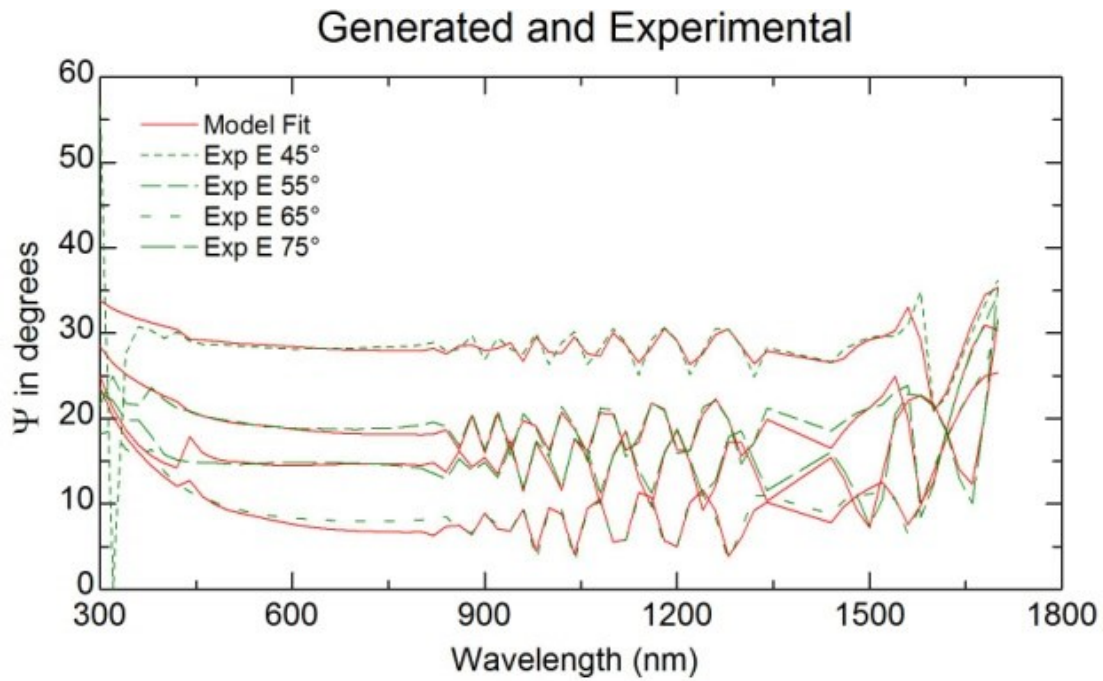


Figure 3.63: Ψ Plots for Panel Location 30.

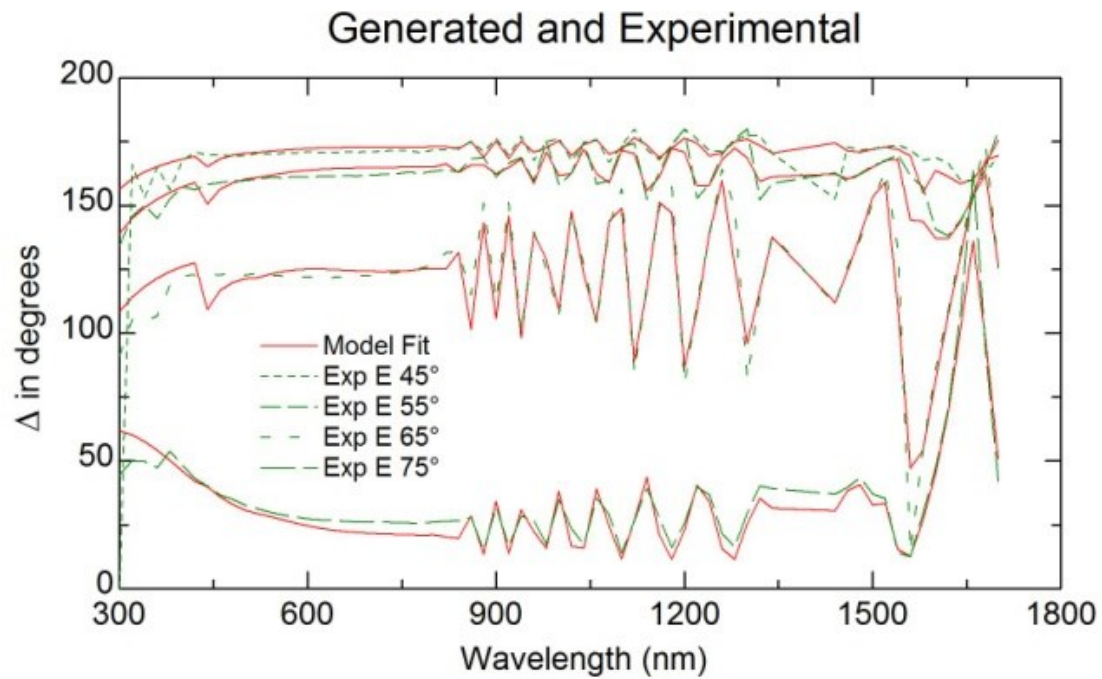


Figure 3.64: Δ Plots for Panel Location 30.

Table 3.49: Optimization Results for Panel Location 30.

data	angles				statistics		
	45°	55°	65°	75°	average	SD%	P
MSE	8.76	8.53	11.98	16.63	11.48	32.94%	0.264
CdS thickness	1821Å	1750Å	1725Å	1798Å	1773Å	2.47%	0.608
CdTe thickness	23881Å	23947Å	23968Å	23900Å	23924Å	0.17%	0.530
surface roughness	525Å	535Å	547Å	574Å	545Å	3.94%	0.548
SR void %	20.6%	19.5%	19.6%	19.4%	19.8%	2.83%	0.052
non-uniformity	2.47%	1.85%	2.45%	3.52%	2.57%	26.92%	0.308

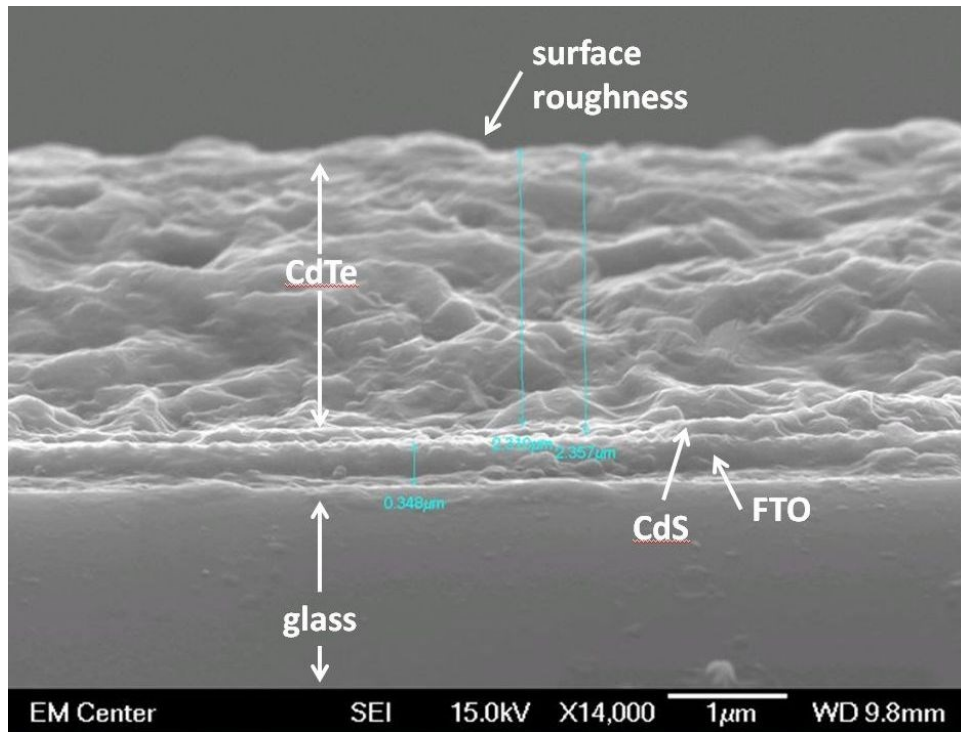


Figure 3.65: SEM Image for Panel Location 30.

Ψ and Δ results for location 41 is shown in Figures 3.66 and 3.67. Table 3.50 shows the optimization results for location 41. Data from this location closely resembled that of location 30. The Anderson-Darling normality test for each parameter across the seven models showed that none tested as non-normal with a 95% level of confidence. The SEM image generated for panel location 41 is shown in Figure 3.68. The measurements show that the CdTe layer

thickness was $2.197\mu\text{m}$, the CdTe and CdS layers were $2.304\mu\text{m}$, and the FTO, SnO_2 , and SiO_2 layers combined were $0.348\mu\text{m}$ thick.

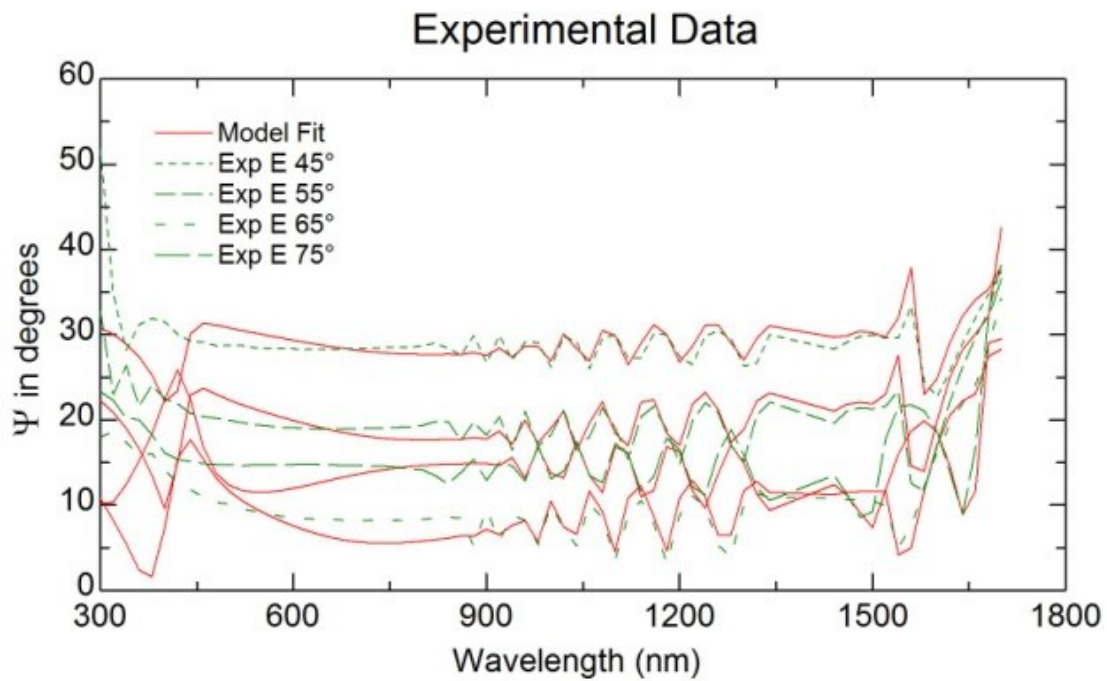


Figure 3.66: Ψ Plots for Panel Location 41.

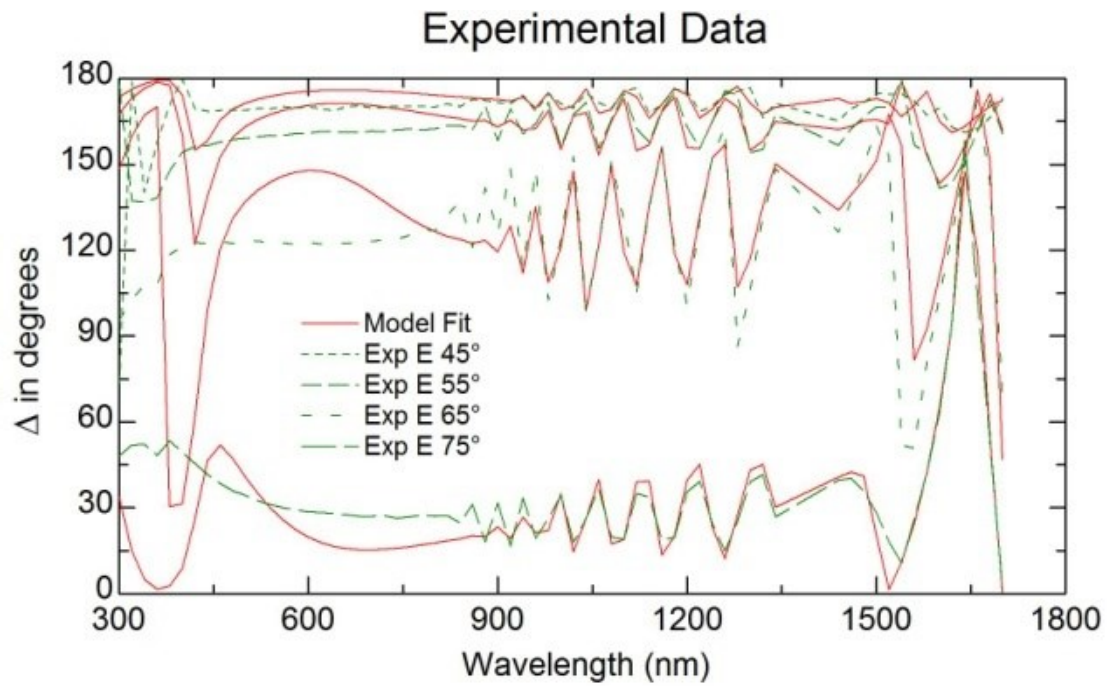


Figure 3.67: Δ Plots for Panel Location 41.

Table 3.50: Variable Angle Multiple Angle Study for Panel Location 41.

data	angles				statistics		
	45°	55°	65°	75°	average	SD%	P
MSE	6.65	7.89	14.73	20.55	12.45	51.89%	0.439
CdS thickness	1733Å	1717Å	1695Å	1753Å	1724Å	1.44%	0.871
CdTe thickness	23703Å	23710Å	23736Å	23635Å	23696Å	0.18%	0.291
surface roughness	523Å	514Å	538Å	553Å	532Å	3.19%	0.801
SR void %	20.1%	19.2%	19.0%	19.3%	19.4%	2.64%	0.165
non-uniformity	2.47%	2.55%	3.29%	3.94%	3.06%	22.57%	0.363

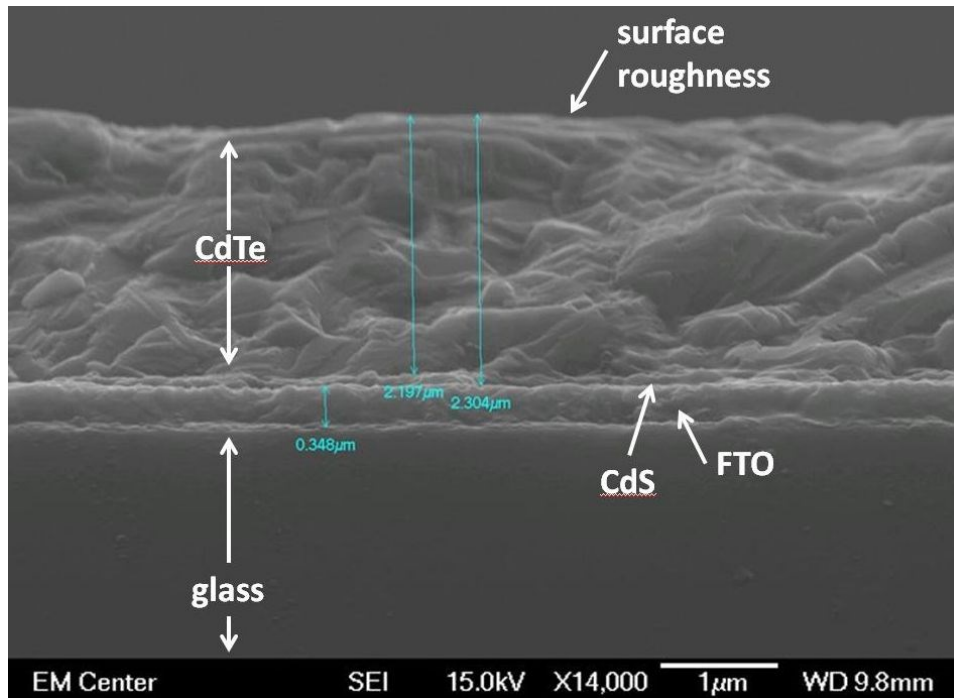


Figure 3.68: SEM Image for Panel Location 41.

Overall results for the Industrial Device Study are shown in Tables 3.51 through 3.53.

Table 3.51 shows a summary of the average stack values and variations of the Industrial Device Study relative to the SEM values. All modeled stack thickness values were within 8% of the SEM values; for location 12 the SE value was within 0.1%. “diff / σ ” is the result of dividing the difference between the model average and SEM values by the standard deviation of the model values. In three cases, this value was less than 0.5, in the remaining three, it was over 3.0. Table 3.52 shows a summary of the results of the Anderson-Darling normality test for the Industrial

Device Study at various certainty levels. All but one (grayed cell) of the distributions tested as normal at the 95% confidence level. Table 3.53 shows a summary of the results of comparing the standard deviation to average values. The uppermost bulk layer for each film stack (CdTe) has a standard deviation within 0.7% of the average.

Table 3.51: Summary of Stack Thickness Values for the Industrial Device Study.

location	SE	SEM	difference	diff / σ
9	25437	24170	+5.24%	4.11
12	26310	26330	-0.08%	0.16
21	23743	23770	-0.11%	0.23
25	27158	27120	+0.14%	0.48
30	23923	23570	-1.50%	3.33
41	23695	21970	+7.85%	20.25

Table 3.52: Summary of Anderson-Darling Normality Testing Results for the Industrial Device Study.

variable	location					
	9	12	21	25	30	41
MSE	0.824	0.406	0.266	0.608	0.264	0.439
CdS thickness	0.516	0.104	0.543	0.450	0.608	0.871
CdTe thickness	0.806	0.860	0.033	0.441	0.530	0.291
surface roughness	0.105	0.611	0.620	0.846	0.548	0.801
SR void %	0.247	0.276	0.812	0.304	0.052	0.165
non-uniformity	0.476	0.212	0.777	0.085	0.308	0.363

Table 3.53 Summary of SD% Values for the Industrial Device Study.

variable	location					
	9	12	21	25	30	41
MSE	34.20%	53.60%	39.88%	29.15%	32.94%	51.89%
CdS thickness	7.89%	2.71%	2.06%	1.54%	2.47%	1.44%
CdTe thickness	0.68%	0.21%	0.24%	0.13%	0.17%	0.18%
surface roughness	3.14%	5.51%	5.87%	3.76%	3.94%	3.19%
SR void %	4.79%	3.80%	5.26%	3.53%	2.83%	2.64%
non-uniformity	47.69%	29.64%	30.66%	24.35%	26.92%	22.57%

A glance at the results from the Industrial Device Study reveals that MSE values appeared to decrease significantly from the Baseline Study numbers despite the fact that the

model waveforms were clearly a visually worse match. However, this is likely an artifact of the lower resolution and not particularly meaningful. The CdS thickness consistently showed values around 1700 Å throughout the sample, suggesting good process control for CdS deposition.

Location 9 showed the worst repeatability for this value, with an SD% (standard deviation to average ratio) value of nearly 8%, while for the other locations, model performance was much better, varying between 1% and 3%. This may be due to the fact that the waveform shape fit for the large wavelength waveforms containing information about the CdS and FTO layers appears to be of lower quality for this set of data. Surface roughness properties remained very consistent over the surface of the panel, with a porosity remaining close to 20%, and average thickness in the 520-550 Å range. Location 21 produced surface roughness variations over 5%, while most of the remaining locations produced variations between 2 and 4%. This appears to be correlated with a greater vertical offset in the Ψ and Δ data for 65° and 75°, respectively. For reasons that are not clear, the bulk CdTe layer values from location 21 produced results that tested as non-normal while the other points produced results that gave much higher P values. As with the 3"x3" results, CdTe thickness remained the most consistent value throughout the study, with all variability values under 0.7%, and for five out of the six locations, it was less than 0.25%. This demonstrates that, with a good sample and model, even lower-resolution data can provide consistent data with both production and laboratory scale production samples.

Comparison of SE and SEM shows that in all cases the stack thicknesses were within 8%, suggesting that the models represent at least somewhat accurate measurements. However, it is curious that in 3 out of the 6 cases, the difference was much less than 1%, but was much higher for the other 3. It is possible this may represent either an error in the relative position of the SE

scan location and the location of the smaller SEM sample that was cut from each sample, or a “false positive” inherent in the models that was very close to the actual data.

Discussion

This study provided a number of key findings for each step in the device manufacturing process as well as key findings pertaining to multiple process steps. These findings suggest SE can detect a variety of material properties in addition to those studied in the main body of results.

Both the Woollam and Baseline Study models were able to provide a good fit for both the stack thickness and optical response of the TEC-15 glass over the range studied. Some variation from the raw data occurred near the ends of the range, suggesting opportunity for further model refinement. The FTO layer produces unusual waveform shapes at wavelengths near $\sim 1500\text{nm}$. This effect continues to be visible in measured SE data even when the thickness is not accurately measurable due to the low transparency of overlying layers. This effect is ultimately the result of conductivity: because of free-carrier absorption in the conduction band, FTO acts as metal in this energy range. In the model, the Drude term carries much of the information on this conductivity. Physically, the fluorine doping has a large effect on the conduction properties, which in turn affect n , k , Ψ , and Δ . A surface roughness layer is necessary for a good model. This layer has a different conductivity than the bulk FTO layer. Transparency and backside reflection were also measured for TEC15 glass.

SEM and SE show the SiO_2 layer may be thinner than originally expected after deposition. Originally it had been thought to be $\sim 270 \text{ \AA}$ thick, and while the value from SE models of the undeposited TEC-15 show this, models for the deposited samples show a reduced value closer to 200 \AA . Figure 4.1 shows an SEM image obtained of the bromine-treated sample from a location near offset point O2 for which gold was not deposited. The SiO_2 layer appears significantly thinner than the SnO_2 layer.

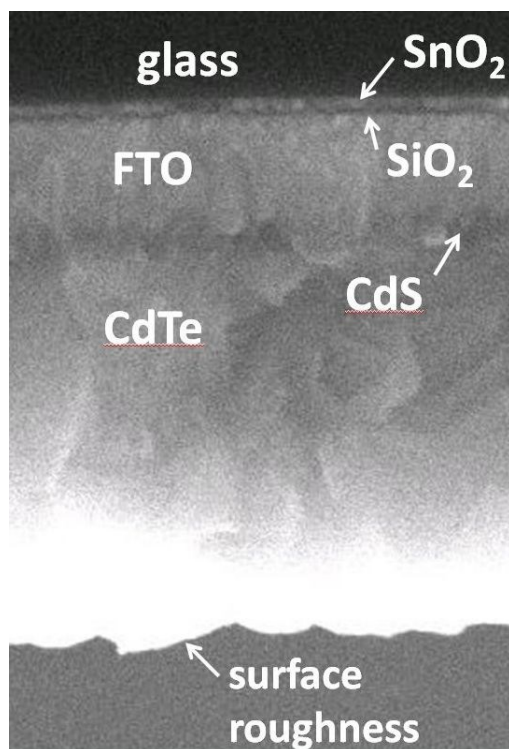


Figure 4.1: Detail of Supplemental SEM Image of the Bromine-treated Sample.

CdS is an n-type semiconductor with complex optical properties; a combination of Gaussian and PSEMI oscillators was used to model the CdS direct gap semiconductor properties and critical points. This produced an exceptionally "tight" fit across several angles, which nominally indicates that the optical properties were modeled effectively, allowing the thickness and other properties to be measured accurately. CdS thicknesses decreased from the center point to all four offset points; however, the decrease was slightly uneven. This may be an artifact of the deposition process.

Multiple oscillators and surface roughness were required for a good CdTe fit. The necessity of modeling the surface roughness has also been reported elsewhere [64, 73]. The n and k value plots for the raw CdTe sample had a relatively flat profile, with the Baseline Study model showing a secondary peak; however, this may be due to surface or thickness effects rather than a physical property of the bulk layer. SE was prevented from accurately measuring the

underlying layers for the raw CdTe sample; it appears this may be due to the thicker CdTe layer reducing the amount of light that reaches these layers; however, SE was still able to measure the CdTe with a high consistency, as well as detect the presence of the underlying layers. Similarly to the CdS layer, thicknesses for the CdTe layer decreased from the center to the offset points; the decrease appeared to vary significantly between the locations, suggesting a somewhat asymmetric deposition profile. Nonuniformity, representing thickness variations between locations separated by more than a few hundred nm (these local “hills” in the film are represented in the surface roughness layer), but within the same ~3 mm diameter scan region, varied significantly; the locations with higher thickness (center, O3, O4) also showed lower nonuniformity values (between about 3% and 5%) than the Woollam Study data or the locations with lower thicknesses (O1 and O2), which had nonuniformity values as high as 10%.

Optical properties show crystalline CdTe characteristics in the treated samples. In general, because better quality (higher efficiency) films are nominally believed to have properties closer to the monocrystalline values, it is generally presumed that films whose optical properties more closely resemble those of monocrystalline materials will tend to produce better-performing devices. Several properties which have been correlated to SE-detectable properties appeared to change with treatments. For the Woollam Study data, the Cl-treated sample had a significantly smaller surface roughness, which may have been responsible for a more “clean” n and k profile, nominally suggesting good crystallinity.

External evidence [50] suggests that a band gap shift seen in SE data between the Cl and Cu treatments may have been caused by a change in lattice parameter. In addition, loss of preferential orientation has been suggested as a possible cause of a vertical shift in n [50]. Both CSU [50] and external research [47] have shown a tendency for CdTe-based compounds have a

preferential orientation in the (111) direction, but CSU XRD data [50] suggests that this tends to fade or disappear after the treatment processes. Changes that have been associated with strain and grain sizes suggest annealing under heat treatment, including grain growth, may be responsible for the loss of orientation. Cu treatment appears to introduce a stabilizing effect. For the Bromine sample, n & k values appeared to closely resemble the Cu-treated sample, except that crystallinity appeared to increase. Since Br is believed to act as an etchant, this is consistent with the hypothesis that the surface roughness hides the crystallinity of the underlying layers, and this effect is reduced by the chemical treatments.

Over the several samples and tests used for this research work, n and k values, oscillator values, and thicknesses were measured for all thin film layers in the CdTe photovoltaic devices studied. Porosity and thickness of the surface roughness were also measured in for all process stages. Inclusion of a surface roughness in the model appeared to be required at all stages in the process for a proper fit. The Baseline Study showed similar trends in optical property waveform shapes, supporting the Woollam Study and its findings. The Multiple Angle and Location Studies demonstrated both the reliability of SE in measuring surface and bulk properties and confirmed the limitations shown in the Woollam Study data with regard to underlying layers.

The Baseline Study demonstrated that band gap and other properties tied to photon energy are often visible in the raw data waveforms, while other properties require modeling for accurate measurements, and others, while detectable, are difficult to measure accurately. For example, thickness nonuniformity was not usually measurable for untreated samples; and when measurable it was in the single digits, suggesting the films are deposited relatively evenly over small areas.

A key advantage of SE is that it is not merely nondestructive, but nonintrusive as well. SE only contacts the sample with a beam of light similar in composition to natural sunlight; it has been demonstrated [77] to function through a window into a vacuum chamber. Thus it would be possible to set up SE equipment outside a chamber so that the SE hardware could be adjusted and maintained without interfering with the production hardware or exposing the SE equipment to chemicals in the manufacturing process, yet still obtain meaningful data from PV devices in production.

4.1. Statistical Significance

To fully understand the statistical significance of a distribution, not only must the basic quantities of average and standard deviation or some equivalent be known, the shape of the distribution must also be understood. Thus the results from the Baseline Study were not statistically significant despite confirmation with SEM, because for each result, there was only one value, and it is not clear that comparing the difference between Woollam and Baseline Study data is meaningful since the two sets of data did not come from the same samples, and the SEM data only measures the total stack thickness with confidence.

For this reason, normality testing of data was performed as explained in Section 2.3.6. The Anderson-Darling test produces a “P-value” giving an estimate of probability that the distribution from which the known data points came is normal. Out of a large number of normal distributions, it may be expected that as many as 5% have P values less than 0.05. Out of 249 sets of values tested during the course of the work described in this dissertation, 10, or just over 4%, tested as non-normal to this level of confidence. However, half of these were MSE value distributions. Out of the 36 sets of MSE values tested, 5, or 14%, had P values less than 0.05. This suggests that although the majority of the MSE distributions did not test as non-normal to a

confidence level of 95%, the normality of MSE values in general appears questionable. Out of the other 183 values tested, 5 had P values less than 0.05; nominally, one would expect 9 values out of 183 to be less than 0.05. There was no clear pattern in the 5 values, so it appears that in general, the results of SE repeated at varying angles, excluding angles where glare is present, may be normal. Table 4.1 summarizes the portion of values found to be normal at various certainty levels in comparison to the expected proportion including the MSE values.

Table 4.1: Portion of Distributions Testing Normal at Various Confidence Levels.

confidence level		50%	75%	90%	95%	99%
% of non-normal distributions	expected	50%	25%	10%	5%	1%
	actual	61.1%	31.0%	12.5%	4.2%	0.0%

In industry, one technique for validating measurement tooling is to compare the standard deviation $\sigma(x)$ for measurements of a given value with the width of the tolerance range between x_{\min} and x_{\max} , where x is the variable measured, x_{\min} is the minimum acceptable value, and x_{\max} is the maximum allowable value. The manufacturer typically desires to have a high probability of correctly detecting not only when the process has fallen out of tolerance specifications, but also whether a process has begun to drift off-center prior to drifting outside the acceptable limits. It is typical to require that the standard deviation of a measurement be within 10% of the process tolerances to allow for a high degree of certainty that the process can be caught before problems occur. The thinking is that, if the data is normally distributed, more detailed analysis is not required, since a difference of 5σ between data at the center of the tolerance and the non-acceptable condition equates to a confidence level of over 99.9%, and the factor of 10 is convenient for quality inspection personnel.

In the case of the CdTe photovoltaic devices produced at CSU, there is not a clearly defined upper and lower limit for the process variables, as the goal is to test various

configurations rather than provide constant output. However, for this research, the goal was to validate SE as having the potential to be effective for studying the samples as an experimental technique. If the uncertainty in a layer thickness value included zero, one can argue that the technique cannot exclude the possibility the layer does not exist, and thus does not provide useful data for that layer. The unacceptable condition was therefore selected to be a state in which SE could not determine with a high degree of certainty that a value was nonzero. Thus, according to this line of reasoning, for those distributions where P is greater than 0.05 and the standard deviation-to-average ratio is 10% or less, the study shows that SE appears to provide meaningful data for that parameter with over 99.9% certainty. In the case of the uppermost bulk layer, the standard deviation to average ratios were typically 1% or less, suggesting SE may have potential as a measurement technique for maintaining thickness values within a tolerance band defined within 10% of the expected value.

4.2. Applicability of SE Data to Device Quality.

An important objective of this study is to examine not only capability, but the general applicability of SE to CdTe devices as a whole. While SE appears to be effective in this role, SE must be capable of helping to solve practical issues to justify further research.

Device efficiency is crucial to CdTe PV device manufacturing quality, as well as the future of the industry. While efficiency of CdTe devices is not as well understood as it could be, several factors are known to be important to efficiency. In general, SE directly measures optical properties only; however, as explained mathematically through the oscillators, the optical properties are the result of interaction between photons, electrons, and the material structure. Thus changes in the physical structure of the material and its electrical properties may be

detected by SE. In both this study and outside work, SE has been shown to detect a number of properties known to have a relationship to PV device performance.

Device layer thicknesses are important for several reasons. If the CdTe layer is too thin, photons may pass through it before being absorbed, resulting in the energy being lost. If the conductive layers are too thin, resistivity will increase and energy will be lost to heat. If the CdS layer is too thin, a nanoscale short circuit, or shunt, can occur. On the other hand, if the layers are too thick, it increases the likelihood that charge carriers are absorbed and the energy lost. This study has demonstrated that SE can detect CdTe device film thickness in a way that is statistically meaningful, and sufficiently precise and accurate to be useful.

Absorptivity determines whether photons transfer energy to charge carriers. SE detects absorptivity directly by two means: by measuring reflection and transmission, and by measuring the extinction coefficient and thickness of the material. The extinction coefficient determines what portion of the photon energy is absorbed, and just as importantly, where in the device that absorption occurs. CdTe forms a p-n (positive-negative) junction with CdS which acts as a virtual p-i-n (positive-intrinsic-negative) junction. Electrically, it is preferable for as many photons as possible to be captured in the intermediate “i” region of the bulk CdTe layer.

Conductivity, as mentioned above, is required to allow charge to leave the cell without loss of energy to heat. SE has been shown to detect peaks in the Ψ and Δ curves in the wavelengths near 1500 nm, where charge carriers are moved by light in conductive materials. If the material conductivity changes, it is therefore likely SE can detect it. SE was shown to detect conductivity of internal layers, which also can be important to performance by reducing thermal loss and improving the current-voltage curve, which is known to effect efficiency.

Crystal structure and defects often determine the fate of individual charge carriers. In CdTe devices, studies have suggested that grain boundaries play a key role in recombination. SE has been shown to detect changes in crystallinity. Changes in grain structure affect crystallinity in several ways. One effect is that the preferential arrangement of the crystals can be altered, which can be detected by XRD. SE has been shown to detect changes in both void fraction and the diffraction coefficient, both of which can be affected by grain structure. The refraction index profile can also reveal information about the crystallinity of the material, and how well a polycrystalline or semi-amorphous CdTe sample mimics the properties of monocrystalline CdTe. Because the major disadvantage of CdTe from an electronic standpoint is the extremely short charge carrier life compared to monocrystalline Si, it is critical to minimize opportunity for recombination. Research [78, 79] suggests grain boundaries are a major source of recombination in CdTe. Crystallinity changes have been correlated to changes in grain structure due to grain growth and loss of preferred orientation. This is characteristic of annealing, which may be the result of exposing devices to high temperatures during chemical treatment. Unfortunately, surface roughness may throw off the appearance of crystallinity, but chemical etchant may reduce this effect. SE thus appears to have potential as a crystallinity monitoring tool, giving input related to both process conditions and performance.

Band gap determines which photons are absorbed by the material, and what portion of the energy of higher-energy photons can be absorbed, so it has a direct bearing on performance. A band gap shift between the Cl-treated and Cu-treated data was seen in n and k value plots and was also visible in the raw Ψ and Δ data. While visual inspection cannot give better resolution than the resolution of the data, numeric analysis methods such as the Tauc plot method appear to have a potential for measuring band gap to a higher accuracy. Device stability increases the life

expectancy of the product, increasing the value of CdTe PV devices to the customer, consumer, and the environment. Device stability is less well understood than efficiency, but it is believed that crystallinity and microstructure play key roles. It is also believed that polycrystalline devices that behave more like crystalline CdTe have greater stability. The basic optical properties of crystalline CdTe are well documented; by comparing SE values to known properties of crystalline CdTe, it may be possible to gain some sense of the stability of the sample.

CdTe PV devices typically lose efficiency away from the center of the device, reducing the efficiency of larger devices. By tracking device quality at multiple locations, it is hoped that process controls can be implemented to improve overall device uniformity. Because SE measures a relatively small region, and that location can be precisely controlled, and readings can be taken in a short amount of time, SE is well suited for examination of uniformity across devices. This study appears to support the hypothesis that thickness and nonuniformity vary significantly with location across most devices, and SE has the potential to detect many properties believed to be associated with changes in efficiency. The root cause of this efficiency loss was not found by this study, but it seems reasonable to hope that future research may correct this.

Summary and Conclusions

5.1. Scientific Incentive.

One of the greatest challenges facing humanity in the early twenty-first century is supplying humanity's energy demand. At the time this is being written, fossil fuels such as oil, coal, and natural gas supply the bulk of human energy use, and will likely continue to do so for many years. However, the supply of these fuels is finite and their use produces carbon dioxide in quantities in the billions of metric tons worldwide. Though this gas is harmless in small quantities, it has been linked to climate change in the fossil record at levels comparable to current levels. While traditional alternate energy technologies such as nuclear and hydroelectric power offer many advantages, major challenges limit the practical possibility of scaling these technologies to replace fossil fuel use. Fortunately, the last few decades have seen significant advances in many areas, but more improvements will be required for a feasible solution. One of the recent developments has been Cadmium Telluride (CdTe)-based thin film photovoltaics, which offer several advantages over traditional silicon wafer-based technologies. However, the achieved efficiencies of CdTe devices are much lower than theoretical values calculated from its bandgap, suggesting room for improvement.

Spectroscopic Ellipsometry (SE) is a research technique which analyzes changes in polarization of light reflected or transmitted by a surface. A mathematical model of the surface is then compared to data and optimized to produce a result. SE is particularly useful in examining thin films, and is capable of measuring properties such as film thickness, number of layers, index of refraction, and extinction coefficient while doing no more damage to the film than exposure to full sunlight. SE is currently used as an industry-standard quality control tool in

the silicon oxide-coated silicon wafer industry. SE has also been used to study CdTe materials as a qualitative basic research tool. CdTe materials are significantly more complex than most monocrystalline semiconductors, and consequentially are less well understood. For this reason, generally accepted models capable of converging to a solution automatically have not been developed.

5.2. Summary of Work.

Samples of devices from 5 steps within the CSU laboratory CdTe device production process were sent to J.A. Woollam for preliminary SE analysis. The results were analyzed by J.A. Woollam engineers, and further analysis was conducted at CSU. Using the models developed in the Woollam Study as a starting point, the Woollam Study was duplicated at CSU using a new set of six samples. A new set of Baseline Study models, with MSE values comparable to the Woollam Study, were produced. Using the samples and models from the Baseline Study, an automated fit was performed for each of several (7) angles to demonstrate the ability of the models to optimize with data from just one angle. The Multiple Angle Study was repeated at multiple locations on each sample to examine the effect of location and demonstrate the flexibility of the SE models generated in the Baseline Study. The Multiple Angle Study was then repeated with a different ellipsometer for 2"x2" samples taken from a 16"x16" panel to further demonstrate the capabilities of SE. All data was subject to basic statistical analysis and comparison to SEM values to provide an initial evaluation of SE as a quantitative quality measurement process.

5.3. Key Findings.

TEC-15 was a fairly well-known substrate material prior to this research; however, data from this project uncovered a number of facts of interest. This material was known to consist of

two layers of tin oxides (SnO_2 and SnO_xF , known commercially as FTO) on a glass substrate separated by a layer of SiO_2 , with the thicker surface layer doped with fluorine. While the ellipsometric properties of SiO_2 , both in amorphous glass form and as a crystalline thin film, are very well understood, FTO is not. Both the Woollam and Baseline Study models use a surface roughness layer with properties that vary from the bulk layer as opposed to a pure intermix of bulk and void, and a gradient of optical properties within the bulk. This is believed to be due to a variation in the doping level with depth within the layer. In addition, a shift in properties was noted at approximately 1500 nm which appears to be consistent with an energy band within which FTO acts as a metal rather than an oxide in regard to photons and electrons. Models had also consistently showed the insulating SiO_2 layer was thinner than expected. SEM images indicated that this was physically correct and not the result of modeling approximations as previously hypothesized.

Both the Woollam and Baseline Study models produced a tight fit for CdS with relatively little manual adjustment between the models, suggesting that the model represented a very accurate approximation of the optical properties of CdS. On the other hand, CdTe, which has a combination of high opacity and low reflectivity, proved much more difficult to model. While the Woollam and Baseline Study models used the same basic structure and oscillators, the n and k profiles were substantially different and the waveform match was less tight, indicating room for improvement in the understanding of the optical properties. However, as demonstrated by confirmation with SEM, SE is nonetheless able to make accurate measurement of the layer thickness, even in cases where the layer is too thick to measure the thicknesses of the underlying layers. Measurement of layers indicated an asymmetrical thickness profile rather than the hypothesized lenticular shape. This suggests a significant asymmetry was present in the

deposition system for the batch the samples were taken from. Treated devices showed n and k curves more characteristic of crystalline materials. Although this is likely partially due to reduction in surface area affects, SE and XRD data also indicated changes in other properties that are consistent with crystallinity changes. Specifically, Cu appears to have a stabilizing effect that affects lattice size. The changes to lattice structure show up in SE as a band gap shift.

SE demonstrated results consistent with the hypothesis that SE has the potential to be a viable quality measurement tool for production of CdTe-based photovoltaic devices. In the majority of cases, the data was within the 95% normality test confidence levels, with standard deviations within 10% of the total values, and with stack thicknesses within 10% of the SEM values, and in many cases, the uppermost bulk layer was measured with accuracy and precision within 1%, which is sufficient to allow SE to provide quantitative quality testing for use as a process control measurement tool. SE was able to detect various properties that are known to be relevant to device quality. By measuring thicknesses at various points on the same sample, SE can detect variations in deposition process consistency. SE was able to detect several properties that are known to be relevant to device efficiency, including layer thickness, index of refraction, extinction coefficient, reflectivity, transmissivity, band gap, and indirectly appeared to detect changes in additional properties such as grain structure and conductivity. It is believed that devices with more monocrystalline-like properties are not only more efficient, but also more stable.

5.4. Specific Contributions to the Body of Knowledge.

SE is a nonintrusive technique that can detect many useful properties without interfering with production. This study has demonstrated the statistical capability of SE in regard to film thickness, and other research suggests SE may also have the potential to accurately measure

other properties, thus providing a combination of information not available with other nondestructive techniques. To the best knowledge of the author, a study of this type, assessing the potential of SE for use as a quality measurement tool, had not been performed prior to this work. The study suggests that SE has excellent potential in this area. While further research will be needed to make this a reality, the study moves SE from a pure research technique in the CdTe field to one for which there exists some evidence of viability for process control. This study provides preliminary data suggesting SE has strong potential as a prospective quantitative quality measurement and process control measurement tool. The study also provides confidence for CSU for developing a permanent CdTe SE program should the university choose to do so.

Bibliography

- [1]. Smalley, Richard. 2003. Humanity's Top 10 Problems. University Professor Lecture Series. <http://cnst.rice.edu/content.aspx?id=246>
- [2]. Lewis, Nathan S. Powering the Planet (PowerPoint presentation). California Institute of Technology. http://nsl.caltech.edu/_media/energy:energy6.pdf
- [3]. U.S. Energy Information Administration. 2011. International Energy Outlook 2011. September 19, 2011. <http://www.eia.gov/forecasts/ieo/>
- [4]. Photovoltaic Summit 2008: Dr. PV, Mr. PV and the Terawatt Dilemma. *Energy Stocks*. <http://www.energystocksblog.com/2008/06/21/photovoltaic-summit-2008-dr-pv-mr-pv-and-the-terrawatt-dilemma/>
- [5]. Williams, Jeremy. How much oil is there left, really? makewealthhistory.org.
<http://makewealthhistory.org/2010/06/11/how-much-oil-is-there-left-really/>
- [6]. Global Carbon Emissions. CO2Now.org. <http://co2now.org/Current-CO2/CO2-Now/global-carbon-emissions.html>
- [7]. Joyce, Shawn Dell. 2009. No Such Thing As Clean Coal. Sustainable Living. Creators.com. <http://www.creators.com/lifestylefeatures/green-living/sustainable-living/no-such-thing-as-clean-coal.html>
- [8]. Centers for Disease Control and Prevention. Documentation for Immediately Dangerous To Life or Health Concentrations (IDLHs). NIOSH Publications and Products. <http://www.cdc.gov/niosh/idlh/124389.html>
- [9]. Korotayev, A., Malkov, A., and Khaltourina, D. 2006. Introduction to Social Macrodynamics: Compact Macromodels of the World System Growth. Editorial URSS, Moscow.

- [10]. Questions Executives and Board Members Should Be Asking Themselves.
Treehugger.com. http://www.treehugger.com/files/2007/03/questions_execu_1.php
- [11]. Lewis, Nathan S. 2003. R&D Challenges in the Chemical Sciences to Enable
Widespread Utilization of Renewable Energy. *Energy and Transportation: Challenges
for the Chemical Sciences in the 21st Century*. The National Academic Press.
- [12]. Iwata, So, and Barber, James. 2004. Biomass Derived Energy. *Curr. Opin. Struc. Biol.*
14: 447-453.
- [13]. Proefrock, Philip. 2008. Solar Produces 1000x More Energy Per Acre than Soy
BioDiesel. *EcoGeek*, March 18, 2008.
- [14]. Solar Cell Breaks the 40% Efficiency Barrier. *Renewable Energy World*, December 7,
2006.
- [15]. U.S. Energy Information Administration. Updated Capital Cost Estimates for Electricity
Generation Plants. *U.S. Energy Information Administration*, November 2010.
http://www.eia.gov/oiaf/beck_plantcosts/
- [16]. Fretwell, Sammy. 2012. Green groups oppose shipping hot waste to SRS. *World News*,
7 September 2012.
- [17]. Hoium, Travis. 2012. Solar Costs Continue to Plummet. *Daily Finance*, June 26, 2012.
- [18]. The History Of Solar Power. *Top Alternative Energy Sources.com*. [http://www.top-
alternative-energy-sources.com/history-of-solar-power.html](http://www.top-alternative-energy-sources.com/history-of-solar-power.html)
- [19]. Anthony, David, and Zheng, Tao. What If Every Residential Home in the United States
Had a Solar Roof? *Helix Recruiting*. [http://helixrecruiting.com/helix-recruiting-solar-
david-anthony](http://helixrecruiting.com/helix-recruiting-solar-david-anthony)

- [20]. Solar Price Falls to New Record Low, Industrial now below 20 cents per kWh.
Renewable Energy World, September 6, 2009.
- [21]. Lindseth, Annie. 2010. Do Solar Panels Produce More Energy Than What Goes Into Making Them? *Get Solar*, October 26, 2010.
- [22]. Brown, Nicholas. 2012. First Solar Sets 14.4% World Record for CdTe Solar Panel Efficiency. *Clean Technica*, January 17, 2012.
- [23]. Wu, Xuanzhi. 2004. High-efficiency Polycrystalline CdTe thin-film solar cells. *Solar Energy* 77 no. 6: 803-814.
- [24]. Shockley, William, and Queisser, Hans J. 1961. Detailed Balance Limit of Efficiency of p-n Junction Solar Cells. *J. Appl. Phys.* 32: 510.
- [25]. Lifton, Jack. 2008. Materials for Solar Photovoltaic Cells II: Tellurium, Not So Rare After All. *Resource Investor*, March 2008,
- [26]. Zweibel, Ken, and Fthenakis, Vasilis. Cadmium Facts and Handy Comparisons.
National Renewable Energy Laboratory. http://www.nrel.gov/pv/cdte_factsheet.pdf
- [27]. Department of Mechanical Engineering, Colorado State University. Materials Engineering Laboratory: Mass Production of Photovoltaic (PV) Modules.
<http://www.engr.colostate.edu/me/facil/mel/>
- [28]. Spottiswoode, William. 1874. *Polarisation of Light*. Macmillan and Co., London.
- [29]. Hall, A.C. 1969. A Century of Ellipsometry. *Surface Science* 16: 1-13.
- [30]. J.A. Woollam Co., Inc. 2007. Tour of Woollam facility, September 2007.
- [31]. J.A. Woollam Co., Inc. *Ellipsometry FAQ*. <http://www.jawoollam.com/faq.html>

- [32]. Wolski, A. Waves on Boundaries. PHYS 370 Advanced Electromagnetism, University of Liverpool, Part 4.
http://pcwww.liv.ac.uk/~awolski/main_teaching_Liverpool_PHYS370.htm
- [33]. The Physics Classroom. Total Internal Reflection. Physics Tutorial, Refraction and Ray Model of Light, Lesson 3. <http://www.physicsclassroom.com/class/refrn/u14l3b.cfm>
- [34]. J.A. Woollam Co., Inc. Light & Materials-Part II: Interaction of Light and Materials. Resources: Tutorial. J.A. Woollam Co., Inc. http://www.jawoollam.com/tutorial_3.html
- [35]. *Guide to Using WVASE 32*, J.A. Woollam Co., Inc., Lincoln NE.
- [36]. J.A. Woollam Co., Inc. 2007. 2007 Advanced Short Course (Series of PowerPoint presentations). September 2007.
- [37]. Nelson, Stephen A. Properties of Light and Examination of Isotropic Substances. EENS 2110 Mineralogy, Tulane University.
<http://www.tulane.edu/~sanelson/eens211/proplight.htm>
- [38]. Hyperphysics. Quarter-Wave Plate. <http://hyperphysics.phy-astr.gsu.edu/hbase/phyopt/quarwv.html>
- [39]. Ellipsometry. The University of Texas at Arlington, 2002.
<http://www.uta.edu/optics/research/ellipsometry/ellipsometry.htm>
- [40]. Fresnel's Equations for Reflection and Refraction. Uppsala University.
www.teknik.uu.se/ftf/education/ftf2/Optics_FresnelsEqns.pdf
- [41]. J.A. Woollam Co., Inc. Dielectric Function. Resources: Tutorial. J.A. Woollam Co., Inc. http://www.jawoollam.com/dielectric_function.html.
- [42]. Hilfiker, James. 2010. Phone interview by author, June 18.

- [43]. Kohli, Sandeep, Manivannan, Venkatesan, Hilfiker, James N., McCurdy, Patrick R., Enzenroth, Robert A., Barth, Kurt L., Smith, Westcott P., Luebs, Richard, and Sampath, Walajabad S. 2009. Effect of Chemical Treatment on the Optical Properties of a Cadmium Telluride Photovoltaic Device Investigated by Spectroscopic Ellipsometry. *Journal of Solar Energy Engineering* 131 2.
- [44]. Manivannan, Venkatesan. 2010. Presentation to I-UCRC, Fort Collins, Colorado, (Powerpoint presentation), June 18.
- [45]. Levi, D., Wu, X., Swartzlander-Guest, A., Hansoon, F., and Matson, R. 2000. Characterization of layer thickness and interdiffusion in CdTe/CdS/ZTO/CTO solar cells. *Conference Record of the Twenty-Eighth IEEE Photovoltaic Specialists Conference*, p. 525.
- [46]. Wehner, J.G.A., Sewell, R.H., Musca, C.A., Dell, J.M., and Faraone, I. 2007. Optical and Structural Properties of CdTe Grown by Molecular Beam Epitaxy at Low Temperature for Resonant-Cavity-Enhanced HgCdTe Detectors. *Journal of Electronic Materials* 36 8: 877-883.
- [47]. Chandra, Sharat, Sundari, S. Tripura, Raghavan, G., and Tyagi, A.K. 2003. Optical Properties of CdTe Nanoparticle Thin Films Studied by Spectroscopic Ellipsometry. *Journal of Physics D* 36 17: 2121-2129.
- [48]. John R. Taylor. 1982. *An Introduction to Error Analysis: The Study of Uncertainties in Physical Measurements*. University Science Books, Mill Valley, CA.
- [49]. Toma, O., Pascu, R., Dinescu, M., Besleaga, C., Mitran, T.L., Scarisoreanu, N., and Antohe, S. 2011. Growth and Characterization of Nanocrystalline CdS Thin Films. *Chalcogenide Letters* 8 no. 9: 541-548.

- [50]. Badano, Giacomo, Baudry, Xavier, and Robin, Ivan C. 2009. In-situ spectroscopic ellipsometry of rough surfaces: Application to CdTe(211)B/Ge(211) grown by molecular-beam epitaxy. *Journal of Electronic Materials* 38 8: 1652-1660.
- [51]. Karmakov, I.E., and Konova, A.A. 2009. Determination of compositional profiles and thicknesses of the etched surface of CdTe and Cd_{0.9}Zn_{0.1}Te by spectroscopic ellipsometry. *2008 IEEE Nuclear Science Symposium and Medical Imaging Conference* 1-9: 5150-5154.
- [52]. Rottkay, K.V., and Rubin, M. 1996. Optical Indices of Pyrolytic Tin-Oxide Glass. *Materials Research Society Symposium Proceedings* 1996, p. 449.
- [53]. Tompkins, Harland A. 1993. *A User's Guide to Ellipsometry*. Academic Press, Inc.
- [54]. Aspnes, D.E. 1982. Optical Properties of Thin Films. *Thin Solid Films* 89: 249-262,
- [55]. Palik, E.D. 1984. Characterization of gold films by surface plasmon spectroscopy. *Journal of the Optical Society of America a-Optics Image Science and Vision* 1 1297.
- [56]. Wooten, F. 1972. *Optical Properties of Solids*. Academic Press, NY.
- [57]. Jellison, G.E., and Modine, F.A. 1996. Parameterization of the optical functions of amorphous materials in the interband region. *Applied Physics Letters* 69: 371.
- [58]. Tiwald, Thomas E., Thompson, Daniel W., Wollam, John A., Paulson, Wayne, and Hance, Robert. 1998. Application of IR variable angle spectroscopic ellipsometry to the determination of free carrier concentration depth profiles *Thin Solid Films* 313-314: 661-666.
- [59]. Dhere, R.G., Al-Jassim, M.M., Yam, Y., Jones, K.M., Moutinho, H.R., Gessert, T.A., Sheldon, P., and Kamerski, L.L. 2000. CdS/CdTe interface analysis by transmission electron microscopy. *Journal of Vacuum Sciences & Technology A* 18: 1604.

- [60]. Chen, Jie, Li, Jian, Sainju, D., Wells, K. D., Podraza, N. J., and Collins, R. W.
Multilayer Analysis of the CdTe Solar Cell Structure by Spectroscopic Ellipsometry.
*Conference Record of the 2006 IEEE 4th World Conference on Photovoltaic Energy
Conversion* 1: 475-478.
- [61]. Rousset, Jean, Olsson, Paer, McCandless, Brian, and Lincot, Daniel. 2008. Structure and
Optoelectronics of Electrodeposited Cadmium Telluride (CdTe₂). *Chemistry of
Materials* 20 20: 6550-6555,
- [62]. Paulson, P.D., and Mathew, Xavier. 2004. Spectroscopic Ellipsometry Investigation of
Optical and Interface Properties of CdTe Films Deposited on Metal Foils. *Solar Energy
Materials and Solar Cells* 82 1-2: 279-290.
- [63]. Choi, Youn-Ok, Kim, Nam-Hoon, Park, JuSun, and Lee, Woo-Sun. 2010. Influences of
thickness-uniformity and surface morphology on the electrical and optical properties of
sputtered CdTe thin films for large-area II-VI semiconductor heterostructured solar cells.
Materials Science and Engineering B 171 1-3: 73-78.
- [64]. Podesta, A., Armani, N., Salviati, G., Romeo, N., Bosio, A., and Prato, M. 2006.
Influence of the Fluorine Doping on the Optical Properties of US Thin Films for
Photovoltaic Applications. *Thin Solid Films* 511: 448-452.
- [65]. Stephens, M. A. 1974. EDF Statistics for Goodness of Fit and Some Comparisons.
Journal of the American Statistical Association 69 no. 347: 730-737.
- [66]. Manivannan, Venkatesan, Enzeroth, Robert A., Barth, Kurt L., Kohli, Sandeep,
McCurdy, Patrick R., and Sampath, Walajabad S. 2008. Microstructural features of
cadmium telluride photovoltaic thin film devices. *Thin Solid Films* 516 6: 1209-1213.

- [67]. Cody, G.D. 1984. The Optical Absorption Edge of a-Si: H. *Semiconductors and Semimetals* 21, part B: 11-82.
- [68]. Lautenschlager, P., Garriga, M., Logothetidis, S., and Cardona, M. 1987. Interband critical points of GaAs and their temperature dependence. *Phys Rev B* 35: 9174-9189.
- [69]. Tauc, J., Grigorovici, R., and Vancu, A. 1966. Optical Properties and Electronic Structure of Amorphous Germanium. *Phys. Status Solidi B* 15: 627.
- [70]. 15-0770. International Centre for Diffraction Data, Newton Square, PA.
- [71]. 41-1445. Powder Diffraction File, International Centre for Diffraction Data, Newton Square, PA.
- [72]. 41-1049. Powder Diffraction File, International Centre for Diffraction Data, Newton Square, PA.
- [73]. Hilfiker, James. 2006. *M-200 Measurements of CdTe and CdS coated Tec-15*. Customer Document provided to W.S. Sampath, Colorado State University. J.A. Woollam, September 13.
- [74]. Kezsmarki, I., and Bordacs, S. 2008. An alternative of spectroscopic ellipsometry: The double reference method. *Applied Physics Letters*, volume 92, issue number 13, article number 131104.
- [75]. Badano, G., Million, A., Canava, B., Tran-Van, P., and Etchberry, A. 2007. Fast Detection of Precipitates and Oxides on CdZnTe Surfaces by Spectroscopic Ellipsometry. *Journal of Electronic Materials* 36 8: 1077-1084.
- [76]. Paulson, P.D., McCandless, B.E., and Birkmire, R.W. 2004. Optical Properties of Cd_{1-x}Zn_xTe films in a device structure using variable angle spectroscopic ellipsometry. *Journal of Applied Physics* 95 6: 3010-3019.

- [77]. Levy, Dean. 2008. NREL Ellipsometry and Silicon Wafer tour and Interview, April 2008.
- [78]. Fang, Zhou, Wang, Xiao Chen, Wu, Hong Cai, and Zhao, Ce Zhou. 2011. Achievements and Challenges of CdS/CdTe Solar Cells. *International Journal of Photoenergy*, volume 2011, article ID 297350.
- [79]. Kum, Maxwell C., Jung, Hyunsung, Chartuprayoon, Nicha, Chen, Wilfred, Mulchandani, Ashok, and Myung, Nosang V. 2012. Tuning Electrical and Optoelectronic Properties of Single Cadmium Telluride Nanoribbon. *The Journal of Physical Chemistry-C*. 116 16: 9202–9208.

Appendix 1

Additional Data

As stated in chapter 3, not all data collected was presented in the main body of this dissertation for the sake of brevity and readability. This appendix contains all values optimized for statistical purposes in the Multiple Angle Study, Multiple Position Study, and Industrial Device Study. Additional data from the studies of the 3"x3" samples is presented in tables A1.1 through A1.30; additional data from the panel study is presented in Tables A1.31 through A1.36. "Ave" is the average value from the various angles, "SD" is the standard deviation, "SD%" is the standard deviation divided by the average and expressed as a percentage, and "Corr" is the linear correlation between the modeled values and the angles. The P values calculated by the Anderson-Darling normality test are found in chapter 3. An asterisk (e.g., "Ave*") indicates that the value in question does not include the 75° data, due to a reflectance issue.

Table A1.1: Data for 3"x3" TEC-15 sample location C (center).

Angle	45°	50°	55°	60°	65°	70°	75°	Ave	SD	SD%	Corr
MSE	10.58	12.31	14.06	15.96	17.09	17.27	18.42	15.10	2.88	19.07	0.98
SnO ₂ thickness (Å)	230	231	231	233	232	233	235	232	1.7	0.75	0.95
SiO ₂ thickness (Å)	278	276	273	269	268	265	262	270	5.6	2.09	-1.00
FTO thickness (Å)	2981	2981	2982	2980	2978	2981	2984	2981	1.7	0.06	0.20
Surface roughness thickness (Å)	381	383	388	393	398	398	398	391	7.3	1.86	0.95
Surface roughness void (%)	57.7	57.5	57.6	57.6	57.6	57.6	57.8	57.6	0.09	0.15	0.30

Table A1. 2: Data for 3"x3" TEC-15 sample location O1.

Angle	45°	55°	65°	75°	Ave*	SD*	SD%*	Corr*
MSE	21.11	18.15	27.99	214.10	22.42	5.05	22.52	0.68
SnO2 thickness (Å)	239	233	244	277	239	5.3	2.24	0.50
SiO2 thickness (Å)	271	267	271	344	270	2.5	0.94	-0.13
FTO thickness (Å)	2991	2996	2968	2822	2985	14.9	0.50	-0.78
Surface roughness thickness (Å)	395	416	404	403	405	10.5	2.60	0.45
Surface roughness void (%)	64.7	65.5	63.2	60.1	64.5	1.13	1.76	-0.63

Table A1.3: Data for 3"x3" TEC-15 sample location O2.

Angle	45°	55°	65°	75°	Ave*	SD*	SD%*	Corr*
MSE	20.14	21.43	30.59	223.10	24.05	5.70	23.69	0.92
SnO2 thickness (Å)	228	223	235	274	229	6.0	2.63	0.58
SiO2 thickness (Å)	222	221	220	262	221	0.6	0.27	-0.97
FTO thickness (Å)	3108	3113	3083	2946	3101	15.9	0.51	-0.78
Surface roughness thickness (Å)	389	409	418	430	405	15.0	3.69	0.98
Surface roughness void (%)	50.5	51.8	51.4	50.0	51.2	51.2	1.29	0.68

Table A1.4: Data for 3"x3" TEC-15 sample location O3.

Angle	45°	55°	65°	75°	Ave*	SD*	SD%*	Corr*
MSE	15.21	14.80	25.97	180.20	18.66	6.33	33.94	0.85
SnO2 thickness (Å)	323	318	326	332	322	4.1	1.28	0.26
SiO2 thickness (Å)	268	254	267	382	263	7.8	2.96	-0.06
FTO thickness (Å)	3139	3164	3131	2944	3145	17.4	0.55	-0.21
Surface roughness thickness (Å)	589	616	615	418	607	15.2	2.50	0.83
Surface roughness void (%)	42.0	44.2	43.6	59.6	43.3	1.14	2.63	0.70

Table A1.5: Data for 3"x3" TEC-15 sample location O4.

Angle	45°	55°	65°	75°	Ave*	SD*	SD%*	Corr*
MSE	18.76	18.26	29.43	190.50	22.15	6.31	28.49	0.85
SnO2 thickness (Å)	295	289	299	299	294	4.9	1.67	0.40
SiO2 thickness (Å)	256	242	255	377	251	8.1	3.23	-0.05
FTO thickness (Å)	3194	3221	3184	2984	3199	19.1	0.60	-0.27
Surface roughness thickness (Å)	626	656	652	641	645	16.0	2.48	0.81
Surface roughness void (%)	44.3	46.5	45.6	43.2	45.4	1.10	2.42	0.59

Table A1.6: Data for 3"x3" CdS sample location C (center).

Angle	45°	50°	55°	60°	65°	70°	75°	Ave	SD	SD%	Corr
MSE	19.35	12.63	9.473	11.6	13.35	17	20.97	14.91	4.26	28.58	0.32
SnO2 thickness (Å)	228	235	238	237	232	232	231	234	3.4	1.48	-0.05
SiO2 thickness (Å)	243	234	231	235	244	247	253	241	7.7	3.20	0.68
FTO thickness (Å)	3243	3231	3228	3232	3240	3243	3245	3237	6.9	0.21	0.46
CdS thickness (Å)	2002	2001	2000	1999	1997	1996	1993	1998	3.1	0.16	-0.97
Surface roughness thickness (Å)	171	171	171	173	174	176	178	173	2.7	1.58	0.96
Surface roughness void (%)	33.5	33.6	33.5	33.3	32.9	32.5	31.7	33.00	0.68	2.06	-0.92

Table A1.7: Data for 3"x3" CdS sample location 01.

Angle	45°	55°	65°	75°	Ave*	SD*	SD%*	Corr*
MSE	19.87	18.49	38.00	174.90	25.45	10.89	42.77	0.83
SnO2 thickness (Å)	253	261	263	261	259	5.3	2.03	0.97
SiO2 thickness (Å)	271	265	268	306	268	3.0	1.11	-0.43
FTO thickness (Å)	2941	2929	2926	2926	2932	8.1	0.28	-0.94
CdS thickness (Å)	1974	1968	1948	1885	1963	13.9	0.71	-0.95
Surface roughness thickness (Å)	251	260	268	387	266	19.4	7.29	0.95
Surface roughness void (%)	16.1	16.2	15.9	16.3	16.1	0.14	0.87	-0.51

Table A1.8: Data for 3"x3" CdS sample location O2.

Angle	45°	55°	65°	75°	Ave*	SD*	SD%*	Corr*
MSE	26.32	28.26	51.57	216.70	35.38	14.05	39.71	0.90
SnO2 thickness (Å)	213	224	226	247	221	7.3	3.28	0.93
SiO2 thickness (Å)	279	282	284	311	282	2.5	0.88	1.00
FTO thickness (Å)	3066	3040	3040	2982	3048	15.0	0.49	-0.86
CdS thickness (Å)	1867	1857	1833	176	1853	17.3	0.94	-0.98
Surface roughness thickness (Å)	175	185	212	301	191	18.9	9.91	0.97
Surface roughness void (%)	34.2	32.8	29.6	24.2	32.2	2.33	7.25	-0.98

Table A1.9: Data for 3"x3" CdS sample location O3.

Angle	45°	55°	65°	75°	Ave*	SD*	SD%*	Corr*
MSE	29.11	33.31	47.48	177.20	36.63	9.63	26.27	0.95
SnO2 thickness (Å)	267	252	254	282	258	8.4	3.28	-0.79
SiO2 thickness (Å)	246	276	285	286	269	20.5	7.60	0.95
FTO thickness (Å)	2941	2953	2959	2938	2951	8.7	0.30	0.98
CdS thickness (Å)	1985	1978	1954	1870	1972	16.3	0.83	-0.96
Surface roughness thickness (Å)	179	189	218	330	195	20.4	10.46	0.96
Surface roughness void (%)	21.5	21.1	19.8	17.0	20.8	0.89	4.29	-0.96

Table A1.10: Data for 3"x3" CdS sample location O4.

Angle	45°	55°	65°	75°	Ave*	SD*	SD%*	Corr*
MSE	30.88	32.87	59.31	235.70	41.02	15.87	38.69	0.90
SnO2 thickness (Å)	155	161	163	199	160	4.3	2.68	0.95
SiO2 thickness (Å)	335	338	346	389	340	5.6	1.64	0.96
FTO thickness (Å)	3060	3041	3034	2886	3045	13.4	0.44	-0.97
CdS thickness (Å)	1739	1729	1698	1602	1722	21.2	1.23	-0.96
Surface roughness thickness (Å)	147	158	191	308	165	22.8	13.79	0.96
Surface roughness void (%)	29.3	27.8	24.1	18.9	27.1	2.67	9.84	-0.97

Table A1.11: Data for 3"x3" CdTe sample location C (center).

Angle	45°	50°	55°	60°	65°	70°	75°	Ave	SD	SD%	Corr
MSE	30.15	29.94	27.91	25.21	26.83	31.78	42.95	30.68	5.85	19.05	0.54
CdTe thickness (Å)	29925	29940	29952	29963	29949	29983	29933	29949	19.5	0.06	0.42
Surface roughness thickness (Å)	492	492	492	492	492	492	492	492	0.3	0.07	0.00
Surface roughness void (%)	24.9	24.9	24.9	24.9	24.8	24.8	24.8	24.8	0.04	0.17	-0.84

Table A1.12: Data for 3"x3" CdTe sample location O1.

Angle	45°	55°	65°	75°	Ave	SD	SD%	Corr
MSE	55.64	43.65	32.60	50.56	45.61	9.97	21.86	-0.34
CdTe thickness (Å)	20273	20331	20330	20281	20304	31.3	0.15	0.10
Surface roughness thickness (Å)	525	522	517	511	518	6.1	1.17	-0.99
Surface roughness void (%)	25.0	25.2	25.3	25.3	25.2	0.14	0.56	0.97
Total stack thickness variation (%)	10.5	9.5	9.2	9.2	9.6	0.61	6.30	-0.88

Table A1.13: Data for 3"x3" CdTe sample location O2.

Angle	45°	55°	65°	75°	Ave	SD	SD%	Corr
MSE	94.73	77.41	75.99	94.54	85.60	10.44	12.20	-0.02
CdTe thickness (Å)	22725	22647	22529	22528	22607	96.5	0.43	-0.95
Surface roughness thickness (Å)	523	522	525	524	524	1.2	0.23	0.61
Surface roughness void (%)	27.5	27.9	28.2	28.3	28.0	0.37	1.31	0.96
Total stack thickness variation (%)	6.6	5.7	5.1	5.7	5.8	0.60	10.41	-0.70

Table A1.14: Data for 3"x3" CdTe sample location O3.

Angle	45°	55°	65°	75°	Ave	SD	SD%	Corr
MSE	105.00	82.87	68.84	74.97	82.92	15.80	19.06	-0.85
CdTe thickness (Å)	26462	26354	26187	26077	26077	171.6	0.65	-1.00
Surface roughness thickness (Å)	489	486	490	492	489	2.5	0.51	0.70
Surface roughness void (%)	25.1	25.0	25.1	25.1	25.1	0.07	0.26	0.22
Total stack thickness variation (%)	4.4	4.1	3.0	4.2	3.9	0.65	16.56	-0.38

Table A1.15: Data for 3"x3" CdTe sample location O4.

Angle	45°	55°	65°	75°	Ave	SD	SD%	Corr
MSE	118.70	94.63	85.63	132.10	107.77	21.40	19.86	0.19
CdTe thickness (Å)	26794	26699	26547	26503	26636	135.2	0.51	-0.98
Surface roughness thickness (Å)	482	482	487	490	485	3.8	0.78	0.95
Surface roughness void (%)	26.0	25.8	25.9	25.9	25.9	0.06	0.24	-0.33
Total stack thickness variation (%)	3.9	2.4	0.0	0.0	1.6	1.91	121.4 1	-0.95

Table A1.16: Data for 3"x3" Cl-treated sample location C (center).

Angle	45°	50°	55°	60°	65°	70°	75°	Ave	SD	SD%	Corr
MSE	30.48	33.58	31.21	30.32	32.51	32.99	41.24	33.19	3.76	11.34	0.66
SnO ₂ thickness (Å)	240	239	255	274	296	278	258	263	20.9	7.94	0.64
FTO thickness (Å)	3423	3344	3542	3606	3684	3690	3556	3549	128.6	3.62	0.74
CdS thickness (Å)	2102	2098	2025	2022	1999	2031	2082	2051	41.5	2.02	-0.41
CdTe thickness (Å)	21449	21445	21452	21463	21466	21467	21475	21460	11.0	0.05	0.95
Surface roughness thickness (Å)	400	400	398	396	396	395	395	397	2.1	0.52	-0.94
Surface roughness void (%)	22.0	21.9	21.8	21.8	21.7	21.6	21.6	21.8	0.14	0.64	-0.99
Total stack thickness variation (%)	2.8	2.0	2.6	2.7	2.9	2.7	2.0	2.5	0.38	14.79	-0.16

Table A1.17: Data for 3"x3" Cl-treated sample location O1.

Angle	45°	55°	65°	75°	Ave	SD	SD%	Corr
MSE	33.43	34.83	44.03	61.75	43.51	13.04	29.96	0.93
CdS thickness (Å)	1866	1862	1787	1573	1772	137.7	7.77	-0.89
CdTe thickness (Å)	17511	17524	17584	17719	17585	95.2	0.54	0.93
Surface roughness thickness (Å)	370	365	362	360	364	4.4	1.20	-0.98
Surface roughness void (%)	23.2	23.2	23.0	22.9	23.1	0.16	0.68	-0.99
Total stack thickness variation (%)	5.1	4.7	5.4	7.0	5.5	1.00	18.04	0.83

Table A1.18: Data for 3"x3" Cl-treated sample location O2.

Angle	45°	55°	65°	75°	Ave	SD	SD%	Corr
MSE	36.54	29.32	39.16	60.75	41.44	13.53	32.64	0.79
CdS thickness (Å)	2135	2112	2092	2097	2109	19.4	0.92	-0.90
CdTe thickness (Å)	17761	17796	17828	17820	17801	29.9	0.17	0.90
Surface roughness thickness (Å)	421	419	420	419	420	0.6	0.13	-0.71
Surface roughness void (%)	22.0	21.7	21.4	21.4	21.7	0.27	1.26	-0.94
Total stack thickness variation (%)	3.4	3.1	3.7	3.5	3.4	0.24	7.13	0.53

Table A1.19: Data for 3"x3" Cl-treated sample location O3.

Angle	45°	55°	65°	75°	Ave	SD	SD%	Corr
MSE	26.35	32.08	40.49	55.11	38.51	12.50	32.46	0.98
CdS thickness (Å)	2025	2036	2059	1903	2006	70.2	3.50	-0.64
CdTe thickness (Å)	19831	19850	19837	19893	19853	28.1	0.14	0.79
Surface roughness thickness (Å)	380	377	379	377	378	1.3	0.36	-0.66
Surface roughness void (%)	22.9	22.5	22.0	22.4	22.5	0.38	1.69	-0.71
Total stack thickness variation (%)	5.1	5.2	5.8	8.6	6.2	1.64	26.55	0.86

Table A1.20: Data for 3"x3" Cl-treated sample location O4.

Angle	45°	55°	65°	75°	Ave	SD	SD%	Corr
MSE	36.07	33.63	45.69	67.33	45.68	15.34	33.59	0.89
CdS thickness (Å)	2082	2071	2062	2024	2059	25.0	1.21	-0.94
CdTe thickness (Å)	21006	21039	21067	21103	21054	40.9	0.19	1.00
Surface roughness thickness (Å)	383.31	382.25	383.42	385.55	383.63	1.4	0.36	0.74
Surface roughness void (%)	26.5	26.2	26.0	25.8	26.2	0.30	1.14	-0.99
Total stack thickness variation (%)	3.7	3.1	3.2	3.8	3.5	0.37	10.74	0.18

Table A1.21: Data for 3"x3" Cu-treated sample location C (center).

Angle	45°	50°	55°	60°	65°	70°	75°	Ave	SD	SD%	Corr
MSE	32.01	29.20	26.68	26.03	27.65	35.39	39.90	30.98	5.12	16.53	0.56
SnO2 thickness (Å)	249	267	294	333	421	389	376	333	65.4	19.65	0.89
FTO thickness (Å)	3711	3592	3452	3339	3209	3085	3106	3356	241.2	7.19	-0.98
CdS thickness (Å)	2130	2135	2137	2142	2202	2225	2125	2157	39.9	1.85	0.45
CdTe thickness (Å)	8818	8802	8789	8779	8772	8765	8752	8782	22.4	0.25	-0.99
Surface roughness thickness (Å)	435	438	442	446	450	453	456	446	7.6	1.71	1.00
Surface roughness void (%)	21.9	21.8	21.7	21.7	21.7	21.7	21.8	21.8	0.05	0.22	-0.41
Total stack thickness variation (%)	4.2	4.9	5.3	5.1	4.7	4.0	2.9	4.5	0.82	18.38	-0.59

Table A1.22: Data for 3"x3" Cu-treated sample location O1.

Angle	45°	55°	65°	75°	Ave	SD	SD%	Corr
MSE	59.15	57.25	47.92	76.68	60.25	12.00	19.92	0.47
CdS thickness (Å)	2056	2192	2248	1800	2074	199.7	9.63	-0.46
CdTe thickness (Å)	8487	8328	8265	8648	8432	171.8	2.04	0.32
Surface roughness thickness (Å)	440	448	453	455	449	6.5	1.45	0.98
Surface roughness void (%)	21.2	21.1	21.2	21.5	21.2	0.15	0.71	0.69
Total stack thickness variation (%)	7.4	8.4	7.6	4.9	7.1	1.49	21.10	-0.72

Table A1.23: Data for 3"x3" Cu-treated sample location O2.

Angle	45°	55°	65°	75°	Ave	SD	SD%	Corr
MSE	32.69	32.25	31.74	56.53	38.30	12.16	31.74	0.75
CdS thickness (Å)	2099	2120	2189	2095	2126	43.6	2.05	0.17
CdTe thickness (Å)	7776	7742	7676	7732	7731	41.5	0.54	-0.61
Surface roughness thickness (Å)	419	426	432	439	429	7.9	1.85	1.00
Surface roughness void (%)	22.7	22.5	22.5	22.6	22.6	0.08	0.34	-0.13
Total stack thickness variation (%)	7.0	6.8	6.2	7.1	6.8	0.43	6.35	-0.06

Table A1.24: Data for 3"x3" Cu-treated sample location O3.

Angle	45°	55°	65°	75°	Ave	SD	SD%	Corr
MSE	53.01	40.83	40.36	74.34	52.14	15.92	30.53	0.52
CdS thickness (Å)	2411	2331	2399	2367	2377	35.9	1.51	-0.22
CdTe thickness (Å)	7035	7104	7048	7046	7058	31.3	0.44	-0.11
Surface roughness thickness (Å)	436	442	444	446	442	4.3	0.97	0.97
Surface roughness void (%)	20.0	20.1	20.3	20.7	20.3	0.31	1.51	0.94
Total stack thickness variation (%)	8.4	6.6	5.2	5.3	6.4	1.50	23.59	-0.92

Table A1.25: Data for 3"x3" Cu-treated sample location O4.

Angle	45°	55°	65°	75°	Ave	SD	SD%	Corr
MSE	45.94	48.25	44.76	77.59	54.14	15.70	29.01	0.75
CdS thickness (Å)	1892	1902	1962	1847	1901	47.6	2.50	-0.21
CdTe thickness (Å)	7104	7087	7010	7099	7075	43.7	0.62	-0.27
Surface roughness thickness (Å)	427	436	445	451	440	10.6	2.40	1.00
Surface roughness void (%)	17.2	16.9	16.8	16.8	16.9	0.18	1.09	-0.87
Total stack thickness variation (%)	2.9	3.0	2.7	2.5	2.8	0.23	8.35	-0.86

Table A1.26: Data for 3"x3" Br-treated sample location C (center).

Angle	45°	50°	55°	60°	65°	70°	75°	Ave	SD	SD %	Corr
MSE	39.67	40.58	45.84	34.47	31.41	32.22	32.22	36.63	5.48	14.97	-0.75
CdS thickness (Å)	2632	2614	2591	2574	2568	2555	2555	2584	29.9	1.16	-0.97
CdTe thickness (Å)	9591	9613	9619	9651	9648	9653	9653	9633	25.1	0.26	0.92
Surface roughness thickness (Å)	546	545	549	549	552	551	551	549	2.5	0.45	0.83
Surface roughness void (%)	19.1	18.9	18.7	18.4	18.2	18.0	18.0	18.5	0.44	2.38	-0.98
Total stack thickness variation (%)	6.6	6.6	6.7	6.5	6.4	6.7	6.7	6.6	0.11	1.62	0.04

Table A1.27: Data for 3"x3" Br-treated sample location O1.

Angle	45°	55°	65°	75°	Ave	SD	SD%	Corr
MSE	35.47	32.89	29.16	51.52	37.26	9.85	26.44	0.58
CdS thickness (Å)	2632	2614	2590	2574	2603	25.7	0.99	-1.00
CdTe thickness (Å)	9591	9612	9619	9651	9618	25.0	0.26	0.97
Surface roughness thickness (Å)	546	545	549	549	547	2.0	0.36	0.74
Surface roughness void (%)	19.1	18.9	18.7	18.4	18.8	0.29	1.55	-0.99
Total stack thickness variation (%)	6.6	6.6	6.7	6.5	6.6	0.08	1.15	-0.46

Table A1.28: Data for 3"x3" Br-treated sample location O2.

Angle	45°	55°	65°	75°	Ave	SD	SD%	Corr
MSE	42.75	44.27	34.29	48.81	42.53	6.07	14.26	0.17
CdS thickness (Å)	1009	1167	447	578	799.86	342.7	42.84	-0.76
CdTe thickness (Å)	12909	12766	1352 ₃	13367	13141	361.5	2.75	0.76
Surface roughness thickness (Å)	378	366	357	349	362.75	12.5	3.44	-1.00
Surface roughness void (%)	24.0	23.9	23.5	23.1	23.62	0.4	1.79	-0.98
Total stack thickness variation (%)	5.8	6.2	5.4	7.2	6.1	0.78	12.69	0.58

Table A1.29: Data for 3"x3" Br-treated sample location O3.

Angle	45°	55°	65°	75°	Ave*	SD*	SD%*	Corr*
MSE	44.01	49.26	44.46	75.81	45.91	2.91	6.34	0.77
CdS thickness (Å)	612	579	434	272	541.76	94.9	17.52	-0.97
CdTe thickness (Å)	14961	15027	15192	15357	15060	119.3	0.79	0.98
Surface roughness thickness (Å)	196	180	166	160	180.89	15.3	8.45	-0.98
Surface roughness void (%)	30.7	32.7	34.5	35.2	32.60	1.9	5.82	0.98
Total stack thickness variation (%)	3.0	2.5	2.9	3.2	2.8	0.28	9.86	0.35

Table A1.30: Data for 3"x3" Br-treated sample location O4.

Angle	45°	55°	65°	75°	Ave	SD	SD%	Corr
MSE	54.73	58.72	47.86	75.92	59.31	11.95	20.15	0.57
CdS thickness (Å)	1023	1056	1057	1009	1036	24.4	2.35	-0.22
CdTe thickness (Å)	16098	16074	16086	16121	16094	20.0	0.12	0.52
Surface roughness thickness (Å)	349	341	337	338	341	5.2	1.51	-0.87
Surface roughness void (%)	26.6	25.9	25.0	23.9	25.4	1.14	4.51	-0.99
Total stack thickness variation (%)	4.8	4.5	3.9	3.5	4.2	0.59	14.10	-0.99

Table A1.31: Data for 16"x16" panel location 9.

Angle	45°	55°	65°	75°	Ave	SD	SD%
MSE	13.93	19.28	23.93	31.89	22.26	7.61	34.2
CdS thickness (Å)	1823	1779	1628	1535	1691	133	7.89
CdTe thickness (Å)	23031	23133	23273	23392	23207	158	0.68
Surface roughness thickness (Å)	553	545	544	514	539	17	3.14
Surface roughness void (%)	23.9	23.1	21.4	23.5	23	1.1	4.79
Total stack thickness variation (%)	4.36	2.78	1.12	2.86	2.78	1.33	47.69

Table A1.32: Data for 16"x16" panel location 12.

Angle	45°	55°	65°	75°	Ave	SD	SD%
MSE	5.87	7.24	11.59	18.83	10.88	5.83	53.6
CdS thickness (Å)	1675	1660	1585	1683	1651	45	2.71
CdTe thickness (Å)	24152	24113	24191	24072	24132	51	0.21
Surface roughness thickness (Å)	499	512	532	566	527	29	5.51
Surface roughness void (%)	21.9	20.4	20.7	20.1	20.8	0.8	3.8
Total stack thickness variation (%)	2.38	1.91	2.46	3.72	2.62	0.78	29.64

Table A1.33: Data for 16"x16" panel location 21.

Angle	45°	55°	65°	75°	Ave	SD	SD%
MSE	8.27	9.27	16.57	18.92	13.26	5.29	39.88
CdS thickness (Å)	1751	1713	1670	1737	1718	35	2.06
CdTe thickness (Å)	21515	21518	21529	21417	21494	52	0.24
Surface roughness thickness (Å)	496	515	549	565	531	31	5.87
Surface roughness void (%)	20.2	18.6	17.8	19.1	19	1	5.26
Total stack thickness variation (%)	2.14	2.7	3.39	4.39	3.15	0.97	30.66

Table A1.34: Data for 16"x16" panel location 25.

Angle	45°	55°	65°	75°	Ave	SD	SD%
MSE	8.85	7.31	10.57	14.26	10.25	2.99	29.15
CdS thickness (Å)	1772	1757	1715	1724	1742	27	1.54
CdTe thickness (Å)	24833	24871	24895	24903	24876	31	0.13
Surface roughness thickness (Å)	536	515	547	564	541	20	3.76
Surface roughness void (%)	21.4	21.2	19.9	20.2	20.7	0.7	3.53
Total stack thickness variation (%)	2.44	2.27	2.58	3.75	2.76	0.67	24.35

Table A1.35: Data for 16"x16" panel location 30.

Angle	45°	55°	65°	75°	Ave	SD	SD%
MSE	8.76	8.53	11.98	16.63	11.48	3.78	32.94
CdS thickness (Å)	1821	1750	1725	1798	1773	44	2.47
CdTe thickness (Å)	23881	23947	23968	23900	23924	41	0.17
Surface roughness thickness (Å)	525	535	547	574	545	21	3.94
Surface roughness void (%)	20.6	19.5	19.6	19.4	19.8	0.6	2.83
Total stack thickness variation (%)	2.47	1.85	2.45	3.52	2.57	0.69	26.92

Table A1.36: Data for 16"x16" panel location 41.

Angle	45°	55°	65°	75°	Ave	SD	SD%
MSE	6.65	7.89	14.73	20.55	12.45	6.46	51.89
CdS thickness (Å)	1733	1717	1695	1753	1724	25	1.44
CdTe thickness (Å)	23702	23710	23736	23635	23696	43	0.18
Surface roughness thickness (Å)	524	514	538	553	532	17	3.19
Surface roughness void (%)	20.1	19.2	19	19.3	19.4	0.5	2.64
Total stack thickness variation (%)	2.47	2.55	3.29	3.94	3.06	0.69	22.57

Appendix 2

Additional Images

For the sake of brevity, a number of images were omitted from the main body of this dissertation and are presented here instead for curious readers.

A2.1. Photograph of the Deposition System.

The 3"x3" test samples used for this study were produced at a laboratory deposition system in the Engineering Research Center (ERC). In 2010, this system underwent major modifications to enable production of a wider variety of layer designs. The partially completed upgraded system is shown in Figure A2.1.

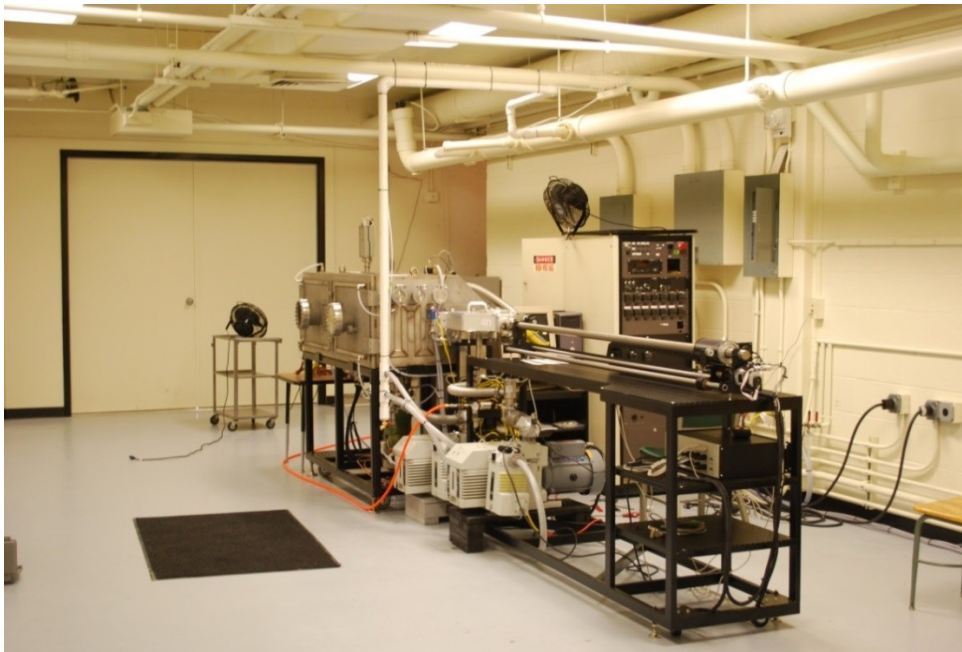


Figure A2.1: Engineering Research Center Solar Cell Manufacturing Facility Undergoing Renovation and Modifications in 2010 (photo by author).

A2.2. WVASE32 Screenshot Images.

WVASE32 software was used in all studies described in the main body of this dissertation. This software package is described in Section 1.5. Figures A2.2 through A2.8 provide a visual sense of the software for interested readers. Figure A2.2 shows the main user

interface. The user interface consists of main window and several sub-windows. Data exported from an ellipsometer can be displayed in the experimental data and graph windows, as shown in Figures A2.3 and A2.4. The Model window, shown in Figure A2.5, displays an overview of the layers in the current model being optimized. Selecting a layer allows you to examine the layer model in depth using a layer window. Figure A2.6 shows an example of a layer window for a “genosc”-type layer model; Figure A2.7 shows the layer window for an “EMA”-type layer model. Figure A2.8 shows an example of a popup window indicating that an analysis procedure is complete.

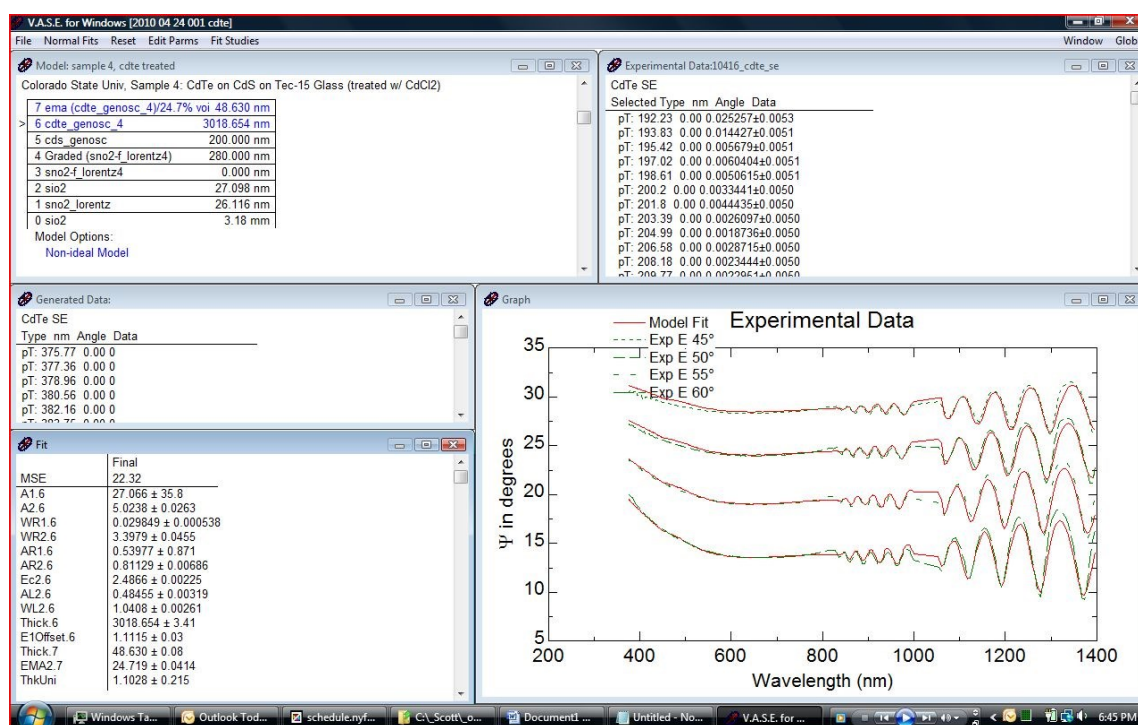


Figure A2.2: Screen Capture of WVASE32.

Experimental Data:10416_cdte_se			
CdTe SE			
Selected Type	nm	Angle	Data
pT:	192.23	0.00	0.025257±0.0053
pT:	193.83	0.00	0.014427±0.0051
pT:	195.42	0.00	0.005679±0.0051
pT:	197.02	0.00	0.0060404±0.0051
pT:	198.61	0.00	0.0050615±0.0051
pT:	200.2	0.00	0.0033441±0.0050
pT:	201.8	0.00	0.0044435±0.0050
pT:	203.39	0.00	0.0026097±0.0050
pT:	204.99	0.00	0.0018736±0.0050
pT:	206.58	0.00	0.0028715±0.0050
pT:	208.18	0.00	0.0023444±0.0050
pT:	209.77	0.00	0.0022951±0.0050

Figure A2.3: “Experimental Data” Window.

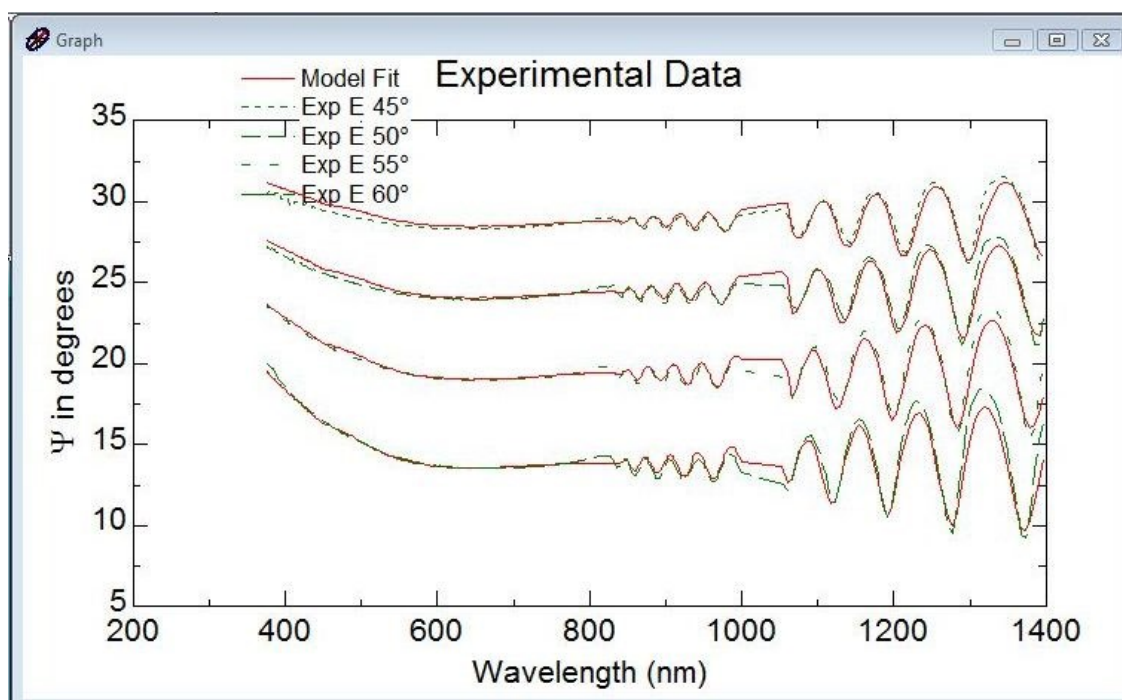


Figure A2.4: “Graph” Window.

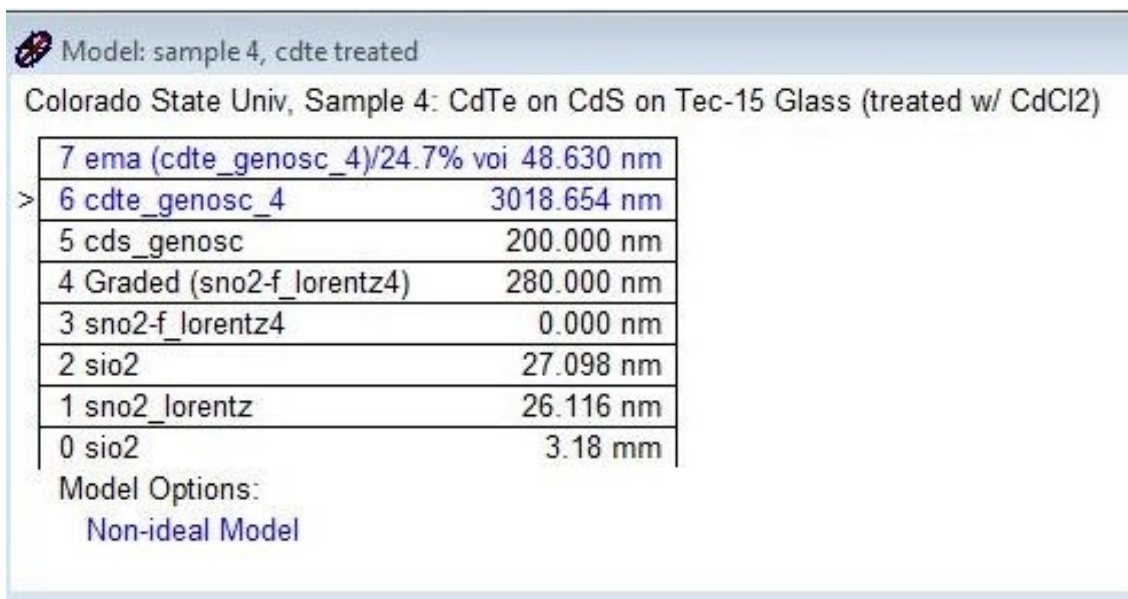


Figure A2.5: “Model” Window.

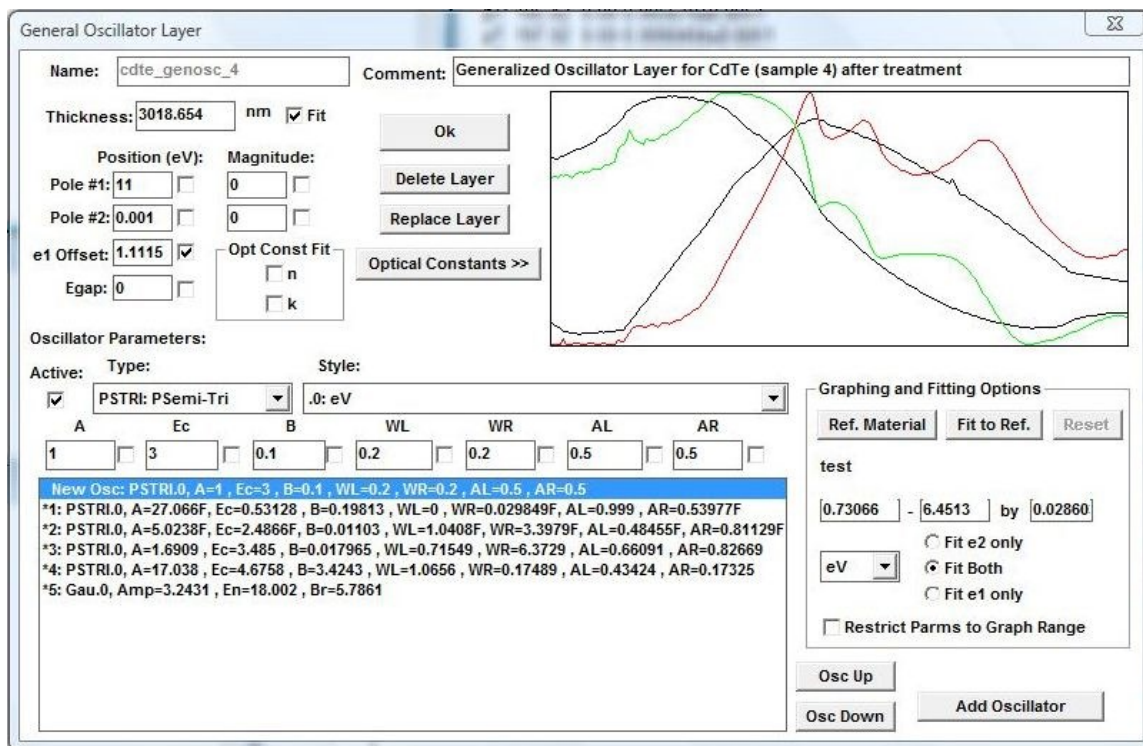


Figure A2.6: User-Defined “Genosc” Layer Window.

Effective Medium Approximation Layer

Comment: Effective Medium Approximation layer

Spectral range of optical constants: 1 - 20000 nm

Thickness: 48.630 nm ☒ Fit # of Constituents: 2

	Mat. Name	Fraction:	
Material #1	cdte_genos	75.281	
Material #2	void	24.719	<input checked="" type="checkbox"/> Fit
Material #3		0	<input type="checkbox"/> Fit

EMA Type

- ☒ Bruggeman
- ☐ Maxwell-Garnett
- ☐ Linear

Depolarization factor: 0.33333 ☐ Fit

Optical Constants >>

Opt Const Fit

- ☐ n
- ☐ k


Ok

Replace Layer

Delete Layer

Figure A2.7: EMA Layer Window.

Calculate MSE

 MSE calculated for current model and currently selected experimental data:

NFit = 14, Ndata = 5850

MSE = 22.32

MSE0 = 22.294

OK

Figure A2.8: MSE Test Results Window.

Appendix 3

Practical Use Study

In addition to the measurement and analysis work for this dissertation, it was desired to use the knowledge of SE gained to propose a production use, for the purpose of demonstrating the potential of SE as a standard quality monitoring system. This project was deemed insufficiently relevant to the primary objective to include in the main body, but is presented here for convenience. A brainstorming session was held to determine the form of the project. The Advanced Deposition System (ADS) was in the final planning stages at the time, and a working simulation already existed (this concept was later modified to save cost but is functionally similar to the completed system that became operational at the ERC in 2010). Therefore it was decided to propose installing an ellipsometer into the ADS for inline quality measurement. Since the ADS was too small to mount an entire ellipsometer inside it, the obvious solution was to disassemble an existing ellipsometer, provide a custom mounting solution for the detector and light source, mount the supporting equipment (lamps, power supply, processor, etc.) on an external cabinet, and reconnect the components via cables, integrating the ellipsometer directly into the ADS.

Detailed measurements were taken of the VASE ellipsometer in the CIF. A model of the detector and light source was created in the same 3D modeling software that had been used to model the ADS. A copy of the simulated ADS model was then added into the file, and mounting location and mechanical solutions were determined. The resulting simulation was then used as a demonstration of the feasibility of performing in-situ SE as part of a CdTe device production process.

Results for the Practical Use Study are shown in Figures A3.1 through A3.3. The ADS system as proposed at the time the study began was used as the starting point for the design. Due to space constraints and the desire to take direct reflection measurements as per the Baseline Study, it was decided to mount the ellipsometer into the forward area of the floor of the deposition chamber, so that it would scan the samples from below. The ADS system design as modified for the Study is shown in Figure A3.1.

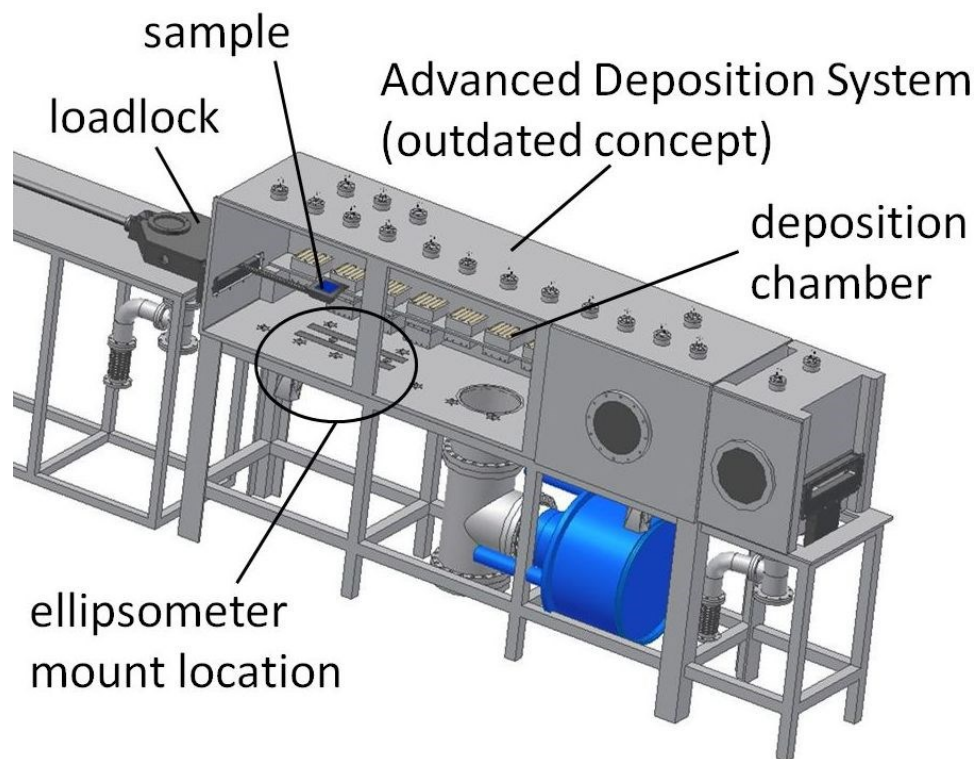


Figure A3.1: Proposal for Installation of In-situ SE Capability into the ADS (model by Toby Dhooge).

A major concern was whether to mount the ellipsometer in the vacuum or outside it. For maintenance reasons, it was decided that mounting inside the chamber could present unacceptable risk to both the equipment and production rate, so it was mounted outside. The general concept was modeled on an NREL design for in-situ SE of silicon wafers. NREL believed it would be possible to account for the glass in modeling. As shown in Figure A3.2, the

ellipsometer observes the sample through a pair of windows in the bottom of the vacuum chamber.

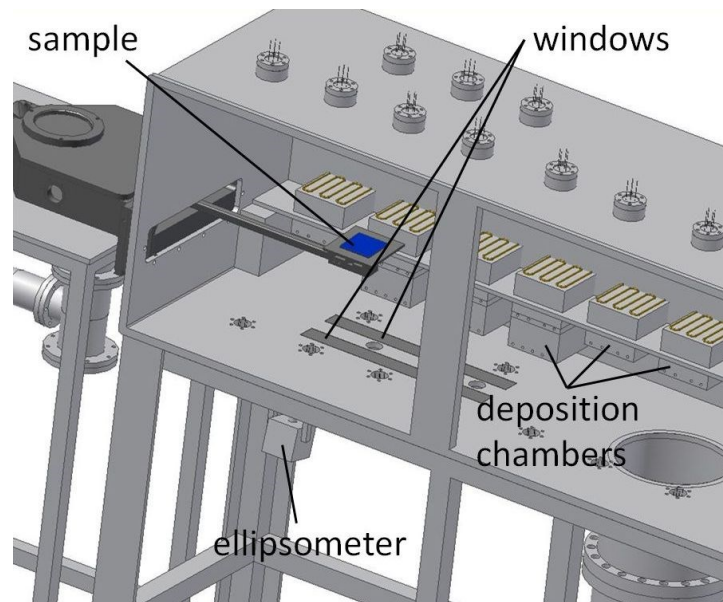


Figure A3.2: Ellipsometry Bay Windows (model by Toby Dhooge).

Figure A3.3 shows how the ellipsometer could be mounted onto the bottom of the vacuum chamber. The detector and light source both are mounted on gimbals which ride on a rail. This allows the horizontal location, beam angle, and target sample location to be adjusted manually when the ellipsometer is maintained. The light beam travels through one window and out the other.

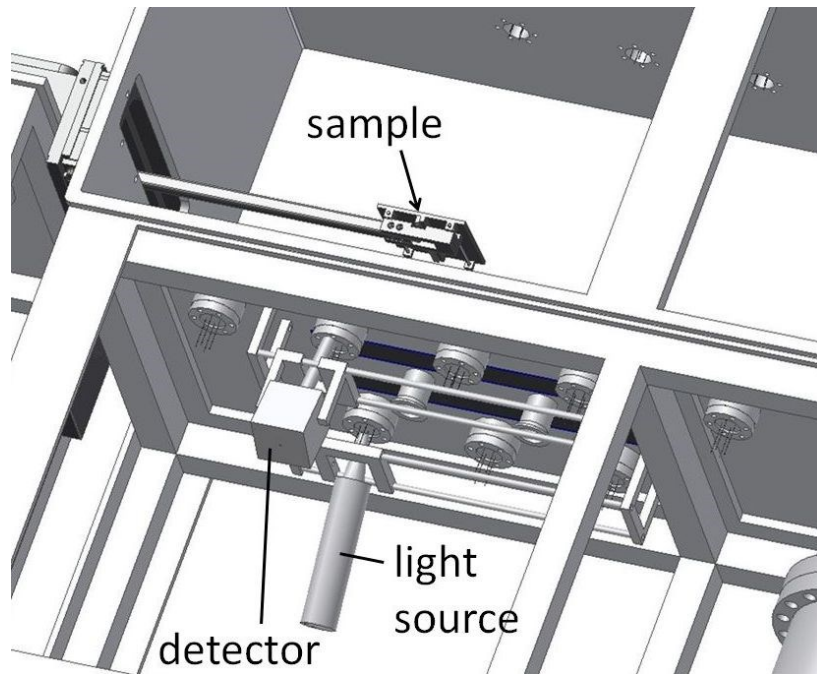


Figure A3.3: Ellipsometer Mounting Rack (model by Toby Dhooge).

List of Abbreviations, Units, and Model Numbers

<u>abbreviation</u>	<u>augmentation</u>
.dat	data file, a filetype used by WVASE32 software to store measured SE data.
.env	environment file, a filetype used by WVASE32 software to store data on a SE model optimization project.
.mat	material file, a filetype used by WVASE32 software to store simulated material properties.
.mod	model file, a filetype used by WVASE32 software to store simulated models of thin films.
2D	two dimensional
3D	three dimensional
Å	angstrom(s) (10 ⁻¹⁰ meters)
ADS	Advanced Deposition System, a CdTe production system built in 2010 at the ERC.
Band Gap	Photon energy required to cause an electron to change to a state where it can be conducted within a material.
Br	bromine
Br treatment	shorthand for the CH ₃ OH:Br immersion process in CdTe device production.
Br-treated sample	Sample of completed device exposed to Br treatment.
CdCl ₂	cadmium chloride
CdS	cadmium sulfide
CdS sample	Sample removed from production process immediately after CdS deposition.
CdTe	cadmium telluride
CdTe sample	Sample removed from production process immediately after CdTe deposition.

CH ₃ OH:Br	methanol-bromine mixture used as a chemical etching solution
CIF	Central Instrument Facility on the Colorado State University main campus
CIGS	copper indium gallium selenide
Cl	chlorine
Cl treatment	shorthand for the CdCl ₂ deposition process in CdTe device production.
Cl-treated sample	CdTe device removed from the production process immediately after Cl treatment.
cm	centimeter (10 ⁻² meters)
Co.	Company
CO ₂	carbon dioxide (“dry ice” in solid form)
CP	critical point(s)
CPPB	critical-point parabolic band
CSU	Colorado State University
Cu	copper
Cu treatment	shorthand for the CuCl deposition process in CdTe device production.
Cu-treated sample	Sample of completed CdTe device.
CuCl	copper chloride
Dektak 150	profilometer produced by Veeco, used by Abound Solar
EDS	energy dispersive X-ray spectroscopy
edit params	menu used by WVASE32 software for editing variables in the fit window.
EMA	effective medium approximation
ERC	Engineering Research Center on the Colorado State University foothills campus
eV	electron volt ($1.60217646 \times 10^{-19}$ joules)
FTO	fluorinated tin oxide

GaAs	gallium arsenide
genosc	generalized oscillator (a user-defined oscillator model)
GW	Gigawatt(s) (10 ⁹ watts)
ID	identification
Inc.	Incorporated
IR	infrared
J	joule(s)
JCPDS	Joint Committee on Powder Diffraction Standards
JSM-6500F	scanning Electron Microscope, manufactured by JOEL, Ltd., at the CIF.
kW	kilowatt(s) (10 ³ watts)
Ltd.	Limited
M-2000	ellipsometer produced by J.A. Woollam Co., Inc.
mm	millimeter(s) (10 ⁻³ meters)
MSE	mean square error
MW	Megawatt(s) (10 ⁶ watts)
NIR	near-infrared radiation
nm	nanometer(s) (10 ⁻⁹ meters)
NREL	National Renewable Energy Laboratory in Golden, Colorado
O ₂	oxygen
Pavillion dv6700	computer produced by Hewlett-Packard, used for SE modelling
p-i-n	positive-intrinsic-negative semiconductor junction
p-n	positive-negative semiconductor junction
p-polarization	polarization of a light beam reflecting off of a surface in a plane formed by the incoming ray and the surface normal
PSEMI	oscillator type used in ellipsometry models for some positive-type semiconductor materials.

PV	photovoltaic
RMS	root mean square
SD	sample standard deviation
SD%	absolute value of a sample standard deviation divided by the sample average and expressed as a percentage.
SE	spectroscopic ellipsometry
SEM	scanning electron microscopy
semi-inf	semi-infinite (too large to produce interference effects)
Si	silicon
SiO ₂	silicon dioxide (glass in amorphous form)
SnO ₂	tin oxide
SnO _x :F	fluorinated tin oxide (also known as FTO)
s-polarization	polarization of a light beam parallel to a surface which reflects the beam.
TEC-15	tempered glass produced by Pilkington Glass in the United Kingdom, with a three layer coating.
TEC-15 sample	sample of TEC-15 substrate removed from the deposition system production line prior to entering the vacuum chamber.
TL	Tauc-Lorentz (a type of oscillator mathematical model)
TW	Terawatt(s) (10 ¹² watts)
μm	micrometer (s) (10 ⁻⁶ meters)
USB	Universal Serial Bus
VASE	variable angle spectroscopic ellipsometry, also, an ellipsometer produced by J.A. Woollam Co., Inc., at the CIF
Woollam	J.A. Woollam, Co., Inc., a company with headquarters in Lincoln, Nebraska
WVASE32	software package developed by J.A. Woollam Co., Inc., for use with the VASE ellipsometer.

XRD	X-ray diffraction
XRF	X-Ray fluorescence